Acoustics of Historic Buildings : Intercomparison of Numerical Methods for Coupled Spaces & Sound Scattering by Piers and Columns in Gothic and Classical Architecture

Antoine Weber

Antoine Weber. Acoustics of Historic Buildings : Intercomparison of Numerical Methods for Coupled Spaces & Sound Scattering by Piers and Columns in Gothic and Classical Architecture. Sound [cs.SD]. Sorbonne Université, 2022. English. NNT : 2022SORUS269 . tel-03853349

HAL Id: tel-03853349
https://theses.hal.science/tel-03853349v1

Submitted on 15 Nov 2022

SORBONNE UNIVERSITÉ
ED 391 - SCIENCES MÉCANIQUES, ACOUSTIQUE, ÉLÉCTRONIQUE ET ROBOTIQUE DE PARIS
INSTITUT JEAN LE ROND ∂'ALEMBERT

Acoustics of Historic Buildings: Intercomparison of Numerical Methods for Coupled Spaces & Sound Scattering by Piers and Columns in Gothic and Classical Architecture

Présenté par:
ANTOINE WEBER

Pour obtenir le grade de:
DOCTEUR DE SORBONNE UNIVERSITÉ

Spécialité: ACOUSTIQUE

Devant le jury composé de:

RÉGIS MARCHIANO	*Prof.*	*Sorbonne Université*	Président
TREVOR COX	*Prof.*	*University of Salford*	Rapporteur
NING XIANG	*Prof.*	*RPI*	Rapporteur
ARIANNA ASTOLFI	*Ass. Prof.*	*Politecnico di Torino*	Examinatrice
BRIAN F. G. KATZ	*DR*	*CNRS*	Directeur

OCTOBRE 2022

Contents

Abstract

Modeling the acoustics of historic buildings such as the Cathédrale Notre-Dame de Paris is of interest for historical and musicological research, in particular to study past states that are no longer measurable today and to experience them through virtual reconstruction. These spaces, with their often extraordinary architecture, present a challenge from this point of view. The thesis is concerned with three aspects.

The first part focuses on the development and evaluation of experimental tools for physical modeling using room acoustic scale models, a tool still widely used to study complex spaces such as concert halls. Three source designs are evaluated in terms of omnidirectionality, which is difficult to achieve at small scales over a wide frequency range. On the receiver side, two approaches are tested to capture the directionality of the sound field, which is crucial from the perspective of our perception.

These buildings can sometimes consist of several interconnected rooms, as is the case with cathedrals composed of different liturgical spaces, which can lead to acoustic couplings between them and thus to non-exponential sound decays. A round robin type study is carried out involving the main numerical methods used today, in order to evaluate their performance with respect to this phenomenon. A 1:20 scale model of a simplified coupled volume system, representing a concert hall, was measured to serve as a physical realistic reference.

The last part deals with the study of sound scattering by column and pier shafts used in Ancient Greek and Gothic architecture. Typical fluted columns as well as some selected geometries in the Cathédrale Notre-Dame de Paris are characterized and the audibility of the reflections is discussed. For this purpose, a numerical tool has been developed using the finite-difference time-domain method. To overcome the staircase approximation, the space near the boundaries of complex geometries is discretized by an unstructured mesh to fit them. The propagation is then treated together with the finite volume method in this part. The method is validated by comparisons with analytic solutions, other numerical methods, and by measurements on scale models of the piers of interest.

Résumé

La modélisation de l'acoustique de bâtiments historiques tels que la Cathédrale Notre-Dame de Paris présente un intérêt pour la recherche historique et musicologique, notamment pour étudier des états passés qui ne sont plus mesurables aujourd'hui et pour en faire l'expérience par une reconstruction virtuelle. Ces espaces, à l'architecture souvent extraordinaire, représentent un défi de ce point de vue. La thèse s'intéresse à trois aspects.

La première partie se concentre sur le développement et l'évaluation d'outils expérimentaux pour la modélisation physique à l'aide de maquettes acoustiques, un outil encore largement utilisé pour étudier des espaces complexes comme les salles de concert. Trois conceptions de sources sont évaluées en termes d'omnidirectionnalité, qui est difficile à obtenir à petite échelle sur une large gamme de fréquences. Du côté du récepteur, deux approches sont testées pour capturer la directionnalité du champ sonore, qui est cruciale du point de vue de notre perception.

Ces bâtiments peuvent parfois être constitués de plusieurs volumes interconnectés, comme c'est le cas des cathédrales composées de différents espaces liturgiques, ce qui peut conduire à des couplages acoustiques entre eux et donc à des décroissances sonores non exponentielles. Une étude de type round robin est réalisée impliquant les principales méthodes numériques utilisées aujourd'hui, afin d'évaluer leurs performances vis-à-vis de ce phénomène. Un modèle à l'échelle 1:20 d'un système de volumes couplés simplifié, représentant une salle de concert, a été mesuré afin de servir de référence physique réaliste.

La dernière partie traite de l'étude de la diffusion du son par les fûts de colonnes et de piliers utilisés dans l'architecture de la Grèce antique et gothique. Des colonnes cannelées typiques ainsi que certaines géométries sélectionnées dans la Cathédrale Notre-Dame de Paris sont caractérisées et l'audibilité des réflexions est discutée. À cette fin, un outil numérique a été développé en utilisant la méthode des différences finies dans le domaine temporel. Pour s'affranchir de l'approximation en escalier, l'espace proche des frontières des géométries complexes est discrétisé par un maillage non structuré pour s'y adapter. La propagation est alors traitée conjointement avec la méthode des volumes finis dans cette partie. La méthode est validée par des comparaisons avec des solutions analytiques, d'autres méthodes numériques, et par des mesures sur des modèles réduits des piliers d'intérêt.

Acknowledgements

There are many people who, in their own way, have made it possible for me to do this work, thanks to the help or inspiration they have given me. To all of them I would like to express my gratitude through these lines, in which, please, do not see any hierarchy.

I would like to thank Brian Katz, my thesis advisor, for agreeing to mentor me in this project, and for supporting me financially beyond the usual three years. I would also like to thank him for the different measurement sessions he allowed me to carry out abroad, in particular in the scale models of two future concert halls, and for introducing me to people I now hold in high esteem. I think of Eckhard Kahle and Evan Green of Kahle Acoustics, whom I thank for showing me how such projects are done, and for their help and expertise.

I would like to express my sincere thanks to each member of the jury. I thank Trevor Cox and Ning Xiang, the rapporteurs, for agreeing to review my manuscript and for doing so conscientiously. I greatly appreciated their constructive comments and corrections, which undoubtedly improved it greatly. I also thank the examinateurs, Regis Marchiano and Arianna Astolfi. It was a pleasure to have all four of them present at my defense, which is a rarity in these pandemic times. I appreciated their insightful questions that broadened my perspective.

I am very grateful to the Institut Jean Le Rond ∂'Alembert for providing me with an ideal environment to accomplish this work. My thanks go to the doctoral students and post-doctoral fellows for whom I have a certain admiration, being surrounded by them all is something very stimulating. I thank the alumni, Raphaël L., Thomas L., Barend B., Arthur L., Aurélie D., Mathis P., Antoine Lu., Antoine La., Valentin G., Virgile T., Alexis B., Sagar P., Alverède S., Hugo D., and Nelson J, for making me feel welcome and quickly integrated. I hope that I have kept up the traditions (long live ∂'Alembière!). I also thank all the others who arrived in the same year as me, Serena C., Adrien R., Ikram D., and Antoine M., and the following ones, Quentin B., Yutao L., Patricia V., Théo B., Camilla Z., Lucas P., Victor F., Ghita B.-E.-B., Ken V.M., Laureline J., Priscila D.M., Jacob M., Yvan G., Simon B., Mashid S., Guillaume D.L., Mikail S., Rodolphe G., Gabriel D., Cécilia G., Cécile R., François R., Camille M., Marcellin P., Grégoire L., Alvaro A.G., Thomas F., Sarah V., Damien B., Nicolas C., Yann B., Daniel M., Victor S.C., Antonio S., Kwami M., Pierre V.D.V., Alexandre L., Amine S., Krishan B., Lila S., Samy L., Alejandro Q.R., and Ludovic A. I have shared with them all moments that have brightened my spirit when it needed it most. A special thanks goes to the best office members, aka 317b, Jeanne V., Franck Z., Toufik S., Cécile L., Clément S., Daniele N., Alice J., and Manuel G., with whom it was a pleasure to share this space more or less every day.

I would like to thank the members of the "Sound and Space" team: David P.-Q., David T., Franck Z. (again), Gonzalo V.C., Sarabeth M., Elliot C.-D., Julien D.M., Martin L., Nolan E., Peter S., Aidan M., Piergiovanni D., and Pierre M., who taught me a lot about the different aspects and disciplines that our field involves.

I thank Laurent Quartier for his help in my experiments and especially in the construction of the columns and pillars. I thank the members of the SAF members, Simona

Otarasanu, Sandrine Bandeira, and Olivier Labbey for making our lives easier and without whom the Institute would not function.

I thank all my friends outside the laboratory, in Paris, Aix, and elsewhere for the support they have given me during this period.

Finally, I would like to thank my parents, my sister Elsa, and my brother Samuel for always being there for me. I am lucky to have you.

Abbreviations

BEM boundary element method

BRIR binaural room impulse response

BVD bounded Voronoi diagram

CVD centroidal Voronoi diagram

DOA direction of arrival

DTF directional transfer function

EDC energy decay curve

FD finite difference

FDFV finite difference finite volume

FDTD finite difference time domain

FFT Fast Fourier Transform

FV finite volume

GA geometrical acoustics

HRIR head related impulse response

HRTF head related transfer function

ILD interaural level difference

ITD interaural time difference

JND just noticeable difference

NFFFT near-field to far-field transform

PML perfectly matched layer

RDLD Reflected-to-Direct Level Difference

RIR room impulse response

SDM Spatial Decomposition Method

SNR signal-to-noise ratio

TDOA time difference of arrival

TSCS total scattering cross section

Chapter 1

Introduction

1.1 Context

The heritage of certain historic buildings is intrinsically linked to their acoustics. Ancient amphitheaters or Gothic cathedrals are striking examples. Thus, these important spaces for historical or archaeological research have given rise to multidisciplinary fields of research such as archaeoacoustics and music archaeology (Aletta et al., 2020; Blake et al., 2015; Scarre et al., 2006). A typical problem is that the shape of a room and its materials define its acoustics which will consequently influence the oral or musical practices that took place there, and that, at the same time, such building can evolve in the course of its history. This more holistic approach is consistent with recent UNESCO resolutions to promote the protection and safeguarding of the world's heritage, both tangible and intangible (UNESCO, 2003, 2017), which are intimately linked for these spaces.

Several research projects have been interested in historic buildings of exceptional acoustics and architecture. We can mention the ERATO (Identification, Evaluation, and Revival of the Acoustical Heritage of Ancient Theatres and Odea) project (Rindel, 2011a; Yüksel et al., 2005), concerned with the study of Greek and Roman theaters and odeons. The CAHRISMA (Conservation of the Acoustical Heritage by the Revival and Identification of the Sinan's Mosque's Acoustics) project (Yüksel, 2000; Yüksel et al., 2003) was focused on the study of Sinan's Mosques and Byzantine Churches, including *Süleymaniye Mosque* and *Hagia Sophia*. The recent EVAA (Experimental Virtual Archaeological-Acoustics) program (EVAA program, 2021) coordinates several projects interested in acoustic cultural heritage, studied with the help of simulations and virtual reality environments (Katz et al., 2019). Among these is the PHE (Past Has Ears) project (Katz et al., 2020a; PHE project, 2021), which focuses on the investigation of methods to simulate and virtually experiment European cultural heritage monuments where acoustics are an important parameter for historical and musicological research.

These historic buildings, crossing the centuries for some, can be completely destroyed, partially deteriorated, or have evolved according to the renovations and architectural tastes of the times. This is the case of two buildings of the PHE project, *e.g.* the *Teatro La Fenice* opera house in Venice, Italy, and the *Cathédrale Notre-Dame de Paris* in France. Both have experienced several fires, most recently in 1996 for the former, which was then rebuilt identically in 2004, and in 2019 for the latter, which is also scheduled to be returned to its state before the incident. Fortunately, they have been the subject of room acoustic measurements to safeguard this part of the intangible heritage. However, the measurements can only reflect the state of the building at the time and at the positions they were carried out. In order to access the acoustics of these spaces in their past states, it is necessary to use modeling methods to simulate them.

Although having acquired a certain maturity, the physical or numerical methods employed for objective or subjective studies in this context still have many aspects that remain to be improved. All the more so if one takes into account all the elements of the transmission chain, *i.e.* the sources, the space, and the listener, that must be reproduced in order to, in the end, achieve an auralization faithful to a real listening situation. The thesis then focuses on different aspects that seem important to improve the modeling of the acoustics of these spaces of exceptional architecture and history.

1.2 Scope of the thesis

1.2.1 Room acoustic scale modeling and coupled volumes

A physical modeling method commonly used in architectural acoustics is the acoustic scale model. It allows to reproduce the physical phenomena occurring at real scale but the performances are often limited by the material of measurements. In a first part we are therefore interested in improving these methods for room acoustic studies. Among our objectives, we wish to investigate some solutions to approach what can be done at real size. First, our goal is to obtain sources that can be used at scale factors of 1:10 to 1:20, and thus operate in the ultrasonic domain while being omnidirectional. Secondly, we evaluate two methods for making recordings that allow us to account for the directionality of the sound field, which is crucial in the context of perception in rooms.

The rooms or volumes constituting the historic buildings can be coupled from an acoustic point of view, such as cathedrals that are composed of different liturgical spaces. It seems then relevant to evaluate the numerical methods used for their modeling with respect to this phenomenon. A round robin study is then conducted for this purpose. As in other studies of this type, a physical reference is obtained from measurements on a 1:20 scale model representing in this case a simple system of two volumes inspired by the dimensions of an existing concert hall with a reverberation chamber, demonstrating the interest of the method when it comes to accuracy for wave phenomena.

1.2.2 Sound scattering by Gothic piers and Classical columns

A feature that can be found in many historic buildings is the use of columns and piers. This is necessary for structural reasons, in order to obtain closed rooms extended in surface, and due to the knowledge and techniques of construction of each era, they can sometimes be present in great number. Nevertheless, they are a challenge from the point of view of some numerical methods used nowadays and their acoustic impact has not been studied to our knowledge.

The impact of a set of circular columns on the acoustic parameters of a concert hall has been studied (Suzumura et al., 2000), but here what interests us at first is the study of the reflections of these objects in isolation. These obstacles to sound are presented in very diverse shapes often reflecting the architectural style in which the building fits. We are concerned with Gothic and Classical architecture. Consequently, like the contributions that were made for the characterization of scattering surfaces, it seems relevant to propose at first methods to evaluate the sound scattering from these objects. It is hoped that this can be used to improve, evaluate, or invent approaches for the modeling of these elements in numerical room acoustic simulations.

For this, it is necessary to use physically accurate methods. Thus, part of the work is devoted to the development of a numerical simulation tool that can handle arbitrary geometries and obtain reliable results efficiently over a wide frequency band. There are methods in the frequency domain solving the Helmholtz equation, but since our objects have a priori a very different behavior depending on the frequency, it seems relevant to use a method in the time domain solving the wave equation. In addition, they allow to visualize the propagation of transients more easily which offers an advantage. Here again we use scale models to have a physical reference to measure and compare.

Instead of looking at the acoustics of rooms with columns as a whole, the audibility of the reflections induced by these obstacles is discussed in relation to the audibility thresholds reported in the literature for single reflections. We then place ourselves in the situation where a source is far from the isolated column, and the listener relatively close to the latter. This is a priori the most favorable case to hear the reflection of the object.

1.3 Thesis organization

Chapter 2 presents a state-of-the-art covering relatively different topics relevant to the problems addressed in this thesis, with fundamentals of room acoustics, coupled volumes, and the modeling methods, but also sound scattering in room acoustics. A review of the literature on the audibility of reflections is given.

Part I focuses on the modeling methods used in room acoustics. In chapter 3, different solutions are proposed to improve the measurements in room acoustic scale models. We are concerned in sources and receivers, so that we aim to achieve the performance and capabilities of full-scale measurements. Our proposals are evaluated accordingly. In chapter 4, we present the round robin study that aims at evaluating numerical methods in the context of the simulation of coupled volume acoustics. The results have been presented at the *23rd International Congress on Acoustics* at Aachen, Germany, in 2019 (Weber et al., 2019).

Part II deals with the study of sound scattering by architectonic columns and piers. Chapter 5 presents the hybrid numerical simulation tool employing the difference and finite volume formalisms developed to conduct these studies. A large part of it concerns its validation. Chapter 6 presents the work carried out to study the scattered reflections from columns and piers found in Gothic and Ancient Greek architecture. The part of this work on Gothic piers of Notre-Dame de Paris is published in the Special Issue “Acoustics, Soundscapes and Sounds as Intangible Heritage” of the journal *Acoustics* (Weber et al., 2022).

Chapter 2

State-of-the-art

2.1 Fundamentals of room acoustics

2.1.1 Room impulse response

The propagation of sound in air, if we neglect the absorption phenomena, can be described by the homogeneous wave equation. When a sound source emits a signal in an enclosed space, the sound propagates in this way to a receiver, then reflections on the walls will produce successive arrivals. The room will thus have an effect on the transmitted signal, which can be characterized by the transfer function of the source-room-receiver system, the room impulse response (RIR).

An example of a RIR is represented at the top of fig. 2.1 in the form of an echogram. It is often conceptually decomposed into three parts. First there is the direct sound, whose arrival time depends only on the relative position of the source and the receiver. A second part is composed of the early reflections, which are more separated in time than the third

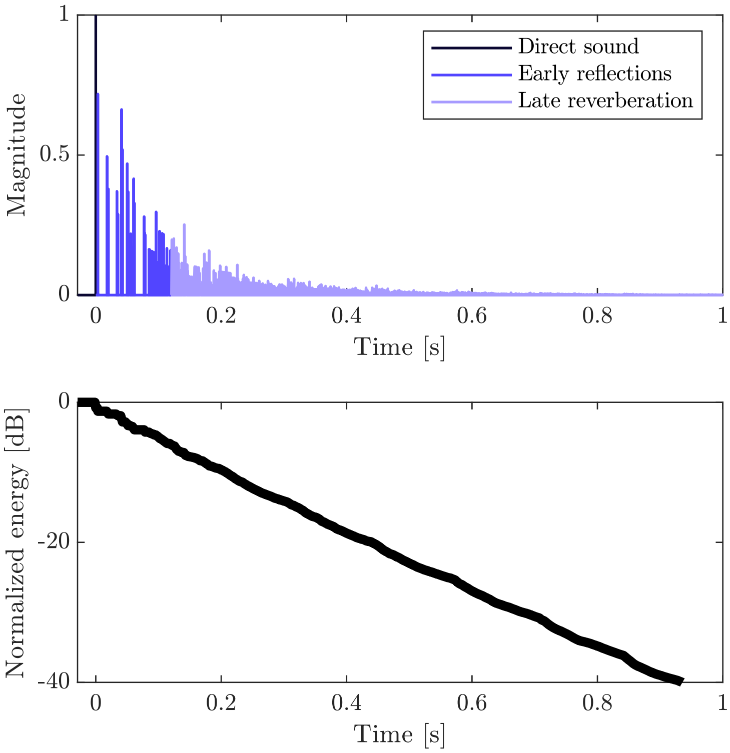

Figure 2.1 Example of a RIR, represented as an echogram (top), and its energy decay curve (EDC) in dB (bottom).

part, the late reverberation formed by a multitude of reflections arriving at very close instants. This decomposition has an interest from a perceptive point of view because the early reflections have an important impact on the perception of the space. The transition time between the latter and the late part is not clearly defined. The "mixing time" has been proposed by Polack (1988), defined as the moment the echo density has reached a sufficient value over a certain time interval to consider the field as diffuse.

The reflections arrive with decreasing amplitudes as time progresses due to the spatial spread of the wavefront, the absorption at the walls and in the air. Beyond the mixing time, if we do not consider the frequency aspects, the impulse response can be seen as one realization of a statistical process, a noise modulated by a decaying exponential. Schroeder (1965) proposed to use the reverse integration of the squared RIR, h^2_{room}, to estimate the ensemble average from only one single realization, resulting in the so-called energy decay curve (EDC),

$$EDC(t) = \int_t^{\infty} h^2_{\text{room}}(\tau)\, d\tau \,. \tag{2.1}$$

The result for the example is given at the bottom of fig. 2.1. It appears to be roughly linear with the vertical axis in dB, illustrating the exponential decay.

2.1.2 Room acoustic parameters

From a RIR, several so-called room acoustic parameters can be estimated. They are defined and standardized in ISO 3382-1 (2009). They have been proposed based on their correlation with perceptual attributes used to subjectively describe the sound perceived in a room. They are used among practitioners to evaluate or as objective criteria to be respected for spaces where good acoustics are of major importance, *e.g.* from the concert hall for good experiences to the open space for acoustic comfort. Some of them are described in the following.

The most known acoustic parameter is the reverberation time, being the first to be introduced by Sabine (1922). It is defined as the duration required for the sound energy level to decrease by 60 dB after the sound source is stopped. Measured RIRs usually contain background noise which limits the dynamic range and prevents it from being estimated directly over such an interval. ISO 3382-1 (2009) suggests to extrapolate it from smaller intervals. They are then noted T_{20} or T_{30} for the times estimated with the intervals from -5 dB to -25 dB or from -5 dB to -35 dB, respectively.

Early decay time, EDT, is similar but it evaluated using the first 10 dB range, *i.e.* starting from the direct sound. It is actually more correlated with perceived reverberance than the reverberation time. Contrary to the latter, it is strongly affected by the presence or absence of early reflections, and, therefore, varies more in relation with the source and receiver positions.

Strength, G, is defined as the ratio between the energy received at a position and that emitted by the same source in free field at 10 m, expressed in dB as

$$G = 10 \log_{10} \left(\frac{\int_0^{\infty} h^2_{\text{room}}(t)\, dt}{\int_0^{\infty} h^2_{\text{free},10m}(t)\, dt} \right) , \tag{2.2}$$

It characterizes the amplification provided by the room and is perceptually correlated with the perceived loudness that relates to our perception of sound intensity.

Clarity, C_{t_e}, is defined as the between early and late energy, expressed in dB as

$$C_{t_e} = 10 \log_{10} \left(\frac{\int_0^{t_e} h_{\text{room}}^2(t)\, dt}{\int_{t_e}^{\infty} h_{\text{room}}^2(t)\, dt} \right) , \tag{2.3}$$

where t_e can be equal to 50 ms or 80 ms, whether the signal of interest is speech or music, respectively. It relates to the perceived clarity of sound. For speech, the early reflection must arrive with shorter delays compared to music as in this case it relates to speech intelligibility that starts to decreases with longer ones.

Definition, D_{t_e}, has also been proposed, calculated as

$$D_{t_e} = \frac{\int_0^{t_e} h_{\text{room}}^2(t)\, dt}{\int_0^{\infty} h_{\text{room}}^2(t)\, dt} , \tag{2.4}$$

mostly used with $t_e = 50\,\text{ms}$ for speech signals. It is directly related to clarity as

$$C_{t_e} = 10 \log_{10} \left(\frac{D_{t_e}}{1 - D_{t_e}} \right) . \tag{2.5}$$

Center time, T_S, is defined as the temporal barycenter of energy of the RIR, expressed in s as

$$T_S = \frac{\int_0^{\infty} t h_{\text{room}}^2(t)\, dt}{\int_0^{\infty} h_{\text{room}}^2(t)\, dt} . \tag{2.6}$$

It can be used as an alternative to the previous energy ratios, providing an estimate for the temporal energy distribution, less arbitrary.

All the parameters presented above can be estimated from omnidirectional RIRs and do not account for our spatial perception of sound. Different parameters have been proposed for this purpose. Early lateral energy fraction, J_{LF}, originates from a proposition of Barron et al. (1981), related to the perceived width of the source, expressed as

$$J_{\text{LF}} = \frac{\int_{5\,\text{ms}}^{80\,\text{ms}} h_{\infty}^2(t)\, dt}{\int_0^{80\,\text{ms}} h_{\text{room}}^2(t)\, dt} , \tag{2.7}$$

where h_{∞} is the RIR obtained with a figure-of-eight pattern microphone at the same position as the omnidirectional RIR, h_{room}, with the null pointed towards the source.

The late lateral energy relative level, L_{J}, is related to listener envelopment and spaciousness, expressed in dB as

$$L_{\text{J}} = \frac{\int_{80\,\text{ms}}^{\infty} h_{\infty}^2(t)\, dt}{\int_0^{\infty} h_{\text{free},10m}^2(t)\, dt} . \tag{2.8}$$

Similarly, binaural room impulse responses (BRIRs) measured with a dummy head can be used to estimate a parameter called inter-aural cross correlation coefficient, IACC_{t_1,t_2}, describing the dissimilarity of the signal at the ears. It is defined as

$$\text{IACC}_{t_1,t_2} = \max_{-1\,\text{ms} < \tau < 1\,\text{ms}} |\text{IACF}_{t_1,t_2}(\tau)| , \tag{2.9}$$

where IACF_{t_1,t_2} is the normalized inter-aural cross correlation function expressed as

$$\text{IACF}_{t_1,t_2}(\tau) = \frac{\int_{t_1}^{t_2} h_{\text{L}}(t) h_{\text{R}}(t)\, dt}{\sqrt{\int_{t_1}^{t_2} h_{\text{L}}^2(t) h_{\text{R}}^2(t)\, dt}} , \tag{2.10}$$

where h_{L} and h_{R} are the binaural RIR at the left and right ear canal, respectively. The time interval $[t_1, t_2]$ can be adapted to early or late part of the BRIR to better correlate with apparent source width or spaciousness, respectively.

In the course of research in auditory perception, just noticeable differences (JNDs), defined as the smallest relative or absolute difference from which a difference is perceptible, have been established for these parameters and are given in ISO 3382-1 (2009). While the presented parameters cover a wide range of perceptual attributes, there are many others that are not covered here or in the standard. These parameters are globally adapted and intended for performance spaces. However, there are spaces where the sound field and its decay are such that these are no longer appropriate, or even become misleading, such as for spaces consisting of several sub-volumes called coupled spaces.

2.2 Acoustics of coupled spaces

When several rooms are connected to each other by partially or fully sound-transparent openings, an exchange of acoustic energy is possible and this can lead to non-exponential decays. This is referred to as coupled spaces or volumes. To better appreciate the conditions under which this can happen, a statistical model for two connected rooms is given in section 2.2.1. Although it may occur unintentionally in some environments such as in worship spaces due to their internal layout for liturgy, it can be of interest especially for concert halls. This is further detailed in sections 2.2.2 and 2.2.3. The acoustic parameters and methods used to describe such sound decays are given in section 2.2.4.

2.2.1 Statistical models

A statistical-acoustics model of energy decay in a system of two coupled volumes was first given by Davis (1925b), and later by Cremer et al. (1982). Kuttruff (2009) gives a more general formulation for systems composed of any number of rooms. These models are based on diffuse-field theory assumptions, according to which the reverberant energy in each volume decays exponentially, as described by Sabine's model, and rooms interact through the exchange of diffuse energy. These models lead to the resolution of a system of ordinary linear differential equations. This system for N rooms can be written

$$V_i \frac{dE_i}{dt} = -\frac{cA_iE_i}{4} + \sum_{\substack{j=1 \\ j\neq i}}^{N} \frac{cS_{ij}(E_i - E_j)}{4} \tag{2.11}$$

where $i = 1, ..., N$, c is the speed of sound, E_i denotes the average energy density in the ith room, V_i is the volume of the ith room, and A_i is the equivalent absorption of the ith room calculated according to Sabine's model as $S_i\bar{\alpha}_i$, where S_i and $\bar{\alpha}_i$ are the total surface area and the averaged absorption coefficient of the ith room, respectively. The coupling area between room i and an adjacent room j is denoted S_{ij}. The resulting system of first order ordinary differential equations, eq. (2.11), can be presented in matrix form and solved by finding the corresponding eigenvalues and eigenvectors, determining the constant terms from initial conditions.

Summers (2005) provides a revised derivation of Cremer et al. (1982) and Kuttruff (2009) models in the case of two subspaces and it is summarized in the following. For a system of two coupled rooms, eq. (2.11) with sources can be written

$$V_1\frac{dE_1}{dt} = \frac{cS_{12}E_2}{4} - \frac{cS_{12}E_1}{4} - 2V_1\delta_1 E_1 + P_1\,, \tag{2.12a}$$

$$V_2\frac{dE_2}{dt} = \frac{cS_{12}E_1}{4} - \frac{cS_{12}E_2}{4} - 2V_2\delta_2 E_2 + P_2\,, \tag{2.12b}$$

where P_1 and P_2 are the source powers injected in the respective subrooms. δ_1 and δ_2 are the decay rate for the uncoupled rooms, following Sabine's theory,

$$\delta_1 = \frac{cA_1}{8V_1}\,, \qquad \delta_2 = \frac{cA_2}{8V_2}\,. \tag{2.13}$$

For a system of linear differential equations, the solutions are linear combinations of the two eigenfunctions of the system, resulting in solutions in the form

$$E_1(t) = E_{I1}e^{-2\delta_I t} + E_{II1}e^{-2\delta_{II} t}\,, \tag{2.14a}$$

$$E_2(t) = E_{I2}e^{-2\delta_I t} + E_{II2}e^{-2\delta_{II} t}\,, \tag{2.14b}$$

where

$$\delta_I = \frac{\delta_1+\delta_2}{2} - \sqrt{\left(\frac{\delta_1-\delta_2}{2}\right)^2 + \kappa^2\delta_1\delta_2}\,, \tag{2.15a}$$

$$\delta_{II} = \frac{\delta_1+\delta_2}{2} + \sqrt{\left(\frac{\delta_1-\delta_2}{2}\right)^2 + \kappa^2\delta_1\delta_2}\,, \tag{2.15b}$$

are the eigenvalues of the matrix describing the coupled differential equations, with κ the mean coupling coefficient

$$\kappa = \sqrt{k_1 k_2}\,, \tag{2.16}$$

calculated as the geometric mean of the coupling coefficients of the subrooms

$$k_1 = \frac{S_{12}}{A_{11}}\,, \qquad k_2 = \frac{S_{12}}{A_{22}}\,, \tag{2.17}$$

where A_{11} and A_{22} are the total equivalent absorption surface area including the contribution of the coupling surface area

$$A_{11} = A_1 + S_{12}\,, \qquad A_{22} = A_2 + S_{12}\,. \tag{2.18}$$

The coefficients E_{I1}, E_{II1}, E_{I2}, and E_{II2} are determined by considering the initial energy densities

$$E_1(0) = E_{I1} + E_{II1}\,, \tag{2.19a}$$

$$E_2(0) = E_{I2} + E_{II2}\,, \tag{2.19b}$$

and by conservation of energy as it must be satisfied independently for the two decay rates of the system, yielding to two systems of coupled equations

$$\left(\frac{c}{4}A_{11} - \delta_I V_1\right)E_{I1} - \frac{c}{4}S_{12}E_{I2} = 0\,, \tag{2.20a}$$

$$\left(\frac{c}{4}A_{22} - \delta_I V_2\right)E_{I2} - \frac{c}{4}S_{12}E_{I1} = 0\,, \tag{2.20b}$$

$$\left(\frac{c}{4}A_{11} - \delta_{II} V_1\right)E_{II1} - \frac{c}{4}S_{12}E_{II2} = 0\,, \tag{2.20c}$$

$$\left(\frac{c}{4}A_{22} - \delta_{II} V_2\right)E_{II2} - \frac{c}{4}S_{12}E_{II1} = 0\,. \tag{2.20d}$$

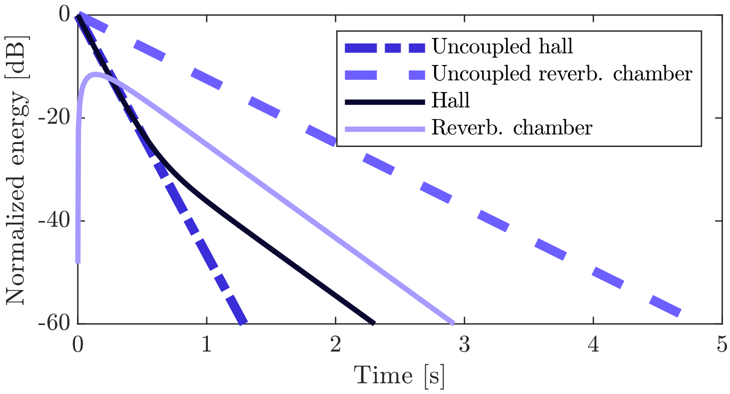

Figure 2.2 Energy densities for a system of two volumes in coupled and uncoupled configuration.

After manipulations, the constants are expressed

$$E_{I1} = \frac{E_1(0) - E_2(0)C_{II}}{1 - C_I C_{II}}\,, \tag{2.21a}$$

$$E_{I2} = C_I \frac{E_1(0) - E_2(0)C_{II}}{1 - C_I C_{II}}\,, \tag{2.21b}$$

$$E_{II1} = C_{II} \frac{E_2(0) - E_1(0)C_I}{1 - C_I C_{II}}\,, \tag{2.21c}$$

$$E_{II2} = \frac{E_2(0) - E_1(0)C_I}{1 - C_I C_{II}}\,, \tag{2.21d}$$

with

$$C_I = \frac{\frac{c}{4} S_{12}}{\frac{c}{4} A_{22} - 2\delta_I V_2}\,, \tag{2.22a}$$

$$C_{II} = \frac{\frac{c}{4} S_{12}}{\frac{c}{4} A_{11} - 2\delta_{II} V_1}\,. \tag{2.22b}$$

Eventually, the values $E_1(0)$ and $E_2(0)$ are determined considering the steady state established with the presence of sources, resulting in

$$E_1(0) = \frac{4}{c} \frac{A_{22} P_1 + S_{12} P_2}{A_{11} A_{22} - S_{12}^2}\,, \tag{2.23a}$$

$$E_2(0) = \frac{4}{c} \frac{A_{11} P_2 + S_{12} P_1}{A_{11} A_{22} - S_{12}^2}\,. \tag{2.23b}$$

Figure 2.2 shows an example of a two-volume system with a hall and a reverberation chamber, the latter more reverberant than the former. Their energy decay in the uncoupled case is indicated by a dash-dotted and dashed line, showing their reverberation times of about 1.3 s and 4.8 s, respectively. In the coupled case, the source is present in the hall. The nonlinear decay in this volume is clearly visible, with two slopes as predicted by the model. In the reverberation chamber, the energy density increases first then decreases following the same late decay.

2.2.2 Coupled volumes in concert halls

We have seen through the statistical model that a room coupled to a more reverberating volume leads to a non-exponential sound decay. This effect has been applied in the design of some concert halls by coupling the main hall hosting the audience, *i.e.* the receivers, and the musicians, *i.e.* the sources, with a more reverberating volume called reverberation chamber. In this case, we have seen that the sound decay is fast at the beginning of the response followed by a slower decay. This has the advantage of producing both a high perceived clarity and reverberance, two characteristics that are contradictory in single-volume rooms.

Concert halls were historically dedicated to a specific type of music, thus being able to accommodate only certain musical ensembles (Beranek, 2004). Nowadays, some concert halls integrate systems allowing variable acoustics in order to adapt the space to the music of a soloist as well as to that of a symphonic orchestra or an intermediate ensemble. For this purpose, several techniques have been developed, some of them are referred to as active because they imply to control the sound field using electro-acoustic transducers (Poletti, 2013). The others are called passive because they use architectonic methods (Boone et al., 2008; Hyon et al., 2021). They have the advantage of preserving the natural aspect of the sound propagation, without the intervention of microphones and loudspeakers. Some coupled volume systems are part of this group and offer variable acoustics by adjusting the coupling area between the main room and the reverberation chamber.

Luizard (2013) lists about ten concert halls incorporating coupled volumes in their design, with and without the possibility of variable acoustics. We can quote the hall of the *Kultur- und Kongresszentrum Luzern* (Johnson et al., 1999) in Switzerland, that has a large reverberation chamber coupled to the hall with multiple rotating doors.

2.2.3 Coupled volumes in worship spaces

Coupled volume effects have also reported in several worship spaces. This is favored by the fact that they are often composed of several spaces of different liturgical functions forming volumes more or less coupled (Pedrero et al., 2014). Martellotta (2009, 2016) explained most of the anomalies he observed in the parameters measured in the Papal Basilicas in Rome, Italy, by means of coupled volume theory. Anderson et al. (2000) considered a coupled volume system to explain the acoustics of *Saint Paul's Cathedral* in London, the United Kingdom. The effect was measured in several churches (Boren et al., 2013; Carvalho, 1995; Chu et al., 2009; Magrini et al., 2002; Zamarreño et al., 2007). *Hagia Sophia* in Istanbul, Turkey, is a monumental building with several domes and sub-spaces, which presents non-exponential sound decays (Sü Gül, 2021; Sü Gül et al., 2018, 2016). Double slopes were found in other dome structures (Alberdi et al., 2019). Bayesian analysis, described briefly in the next section, was performed on the energy decays measured in *Bristol Cathedral* in the United Kingdom (Álvarez-Morales et al., 2019), or in the crypt of the *Catedral de la Santa Cruz de Cádiz* in Spain (Martellotta et al., 2018).

2.2.4 Acoustical coupling parameters

The parameters of ISO 3382-1 (2009) described in section 2.1.2 are not adapted to non-exponential decays, especially the reverberation time. Several quantifiers have been proposed to quantify a double slope effect. Some are based on ratios of decay times evaluated on different energy intervals, such as T_{60}/T_{15} (Ermann, 2005), LDT/EDT (Bradley et al., 2009), or LDT/T_{10} (Bradley et al., 2010) where LDT is the late decay time esti-

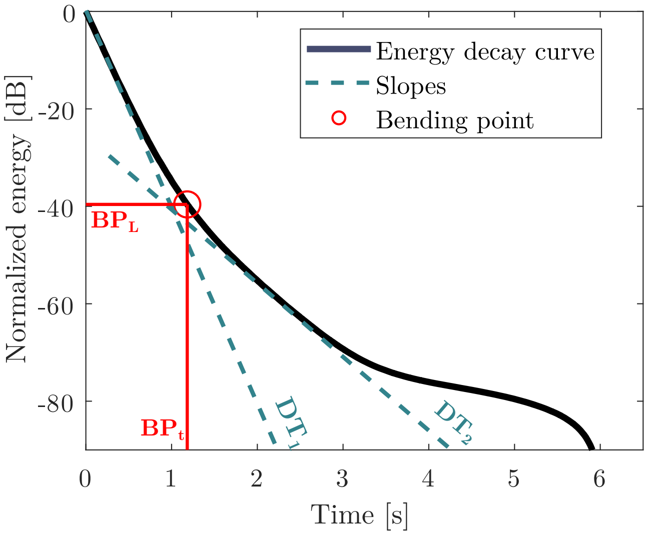

Figure 2.3 Double slope acoustical parameters estimated by Marching Line (Luizard et al., 2011) on an example of EDC.

mated from $-25\,\mathrm{dB}$ to $-35\,\mathrm{dB}$ on an EDC. Unfortunately, they do not allow a complete description of the decay, and can not always been obtained when the signal-to-noise ratio (SNR) is not high enough. Bradley et al. (2005, 2009) also proposed to use the decay ratio, *i.e.* the ratio between the decay time of the first and the second slope. To fully describe a double-slope non-exponential decay, they proposed to estimate conjointly ΔdB, defined as the length of the interval between the intersections of the two slopes with the vertical axis at $t = 0$, *i.e.* the direct sound.

Furthermore, in real spaces it is possible to observe energy decays with more than two slopes (Sü Gül et al., 2018). The different decay times can then be estimated with the help of Bayesian inference methods (Xiang et al., 2011, 2001, 2003). These methods assume that the EDCs are modeled by a sum of decreasing exponential functions. They are therefore said to be model-based.

Luizard et al. (2011) proposed a different method to estimate the different decay times. It is called the Marching Line method. It is based on a direct comparison between the decay curve and linear regressions. It provides the number of slopes and the corresponding decay rates, as well as the time and level of the bending points between two consecutive slopes. Figure 2.3 shows an example of the estimated parameters from a given EDC presenting a double slope. The employed parameters are the equivalent reverberation times DT_1 and DT_2 of the first and second slope, respectively, and the coordinates of the bending point in time BP_t and level BP_L, defined on the EDC.

2.3 Modeling methods in room acoustics

As already mention, the first statistical model was proposed by Sabine (1922). Its assumptions make it valid for rooms that are sufficiently mixing and weakly absorbing. Eyring (1930) and Kuttruff (2016) proposed other models more adapted for rooms that are more absorbing. Summers et al. (2004) proposed to improve the equivalent models of Cremer et al. (1982) and Kuttruff (2009) for coupled volumes using their assumptions to better account for the non-diffuse transfer of energy. Luizard et al. (2012) proposed a model that account for the spatial dependency through an added term similarly to the revised theory of Barron et al. (1988).

These statistical models can be used to simulate the late reverberation of the RIRs of some spaces, and could be perceptually valid. However, they can not simulate the early reflections, that strongly depend on the relative positions of the source, the receiver, and the environment. In order to model the sound propagation in rooms for objective studies, visualization, or auralization, different methods have been developed. We present in section 2.3.1 the main numerical methods grouped into two families: the geometrical and wave-based methods. In section 2.3.2 is presented the physical methods using acoustics scale models, with their history, the principle, and some examples of studies involving them.

2.3.1 Numerical methods

2.3.1.1 Geometrical methods

One family of methods that are used to model sound propagation in an enclosure is based on the assumption that sound travels like rays, referred to as geometrical room acoustic modeling techniques. The wave phenomena are neglected, which is valid at high frequencies, where the wavelengths are small compared to the dimensions of the room and the obstacles. An exhaustive overview of these methods is given by Savioja et al. (2015). We briefly present a few of them in the following.

The image source method is a concept that can actually provide exact solutions for certain spaces such as a shoe-box with Dirichlet or Neumann boundary condition. In the latter case, the walls can be seen as perfect mirrors, analogously to optics, that create mirrored images of the source called image sources. Allen et al. (1979) provided the first numerical implementation for impedance boundary conditions. It is often used in geometrical room acoustic software to model the first reflection orders directly in pressure domain.

Another approach is the ray tracing, a stochastic method. In this case, a large number of rays is shot in all directions, uniformly distributed in the case of an omnidirectional source, from its position. As they are considered as infinitely thin, they are collected at a receiver position that occupy some volume. Each ray carries some energy that decreases along the propagation following the inverse square law. They also loose some energy at each reflection according to the absorption coefficient attributed. The method can accommodate with mixed reflections that are partially specular and diffuse with the help of scattering coefficients that determine the proportions. It also possible to consider more complicated behavior such as angle-dependent absorption and/or scattering. They are overall strongly related to methods employing the concept of sound particles.

Beam tracing methods can be seen as generalizations of the previous one where the rays are replaced with beams dividing the emitting sphere, with surfaces representing the wave fronts. Approaches employ pyramidal beam (Farina, 1995; Noe et al., 2006) with a triangular section defined by three rays, others use conical beams (CATT-Acoustic/TUCT, 2016). They allow to better account for curved surfaces using adaptive beam splitting when reflecting on surfaces modeled in several plane elements (Noe et al., 2006).

These methods have been augmented to better account for wave-related phenomena such as diffraction at edges (Calamia, 2009; Noe et al., 2006; Svensson et al., 1999).

The radiosity method is based on the assumption that the boundaries reflect the sound in a diffuse manner according to Lambert's cosine law (Kuttruff, 2016). In that case, the reflected energy is uniformly distributed and, therefore, the exchange of energy between the boundaries, representing the reflections, is uniquely determined by their relative positions. Siltanen et al. (2007) proposed a generalization called the room acoustic rendering equation that can handle non-diffuse reflections.

The image source method directly delivers a pressure signal, while the other methods are usually formulated as energy-based methods that lead to an echogram. Different strategies are employed to reconstruct phase. Other alternatives such as the phased beam tracing has been proposed to directly obtain the pressure rather than an echogram (Jeong, 2012).

2.3.1.2 Wave-based methods

Wave-based methods refer to the numerical methods that solve the wave equation. We briefly present in the following different popular methods that have been used to solve the complex problem that constitutes the propagation of sound in a room. They are usually considered as more computationally expensive than the geometrical methods, but more accurate.

Finite-difference methods are among the oldest methods to solve partial differential equations. Applications to room acoustics were done by Botteldooren (1995), limited to the low-frequency range. It has been shown to be equivalent to the digital waveguide mesh, another family developed for room acoustic applications. More details are given in section 5.1, as the method is used to solve our scattering problems. A rather exhaustive review of the method and its development for room acoustic applications is given by Hamilton (2016). Bilbao et al. (2017, 2016) provide a framework employing the finite volume method to avoid the staircase approximation that is classically used for non-conformal boundaries. It can be seen as a generalization of the finite-difference that can be applied on unstructured meshes.

The finite element method is another popular method for solving partial differential equations that also requires to discretize the spatial domain, but the elements do not have to be regular, similarly to finite volume. The space is subdivide is finite elements, usually tetrahedron, for a 3D space. The method may be applied in the frequency domain to obtain the transfer function, reflecting the steady-state behavior. A RIR may be then recovered by inverse Fourier transform (Nørgaard et al., 2021). But it also exists in the time domain (Okuzono et al., 2010, 2016).

The boundary element method, as its name indicate, is based on the discretization of the boundaries, reducing greatly the degrees of freedom of the problem compared to the volumetric methods presented above. Similarly to the previous method, it exists in the time (Hargreaves, 2007; Lam et al., 2012) and the frequency domain (Henriquez et al., 2010; Li et al., 2022). A review of the method for general acoustic problems is given by Liu (2019).

A lot of other methods exist that can not be detailed here. A brief non-exhaustive list of promising approaches is nonetheless given: the discontinuous Galerkin method (Wang et al., 2021), the pseudospectral time-domain method (Spa et al., 2010), the adaptive rectangular decomposition (Antani et al., 2013; Raghuvanshi et al., 2009), and the spectral element method (Pind et al., 2019).

2.3.2 Physical methods - Acoustic scale model

In spite of the progress of numerical methods, physical scale models are still a widespread tool in architectural acoustics, in particular for investigating the acoustics of complex rooms such as concert halls or for characterizing sound scattering surfaces. They offer the advantage of accounting for all wave phenomena occurring in full-scale problems, provided that they are representative of them. In the case of airborne sound scattering by a rigid object, if the thermo-viscous and molecular relaxation effects are neglected, the full-scale results are obtained, depending on the domain considered, by frequency transposition or time dilation of the scale model results. Moreover, they can be used as validation tools by providing reference results from measurements.

2.3.2.1 History & principle

Historically, acoustic scale models were the first experimental devices to visualize the propagation of wave fronts in a closed space (Orlowski, 2020; Rindel, 2002). Ripple tanks, whose edges define a longitudinal section of the room, were used. They were filled with water, and ripples on the surface were generated with a mechanical vibrator. Davis (1925a) showed that despite some differences in dispersion, with enough water depth, the method was able to reproduce the acoustic wave phenomena in a satisfactory manner. He even considered different fluid such as mercury. Sabine (1922) used another method related to schlieren photography, which he called a modification of the Teoppler-Boys-Foley method of photographing air disturbances. Teoppler is the inventor of the technique in the 19th century for the study of shock waves (Krehl et al., 1995) and Foley et al. (1912) adapted it to sound waves. Similarly, the propagation was visualized in a back-illuminated 2D section of interest. A pulse was generated with an electric spark. The wavefronts were then visible on photographic papers or directly due to the refraction they induce on the light (Knudsen, 1970). This was later developed by Davis et al. (1926), and also by Osswald (1930b), as shown in fig. 2.4 where contact prints of photographs he obtained are represented, used *e.g.* to study the acoustics of a hall with a variable volume represented number 19 to 22.

Optical methods were also considered, similarly to geometrical acoustics. The models could be in 2D section with polished metal edges to be more reflective. Light rays were emitted with the help of a circular screen with holes in it, and the model was filled with smoke so that they could be seen by diffusion (Knudsen, 1932). Three dimensional models were also used with a similar technique (Vermeulen et al., 1936), or for the positioning of certain elements such as reflectors (Knudsen, 1970).

Beyond visualization, Spandöck (1934) was the first, with the audio techniques of its time, to propose the direct use of three-dimensional 1:5 scale models to hear how a signal would sound in the full-scale spaces, becoming the precursor of auralization. He would play it inside a model at accelerated speed, according to its scale factor, record it at high speed, accordingly, and then listen to it at normal speed. Around the same period, Dungen (1933) applied the similarity laws to room acoustics. This can be summarized by considering the two fundamental relations

$$c = \frac{d}{t} = f\lambda \,, \tag{2.24}$$

where c is the speed of sound, related to the distance traveled by a wave d over the time of flight t, but also to its frequency f and its wavelength λ. When using a scale model,

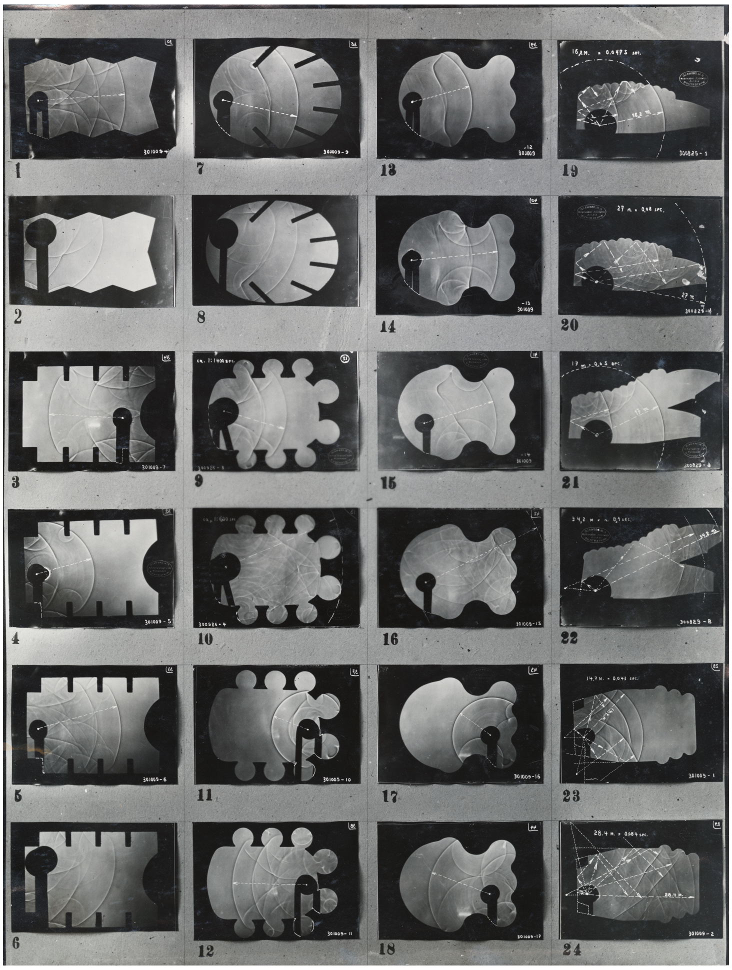

Figure 2.4 Photographs by Osswald (1930a) using the schlieren technique to study different hall sections.

with the dimensions reduced by a factor S, a wave will travel a distance d_m and have a wavelength λ_m that are reduced accordingly as

$$d_m = \frac{d}{S} \quad \text{and} \quad \lambda_m = \frac{\lambda}{S}\,, \tag{2.25}$$

and, as the speed of sound do not change, it follows that

$$t_m = \frac{t}{S} \quad \text{and} \quad f_m = Sf\,, \tag{2.26}$$

where t_m, and f_m are the time and frequency in the scale model. Therefore, the smaller the model, the higher the frequency.

2.3.2.2 Room acoustic scale models

With the advancement of technology, the use of scale models for room acoustic design and research began to gain acceptance (Burgtorf, 1967; Harwood et al., 1970, 1972, 1975; Jordan, 1973; Pallett et al., 1976). Brebeck et al. (1967) used 1:8 to 1:10 scale models. Their sound sources were an electric spark for objective measurements, and an electrostatic loudspeakers that could operate up to 100 kHz for subjective measurements (Orlowski, 2020). Although this is sufficient to cover a large part of the audible spectrum, the similarity laws do not take into account the increased absorption of air at high frequencies. For this, the air was dried to a very low relative humidity, being then less absorbent, with a good match for these scales. Later, smaller scales were used with this technique, up to 1:50 (Barron et al., 1979). However, it is not sufficient for accurate scaling for frequencies above 50 kHz. Replacing air by nitrogen in airtight models was also a practice, as its sound absorption is lower, but it is not convenient to access the inside of the model. In that case, the relations given eq. (2.26) are modified in

$$t_m = \frac{t}{KS} \quad \text{and} \quad f_m = KSf\,, \tag{2.27}$$

where $K = c_m/c$, with c_m the speed of sound in the fluid used in the model (Polack et al., 1989). With the advent of digital technology, this excess of absorption could be compensated numerically (Barron et al., 1979). This consists in time-varying filters with increased gain over time. To avoid increasing the background noise at long time, it is recommended to first perform an extension of the decay (Ćirić et al., 2012). Another method was proposed by Hornikx et al. (2008) using the continuous wavelet transform.

The impedance of materials must also be scaled. For predominantly reflective rooms, this is not too much of a problem. The most absorbent surface for a concert hall is the area occupied by the audience, so special care must be taken to model it with correct absorption (Day, 1968). Small-scale reverberation chamber measurements were also conducted to find materials that satisfactorily reproduce full-scale materials used in room acoustics (Jeon et al., 2009; Luizard, 2013).

Many projects of concert halls and auditoriums have used acoustic models for their design (Barron, 1997; Boone et al., 1994; Orlowski, 2020) and still do today. We can mention the *Philharmonie de Paris* (Katz et al., 2015) in France composed of curved surfaces, *Stavanger Konserthus* (Jurkiewicz et al., 2015) in Norway, or the *Elbphilharmonie* (Quiquerez et al., 2018) in Hamburg, Germany. *Örgryte New Church*, a neo-Gothic church built at the end of the 19th century in Göteborg, Sweden, has been scale-modeled as reported by Kleiner et al. (2010), probably during renovations.

In research, they are used to investigate the effect of diffusers on room acoustics in an objective (Kim et al., 2011) and subjective way (Jeon et al., 2020; Ryu et al., 2008), taking up Spandöck's idea. Ouis (1999) investigated the effect of a long hard strip in a room, and compared scale model measurements with an analytic diffraction model. They allowed to study the sound fields in coupled volumes with some spatial resolution (Pu et al., 2011; Xiang et al., 2018), or to study the effect of the coupled surface area and shape on the double slope effect (Luizard et al., 2014a). They can indeed provide reference measurements to test different algorithms (Aretz et al., 2009; Lam, 1996; Rindel, 2011b), or their capability regarding the prediction of certain phenomena such as coupled volume acoustics (Escolano et al., 2013; Luizard et al., 2013; Xiang et al., 2009).

They have also been useful for the study of historic buildings or sites that have suffered degradation or even no longer exist. We can quote the study of Canac (1967) on the acoustics of the Roman Theater of Orange, France, or the more general study of ancient amphitheaters by Farnetani et al. (2005) with a modular model. Katz et al. (2011) used a 19th century model of a particular roof frame present in the collections of the *Musée des Arts et Métiers*, Paris, France, to examine its acoustical impact. Recently, the acoustics of the prehistorical site of Stonehenge has been investigated in its original state with measurements on a 1:12 scale model (Cox et al., 2020).

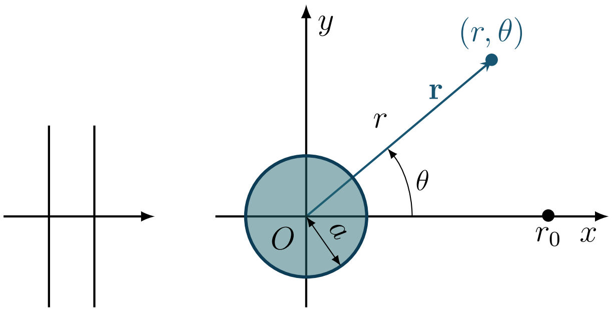

Figure 2.5 Coordinate system for a cylinder under plane wave or cylindrical incidence.

2.4 Scattering by cylindrical obstacles

The obstacles that interest us in part II are cylindrical in shape. It therefore seems relevant to first detail the existing analytic solutions for simple shapes such as the infinite circular cylinder. Wave scattering by cylindrical objects has been of interest for a long time and different methods have been applied to address different geometries, boundary conditions and frequency ranges. Lord Rayleigh was the first to derive wave scattering by small obstacles compared to the wavelength (Strutt, 1871). After him, analytic solutions using partial wave series expansion method have been derived for simple shapes (Bowman et al., 1988; Morse et al., 1986).

We provide in this section background on the sound scattering by cylindrical obstacles. Section 2.4.1 details the derivation of the analytic solutions for the circular cylinder case with plane wave, cylindrical, and spherical incidence. Section 2.4.2 recalls the scattering quantities used to quantify the scattering strength and directivity of an obstacle. Section 2.4.3 presents an exact analytic formulation for the problem of multiple scattering by a set of parallel circular cylinders.

2.4.1 Series solutions for stationary circular cylinder

2.4.1.1 Plane wave incidence

First, we present the case of a harmonic incident plane wave traveling in a direction perpendicular to the axis of a rigid and motionless infinite cylinder of radius a as shown in fig. 2.5. The wave propagates along the x-axis and, using the complex notation, the incident pressure P_i can be expressed

$$P_i(r,\theta,t) = p_0 e^{i(kx-\omega t)} = p_i(r,\theta)e^{-i\omega t}\,, \tag{2.28}$$

with p_0 its amplitude, k its wavenumber, and ω its angular frequency. The complex amplitude of the incident wave p_i can be decomposed on the basis of cylindrical harmonics (Morse et al., 1986) as

$$p_i(r,\theta) = p_0 e^{ikx} = p_0 e^{ikr\cos\theta} = p_0 \sum_{n=-\infty}^{\infty} i^n J_n(kr) e^{in\theta}\,, \tag{2.29}$$

where J_n are the Bessel functions of the first kind. The scattered pressure, defined as

$$p_s = p - p_i\,, \tag{2.30}$$

where p is the total pressure field, can also be decomposed as a series of cylindrical functions as

$$p_s(r,\theta) = \sum_{n=-\infty}^{\infty} [A_n H_n^{(1)}(kr) + B_n H_n^{(2)}(kr)] e^{in\theta}\,, \tag{2.31}$$

where $H_n^{(1)}$ and $H_n^{(2)}$ are respectively the Hankel functions of first and second kind, and A_n and B_n are the unknowns to determine. With the chosen time dependence $\exp(-i\omega t)$, $H_n^{(1)}$ and $H_n^{(2)}$ are representative respectively of an outgoing and incoming wave. Since the scattered pressure must satisfy the Sommerfeld radiation condition, we must have $B_n = 0$. And so, the total pressure in the fluid is

$$p(r,\theta) = p_i(r,\theta) + p_s(r,\theta) = \sum_{n=-\infty}^{\infty} [p_0 i^n J_n(kr) + A_n H_n^{(1)}(kr)] e^{in\theta}\,. \tag{2.32}$$

The unknowns A_n are determined so that they satisfy the boundary conditions. In the case of a rigid (or hard) and motionless cylinder, the radial component of the particle velocity must be zero on the surface of the former, which is equivalent to

$$\left.\frac{\partial p}{\partial r}\right|_{r=a} = 0\,. \tag{2.33}$$

It follows that

$$A_n = -p_0 i^n \frac{J_n'(ka)}{H_n^{(1)\prime}(ka)} \qquad \forall n \in \mathbb{Z}\,, \tag{2.34}$$

where primes denote differentiation with respects to the argument.

It may be convenient to rearrange in the form

$$A_n = p_0 i^n T_n(ka) \qquad \forall n \in \mathbb{Z}\,, \tag{2.35}$$

where T_n are called modal scattering coefficients (Swearingen et al., 2012) or partial-wave scattering amplitudes (Überall, 1985) as they describe the amplitudes of each mode in the infinite series. We finally obtain for the rigid case, noted with an exponent "hard" :

$$T_n^{\text{hard}}(ka) = -\frac{J_n'(ka)}{H_n^{(1)\prime}(ka)} \qquad \forall n \in \mathbb{Z}\,. \tag{2.36}$$

In the case of a cylinder with locally reacting boundary condition, the normal velocity at a point on the surface depends only on the local pressure at this point (Pierce, 2019), which is equivalent to

$$p(r=a,\theta) = Z_s \frac{i}{\omega\rho} \left.\frac{\partial p}{\partial r}\right|_{r=a}\,, \tag{2.37}$$

where $Z_s = \rho_s c_s$ is defined as the specific acoustic impedance of the cylinder surface, with ρ_s and c_s being respectively the density and the sound velocity of the cylinder while ρ is the density of the surrounding fluid medium.

It follows that for such an impedance cylinder the modal scattering coefficients T_n^{imp} are

$$T_n^{\text{imp}}(ka) = -\frac{J_n(ka) - i\frac{Z_s}{\rho c} J_n'(ka)}{H_n^{(1)}(ka) - i\frac{Z_s}{\rho c} H_n^{(1)\prime}(ka)} \qquad \forall n \in \mathbb{Z}\,. \tag{2.38}$$

This boundary condition is often used in room acoustics when the impedance of the boundary is independent or weakly dependent on the angle of incidence of the wave (Morse et al., 1944), such as surfaces of porous materials used as sound absorbents (Pierce, 2019). It allows to take into account the vibration of the surface caused by a local external pressure, but this first has no influence on the vibration of the neighboring points.

By observing the asymptotic behavior with respect to Z_s of eq. (2.38), one can verify that the hard case is retrieved in the limit of infinitely large impedance :

$$\lim_{Z_s \to +\infty} T_n^{\mathrm{imp}}(ka) = T_n^{\mathrm{hard}}(ka)\,. \tag{2.39}$$

Similarly, the scattering amplitudes T_n^{soft} for a pressure-release (or soft) cylinder is retrieved for $Z_s = 0$,

$$T_n^{\mathrm{soft}}(ka) = -\frac{J_n(ka)}{H_n^{(1)}(ka)} \qquad \forall n \in \mathbb{Z}\,. \tag{2.40}$$

Although the sounds sources encountered in the field of room acoustics undergo a spherical divergence, a plane wave can be a good local approximation in the case of a source at a large distance from the scatterer (Medwin et al., 1998). The common criteria for this approximation to be valid is when the distance R between a spherical source origin and a scatterer of characteristic size a meets the condition :

$$R \geq \frac{4a^2}{\lambda} \qquad \text{and} \qquad R \geq \lambda\,. \tag{2.41}$$

One can note that the first inequality is equivalent to the far-field region of any source or object.

2.4.1.2 Cylindrical wave incidence

We now consider the case of a harmonic line source whose axis is parallel to the cylinder. The line source is perpendicular to the xy-plane and located on the x-axis at a distance $r_0 \geq a$ from the origin of the coordinate system shown in fig. 2.5. In this configuration, the problem is again invariant along the direction of the cylinder axis.

With the same time dependence as in the case of plane wave incidence, the complex amplitude of the cylindrical wave generated by the line source located away from the origin is given by

$$p_i(r,\theta) = H_0^{(1)}(k|\mathbf{r} - r_0\mathbf{e_x}|)\,, \tag{2.42}$$

where $\mathbf{e_x}$ is the x-axis unit vector. Using the addition theorem for Hankel functions (Balanis, 2012), the wave can be expressed as an infinite series of cylindrical functions originating at the origin of the proposed coordinate system. It gives

$$p_i(r,\theta) = p_0 \sum_{n=-\infty}^{\infty} e^{in\theta} \begin{cases} J_n(kr)H_n^{(1)}(kr_0) & \text{for } r \leq r_0\,, \\ J_n(kr_0)H_n^{(1)}(kr) & \text{for } r \geq r_0\,. \end{cases} \tag{2.43}$$

Compared to the previous problem, only the source term is modified and the scattered wave can still be expressed as a series of cylindrical functions describing divergent cylindrical waves as written eq. (2.32). Considering again the more general case of an impedance cylinder with the boundary condition already given eq. (2.37), the scattered wave is eventually written

$$p_s(r,\theta) = p_0 \sum_{n=-\infty}^{\infty} e^{in\theta} T_n^{\mathrm{imp}}(ka) H_n^{(1)}(kr) H_n^{(1)}(kr_0)\,, \tag{2.44}$$

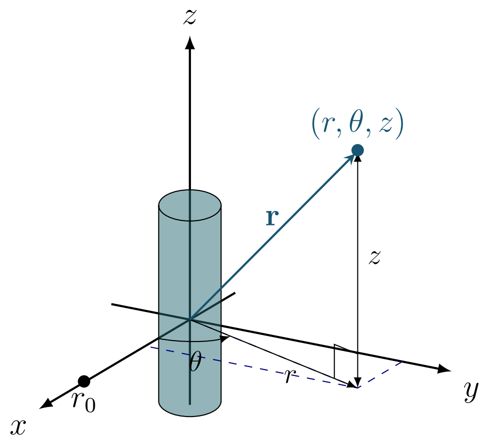

Figure 2.6 Coordinate system for a cylinder and a monopole source.

with T_n^{imp} already given eq. (2.38). Thus the total field may be written :

$$p(r, \theta) = p_0 \sum_{n=-\infty}^{\infty} e^{in\theta} \begin{cases} H_n^{(1)}(kr_0) \left[J_n(kr) + T_n^{\text{imp}}(ka) H_n^{(1)}(kr) \right] & \text{for } a \leq r \leq r_0 \,, \\ H_n^{(1)}(kr) \left[J_n(kr_0) + T_n^{\text{imp}}(ka) H_n^{(1)}(kr_0) \right] & \text{for } r \geq r_0 \,. \end{cases} \tag{2.45}$$

2.4.1.3 Monopole source

Acoustic sources encountered in room acoustics radiate in complex ways, and especially natural sources such as human voices (Pörschmann et al., 2021), talking or singing, or musical instruments (Pätynen et al., 2010). In theory, such sources could be constructed by assembling simpler sources, which can also be qualified as elementary, such as monopoles and dipoles with proper amplitudes, orientations and phases, so it seems relevant to examine the problem in the case of a point source.

The complex pressure amplitude p_i at an arbitrary point with coordinates (r, θ, z) as shown in fig. 2.6 due to a harmonic monopole source located at a distance $r_0 \geq a$ on the x-axis with a unit vector $\mathbf{e_x}$ can be expressed as

$$p_i(r, \theta, z) = p_0 \frac{e^{ik|\mathbf{r} - r_0 \mathbf{e_x}|}}{|\mathbf{r} - r_0 \mathbf{e_x}|} \,. \tag{2.46}$$

Using the relation ((6.616.3) in Gradshteyn et al. (2007)) called the Weyrich's formula

$$\int_{-\infty}^{\infty} e^{-itx} H_0^{(1)}(r\sqrt{\alpha^2 - t^2}) \, dt = -2i \frac{e^{i\alpha\sqrt{r^2+x^2}}}{\sqrt{r^2 + x^2}} \,, \tag{2.47}$$

with $0 \leq \arg\sqrt{\alpha^2 - t^2} \leq \pi$, $0 \leq \arg\alpha \leq \pi$, $(r, x) \in \mathbb{R}$ and the addition theorem for Hankel function similarly to eq. (2.43), it is possible to write a monopole source in terms of cylindrical functions, requiring however an integration over all axial wavenumbers, and thus

$$p_i(r, \theta, z) = p_0 \frac{i}{2} \sum_{n=-\infty}^{\infty} e^{in\theta} \int_{-\infty}^{\infty} \begin{cases} J_n(k_r r) H_n^{(1)}(k_r r_0) e^{ik_z z} \, dk_z & \text{for } r \leq r_0 \,, \\ J_n(k_r r_0) H_n^{(1)}(k_r r) e^{ik_z z} \, dk_z & \text{for } r \geq r_0 \,, \end{cases} \tag{2.48}$$

with $k_r = \sqrt{k^2 - k_z^2}$ and k_z being respectively the radial and axial wavenumbers.

Given such expansion for the incident field, it seems convenient to look for the expression of the scattered field in the form

$$p_s(r,\theta,z) = \sum_{n=-\infty}^{\infty} e^{in\theta} \int_{-\infty}^{\infty} A_n H_n^{(1)}(k_r r) e^{ik_z z}\, dk_z\,, \tag{2.49}$$

which ultimately leads to

$$A_n = p_0 \frac{i}{2} T_n^{\text{imp}}(k_r a) H_n^{(1)}(k_r r_0)\,. \tag{2.50}$$

This solution and the previous ones are not in closed form as they are expressed as infinite series. In practice, it is necessary to truncate the series and the solution is computed numerically by summing a finite number of modes. While with modern computers it would be possible to calculate the terms of the series until the value of the last one reaches the machine epsilon, this would result in an excessive computation time since, most of the time, such precision is not required depending on the intended applications. For circular cylinders, a number of modes N_m with controlled truncation error on the modal coefficients can be calculated with the formula

$$N_m = \left[ka + \left(\frac{1}{2\sqrt{2}} \log 2\sqrt{2}\pi ka \epsilon^{-1} \right)^{\frac{2}{3}} (ka)^{\frac{1}{3}} + 1 \right]\,, \tag{2.51}$$

where ϵ is the desired error bound, as derived by Antoine et al. (2008). $[\cdot]$ denotes the integer part in this particular case.

The integration required in eqs. (2.48) and (2.49) can be computed numerically with the trapezoidal method (Swearingen et al., 2012) or the Simpson's rule (Fuller, 1989). In the far field, it is possible to use the method of stationary phase (Lui et al., 2010; Skelton et al., 1997). The asymptotic forms are given by Bowman et al. (1988).

2.4.2 Scattering characterization

The same modal coefficients are found whatever the incidence, they therefore characterize the scattering from the obstacle. The characterization is also normally done with plane wave incidence to remove the source distance parameter. In far field, the Hankel functions have an asymptotic behavior such that p_s in eq. (2.32) can be separated in the general form

$$p_s(r,\theta) \underset{r\to+\infty}{=} p_0 f_\infty(\theta_s) \frac{e^{ikr}}{\sqrt{r}} + \mathcal{O}\left(\frac{1}{r}\right)\,, \tag{2.52}$$

where f_∞ is the form function (Valier-Brasier et al., 2021) or the far-field pattern (Colton et al., 2013) only dependent on the scattering angle $\theta_s = \theta - \theta_0$, where θ_0 is the directional angle of the incident plane wave. For the infinite circular cylinder, it is expressed as

$$f_\infty(\theta_s) = \frac{1-i}{\sqrt{\pi k}} \sum_{n=-\infty}^{\infty} T_n e^{in\theta_s}\,. \tag{2.53}$$

The radial time-averaged scattered intensity in the far field is therefore expressed as

$$\mathbf{I_s} \cdot \mathbf{e_r} = I_i \frac{|f_\infty(\theta_s)|^2}{r}\,, \tag{2.54}$$

where I_i is the incident intensity and $\mathbf{I_s}$ is the time averaged scattered intensity, calculated as

$$\mathbf{I_s} = \frac{1}{2}\mathrm{Re}(p_s\overline{\mathbf{v_s}})\,, \tag{2.55}$$

where $\mathbf{v_s}$ is the scattered complex velocity, "$\overline{\cdot}$" denotes complex conjugation and $\mathrm{Re}(\cdot)$ is the real part. $|f_\infty(\theta_s)|^2$ is the differential scattering cross section that is the main quantity to characterize the angular distribution and the strength of the scattering by an object. For a circular cylinder,

$$|f_\infty(\theta_s)|^2 = \frac{2}{\pi k}\left|\sum_{n=-\infty}^{\infty} T_n e^{in\theta_s}\right|^2 . \tag{2.56}$$

The differential backscattering cross section is expressed on a logarithmic scale as the monostatic target strength defined as the ratio between the differential scattering cross section in the opposite direction to the incidence and a reference surface (Pierce, 2019). The bistatic target strength is the measure for the other angles of scattering. Their definition is suited for finite three-dimensional objects, but in this work we limit ourselves to two-dimensions, and we define it

$$\mathrm{TS}(\theta_s) = 10\log_{10}|f_\infty(\theta_s)|^2 . \tag{2.57}$$

The total scattering cross section (TSCS) σ is defined has the ratio between the scattered intensity integrated over a contour (or suface in 3D) enclosing the objects, *i.e.* the time-averaged scattered power, and the incident intensity. In the far field, the contour can be a cylinder of large radius r (Medwin et al., 1998), resulting in

$$\sigma = \int_0^{2\pi} |f_\infty(\theta_s)|^2\, d\theta_s\,. \tag{2.58}$$

In the near field, it can be expressed

$$\sigma = \frac{1}{I_i}\oint_\Gamma \mathbf{I_s}\cdot\mathbf{n}\,d\Gamma\,, \tag{2.59}$$

where Γ is the integration closed contour, $\mathbf{n}$ is the unit normal vector oriented towards the exterior (Hu et al., 2013). For a circular cylinder,

$$\sigma = \frac{4}{k}\sum_{n=-\infty}^{\infty} |T_n|^2 . \tag{2.60}$$

It can be interpreted as the effective length intercepting part of the power carried by the incident wave to be retransmitted as a scattered wave, as it can be seen by multiplying eq. (2.59) by the incident intensity I_i.

The scattering phase function $P(\theta_s)$, defined as

$$P(\theta_s) = \frac{|f_\infty(\theta_s)|^2}{\sigma}\,, \tag{2.61}$$

describes the angular distribution of scattered sound over the scattering angles θ_s. Its integral over the full circle is equal to 1, using the far-field definition of σ given eq. (2.58).

Therefore, the scattering directivity in the far-field can be further characterized by computing the anisotropy or asymmetry factor g defined as

$$g = \int_0^{2\pi} P(\theta_s)\cos(\theta_s)\,d\theta\,, \tag{2.62}$$

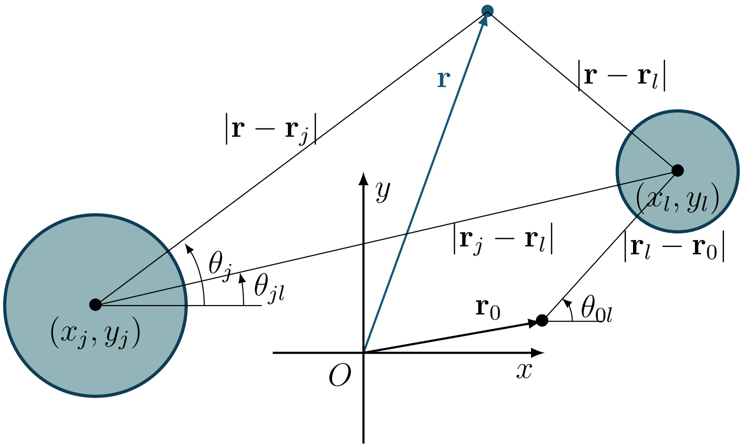

Figure 2.7 Coordinate system for a configuration of parallel cylinders.

which corresponds to the first Legendre moment. This parameter is comprised between -1 and 1 and it is used in light scattering to globally quantify preferential scattering directions of sub-wavelength particles (Lorenzo, 2012). Values of g close to 0 are an indication of symmetry between forward and backward directions. If $g = -1$ then it indicates full backward scattering, while $g = 1$ is complete forward scattering.

In practice, these quantities are dependent on the plane wave incidence angle θ_0 for non-circular cylinders. In that case, they are noted $\mathrm{TS}(\theta_0, \theta_s)$, $\sigma(\theta_0)$, $P(\theta_0, \theta_s)$, and $g(\theta_0)$.

2.4.3 Multiple scattering

The effect of multiple scattering involving circular cylinders has been studied in several contexts. The problem of a single circular cylinder near a rigid plane (Bertrand et al., 1976; Twersky, 1952) or a corner has been investigated (Hasheminejad et al., 2006). Multiple scattering effects between arrays of parallel cylinders in front of a Schroeder diffuser have been considered to improve diffusion (Pogson et al., 2010). Recently, array of regularly spaced identical rigid cylinders on a rigid plane have shown to produce surface wave corresponding to resonances of different origin depending on the cylinder spacing and their radius (Berry et al., 2019). Clusters of parallel cylinders are also used to design acoustic metamaterials for different applications such as acoustic cloaks (Jo et al., 2015), sonic crystals as sound diffusers with regular (Redondo et al., 2013) and pseudo-random (Hughes et al., 2010) configurations or for attenuation as sound barriers (Krynkin et al., 2011; Sánchez-Pérez et al., 2002; van der Aa et al., 2015).

An exact solution can be formulated for a configuration of parallel cylinder as shown in fig. 2.7 (Linton et al., 1990; Umnova et al., 2006). The total pressure field at a point of coordinate $\mathbf{r}$ at the exterior of any of them can be expressed as

$$p(\mathbf{r}) = p_i(\mathbf{r}) + \sum_{j=1}^{N} p_s^{(j)}(\mathbf{r}-\mathbf{r}_j)\,, \tag{2.63}$$

where $\mathbf{r}_j$, $j = 1, \ldots, N$, are the coordinates of the centers of the N cylinders of radius a_j. The incident pressure p_i can be a plane wave (eq. (2.29)) or a line source (eq. (2.42)). The scattered pressure $p_s^{(j)}$ by a cylinder j can be written

$$p_s^{(j)}(\mathbf{r}-\mathbf{r}_j) = \sum_{n=-\infty}^{\infty} A_n^{(j)} T_n^{(j)} H_n^{(1)}(k\,|\mathbf{r}-\mathbf{r}_j|) e^{in\theta_j}\,, \tag{2.64}$$

where $A_n^{(j)}$ are the unknown coefficients, and $T_n^{(j)} = T_n(ka_j)$, given eqs. (2.36), (2.38) and (2.40) for rigid, impedance, and soft boundaries, respectively. Using the Graf's addition theorem, it can be further expressed

$$p_s^{(j)}(\mathbf{r}-\mathbf{r}_j) = \sum_{n=-\infty}^{\infty} A_n^{(j)} T_n^{(j)} \sum_{m=-\infty}^{\infty} \begin{cases} J_{n-m}(k\left|\mathbf{r}_j-\mathbf{r}_l\right|)e^{i(n-m)\theta_{jl}} H_m^{(1)}(k\left|\mathbf{r}-\mathbf{r}_l\right|)e^{im\theta_l} \\ \qquad \text{for } \left|\mathbf{r}-\mathbf{r}_l\right| \geq \left|\mathbf{r}_j-\mathbf{r}_l\right|, \\ H_{n-m}^{(1)}(k\left|\mathbf{r}_j-\mathbf{r}_l\right|)e^{i(n-m)\theta_{jl}} J_m(k\left|\mathbf{r}-\mathbf{r}_l\right|)e^{im\theta_l} \\ \qquad \text{for } \left|\mathbf{r}-\mathbf{r}_l\right| \leq \left|\mathbf{r}_j-\mathbf{r}_l\right|. \end{cases} \tag{2.65}$$

For a line source, the total field exterior to a cylinder l with $\left|\mathbf{r}-\mathbf{r}_l\right| \leq \left|\mathbf{r}_j-\mathbf{r}_l\right|$ can therefore be written

$$\begin{aligned} p(\mathbf{r}-\mathbf{r}_l) = &\sum_{m=-\infty}^{\infty} J_m(k\left|\mathbf{r}-\mathbf{r}_l\right|)e^{im\theta_l} H_m^{(1)}(k\left|\mathbf{r}_l-\mathbf{r}_0\right|)e^{-im(\pi+\theta_{0l})} \\ &+ \sum_{n=-\infty}^{\infty} A_n^{(l)} T_n^{(l)} H_n^{(1)}(k\left|\mathbf{r}-\mathbf{r}_l\right|)e^{in\theta_l} \\ &+ \sum_{\substack{j=1\\ j\neq l}}^{N} \sum_{n=-\infty}^{\infty} A_n^{(j)} T_n^{(j)} \sum_{m=-\infty}^{\infty} H_{n-m}^{(1)}(k\left|\mathbf{r}_j-\mathbf{r}_l\right|)e^{i(n-m)\theta_{jl}} J_m(k\left|\mathbf{r}-\mathbf{r}_l\right|)e^{im\theta_l}. \end{aligned} \tag{2.66}$$

After application of the boundary conditions, and using the orthogonality of the functions $e^{im\theta_l}$, it leads to an infinite system of equations

$$A_m^{(l)} + \sum_{\substack{j=1\\ j\neq l}}^{N} \sum_{n=-\infty}^{\infty} A_n^{(j)} T_n^{(j)} H_n^{(1)}(k\left|\mathbf{r}_j-\mathbf{r}_l\right|)e^{in\theta_j} = -\frac{i}{4} H_m^{(1)}(k\left|\mathbf{r}_l-\mathbf{r}_0\right|)e^{-im\theta_{0l}}. \tag{2.67}$$

Similarly to the previous solutions, the number of modes must be truncated. When the configurations contain a large number of cylinders, close to each other, the system can be very demanding to solve. Recently, Rohfritsch et al. (2019) developed a method to solve such linear system based on an iterative method. The number of modes are limited when a certain tolerance is attained. To limit the size of the system, they introduced a cutoff radius for each cylinder that restricts the interactions considered to those with the surrounding cylinders.

2.5 Scattering in room acoustics

As introduced in section 2.1, the early reflections are important as they are related to our perception of the surrounding space through sound. When they are too strong, they can be unpleasant and mislead us as to the location of the source. But they also can be desirable in a concert hall, *e.g.* for the musicians on stage so they can hear themselves and the others.

Acoustic treatments such as absorbers or diffusers are used to better control them. The latter have the advantage to do so without removing energy. They aim do redistribute it spatially and temporally (Cox et al., 2016).

2.5.1 Surface diffusers

Acoustic surface diffusers are used in room acoustics planning to control the reflections on the wall. Their functions are to spread spatially and temporally the wave front, change the specular reflection in what is called a diffuse one in this field.

They are usually characterized in terms of scattering and diffusion coefficients. The scattering coefficient is defined as the ratio between the energy scattered away from the specular direction and the total reflected energy. It is used in geometrical room acoustic simulations. The diffusion coefficient is the autocorrelation function of the scattered field, that measure its uniformity. Their measurements are standardized procedures that are described in ISO 17497-1 (2004) and ISO 17497-2 (2012) for the scattering and diffusion coefficients, respectively.

Their effects on the sound field of concert halls have been evaluated perceptually and objectively by examining the room acoustic parameters with scale (Jeon et al., 2020; Kim et al., 2011; Ryu et al., 2008) and computer (Jeon et al., 2020; Shtrepi et al., 2015, 2017) models.

2.5.2 Volume diffusers

In contrast to acoustic surface diffusers, obstacles in a room can scatter a wave in all directions when it reaches it, if their size is comparable to the wavelength. In this case, the term volumetric diffuser has been proposed (Cox et al., 2016). Examples of modern application are the canopy of reflectors suspended above some concert hall stages (Rindel, 1991) or hanging panels in reverberation chambers (Bradley et al., 2014). As they are finite-sized objects they usually have less effect on long wavelengths (Rindel, 1986), and the effect of curvature of reflector panels on this frequency limit has been considered (Szeląg et al., 2014). Rathsam et al. (2010) studied the influence of the convexity of the edges of planar reflector panels. They proposed a simplified audibility criterion to examine if they provide audible reflections. For wavelengths of comparable size, the waves can propagate around the obstacle and are strongly diffracted, notably in the shadow zone (Medwin et al., 1998).

Hughes et al. (2010) studied different types of two-dimensional volumetric diffusers such as arrays of slats or cylinders, and percolation structures. Their performance is characterized similarly to surface diffuser with a diffusion coefficient that quantify the omnidirectionality of the scattered field excluding the shadow region. The backscattered intensity is compared to that of a rigid strip of equal width in order to evaluate their scattering strength. They realized measures on scale models with a boundary layer technique and simulations with boundary element method (BEM) in the frequency domain. Overall, they found that arrays of cylinders had great diffusing abilities compared to the other tested structures, but with limited scattered strength at low-frequency.

Suzumura et al. (2000) studied the effect of circular columns placed close to the walls of a concert hall on the room acoustic parameters, similarly to the studies with surface diffusers.

2.5.3 Audibility of reflections

The audibility of early reflections is usually expressed in terms of detection threshold, masked threshold, or audibility threshold, defined as the highest level of a reflection just before it becomes inaudible, relative to the direct sound (Olive et al., 1988). It depends on many factors, including the direction of the reflection, its delay, the signal type, its spectrum or the environment.

2.5.3.1 Specular reflection

Burgtorf (1961) studied the situation where the impulse response is composed of the direct sound and a delayed peak, representing a specular reflection. The test signal consisted of speech at 70 dB presented to the participants with frontal incidence. This led to the establishment of an empirical linear relationship relating the threshold to the time delay:

$$\mathit{\Delta} L = -0.575 \mathit{\Delta} t - 6\,, \tag{2.68}$$

where $\mathit{\Delta} L$ is the audibility threshold in dB and $\mathit{\Delta} t$ is the time delay in ms. For longer delays after the direct sound, the threshold decreases. Brunner et al. (2007) studied the audibility of comb filter distortion, which is analogous to a single early specular reflection in a diotic situation. They used different test signals including a piano phrase, speech and a snare drum roll. They found for this latter, on average of all subjects, that a reflection of a relative level of −18 dB was audible considering short delays from 0.1 ms to 15 ms. The thresholds were increased for the other test signals that are more continuous, in agreement with previous studies (Burgtorf et al., 1964). Olive et al. (1988) found a similar range of values for a single frontal coincident reflection and pink noise for the same delay, as well as the same dependence on the signal type. They considered the effect of direction and found that the thresholds were lowered when the delayed sound was coming from lateral directions. Other studies led to the same conclusions (Begault et al., 2001; Burgtorf et al., 1964; Zhong et al., 2018). The effect of reverberation is similar to the difference existing between continuous and impulse signal (Olive et al., 1988). Begault et al. (2003) proposed "rules of thumb" based on these results such that early reflections will be inaudible if their levels are less than −22 dB relative to the direct sound for a 3 ms delay, lowered to −31 dB for 15 ms to 30 ms, and that a modest amount of reverberation added in the stimuli increases the thresholds by up to 11 dB. All these studies also reported large variations across participants.

In order to study more realistic configuration where the spectrum can be modified due to surface absorption, the effect of spectral content of reflection has been considered. Olive et al. (1988) have low-pass filtered the reflection signal at different cut-off frequencies. They found overall higher thresholds for filtered reflections compared to broadband ones. Walther et al. (2013) studied this effect on the echo suppression threshold, which does not correspond directly to the detection threshold, but is strongly correlated with it. They found a similar dependence for low-frequency filtering, while high-frequency overlaps led to less echo suppression with the highest sensitivity around 2 kHz, that could indicate that high-frequency reflection are more detectable. If this is the case, then it favors the detection of the backscattering of the geometries studied, that is overall increased at high frequencies.

2.5.3.2 Diffuse reflection

The effect of diffusion has been studied recently by Robinson et al. (2013a) on the echo suppression thresholds. White Gaussian noise was multiplied with gamma distributions of different parameters to emulate the temporal spreading and envelope of diffuse reflections. In comparison to specular reflections with the same peak amplitude, diffuse reflections were more detectable indicating that integrated power of the reflection is probably a better indicator to predict its audibility. Wendt et al. (2021) considered reflections from a finite wall modeled with Lambertian surface. They found similar results that they attributed to the temporal position of the energy centroid for a diffuse reflection in relation to the forward masking pattern of the direct sound. In addition, they provide relationships linking the masking thresholds to the logarithm of the time differences of arrival with excellent correlations to the experiments.

Our ability to perceptually discriminate between different reflections from surfaces with respect to their topology inducing spectral coloration has been studied by Kleiner et al. (1992) and with finite-difference time-domain method simulations by Meyer et al. (2019). Kritly et al. (2021) also used this numerical method to perceptually evaluate our ability to hear the difference of the reflected sound from different walls in a passive echolocation task. They simulated reflections from a flat wall, with different curves, a crenelated one, and a staircase. The latter produced diffuse reflection accompanied with strong spectral variations distinct from the others, and, at large distance (5 m), was the one that the participants could discriminate the most.

Part I

Room acoustic scale modeling & coupled volumes

Chapter 3

Investigations on experimental tools for acoustic scale model

As already introduced in section 2.3.2, scale models are tools still used in the field of room acoustics for complex projects such as concert hall design and research. They allow physical modeling of space approaching reality and thus highlight phenomena difficult to simulate numerically in large spaces. In addition, they offer a tangible support that can be modified relatively easily to test different architectural elements and their effects on the sound field. However, following the principle of similarity, the measurement equipment has to operate partly in the frequency domain of ultrasound.

In this chapter, we investigate different solutions regarding the sources and receivers used in architectural acoustic scale model. In section 3.1, we focus on the sources. In the context of room acoustics parameter measurements, the international standard ISO 3382-1 (2009) recommends that the source be omnidirectional and provides a procedure to evaluate their directivity. Following this objective, several types of sources have been proposed in the literature for room acoustic scale models, presented in section 3.1.1. In section 3.1.2, we present our three designs. Two of them are tweeter arrays, similar to the sources traditionally used for room acoustics measurements. The number of elements needed and their configuration, is estimated from the octave-band directivity measurements of the individual elements expressed in the real spherical harmonic basis so that they can be manipulated in space. Another one uses an inverted horn mounted on a tweeter. A prototype is built for each and evaluated for omnidirectionality according to the standard qualification procedure (ISO 3382-1, 2009) for 1:10 and 1:20 scale factors. The results are presented in section 3.1.3.

In section 3.2, we investigate two receiver solutions that can capture the directionality of the sound field. The idea of using this type of physical modeling to perform perceptual studies is not new, but requires special receivers to account for the three-dimensional character of the sound field. At full scale, the two main approaches are binaural or ambisonic microphone array recordings. Different studies using these methods in scale models are detailed in section 3.2.1. In section 3.2.2, we report the results of our 1:8 scale artificial head design based on the Neumann KU 100 commercial model, compared to the latter. In section 3.2.3, we present the Spatial Decomposition Method (SDM) proposed by Tervo et al. (2013a), an alternative method to encode a set of impulse responses captured in a small volume into a set of image-sources. These two techniques are evaluated in the context of measurements in a 1:10 scale model of a future concert hall in section 3.2.4. Eventually, discussions and conclusions are provided in section 3.3.

3.1 Sources

3.1.1 Review of existing

Measurements in scale models require, depending on the scale factor, sources to cover a wide range of frequencies, partly in the ultrasonic field. One of the first type of source that has been used is the spark source (Burgtorf, 1967; Rindel, 2002). A spark is produced between two nearby electrodes. This solution is appealing for providing a point source of limited size, with high power and a fairly omnidirectional radiation over a wide frequency band (Ayrault et al., 2012; Hidaka et al., 1989; Polack et al., 1989). However, powerful discharges can produce shock waves that are not suitable for the study of linear acoustics (Hak et al., 2009). In addition, they tend to heat the surrounding air and the pulses have waveforms that vary with each use, since they are dependent on the geometry of the electric arc.

Recently, an optoacoustic source has been proposed (Gómez Bolaños et al., 2013). A laser is used to induce a pressure pulse by focusing a beam at one point in space. It has been shown to have good repeatability and offers the advantage of being non-invasive, but also produces a non-linear propagating wave.

A miniature blank pistol was also used as an impulse source for the measurements in the *Philharmonie de Paris* acoustic scale model (Katz et al., 2015). The barrel was 2 mm large and the total size was about 4 cm. However, it is less repeatable and requires manual triggering which makes it less practical to use and does not allow access to the time of flight between the source and a receiver as is the case when they are synchronized.

Piezoelectric materials have been used to design dodecahedral sources similar to those used in room acoustic measurements (Braun, 1984; Chojnacki et al., 2016; Tahara et al., 2003). Piezoceramics, such as PVDF, resonate in the ultrasonic frequency range, which makes them a good candidate, however, they may have difficulty in radiating in the air (Saffar, 2021). Similarly, tweeter-based sources, based on spherical tweeter arrays, have also been proposed (Aretz et al., 2009; Katz et al., 2015; Luizard, 2013; Luizard et al., 2014b). Xiang et al. (1993) combined a dodecahedral source, consisting of 11 tweeters, with a PVDF piezoelectric film stretched over a bi-conical shape for the higher frequencies. They are more reproducible than the impulse sources. Moreover, they offer the advantage of being able to emit certain signals and thus use classical measurement techniques of room acoustics. Nevertheless, their radiation patterns may be less omnidirectional at high frequencies due to the increased directivity of the individual elements.

3.1.2 Proposed designs

Leishman et al. (2006) studied different speaker arrangements based on platonic solids, including the dodecahedron, and evaluated their omnidirectionality for room acoustics measurements. He showed that a tetrahedral shape could offer equivalent performance to a dodecahedron when considering the qualification procedure of the standard (ISO 3382-1, 2009). Another solution to obtain an omnidirectional source has been proposed originally by Lahti (1985), and reconsidered recently (Cobo et al., 2013; Ibarra et al., 2018; Ortiz et al., 2014; Polack et al., 2001). It consists in using an inverted horn, placed on a loudspeaker, to concentrate the energy at one point. This principle has also been used for studies involving acoustic scale models (Hornikx et al., 2008; Orlowski, 1981; Ouis, 1999), but with a straight tube.

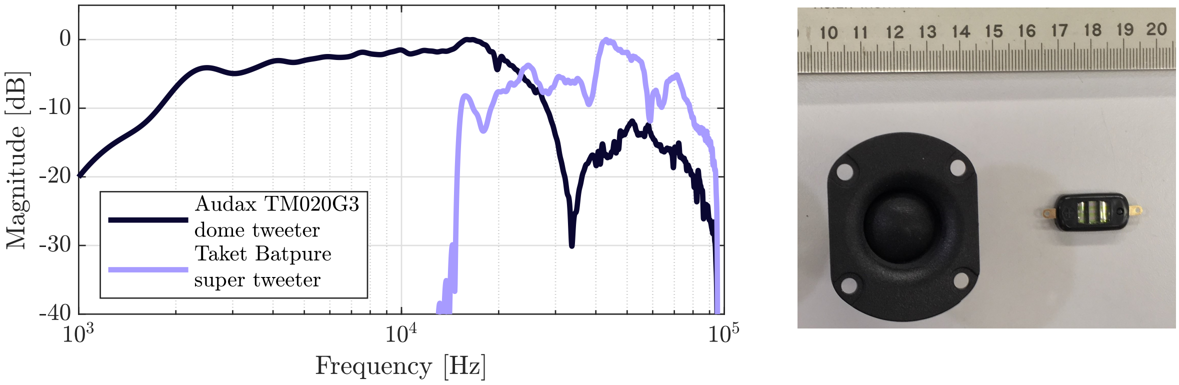

(a) (b)

Figure 3.1 Normalized magnitude responses (a) and a photograph (b) of the tweeters used for the designs: (left) Audax TM020G3 dome tweeter and (right) Taket Batpure "super tweeter".

Three designs are tested here, two of them are tweeter arrays, and one uses a reversed horn. The tweeters used for these sources are shown in fig. 3.1b. On the left, there is an Audax TM020G3 tweeter dome with a 20 mm diameter membrane. On the right, it is the Taket Batpure, a "super tweeter". It is so called because it is designed to emit in the ultrasonic field. They work with piezoelectric films laminated to each side of a wave-shaped ribbon of approximate dimensions 10 mm by 20 mm. By applying a voltage difference, it moves like an accordion and radiates sound under the same principle as Oscar Heil's Air Motion Transformers (Heil, 1972). Hidaka et al. (2010) developed a miniature dodecahedron using this particular piezoelectric transducer. Their magnitude responses normalized to their maximum, measured on axis in non-baffled condition, are represented in fig. 3.1a. The dome tweeter has a flat response from 2 kHz to 30 kHz. A large drop of magnitude is observed around 32 kHz, above, it radiates a reasonable relative level. The super-tweeter magnitude response is overall flat from 19 kHz to 78 kHz with variations comprised in a 12 dB range.

In order to propose an arrangement for both elements that meets the requirements of the standard, it is proposed to estimate a minimum arrangement based on the measured directivities of the individual elements. By projecting these directivities onto the spherical harmonic basis, it is possible to manipulate them in space and add them together to estimate the directivity of an array.

3.1.2.1 Directivity of individual elements

Their far-field directivity patterns have been measured in the anechoic chamber or a highly absorbing room of Sorbonne Université in a non-baffled configuration. The tweeter was rotated with the help of a turntable (Brüel & Kjær Turntable System Type 9640), and driven by an amplifier (Samson Servo 120a). The signals were recorded using a GRAS 40DP 1/8" microphone mounted on a 1/4" preamplifier (GRAS Type 26AC), connected to a microphone conditioner (Brüel & Kjær Nexus 2690-A). All were connected to an audio interface (RME Babyface) configured at a sample rate of 192 kHz. The exponential swept sine method (Müller et al., 2001) was used with signal covering frequencies from 1 kHz to 95 kHz over 1 s. Impulse responses were obtained with a 5° angular step and the emission and acquisition of signals as well as the control of the turntable were performed with

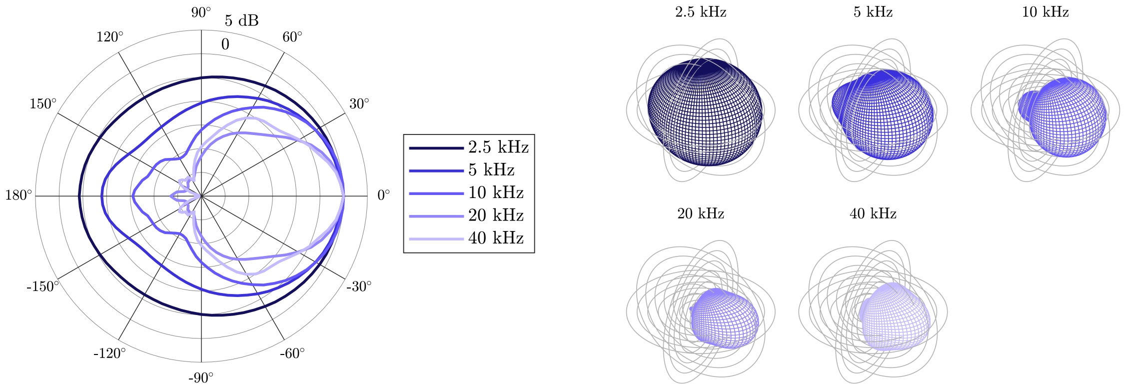

(a) (b)

Figure 3.2 Average octave-band directivity patterns of the tweeter TM020G3. **(a)** Polar diagrams. **(b)** Reconstructed 3D patterns with spherical harmonics (order 6). Axisymmetry is assumed.

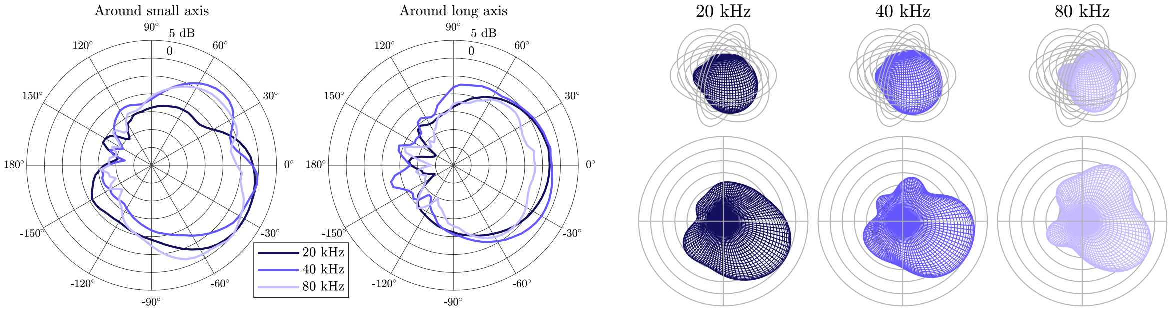

(a) (b)

Figure 3.3 Average octave-band directivity patterns of the Taket Batpure "super tweeter" measured around the small and the long axis of the radiating surface. **(a)** Polar diagrams. **(b)** Reconstructed 3D patterns with spherical harmonics (order 6).

MATLAB 2018b through an automatic procedure. The dome tweeter is only measured in a plane containing its axis, on a semicircle. The super tweeter is not circular. Its directivity is, therefore, measured in the two planes containing the symmetry axes of the radiating surface, over a full circle.

Figure 3.2a shows the results obtained for the dome tweeter for the octave bands from 2.5 kHz to 40 kHz. Its behavior is similar to that of a rigid piston, with a more directional radiation as the frequency increases. For the 2.5 kHz and 40 kHz bands, the angular coverages at -3 dB are about 120° and 40°, respectively. We can see that the tweeter appears a little less directional at 40 kHz compared to 20 kHz, probably due to the reflections and diffraction at the edges.

Figure 3.3a shows the directivity patterns the super tweeter. It radiates in a usable way on the bands from 20 kHz to 80 kHz. Note that for this last band, it only covers the first two one-third octave bands, with an upper limit frequency at about 88 kHz. Compared to the dome tweeter, the radiation does not seem to become more directional as the frequency increases. However, there is a large variability between the different octave bands and measurement planes. The beam appears to be more symmetrical in the plane perpendicular to the long axis of the radiating surface, and is wider on average, compared to the other measurement plane. In the latter, the directivity patterns show that some directions may be favored, probably due to geometric irregularities and deformations present on the piezoelectric ribbon.

3.1.2.2 Spherical harmonic representation

The spherical harmonics form an orthogonal basis of functions defined on the surface of a sphere. In the following, we want to determine a spherical harmonic representation of the average octave-band directivities, that are obtained by quadratic mean. We then use the real-valued spherical harmonic basis functions, defined as

$$Y_{n,m}(\theta,\phi)=\sqrt{\frac{2n+1}{2\pi\left(1+\delta_m\right)}\frac{(n-|m|)!}{(n+|m|)!}}P_n^{|m|}(\cos\theta)\begin{cases}\sin|m|\phi & \text{for } m<0\,, n\leq|m|\,,\\ \cos|m|\phi & \text{for } m\geq 0\,, n\leq|m|\,,\end{cases} \tag{3.1}$$

where (θ,ϕ) are the polar and azimuthal angles in a spherical coordinate system, δ_m is the Kronecker delta function, $P_n^{|m|}$ are the associated Legendre polynomials. In this form, the square root term ensures the orthonormality of the basis.

This basis is suitable to represent our average quantities since any real square-integrable function ψ defined on a sphere can be expanded in the form

$$\psi(\theta,\phi)=\sum_{n=0}^{\infty}\sum_{m=-n}^{n}\alpha_{n,m}Y_{n,m}(\theta,\phi)\,, \tag{3.2}$$

where $\alpha_{n,m}$ are the real spherical harmonic coefficients (Driscoll et al., 1994). As the basis is orthogonal, they can be obtained by projection,

$$\alpha_{n,m}=\int_{S^2}\psi(\theta,\phi)Y_{n,m}(\theta,\phi)\,d\Omega\,, \tag{3.3}$$

where $d\Omega=\sin\theta d\theta d\phi$ is the differential surface area on the 2-sphere surface S^2.

In practice, the order of decomposition is limited to a finite order N, and an approximation $\tilde{\psi}$ of ψ is

$$\tilde{\psi}(\theta,\phi)=\sum_{n=0}^{N}\sum_{m=-n}^{n}\alpha_{n,m}Y_{n,m}(\theta,\phi)\,, \tag{3.4}$$

where only the first $(N+1)^2$ modes are considered in the decomposition.

Moreover, the field is measured at discrete positions on a sphere centered on the considered tweeter, so the continuous spherical harmonic transform given eq. (3.3) must be expressed in a discrete form. Equation (3.4) can be written in matrix form

$$\boldsymbol{\psi}=\mathbf{Y}\boldsymbol{\alpha}\,, \tag{3.5}$$

where

$$\boldsymbol{\psi}=\begin{bmatrix}\psi(\boldsymbol{\theta}_1) & \dots & \psi(\boldsymbol{\theta}_j) & \dots & \psi(\boldsymbol{\theta}_L)\end{bmatrix}^T\,, \tag{3.6}$$

$$\mathbf{Y}=\begin{bmatrix}Y_{0,0}(\boldsymbol{\theta}_1) & \dots & Y_{N,N}(\boldsymbol{\theta}_1)\\ \vdots & Y_{n,m}(\boldsymbol{\theta}_j) & \vdots\\ Y_{0,0}(\boldsymbol{\theta}_L) & \dots & Y_{N,N}(\boldsymbol{\theta}_L)\end{bmatrix}\,, \tag{3.7}$$

$$\boldsymbol{\alpha}=\begin{bmatrix}\alpha_{0,0} & \alpha_{-1,0} & \dots & \alpha_{N,N}\end{bmatrix}^T\,, \tag{3.8}$$

with $\boldsymbol{\theta}_j$ the angular measurement positions of sampling points, $j = 1, \ldots, L$. It is then possible to estimate the coefficients with

$$\tilde{\boldsymbol{\alpha}} = \mathbf{Y}^{\dagger}\boldsymbol{\psi}\,, \tag{3.9}$$

where $\mathbf{Y}^{\dagger}$ is the Moore-Penrose pseudoinverse of $\mathbf{Y}$, giving the optimal coefficients $\tilde{\boldsymbol{\alpha}}$ in the least square sense.

The measurement positions of the receiver are limited to one plane for the dome tweeter and two planes for the super tweeter. This can lead to a very bad conditioning of $\mathbf{Y}$, since in this case some functions of the truncated basis will sometimes be entirely or partially defined null on these positions. A solution for the case of the dome tweeter is to use its axisymmetry and add positions covering the sphere. Another, more general, solution is to calculate the reduced row echelon form of $\mathbf{Y}$ using Gauss-Jordan elimination before solving the system. This will discard the functions that cause the bad conditioning.

The average octave-band directivity patterns are represented using a truncation at the order 6 ($N = 6$). The results of the decomposition are represented as 3D radiation patterns in figs. 3.2b and 3.3b. It is now possible to perform rotation and translation operations to orient them in any direction. We restrict ourselves to rotations for our estimations. By adding the coefficients obtained for different orientations, we obtain the directivity of the ensemble. Obviously, this gives a very rough estimate of the final result since we are dealing with average quantities. This is equivalent to assuming that the beams are incoherent. Furthermore, no translation is considered here although it may have a detrimental effect on the omnidirectionality of the final design.

It was estimated that a set of 4 dome tweeters arranged in a tetrahedron could produce an omnidirectional source according to the standard qualification procedure (ISO 3382-1, 2009). A box in the shape of a regular truncated tetrahedron, *i.e.* the faces with the tweeters are regular hexagons, is then proposed, shown in fig. 3.5a. Its size is minimal, and constrained by that of the tweeters, in particular to ensure the assembly and wiring. For the super tweeter, it was estimated that an arrangement of 4 elements as shown in fig. 3.5b was sufficient.

3.1.2.3 Inverted horn

An inverted horn was designed for the dome tweeter. Its profile is conical. Its dimensions are 34 mm diameter at the base, 3.3 mm at the aperture, and 87 mm long. It represents approximately a 1:2 scale version of one of the designs proposed by Ortiz et al. (2014), adapted to the dimensions of the tweeter. The cone has been 3D printed in polylactic acid with a Ultimaker S5. A photograph is shown in fig. 3.5c.

The presence of the cavity with a small opening in front of the tweeter will induce resonances, as observed by Cobo et al. (2013), Ibarra et al. (2018), Orlowski (1981), Ortiz et al. (2014), and Polack et al. (2001). Figure 3.4 shows the impulse and frequency response of the tweeter with the horn measured on axis where the effect is clearly visible. The time for the impulse to reach -20 dB relative to its maximum level is about 40 ms and the frequency response peaks are about 1900 Hz apart. Inverse filtering techniques were considered to obtain a shorter impulse and a flatter response by Cobo et al. (2013), Ibarra et al. (2018), and Ortiz et al. (2014) constructed from the measured on-axis response, which leads to a lesser benefit for the other directions.

These aspects are not addressed in the standard ISO 3382-1 (2009), but it seems legitimate to consider that in this current state, without any processing to mitigate the

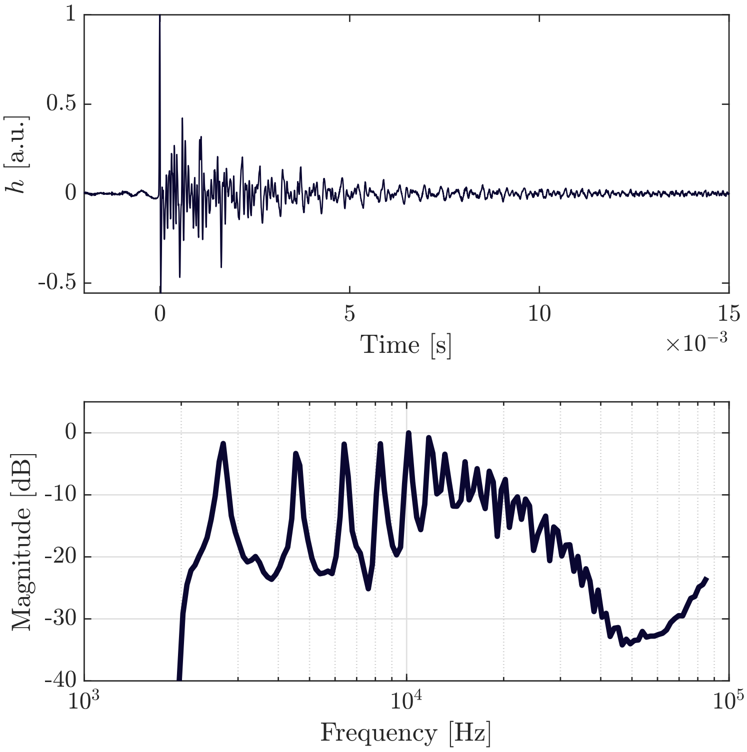

Figure 3.4 Impulse response (top) and normalized frequency response (bottom) with one-twelfth octave-band smoothing with the inverted horn measured on axis with a Feichter M1 microphone.

resonances, the source is not the most suitable for subjective experiments as some coloration are introduced (Orlowski, 1981), or for some acoustical parameters such as C_{80} considering the duration of the impulse. It seems, however, usable for estimating octave-band parameters that rely more on the late field such as the reverberation time.

3.1.3 Assessment of omnidirectionality

The standard (ISO 3382-1, 2009) describing the measurement procedures of the room acoustical parameters presented in chapter 2 specifies that the source used should be as omnidirectional as possible. It provides the maximum deviations from perfect omnidirec-

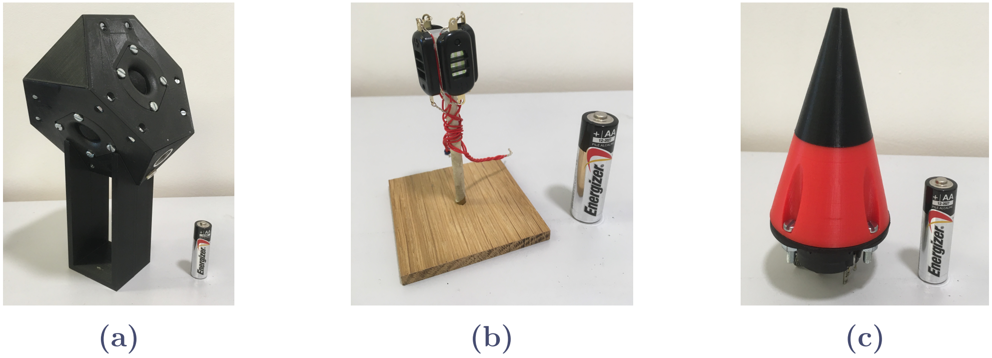
(a) (b) (c)

Figure 3.5 Photographs of the proposed source designs: **(a)** tetrahedral, **(b)** super-tweeter array, and **(c)** inverted horn source.

Table 3.1 Maximum deviations of directivity prescribed by ISO 3382-1 (2009).

Octave band [Hz]	125	250	500	1000	2000	4000
Maximum deviation [dB]	±1	±1	±1	±3	±5	±6

tionality allowed per octave band, given in table 3.1. The directivity of the source should be measured in the far field at a distance greater than 1.5 m, with an angular step of at least 5°. The values must be then smoothed by “gliding” averaging over 30° arcs. They are eventually normalized to the energetic average over the full circle, and the positive or negative deviations in dB must remain within the prescribed limits.

Each design has been measured in agreement with the standard, similarly to the measurement of the individual elements as described section 3.1.2.1. The measurement plane for the tetrahedral source was perpendicular to one of its 2-fold axis and intersected an edge at its half. The super-tweeter array is measured over two planes, the azimuthal plane, considering its orientation in fig. 3.5b, and a median plane containing the long axes of two of the four elements. For the source with an inverted horn, the measurement plane contained its axis of symmetry and the open end was positioned on the axis of rotation of the turntable.

3.1.3.1 Tetrahedral tweeter array

The octave-band directivity patterns of the truncated tetrahedron source are shown in fig. 3.6a. It is visibly omnidirectional over the 2.5 kHz octave band. At 5 kHz, the minimum relative level is around −9 dB in the direction between tweeters. Above, the relative levels for these directions is not minimal, probably due to the reflections and diffraction on the enclosure.

The results of the qualification procedure are represented in fig. 3.6b. The directional deviations estimated using the spherical harmonic representation are also shown. They are compared to the limits of the standard (table 3.1) transposed for 1:10 and 1:20 scale factors. The source respects globally the limits of the standard except for the 500 Hz octave band for both scale factors and also for the 250 Hz octave band at 1:20 scale. Contrary to the estimations, the source is more impacted by the directivity of the individual elements over the 2.5 kHz octave band. For the higher frequencies, it seems to benefit from the reflections on the box as observed in the directivity patterns.

3.1.3.2 Super-tweeter array

The octave-band directivity patterns of the super-tweeter array in the two measurement planes are shown in fig. 3.7a. The source appears to be more omnidirectional in the azimuthal plane. However, we can notice a lack of energy in the direction at 180°, that corresponds to the microphone facing one of the super tweeter. This could be due to variability between elements which has not been determined here. In the median plane, the minimal relative levels are found at the positions aligned with the stand, adding some occlusion.

The results of the qualification procedure for the two planes are shown in fig. 3.7b. For a 1:10 scale factor, the deviations in both planes are between the limits. For a 1:20 scale factor, the deviations in the median are above the limits for the 1000 Hz octave band.

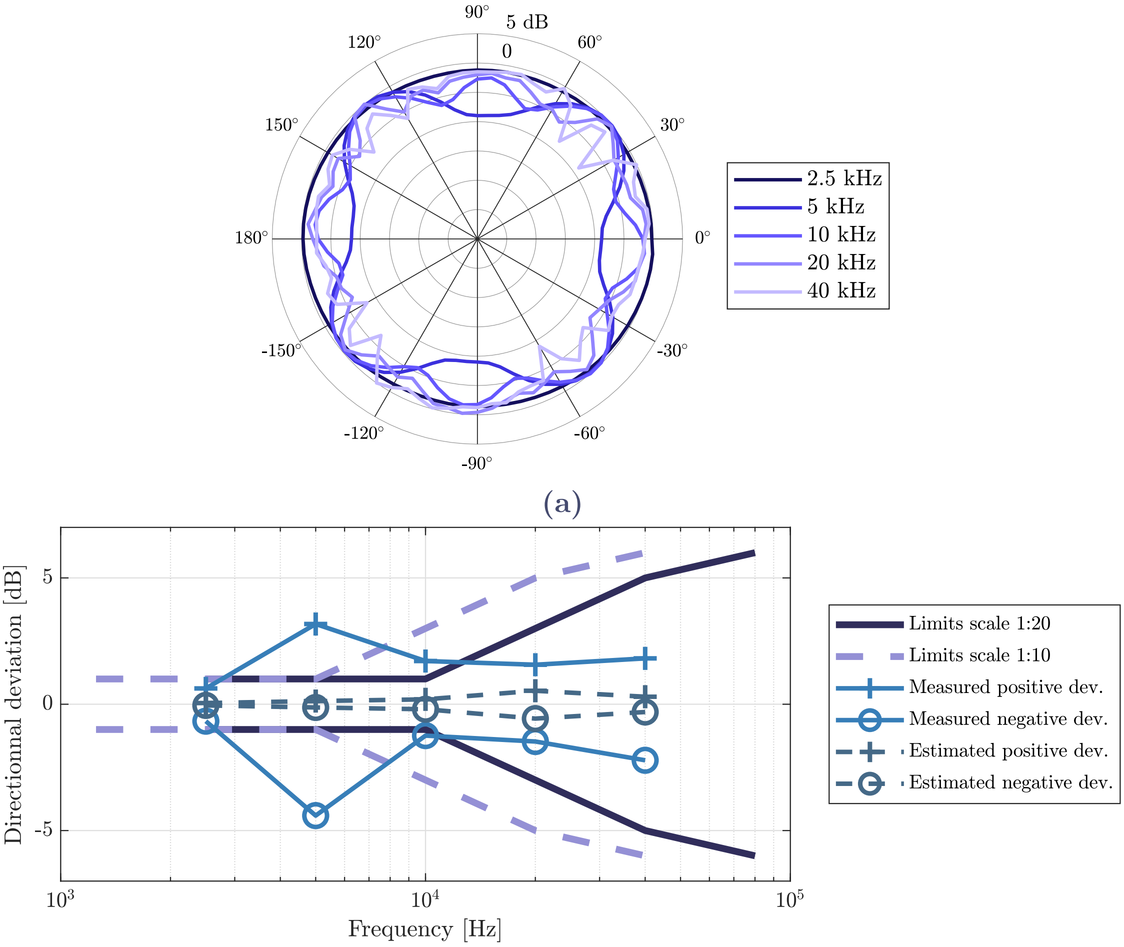

(a)

(b)

Figure 3.6 Measured average octave-band directivity patterns **(a)**, and measured and estimated directional deviations **(b)** compared to the maximum acceptable deviations from ISO 3382-1 (2009) for 1:10 and 1:20 scale factors of the tetrahedral tweeter array.

3.1.3.3 Inverted horn tweeter

The octave-band directivity patterns of the tweeter coupled with an inverted horn are shown in fig. 3.8a. Compared to the tweeter alone, the omnidirectionality is visibly improved. It appears an increased directivity as the frequency increases, but the angular coverage at −3 dB is more than 180°, except for the 40 kHz octave band. The minimum relative levels are found near the back of the tweeter, around 180° but not on axis.

The measured deviations are shown in fig. 3.8b. The maximum positive deviations comply with the standard for both scale factors. The negative deviation over the 5 kHz octave band is the only one that is below the limits for the 1:20 scale factor. At 1:10, only the 125 Hz octave band is not respected, the negative deviation being −2 dB. Although the directivity patterns appear to be omnidirectional, at least more than the previous sources, the occlusion by the horn and tweeter body causes these deviations.

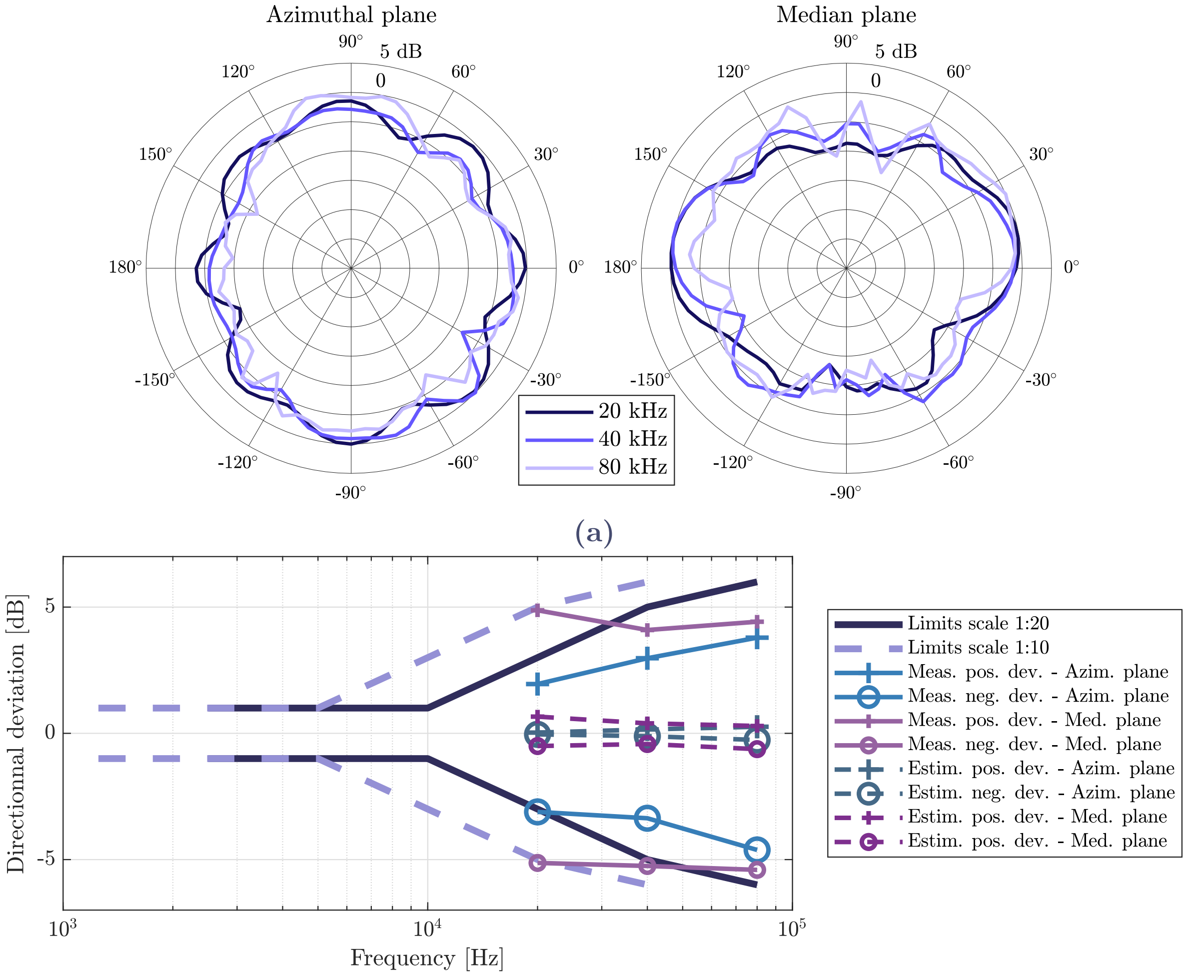

(a)

(b)

Figure 3.7 Average octave-band directivity patterns **(a)** measured in the azimuthal and median planes, and measured and estimated directional deviations **(b)** compared to the maximum acceptable deviations from ISO 3382-1 (2009) for 1:10 and 1:20 scale factors of the super-tweeter array.

3.2 Receivers

Room acoustic scale model measurements are often limited to omnidirectional impulse responses, without the possibility to analyze the spatial parameters that are closely related to the acoustic qualities of spaces from a perceptual point of view. The intrinsically spatial content of the sound field is accessible through directional (or spatial) room impulse responses. They are useful for many applications such as the estimation of spatial acoustic parameters (ISO 3382-1, 2009) or three-dimensional auralizations (Tervo et al., 2013a), thus constituting a precious tool for the improvement or the study of room acoustics (Embrechts, 2016). They can be captured with spherical microphone arrays (Core Sound, 2022; mh acoustics LLC, 2022) but they are not adapted to room acoustic scale models with typical scale factors as their bandwidth do not make it possible to cover the necessary frequency range and their large dimensions can disturb the sound field.

Another approach consists in capturing the sound field with an artificial human head

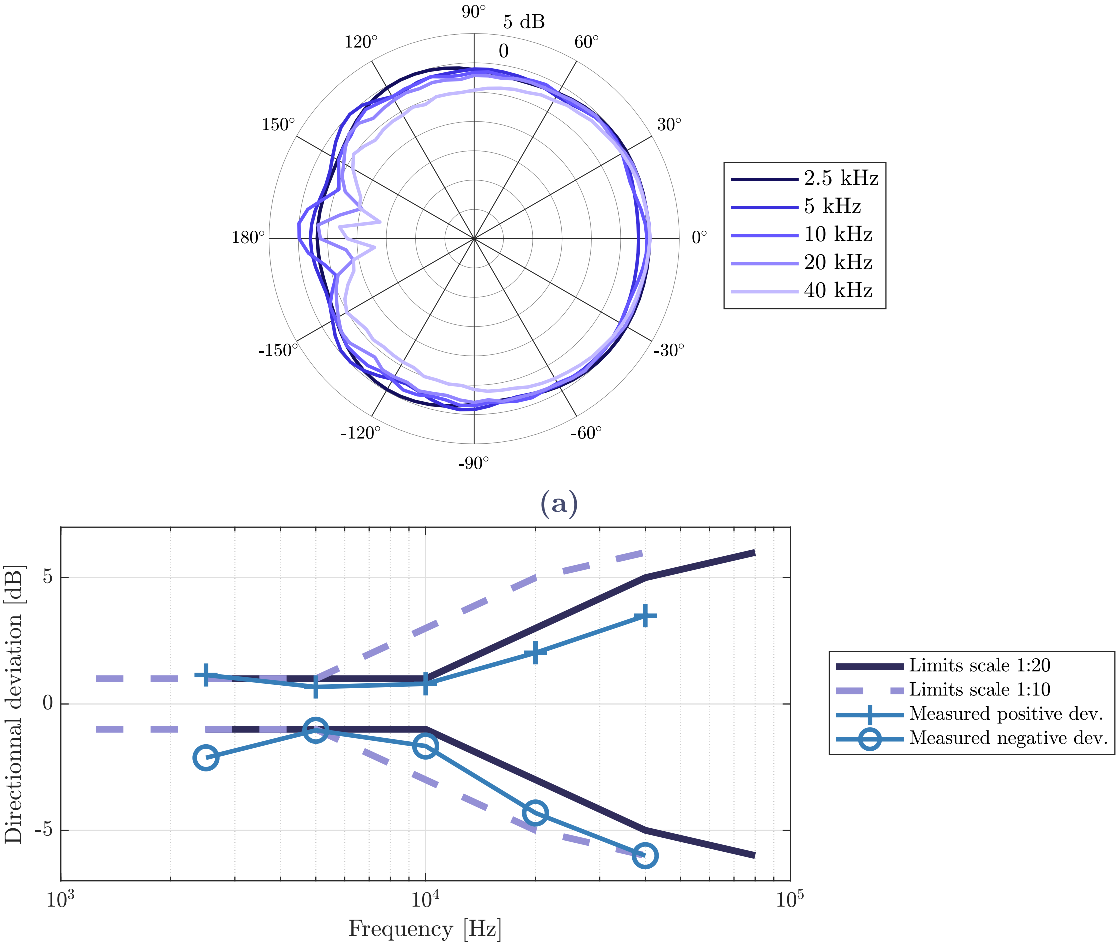

(a)

(b)

Figure 3.8 Measured average octave-band directivity patterns (a), and measured and estimated directional deviations (b) compared to the maximum acceptable deviations from ISO 3382-1 (2009) for 1:10 and 1:20 scale factors of the dome tweeter with an inverted horn.

equipped with a microphone at each eardrum, known as binaural recording. Thus, by rendering such a recording to each listener's ear, it reproduces the natural human sound perception. This technique captures certain cues that allow us to localize the provenance of the sound such as the interaural level differences (ILDs), the interaural time differences (ITDs), and spectral cues. They are included in what is called the head related transfer function (HRTF) in the frequency domain or head related impulse response (HRIR) in the time domain, specific to each morphology. It is actually a set of transfer functions or impulse responses with a pair for each source position, covering a spherical grid. These dummy heads are also used to measure IACC in BRIRs as presented in section 2.1.2.

We propose in the following two approaches to extend room acoustic scale modeling to the spatial domain. First, a brief review of methods proposed in the literature is given in section 3.2.1. Then, the first one presented is an artificial head at 1:8 scale based on a commercial model, Neumann model KU 100, equipped with miniature microphones designed for HRTFs measurements. The second one is based on the SDM (Tervo et al., 2013a), adapted to small scales.

3.2.1 Review of existing

As already introduced in section 2.3.2, Spandöck (1934) extended room acoustic scale models to the perceptual domain by auralization for subjective auditory evaluations. He was nevertheless limited by the analog equipment of his time. This idea was later revisited by several authors as digital audio techniques developed (Grillon et al., 1996; Hidaka et al., 1989; Polack et al., 1993). To use this technique with binaural receivers, it was proposed to approximate a listener by a rigid sphere model or another simplified shapes, with two microphones at the position of the ears, placed on a torso (Hidaka et al., 1989; Jurkiewicz et al., 2015; Katz et al., 2015; Orlowski, 1981). More realistic scale dummy heads, based on commercial (Robinson et al., 2013b; Xiang et al., 1993) or custom (Jeon et al., 2020; Xiang et al., 1991) models, have also been used, notably to investigate the perceptual effects of diffuse reflections (Jeon et al., 2020; Robinson et al., 2011; Ryu et al., 2008).

Suzuki et al. (2019, 2018) proposed to adapt the ambisonic recording technique to scale models. At full scale, this technique employs microphone arrays that are not suitable for small scales. Instead, they used a single microphone that they moved to several points covering a small volume of space with the help of a motorized and a manual stage. A RIR is measured at each of the points with an omnidirectional source at a fixed position. This set of responses is then used to decompose the field arriving over this small volume into plane waves, one for each time window, expressed using the spherical harmonic basis. This representation can then be decoded, still using this basis of functions, to reproduce the sound field with the estimated plane waves over a loudspeaker array, circular in their case.

3.2.2 Scale "Fritz" dummy head

The miniature dummy head is designed based on the Neumann model KU 100, sometimes named "Fritz". This artificial head model has been the subject of several interlaboratory studies in the context of measurements of HRTF (Andreopoulou et al., 2015), and simulations (Greff et al., 2007; Gumerov et al., 2010). For these activities, a MRI scan of the head was conducted to obtain a high resolution mesh of the head to be used for BEM simulations. This mesh was imported in Blender and reduced by a factor 8 in dimensions. It was manufactured by 3D printing using a polyamide powder sintering process, thus allowing good reproduction of the details of the outer ears. Nevertheless, their thickness had to be increased for strength reasons. Only the back of the pinna is modified. It is designed to open along the median plane. A Feichter M1 microphone, previously inserted in a printed plug with a semi-rigid material, is positioned in each half in a cavity designed for this purpose. The two halves are assembled with flexible pins in the same semi-rigid material, allowing positioning and holding.

3.2.2.1 Measurements

The HRIRs were measured in the anechoic chamber of Sorbonne Université. They were restricted to the azimuthal plane, with an Audax TM020G3 dome tweeter as a source placed in far field, at approximately 3 m from the head. The head was placed on a turntable (Brüel & Kjær Turntable System Type 9640), with the rotation axis passing through the median plane of the head and the axis between the ear drums, *i.e.* the microphones. The exponential swept sine method (Müller et al., 2001) was used with a signal

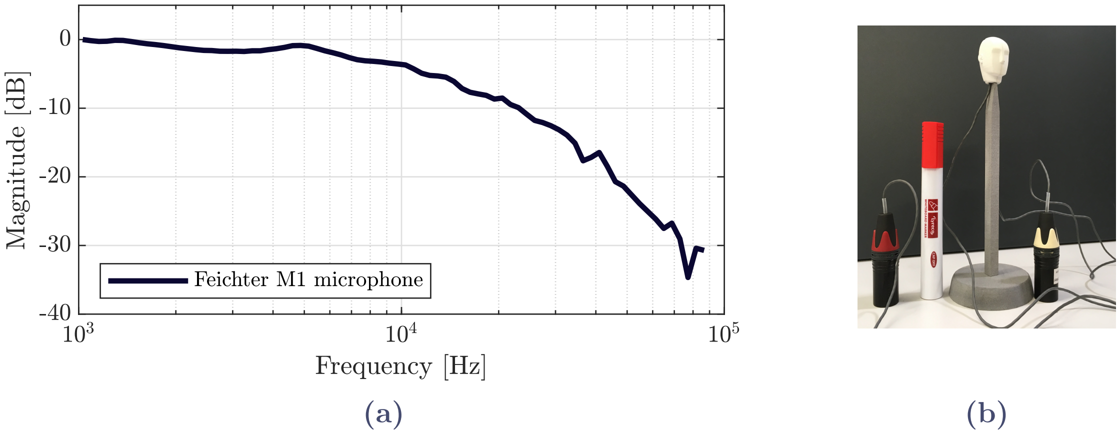

(a)

(b)

Figure 3.9 Normalized magnitude response (a) of Feichter M1 microphone with one-twelfth octave-band smoothing and a photograph (b) of the scale "Fritz" head.

spanning frequencies from 1 kHz to 95 kHz over 5 s. Similarly to previous measurements, the procedure was automatic and controlled with MATLAB 2018b.

3.2.2.2 Comparison with the full scale artificial head

The validation of the scale artificial head is done by comparing it with the full scale Neumann KU 100. As already mentioned, this particular model has been used in an interlaboratory comparison of HRTF measurements providing results of ITDs of the multiple participants. Different sets of HRIRs are also available in databases. The set chosen is the one provided by Bernschütz (2013), consisting in a set of HRIRs measured every 1° for a source at 3.25 m in the azimuthal plane.

We compare in the following the magnitude of the directional transfer functions (DTFs), defined as the frequency-dependent parts of the HRTFs (Bomhardt, 2017), calculated as

$$|\mathrm{DTF}(\theta_i)| = \frac{|\mathrm{HRTF}(\theta_i)|}{D}\,, \tag{3.10}$$

where D is the the surface-weighted arithmetic mean from all magnitudes of the set, corresponding to the arithmetic mean in our case. This also makes it possible to eliminate the response of the equipment.

Figure 3.10 shows the magnitude of the obtained DTFs for 4 azimuthal directions: front, right, back, left. They are compared to those obtained from the measurements conducted by Bernschütz (2013) on the real model. The frequency axis has been scaled to represent the full-scale frequencies, and it is limited at 7 kHz that corresponds to the edge frequency of the 40 kHz at the 1:8 scale. The results are in good agreement up to about 4 kHz, with ±2 dB differences. The expected behavior of ILDs, *i.e.* no difference for a source at the front or back, and similar differences for a source at the right and the one diametrically opposite with small differences at low frequency, less than 1 dB below 300 Hz, is reproduced. The magnitudes of the two different ear canals for the front and back azimuth are comparable on the considered frequency range. Above 4 kHz, the limitations of the equipment appear with large deviations, in particular if we consider the contralateral ear for a source localized on the right or the left, where the highest deviations are observed.

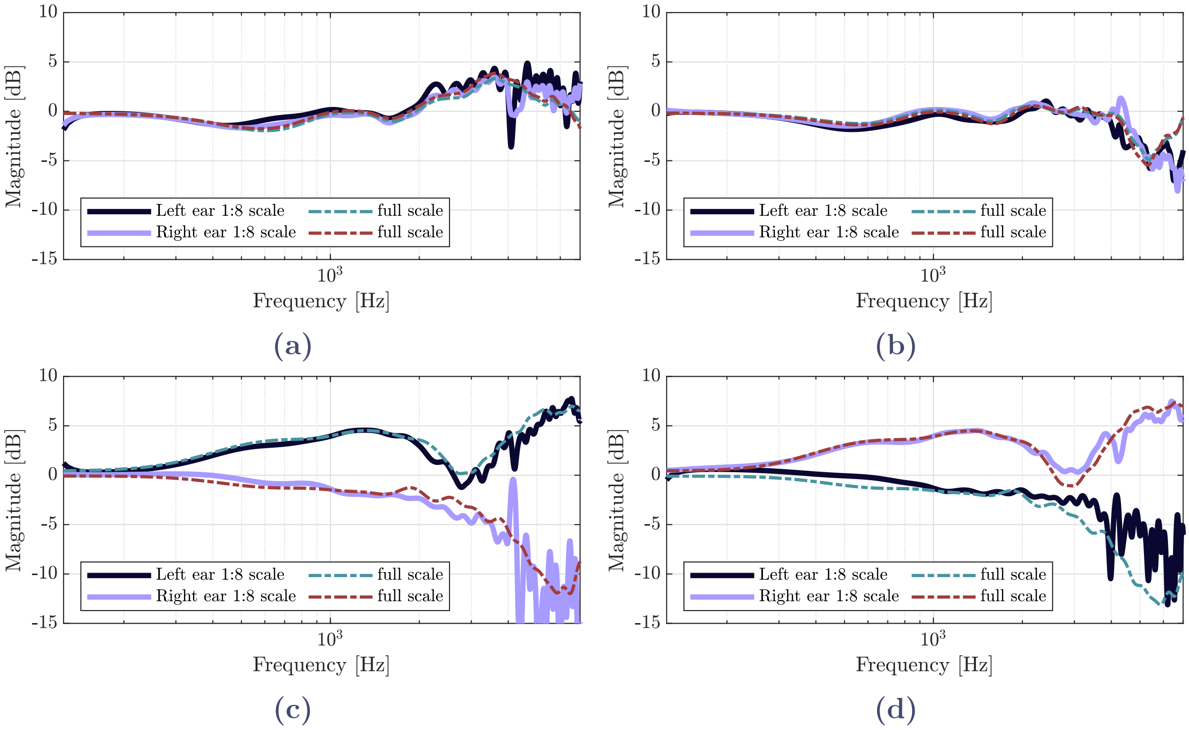

(a)

(b)

(c)

(d)

Figure 3.10 Measured DTFs of the 1:8 scale “Fritz” head compared to full scale (Bernschütz, 2013) for a source localized at the **(a)** front, **(b)** back, **(c)** left, and **(d)** right in the azimuthal plane. The frequency axes correspond to the full scale.

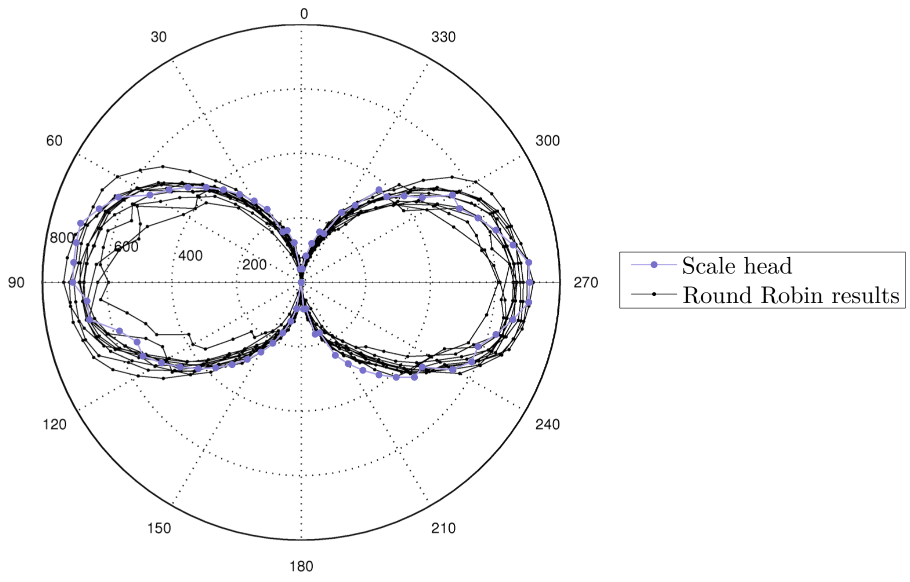

Figure 3.11 Estimated ITDs of the scale “Fritz” head in µs compared to the results of the inter-laboratory Round Robin on HRTF measurements (Andreopoulou et al., 2015).

Figure 3.11 shows the ITDs estimated using the same threshold method as Andreopoulou et al. (2015) overlaid on the results of their study for comparison. The onset of each HRIR is defined as the first sample greater than $-10\,\mathrm{dB}$ relative to the peak value. With this method, the results found are integer multiples of samples. When converted to full scale, *i.e.* the time is multiplied by 8, as presented here, ITDs are quantized in steps of about 42 µs. The expected ITDs are reproduced and a good symmetry is observed with respect to the median plane. In the inter-laboratory comparison of HRTF measurements (Andreopoulou et al., 2015), a strong variability of ITDs was found between the different submissions, up to 235 µs for the lateral directions. Comparing our results to all the submissions, the estimated ITDs are in general agreement if we consider the quantization in our results.

3.2.3 Spatial decomposition method

The Spatial Decomposition Method (SDM) is a spatial encoding technique using a parametric approach that can be applied to any compact microphone array geometry (Tervo et al., 2013a). It has been used for spatial analysis and auralization of concert halls (Pätynen et al., 2016), and also for their graphical representation (Pätynen et al., 2013; Tervo et al., 2013b). These tools are implemented in a MATLAB package, the SDM Toolbox (Tervo, 2020). The method is based on the assumption that the sound field arriving on the compact microphone array can be described as a succession of plane waves and thus a spatial impulse response can be decomposed into a set of discrete pressure values and their corresponding direction of arrival (DOA), *i.e.* an image-source is attributed at each time sample. The direction of each image-source is estimated using least square solution for time difference of arrival (TDOA) and its pressure value is ideally provided by the signal at the geometric center of the array.

For an array recording N RIRs $h_i^{(k)}$ at locations $\mathbf{r}_i$, $i = 1, \dots N$, windowed around the sample of interest k with a Hann window of size L, TDOA $\tau_{i,j}^{(k)}$ between the microphones i and j for this time sample can be estimated by finding the delay that maximizes the cross-correlation between the two signals, *i.e.*

$$\hat{\tau}_{i,j}^{(k)} = \arg\max_{\tau}\{R_{i,j}^{(k)}(\tau)\}\,, \tag{3.11}$$

where

$$R_{i,j}^{(k)}(\tau) = \mathcal{F}^{-1}\{H_i^{(k)}(\omega)\bar{H^{(k)}}_j(\omega)\} \tag{3.12}$$

with $\mathcal{F}^{-1}$ the inverse discrete Fourier transform, $H_i^{(k)}(\omega)$ and $H_j^{(k)}(\omega)$ are the dicrete Fourier transforms of the windowed RIRs, and “$\bar{\cdot}$” denotes complex conjugation. The method uses interpolation on a Gaussian curve (Zhang et al., 2005) to refine the estimation to subsample accuracy.

The average direction of the wave can then be estimated using the least square solution for the slowness vector

$$\mathbf{m}_k = \mathbf{V}^{\dagger}\hat{\boldsymbol{\tau}}_k\,, \tag{3.13}$$

where $\mathbf{V}^{\dagger}$ is the Moore-Penrose pseudoinverse of $\mathbf{V}$, the microphone position difference vector,

$$\mathbf{V} = \begin{bmatrix}\mathbf{r}_1 - \mathbf{r}_2 & \mathbf{r}_1 - \mathbf{r}_3 & \dots & \mathbf{r}_{N-1} - \mathbf{r}_N\end{bmatrix}^T\,, \tag{3.14}$$

and $\hat{\boldsymbol{\tau}}_k$ is the corresponding TDOA estimate vector,

$$\hat{\boldsymbol{\tau}}_k = \begin{bmatrix}\hat{\tau}_{1,2}^{(k)} & \hat{\tau}_{1,3}^{(k)} & \dots & \hat{\tau}_{N-1,N}^{(k)}\end{bmatrix}^T\,. \tag{3.15}$$

The DOA $\mathbf{n}_k$ is obtained by

$$\mathbf{n}_k = -\frac{\mathbf{m}_k}{|\mathbf{m}_k|}\,. \tag{3.16}$$

The image-source coordinates for the time sample k are eventually deduced considering its distance $d_k = ck/f_s$ to the compact array, and its amplitude is given by the pressure value of an omnidirectional microphone of the array, ideally at the center but it has been shown that choosing any of them did not have a great impact.

An image-source can be attributed to each time sample by sliding the window. Its size is bounded by the size of the array, so that a wave has crossed the array entirely to be able to estimate its direction. Using long windows results in considering several sound waves arriving at the same time that can result in errors regarding the DOA estimation. The optimal parameters for the method have been investigated by Amengual Garí et al. (2021) with simulations using the image-source method. For a microphone array composed with 7 omnidirectional capsules, one at the center and 6 arranged as pairs in orthogonal directions, the optimal array diameters are 5 cm and 10 cm, resulting in the lowest and similar DOA errors. Concerning the window length, for the 10 cm array, the optimal sizes are around 36 and 64 samples for a sampling frequency of 48 kHz.

3.2.4 Measurements in a 1:10 concert hall scale model

These methods are tested in a 1:10 scale model of a concert hall. The model has been constructed to plan the acoustics of the future concert hall of the *Sinfonia Varsovia Centrum* in Warsaw, Poland, designed by *Atelier Thomas Pucher*. Its design is intended to combine the shoe-box hall acoustics with the visibility that offers a vineyard hall seating arrangement. To achieve this, the walls form a box that contains three levels of large oval-shaped ribbon balconies surrounding the stage. It is planned to accommodate 1800 people. The particular reason to build a scale model in this case is that the balconies and the suspended reflectors form curved surfaces that are difficult to model with geometrical room acoustic simulation software.

The acoustic consultants in charge are *Müller-BBM*, Berlin, Germany, for the design team and *Kahle Acoustics*, Brussels, Belgium, for the project owner. On behalf of the latter, we have conducted a series of measurements. It constitutes a practical case to evaluate the viability of the proposed tools. We do not provide here a systematic comparison of measurements with the acoustic criteria set for this hall. Results for the reverberation time are nevertheless presented.

3.2.4.1 Scale model

The scale model is mainly made of wood, and the curved surface such as the fronts and the undersides of the balconies, or the suspended ring reflectors are finished with plaster. Figure 3.12 shows two spherical photographs from the top balcony from the back of the stage (fig. 3.12a) and from the rear of the hall(fig. 3.12b). All the surfaces are painted to make them more reflective, except the wall located behind the stage that is made of glass. The absorption is provided by the chairs where a piece of felt is hung. The model has been constructed by Pracownia Tryktrak (2020).

3.2.4.2 Measurements and methods

Four different sources were used during the measurement sessions. Figure 3.13a shows one configuration of them on stage. From left to right, there are a Dr-Three[1] dodecahedral

---

[1] http://www.dr-three.com/

(a) (b)

Figure 3.12 Spherical photographs of the *Sinfonia Varsovia Centrum* concert hall scale model from the top balcony, from the back of the stage **(a)** and the hall **(b)**.

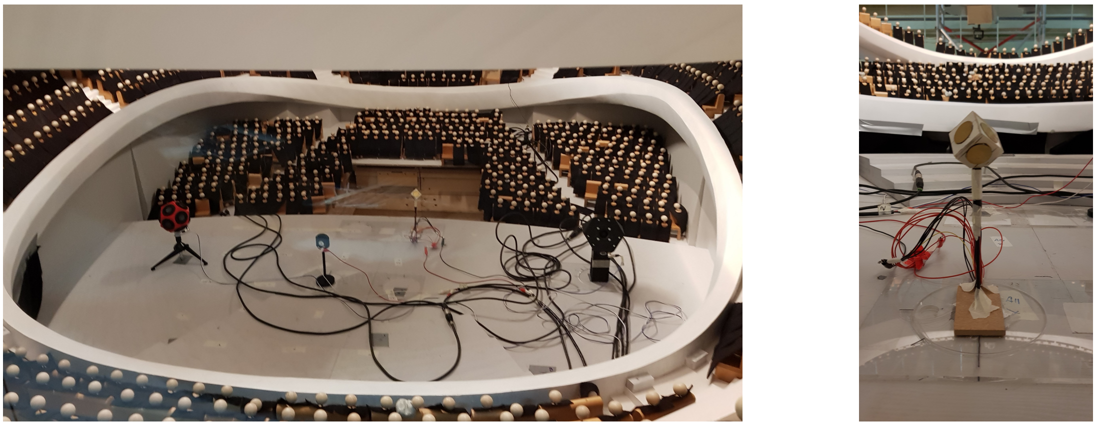

(a) (b)

Figure 3.13 Photographs of the sources. **(a)** One configuration on stage, from left to right: dodecahedral, single tweeter, cubic, and tetrahedral source. **(b)** Detail of the cubic source with the rotating board.

source, a single dome tweeter, a custom piezoelectric cubic source, and the tetrahedral source presented in section 3.1. The single tweeter is an Audax TM020G3 used in section 3.1 to obtain a directive source that could represent the voice directivity, but it is not exploited here. Figure 3.13b shows the piezoelectric cubic source in more detail. Six piezoelectric chips are mounted on each face on a cube of about 3 cm edge. Each source was installed on a rotating board to perform several source rotations when recording the omnidirectional RIRs. They were driven by a Samson Servo 120a amplifier. The microphone used for the latter, as well as for the set of RIRs for SDM is a Feichter M1, the same as those which equip the scale dummy head. Source and receiver positions are indicated in appendix A.

A set of 8 impulse responses was recorded to apply SDM, one at each corner of a cube of 3.7 mm edge, representing a 64 mm diagonal at full scale. For this purpose, two micrometric linear manual stages were mounted perpendicularly to move the microphone attached to the end of a rigid arm in the horizontal plane as shown in fig. 3.14b. The assembly was fixed on a support adapted to the seat of the model. The sources were not moved or rotated between each measurement, and the configuration chosen is the one shown in fig. 3.13a. To move the microphone in the vertical direction, a precision

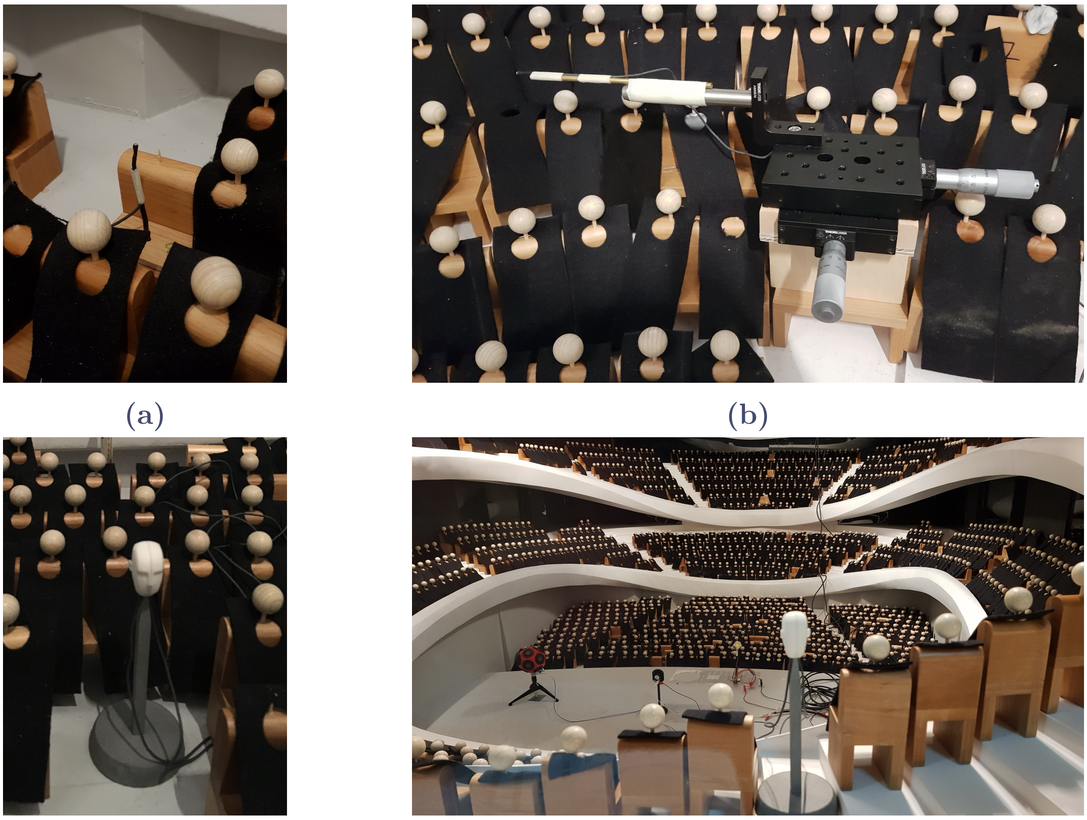

(a) (b) (c) (d)

Figure 3.14 Photographs of the receivers. **(a)** Omnidirectional microphone. **(b)** Manual stages with an omnidirectional microphone. Scale head in the parterre **(c)** and behind the stage **(d)** facing the cubic piezoelectric source.

wedge of the correct thickness was installed between the support and the stages. However, this proved to be too imprecise, introducing a rotation during reassembly, restricting the analysis to the lateral plane.

The BRIRs were recorded with the head facing the piezoelectric cubic source positioned at SP1 as shown in fig. 3.14d. The calculation of IACC is therefore only valid for the latter.

All the RIRs have been obtained using the swept sine method. The logarithmic sweep duration was a 1 s repeated twice for each source, spanning frequencies from 1.5 kHz to 90 kHz. All were connected to an audio interface (RME Fireface 802) configured at a sample rate of 192 kHz, controlled with MATLAB 2018b. The temperature and humidity were regularly measured to apply the proper numerical air absorption compensation.

3.2.4.3 Results

Counting the three presumed omnidirectional sources, their rotations, and the receiver positions, 144 RIRs were measured. Figure 3.15 represents the distribution of T_{20} that have been estimated for the 250 Hz to 2000 Hz octave band. The average at mid-frequencies is around 2.1 s. The distributions appear centered, and half of the measured positions are within ±1 JND from the mean in their respective octave band.

BRIRs have been measured at 12 positions across the hall. The interaural decorrelation

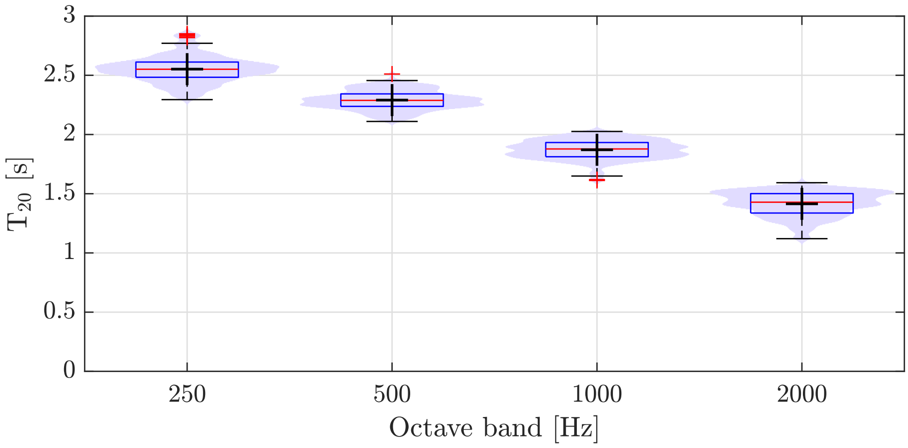

Figure 3.15 Kernel density estimates and box plots of reverberation time T_{20} obtained from 144 RIRs. Mean is indicated with a black cross.

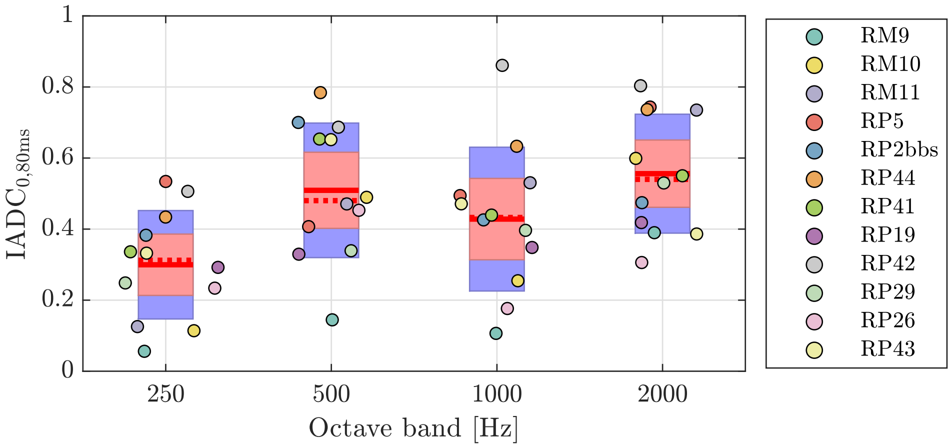

Figure 3.16 Early interaural decorrelation coefficient, $\mathrm{IADC}_{0,80\,\mathrm{ms}}$, for 12 receiver positions and the piezoelectric cubic source at SP1, indicated in appendix A. Bars represent ±1 standard error of the mean (red) and ±1 standard deviation (blue). Solid and dotted (red) lines represent means and medians, respectively.

coefficient for the early part defined as $\mathrm{IADC}_{0,80\,\mathrm{ms}} = 1 - \mathrm{IACC}_{0,80\,\mathrm{ms}}$ (Xiang et al., 2019), for each one is represented in fig. 3.16. For this time interval, high values of the coefficient correlate with greater values of subjective apparent source width (Beranek, 2008). At mid-frequencies, more than half of the positions are below 0.5 which can be considered as a satisfactory value regarding concert halls. Some positions such as RP42 and RP44 rank high compared to the others. These particular positions were located close to the corners of the rear of the hall (see appendix A), probably resulting in a strong lateral reflection.

As already mentioned the relative positions of the microphone during the spatial RIRs measurements is know precisely in the horizontal plane only, the spatial analysis is therefore restricted to this one. The window length for DOA estimation is 100 samples at 44 100 Hz sampling frequency, higher than the limit due to the array size, chosen to match the average length of the impulse responses (in free field) produced by the sources. A 2 kHz low-pass butterworth filter of order 3 has been applied to all RIRs as a compromise between bandwidth for the localization method and frequency band where the sources can be considered as more omnidirectional. Figure 3.17 represents the cumulative energy dis-

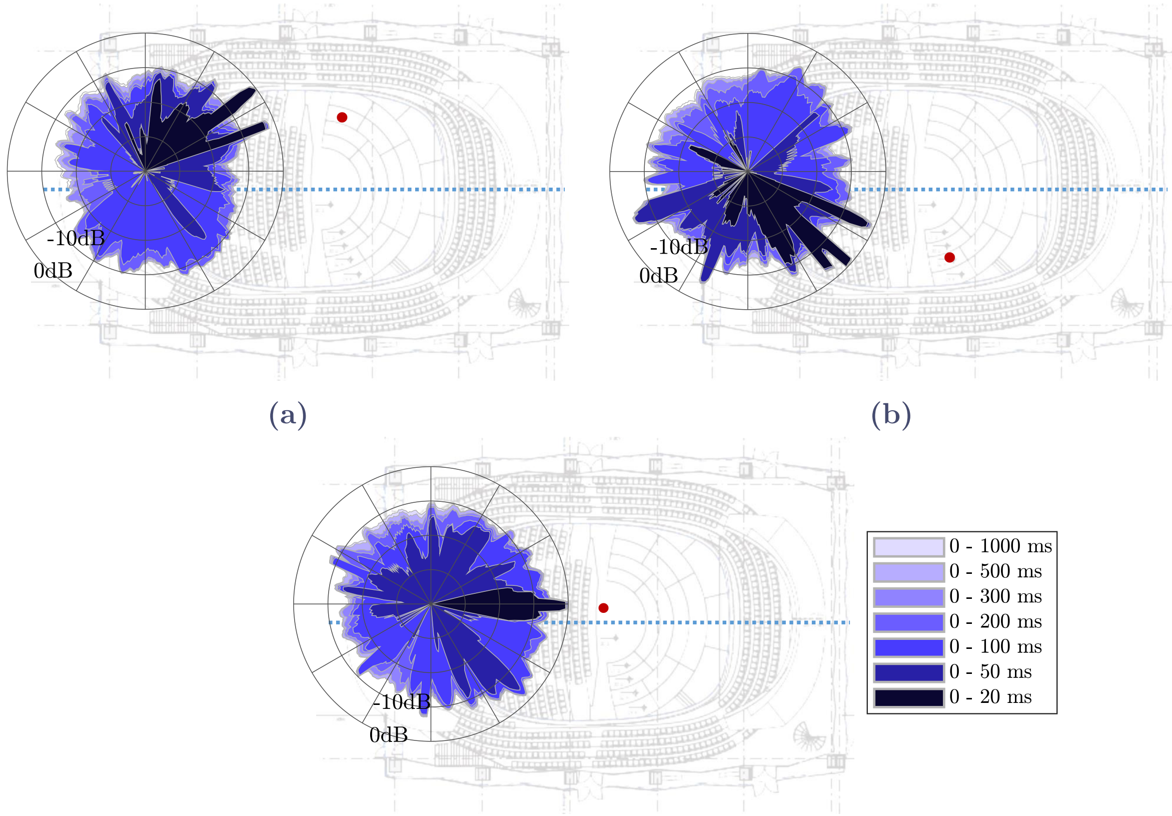

(a) **(b)**

(c)

Figure 3.17 Cumulative energy distributions in the lateral plane obtained by SDM at position RM3 for three different sources: **(a)** tetrahedral, **(b)** dodecahedral, and **(c)** cubic source. Their position is indicated with a red dot.

tributions over increasing time intervals from 0 ms to 20 ms, 50 ms, 100 ms, 200 ms, 300 ms, 500 ms, and 1000 ms. For all three sources, the direction of the direct sound seems to be estimated satisfactorily considering the distributions for the first time interval. Lateral reflections are observed in the early part, 50 ms after the direct sound. These reflections for the sources on the sides of the stage are in good correspondence, with nevertheless some estimated directions with rather high relative levels for the dodecahedral source (fig. 3.17b), from the back notably. Comparing our results with the energy distributions provided by Tervo et al. (2013b) for several halls including shoebox-, vineyard-, and fan-shaped concert halls, the present hall corresponds more to the shoe-box halls, where the presence of lateral reflections results in more triangular distributions.

3.3 Discussions and conclusions

In this chapter we have reported our results of investigations concerning the design of omnidirectional sources and spatial receivers for room acoustic scale models.

3.3.1 Sources

Three source designs were proposed and evaluated according to the ISO 3382-1 (2009) standard procedure for 1:10 to 1:20 scale factors. Among them, two were tweeter arrays whose configuration was estimated from the directivity of the individual elements. The estimation method was based on octave-band averages and did not take into account many other factors such as reflections from the source body. It could be improved by working with complex pressure or narrower bands, and by taking translations into account.

The tetrahedral source was found to be more adapted for low-frequency range. It did not fully comply the standard but rotations could be envisaged to estimate room acoustic parameters. Its enclosure is only a prototype and a more spherical design could be envisaged. The super-tweeter array could be used in association to cover the high-frequency range.

The latest design using an inverted horn visibly improved the omnidirectionality compared to the tweeter alone, but introduced strong resonances. Further investigations on methods to mitigate them to consider using it for perceptual studies is needed. However, in this state, the source could be used for late field parameter measurements. Furthermore, only one horn geometry has been fabricated here, but other profiles and dimensions associated with different tweeters could be tested.

3.3.2 Receivers

Using scale model for perceptual testing is not a new idea, but it is necessary to be able to capture the spatiality of the sound field from a listener's point of view. At full scale, the most common methods are binaural or ambisonic recordings.

Artificial heads have already been adapted to scale models in different studies. Here we have presented the first 1:8 reproduction of the Neumann KU 100 artificial head, a model widely used in the community. The measurements showed that is satisfactorily reproduced ITDs and ILDs of the full scale model. However, the microphones and especially the sound source used only achieved a sufficient SNR up to about 4 kHz at full scale. It was tested in the context of IACC measurements in a concert hall model built at a scale of 1:10, therefore not directly appropriate but could represent a larger than average person. Preliminary listening by the author has shown that frequency extrapolation methods should be considered.

SDM also tested in this model and had the advantage that it could be used at any scale. It is an alternative to ambisonic recordings. The method was adapted by moving an omnidirectional microphone to several points in a compact volume in space and a RIR was measured at each. Only the visualization of the directionality of the sound field in the lateral plane was possible. Measurements in a controlled space should be considered to evaluate the method more precisely, with a third axis to access the three-dimensional sound field.

Chapter 4

A round robin on room acoustical simulations of a coupled volume case

The advantages and limitations of most numerical methods in room acoustics have to date been primarily evaluated in single-volume room conditions, placing emphasis on early reflection components and the early part of the room acoustic impulse response. Few studies have examined the capabilities of simulations to model correctly the case of coupled volumes, where the late part of the impulse response is not a simple extension of the early part and needs to be accurately represented. This chapter presents a round robin type study comparing the results of different numerical simulation tools with measurements carried out in an acoustic scale model of a coupled volume system.

The preliminary results of the study described in this chapter were the subject of a publication in an international conference proceedings (Weber et al., 2019). However, in the latter, the simulations were compared with the statistical model from coupled volume theory (Cremer et al., 1982; Summers, 2005) whose parameters have been defined from measurements of the scale model to ensure its physical realism. In the following, more direct comparisons between simulations and measurements will be made since the statistical model does not allow the positions of sources and receivers to be taken into account (Luizard et al., 2014b). In addition, similar studies have been published concomitantly with the one proposed here, allowing a more exhaustive review of the obtained results.

First, the results of these similar studies are briefly presented in section 4.1. We then present the methods chosen in this Round Robin in section 4.2, *i.e.* the scale model, the measurements as well as the procedure that the participants had to follow are described. A brief description of each software involved including their own parameter settings is given in section 4.3. The results are finally presented and discussed in section 4.4 in the light of similar published studies.

4.1 Previous studies

Three round robin type studies on room acoustical numerical simulations have been conducted between 1994 and 2002 (Bork, 2000, 2005a,b; Vorländer, 1995), which compared the results of different algorithms with measurements in single volume spaces. The procedure followed was close to that encountered in acoustic planning in the field of building design and construction. First the acoustic materials were either described, later the acoustic properties of the materials were prescribed according to measurements or data tables for uniformity. These studies have highlighted some trends between simulation tools, while also showing the importance of user variability and input data quality. The last large study of this type (Brinkmann et al., 2019) was based on eleven scenarios.

Eight scenes are simple configurations. They were designed to isolate specific acoustical phenomena such as single and multiple reflections on finite and infinite plates, scattering, diffraction, the seat dip effect, or a coupled room. The three other scenes are complex rooms representing real-world listening environments. In addition they extended the study to the evaluation in the perceptual domain through auralizations.

The coupled volume scenarios studied in Brinkmann et al. (2019) are more complex as they are based on two real rooms separated by a large hinged door with inhomogeneous absorption in the less reverberant space. Two different door opening angles have been tested, 30.4° and 4.1°. While the double slope decay is clearly visible in the measured data, their simulations exhibit only a strong coupling behavior, *i.e.* a small difference between the two slopes of the decay. This results have been attributed to erroneous boundary condition data (Aspöck et al., 2019). A similar procedure, to the one we propose, has been applied in Aspöck et al. (2019) on these scenarios. After adjustment of the boundary conditions, simulation are in good agreement with the measurements for the strongly coupled case while it is not the case for the weakly coupled case (door slightly opened). It could indicate that for more complicated geometries, when the sound field is obstructed, geometrical acoustics methods have difficulties to accurately model coupled volume acoustics in weak coupling conditions.

Luizard et al. (2013) compared numerical simulations with measurements made in the same scale model as the one used here, apart from slight modifications of the configuration and the materials of the main room. The numerical methods included two commercial software based on geometrical acoustics (GA): CATT-Acoustic (Dalenbäck, 1996) and ODEON (Naylor, 1993), as well as two wave-based methods: BEM and finite difference time domain (FDTD) method. They observed that the geometrical methods were in better agreement with the measurements. The large discrepancies found for the latter were attributed to the approximations employed for the numerical mesh, *i.e.* staircase approximation for FDTD and uniform element density for BEM, unrealistic boundary conditions, lack of consideration of air attenuation, and the calibration procedure not being sufficiently accurate.

4.2 Methods

4.2.1 Scale model

The physical scale model is a simplified coupled volume system of two rooms with dimensions representing a 1:20 scale concert hall. It has been used in previous studies on coupled spaces (Luizard et al., 2014a, 2013, 2014b), though the exact configuration of the main room and its materials have been changed from those studies. The two rooms are formed by two open boxes that can be joined around a common wall that can be solid to obtain independent closed volumes or with an aperture when it is desired to achieve an acoustic coupling. Photographs of the scale model are shown in fig. 4.1. The outer structure is made of rigid polyvinyl chloride at the floor and the side walls while the ceiling is in polymethyl methacrylate, a transparent material to allow visual observation of the interior of the model during measurements. Moreover, in order to avoid flutter echoes that can occur in such shoebox-shaped geometries, slightly tilted medium density fiberboards are placed on the side and rear walls with an angle of 2°. This is apparent in fig. 4.2 showing schematic views of the coupled volume system at full scale. The main room (fig. 4.1a) has its lateral walls covered with a lightly absorptive and diffusive

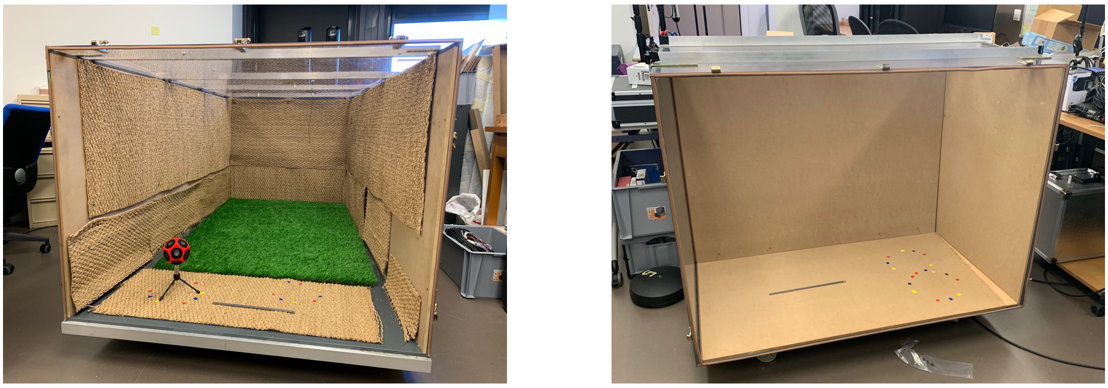

(a) (b)

Figure 4.1 Photographs of the scale models of the rooms: **(a)** Main room and **(a)** reverberation chamber.

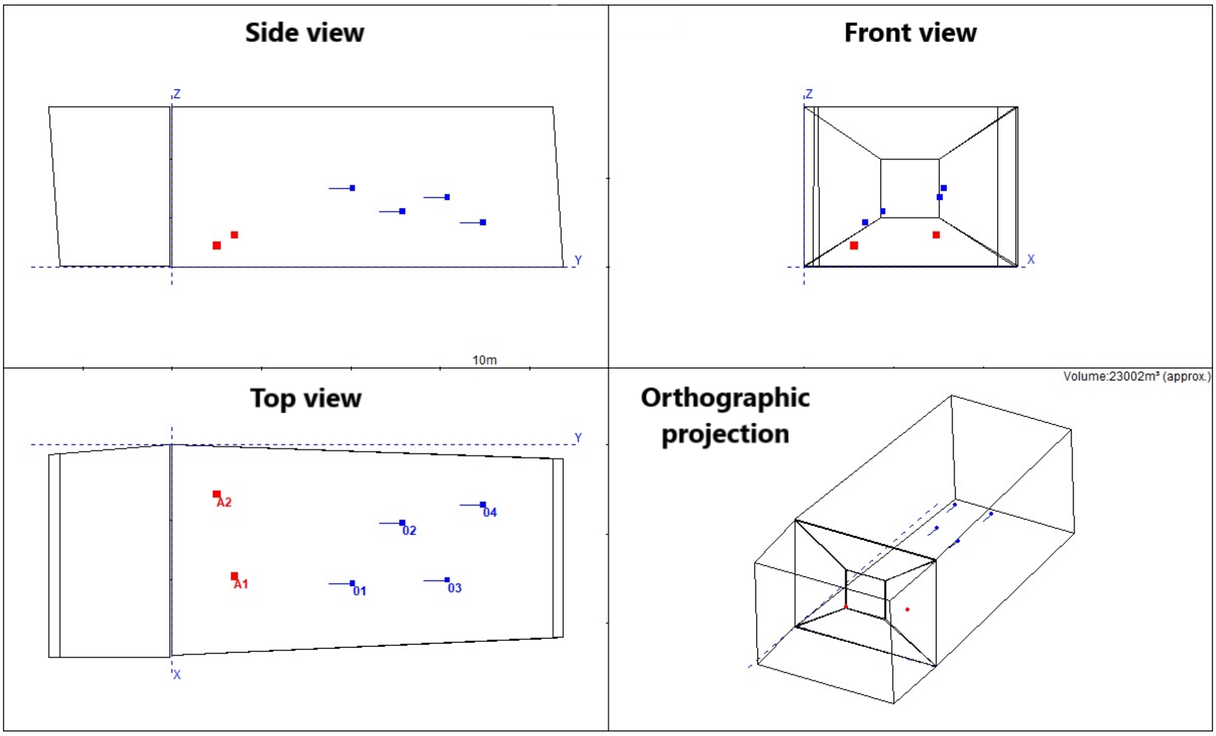

Figure 4.2 Schematic views of the coupled volume system

material made with braided seagrass while the floor is partly covered with artificial turf. No additional material is added to the reverberation chamber (fig. 4.1b), the materials in place ensuring greater reverberation than the main room despite its lower volume.

At full scale, the main room and the reverberation chamber are approximately 17 000 m^3 and 5400 m^3, respectively. These volumes are comparable to those constituting the exiting concert hall of the Kultur- und Kongresszentrum of Luzern, Switzerland (Johnson et al., 1999) built on the principle of coupled volumes to allow variable acoustics by adjusting the coupling, as mentioned in section 2.2.2. The acoustic coupling is achieved with a single centered rectangular aperture whose surface area is approximately 1 % of the total surface area of the main room's walls. All the geometric data of the full-scale model can be found in the invitation sent to the participants included in appendix B.

4.2.2 Measurements

Measurements were conducted with a miniature dodecahedral loudspeaker (Dr-Three 3D-032) as a sound source, visible in fig. 4.1a, driven by an amplifier (Samson Servo 120a) with several microphone receivers (DPA 4060). All were connected to an audio interface (RME Fireface 800) configured at a sample rate of 192 kHz and controlled via MATLAB 2018b. The exponential swept-sine technique was used to obtain the room impulse responses. Frequencies spanned 200 Hz to 60 kHz, covering the octave band of interest centered on 1 kHz at full scale. Due to the directivy of the source at high frequency, three source rotations are performed for each positions.

4.2.3 Calibration procedure

In order to avoid issues regarding different implementations of absorption and impedance conditions across numerical methods, a calibration scheme was used. The reverberation time in each room was prescribed according to scale model measurements in the uncoupled configuration. For simplicity, participants were instructed to adjust material properties of walls uniformly for each room (*i.e.* all walls of each volume have the same material definitions) to match the prescribed reverberation times. Measurements and simulations were carried out for 2 source and 2 receiver positions in the reverberation chamber and 2 source and 4 receiver positions in the main room (see appendix B). Measured impulse responses were numerically compensated for scaled air attenuation in the scale model. Prescribed average T_{30} in the main room and the reverberation chamber was 1.26 ± 0.064 s and 4.52 ± 0.065 s, respectively.

4.3 Entry descriptions

Solicitations for participants in this study were done via requests over email to a number of persons involved in the research, development, or use of room acoustics simulations. They were provided with all the geometrical data needed for the construction of the 3D model, as well as the instructions concerning the calibration procedure based on the uncoupled acoustic parameters. This invitation is included in appendix B. In total, there were 11 different entries using 10 different numerical methods with 3 wave-based methods, and 7 geometrical acoustic implementations. A short description of the programs used, mostly provided by participants, and their parameters are presented in arbitrary order.

I-Simpa: Version 1.3.4 is an open-source graphical user interface developed to host three-dimensional numerical codes for the modeling of sound propagation in complex geometrical domains. The calculation code used was SPPS (from French *"Simulation de la Propagation de Particules Sonores"*), version 2.2.1, based on a particle-tracing method (Picaut et al., 2012). The radius of the receivers was set to 10 cm, 50 million particles were used for each source and were collected using time slots of 20 ms.[1]

Wave-based: Two academic participants used CE-FDTD methods with different schemes. One used an implementation of the 3D standard rectilinear scheme, known as standard leapfrog scheme (SLF) while the other used the interpolated wideband (IWB) scheme. A description of those schemes may be found in Kowalczyk et al. (2010). The SLF scheme used a $c = 344\,\mathrm{m\,s^{-1}}$, $f_s = 18\,933\,\mathrm{Hz}$, a spatial grid of 31.5 mm and $\Delta t = 52.82\,\mu\mathrm{s}$.

---

[1] The resulting data were echograms, not impulse responses. In consequence, no 1 kHz-octave band filter was applied.

The IWB scheme used $c = 340\,\mathrm{m\,s^{-1}}$, spatial grid of 8.5 mm, and $\Delta t = 23.75\,\mu\mathrm{s}$. The room surface boundaries were assigned to be locally reacting and the impedance is frequency-independent in both implementations. A third entry used a software developed at the University of Edinburgh based on a hybrid finite difference and finite volume method. A description of the finite volume method part used in this implementation is given in Bilbao et al. (2017).

RAMSETE: Version 3.02 uses a Pyramid Tracing algorithm capable of solving the sound propagation problems in large enclosures or outdoors (Farina, 1995). The method employed was pyramid tracing with surface scattering and edge diffraction up to the second order. Discrete paths were saved up to fourth order. The number of pyramidal beams launched by each source was 32 768 and the energetic impulse responses were computed with a resolution of 1 ms.

CATT-Acoustic: TUCT v2.0e:1.01 algorithm 1 (CATT-Acoustic/TUCT, 2016) was used. Ray split-up between diffuse and specular reflections are performed randomly with a probability determined by the scattering coefficient (max split-order= 0). Calibration of the main room used 716 486 rays, the reverberation chamber 638 082 rays, for each source. The coupled configuration used 2 000 000 rays with auto-edge scattering applied on the aperture edge planes.

ODEON: Simulations were performed using ODEON Combined version 15.13 (ODEON, 2018). The calculation model is hybrid, using image source method plus radiosity for early reflections and ray tracing plus radiosity for late reflections. Reflections of first and second order were treated as early reflections. A total of 16 000 rays were used for late reflections for each source. Ray tracing was made using the method of reflection based scattering.

RAVEN: The Room Acoustics for Virtual ENvironnements software, developed at RTWH Aachen University (Schröder, 2011; Schröder et al., 2011), uses a hybrid algorithm that combines Image Source Method for the direct sound and early reflections with ray-tracing for the late reverberation, with ray tracing calculating an energy decay histogram based on specular reflections of order 3, diffuse reflections for order 1, and diffuse energy based on the diffuse rain model. One participant used the 2018.v2 version with 500 000 rays for the calibration of the absorption coefficients and 1 000 000 rays for the coupled rooms simulations. A second entry used 2019.v1 version with 500 000 rays for all simulations. They both used image sources for specular reflections up to the second order and ray-tracing parameters set to 1 m for the radius of the detection sphere with time slots of 10 ms.

Path tracing: One entry employed a geometrical acoustics simulation method based on unidirectional path tracing from the receiver position with next event estimation, a computer graphics method of rendering images of three-dimensional scenes, also termed "diffuse rain" in acoustics (Schröder, 2011). Materials are described by a glossy Phong reflectance model, an empirical reflection model used in computer graphics, that is controlled by the scattering coefficient. Energy decay histograms are computed for each band at full sample rate, converted to pressure envelopes, then the per-band pressure envelopes are multiplied by filtered white noise and summed to compute the pressure IR.

SoundPLANnoise: Version 8.2 using the Sound Particle Diffraction method (Stephenson, 2018) was used. It incorporates specular and diffuse reflections, transmission, room scattering, and geometrical diffraction. Diffuse reflections are modeled according to the Lambert cosine law and diffraction is performed according to the uncertainty-based diffraction theory (Stephenson, 2010), which allows for arbitrary diffraction orders. The ener-

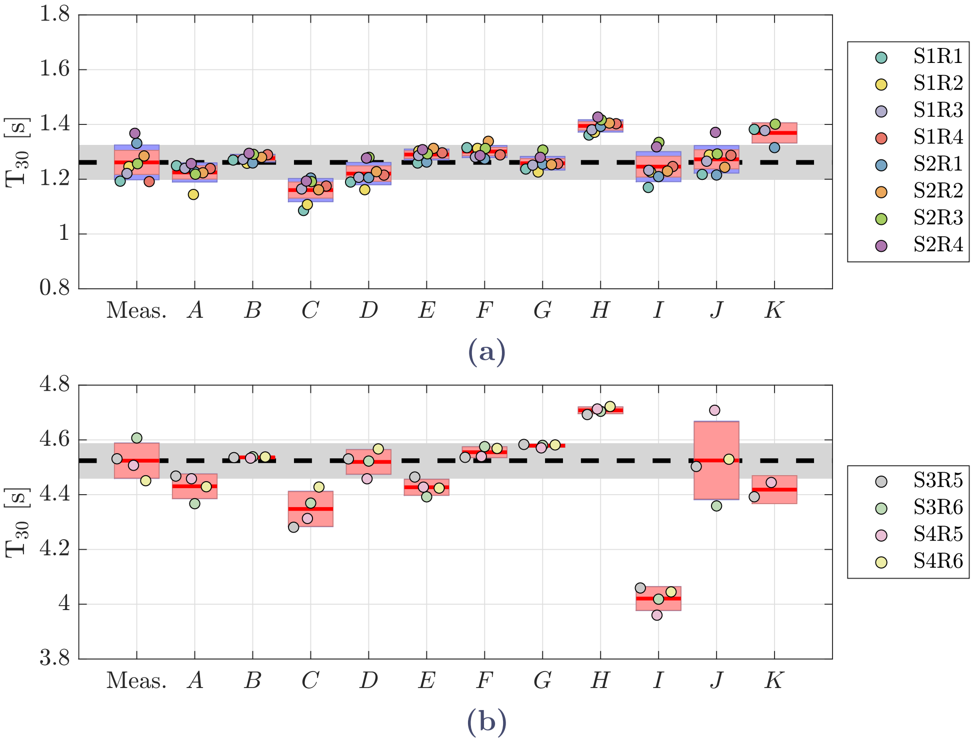

Figure 4.3 Reverberation times T_{30} from measured and simulated RIRs for the main room **(a)** and the reverberation chamber **(b)** in uncoupled configuration. Individual source-receiver pair data points are represented with an attributed color. Mean is indicated with a red line, and ±1 standard error of the mean and ±1 standard deviation with a red and blue rectangle, respectively.

getic impulse responses were computed with a resolution of 1 ms[1].

The main room has a large surface area of diffusing materials with a characteristic roughness depth of 6 cm at full scale, while the second room has smooth walls. For the 1 kHz octave-band, scattering coefficients of 20 % and 10 % were suggested for the two rooms respectively. However, due to differences in implementations of such parameters, this was not a controlled parameter. For example, in the wave-based methods, one participant modeled wall roughness directly with a diffuser design.

Participants were asked to submit simulated room impulse responses in audio WAV format in order to apply the same routine for acoustical parameter calculations and thus avoid introducing another source of divergence from different implementations (Cabrera et al., 2016; Katz, 2004). In the following results section, entries have been randomly assigned identification letters from *A* to *K*, to ensure anonymity. The only grouping that we can provide is that *A* to *H* are geometrical methods, while *I* to *K* are wave-based methods.

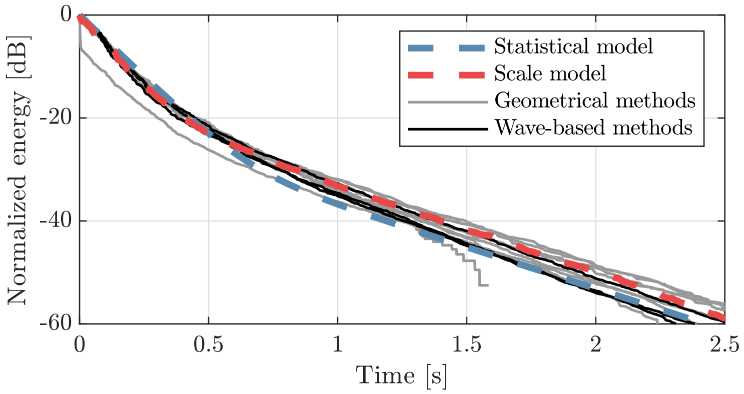

Figure 4.4 Statistical, measured, and simulated energy decay curves of the coupled configuration for the 1 kHz-octave band for **S1R3** position. Entries are not specified, but geometrical and wave-based methods are represented with common colors.

4.4 Results

4.4.1 Calibration of reverberation times

Figure 4.3 shows the reverberation times T_{30} for each source-receiver pair calculated from measured and simulated RIRs. Each source-receiver position is represented with an attributed color. For both rooms, the highest relative difference is 11 %. Overall, the calibration procedure was respected. The variances of the results from the simulations was lower than the measurements except for entry J in the reverberation chamber shown in fig. 4.3b. This can be explained by the fact that the physical has inhomogeneous boundary conditions, contrary to the simulations. The participants had the choice to only use half of the source-receiver positions due to computation time, this was only done by entry K. These variances in the calibration stage exceeded expected differences resulting from T_{30} calculations from RIRs, which were on the order of 3 % to 5 % (Katz, 2004), and would be expected to be even less for noise-free RIRs. This also exceed the JND for the reverberation time which is usually considered to be 5 %. Entry I reported difficulties with the calibration of the reverberation time of the chamber due to the sensitivity of the results to the resolution of the absorption coefficients in their implementation.

Comparing the simulations between themselves, the spatial variations of T_{30} do not correspond, although they consider a homogeneous absorption at the walls. Nevertheless, we can mention the pair S2R4 in fig. 4.3a for which the reverberation time is relatively high for each submission, except for H, but also in the measurement. This highlights the important role of diffuse reflections on the spatial variation of the sound decays even in simple rooms. Some methods lead to a low spatial variation compared to others, such as B, E, F, G, and H, and this seems to be maintained from one room to another.

4.4.2 Coupled volumes acoustical parameters

The energy decay curves from the measured and simulated room impulse responses for one source-receiver pair in the octave band of interest is presented in fig. 4.4. The double-slope decay behavior expected for a coupled volume system is clearly visible for all entries and, based on visual impression, they seem to be in good agreement with the

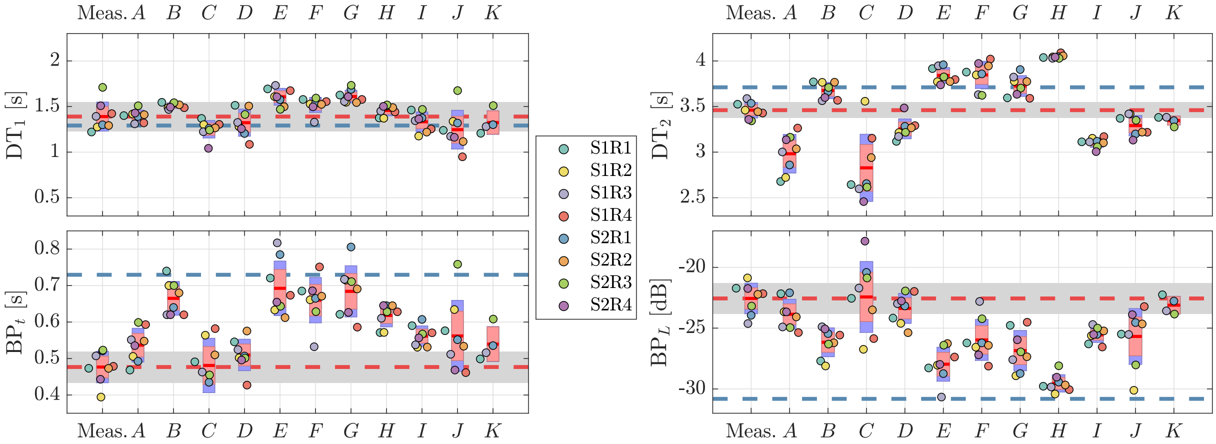

Figure 4.5 Comparison of resulting acoustical parameters from ML from measured and simulated RIRs. Individual source-receiver pair data points are represented with an attributed color. Bars represent ±1 standard error of the mean (red) and ±1 standard deviation (blue). Dashed lines represent the statistical model (blue) and the average measured (red) results. Grey bars are ±1 standard deviation of the measurements.

statistical model's EDC in particular for the late decay time, but also in better agreement with the measurement as expected because the statistical model can not reproduce the spatial variation of double slope decays (Luizard et al., 2014b).

Figure 4.5 shows the coupled volume acoustic parameters obtained with the Marching Line method (Luizard et al., 2011), as described in section 2.2.4, for the scale model measurements and the simulations. and those using the statistical energy balance model. The statistical model results are also indicated with blue dash lines. Comparing the latter with the measurements, the decay rates DT$_1$ and DT$_2$ are in well agreement with relative differences of 8 % and 7 %, respectively. The most notable difference between the statistical model and the physical model concerns the bending point. The statistical model predicts a transition occurring later and lower in level than was measured with $\Delta\mathrm{BP_t}$=0.2 s and $\Delta\mathrm{BP_L}$=7 dB, taking into account the margin of the standard deviation. Of primary interest are the decay rates of the different simulations, which approach those of both the statistical model and the measurements, considering the previous remarks. For the main volume, DT$_1$ of entries C, D, I, J, and K show good agreement with the statistical model on average, while the remaining entries are in better agreement with the measurements. The scale results are slightly higher than the statistical model, but not to the same degree than E or G. In almost perfect contrast, those performing well for DT$_1$, with regard to the statistical model, as well as A, underestimated DT$_2$, except J and K that are in agreement with the measurements. The remaining entries, except H, provided comparable values to the statistical model, and B falls in between it and the measurements.

Regarding the bending point, those methods that are in better agreement with the statistical DT$_2$ also matched the statistical model of BP$_t$, such as B, E, F, G, and H. The remaining entries result tend more towards the results of the scale model. These hold for BP$_L$, all methods and all source-receiver positions resulted in higher values than statistical model, with the same group A, C, D, I, J, K resembling more the results of the scale model.

The differences present for the uncoupled calibration phase are found in the coupled decay times as a general trend, but it is noted that entries with the highest calibration differences did not have the most extreme parameter predictions, *e.g.* entry I. In addition, entry H appears to have a significantly stronger direct sound component (see fig. 4.4) which accounts for it being a relative outlier for $\mathrm{BP_L}$.

Regarding trends across similar methods, while maintaining anonymity, it can be said that wave-based methods were relatively consistent with respect to double-slope parameter results. The commonalities of the remaining methods makes it difficult to separate them further in any attempt to explain the observed data groupings. In addition, further explaining the observed differences from the implementation of the boundary conditions could lead to a breach of anonymity.

Variances for parameter $\mathrm{DT_1}$ are smaller than observed for the measured data, except for entry J. For other parameters, numerical simulations exhibit larger variances, except entries H and I; entries B and D have similar variances compared to measurements. All entries simulated the 8 source-receiver pairs, except K that only used source S1. Considering the same positions, this entry has a higher variance only for $\mathrm{DT_2}$. Similarly to the observations made for the calibration of reverberation times, the spatial variation of the parameters strongly differ between methods. For example, the positions with maximum and minimum values, sometimes being outliers, are often different from one method to another.

4.5 Discussions and conclusion

One limitation in the present study is that the model had inhomogeneous absorption, while this was not the case for the simulations. This limits the validity of the comparisons that we can make between the results of measurements and those of simulations. Furthermore, a comparison with the present statistical model is also limited by the fact that it does not reproduce the spatial variation of decays that can exist for such a system. However, the measurements allowed to verify that the present system clearly exhibits double slope decays, and thus provide a common case with realistic physical parameters to model numerically, all methods then employing an assumption of homogeneous wall absorption in each of the two rooms. Moreover, a calibration procedure was used to compare the methods between them.

With respect to this point, although it was globally respected, there remain important differences with respect to what could have been expected. It would have been convenient to provide a calculation code allowing to estimate the reverberation time with a common tool, and thus to get rid of this source of variations. The participant of method I reported that the impedance parameter did not have enough resolution to reach the prescribed value in the case of the reverberation chamber. This has since been resolved, however, and it is likely possible that the results would have been slightly different.

Perceptual thresholds regarding double-slope decay parameters have been examined by Luizard et al. (2015). For a system of coupled volumes with a configuration comparable to the one used in the present work, just noticeable differences were around 10 % for $\mathrm{DT_1}$ and 20 % for $\mathrm{DT_2}$, $\mathrm{BP_t}$, and $\mathrm{BP_L}$. Overall, differences observed among simulations exceeded these thresholds on average for at least one parameter compared with the statistical or the physical model.

This study presented a simplified test case to compare the ability of various numerical methods for room acoustic simulations to reproduce or predict classical coupled volume behavior. Contrary to the previous study of Luizard et al. (2013), these results show that the tested methods are capable of representing coupled volume behavior, although not all results are consistent with statistical theory or comparable to measurements. Comparisons of methods shows the range of values (variance) across the 8 source-receiver pairs varies significantly, potentially highlighting issues regarding local variations being poorly represented for some methods. Future study could provide a more detailed geometrical model with specific material properties determined though laboratory measurements similarly to the previous round robin studies (Aspöck et al., 2019; Bork, 2000, 2005a,b; Brinkmann et al., 2019; Vorländer, 1995). Such input data should allow for direct comparisons of simulated results to the physical scale model, which is not appropriate in the current study due to the simplifications in the model and homogeneous application of material properties.

Part II

Sound scattering by architectural piers and columns

Chapter 5

A hybrid finite difference and finite volume time domain method

The sound scattering by complex geometries can be studied with the help of computational methods. They can be separated into two families: the frequency domain and time domain methods. The former solves the Helmholtz equation and allows to obtain the steady-state harmonic response. The latter solves the wave equation and offers the advantage to give a broadband result with a single simulation using a pulse excitation source. This is particularly interesting in our case, as our goal is to characterize the scattering properties of obstacles over a large part of the audible spectrum. In this sense, they can be seen as the computational equivalent of physical measurements.

In this chapter, we present the hybrid time domain method developed to study sound scattering by cylindrical obstacles of complex geometries. They are considered to be immovable and their boundaries are locally reactive. The method is based on the generation of a hybrid mesh with a regular structured part where the finite difference (FD) time domain method applies and an unstructured mesh conforming to the boundaries of the objects treated with a finite volume (FV) time domain method. The method is limited to two dimensions of space. Since the characterization of acoustic scattering properties is ideally done with an incident plane wave, it is possible to restrict ourselves to the plane perpendicular to the cylinder axis. Moreover, as a scattering event happens on a short time, absorption of the medium, air in our case, can be neglected.

First, we recall in section 5.1 basics of the FD methods applied to solve the wave equation and we introduce the formalism used. Then, the FV method is presented in section 5.2, based on recent works that formalize it for applications in room acoustics. Then, we present in section 5.3 how the two methods are used together through the generation of hybrid meshes adapted to the characterization of finite obstacles that interest us. The proposed method is compared with analytic solutions for the rigid circular cylinder case and other numerical codes such as BEM or developed to solve multiple scattering problems in section 5.4. Finally, discussions and conclusions are given in section 5.5.

5.1 Finite Difference Method

FD methods form probably the oldest family of numerical methods for solving ordinary differential equations and partial differential equations (Boole, 2009). The key idea of these methods is to replace the derivatives appearing in a differential equation governing a physical system by finite differences that approximate them. The derivative of a continuous and differentiable function f at x can be defined by

$$\left.\frac{\mathrm{d}f}{\mathrm{d}x}\right|_x = \lim_{\Delta x \to 0} \frac{f(x+\Delta x) - f(x)}{\Delta x}. \tag{5.1}$$

Using this definition, one could approximate the derivative by the so called Newton's difference quotient :

$$\left.\frac{\mathrm{d}f}{\mathrm{d}x}\right|_x = \frac{f(x+\Delta x)-f(x)}{\Delta x} + \varepsilon, \tag{5.2}$$

where ε is an error term whose asymptotic behavior with respect to Δx will be specified in the following. Equation (5.2) is known as *forward difference.*

The common and general way to find the expressions of the derivative approximations is to write the Taylor series expansions of f (considered infinitely differentiable for convenience) about $x+\Delta x$ and $x-\Delta x$, two points neighboring of x, and thus

$$f(x+\Delta x) = f(x) + \Delta x \left.\frac{\mathrm{d}f}{\mathrm{d}x}\right|_x + \frac{\Delta x^2}{2!}\left.\frac{\mathrm{d}^2f}{\mathrm{d}x^2}\right|_x + \frac{\Delta x^3}{3!}\left.\frac{\mathrm{d}^3f}{\mathrm{d}x^3}\right|_x + \cdots, \tag{5.3a}$$

$$f(x-\Delta x) = f(x) - \Delta x \left.\frac{\mathrm{d}f}{\mathrm{d}x}\right|_x + \frac{\Delta x^2}{2!}\left.\frac{\mathrm{d}^2f}{\mathrm{d}x^2}\right|_x - \frac{\Delta x^3}{3!}\left.\frac{\mathrm{d}^3f}{\mathrm{d}x^3}\right|_x + \cdots. \tag{5.3b}$$

The *forward difference* is retrieved from eq. (5.3a) while the *backward difference* is obtained from eq. (5.3b), giving respectively

$$\left.\frac{\mathrm{d}f}{\mathrm{d}x}\right|_x = \frac{f(x+\Delta x)-f(x)}{\Delta x} + \mathcal{O}(\Delta x), \tag{5.4a}$$

$$\left.\frac{\mathrm{d}f}{\mathrm{d}x}\right|_x = \frac{f(x)-f(x-\Delta x)}{\Delta x} + \mathcal{O}(\Delta x), \tag{5.4b}$$

with $\mathcal{O}(\Delta x)$ being the notation for the error term resulting from the truncation in the series, meaning that the error is proportional to Δx for those two approximations. They are said to be *first order accurate* or *consistent at the first order.*

Otherwise, subtracting eq. (5.3b) from eq. (5.3a) and dividing by Δx yields

$$\left.\frac{\mathrm{d}f}{\mathrm{d}x}\right|_x = \frac{f(x+\Delta x)-f(x-\Delta x)}{2\Delta x} + \mathcal{O}(\Delta x^2), \tag{5.5}$$

which is called the *central difference.* In this case the approximation is *second order accurate.*

Obtaining an approximation of the second derivative of f is also feasible by adding eqs. (5.3a) and (5.3b) and rearranging the terms, which results in

$$\left.\frac{\mathrm{d}^2f}{\mathrm{d}x^2}\right|_x = \frac{f(x+\Delta x)-2f(x)+f(x-\Delta x)}{\Delta x^2} + \mathcal{O}(\Delta x^2), \tag{5.6}$$

which is also *second order accurate.* Another way to arrive at this approximation is to apply a *forward difference* and then a *backward difference* (or the other way around).

We have presented the finite differences approximations for a one-variable function but our problems are described by partial differential equations whose solutions are multivariate functions dependent of space and time. Furthermore, substituting the derivative terms of a differential equation by these finite differences leads to discretize the solution on a finite number of points. Considering a multidimensional continuous function f dependent of time t and space $\mathbf{x} = (x, y) \in \mathbb{R}^2$ with x and y being the coordinates in a Cartesian system with two dimensions. The objective is to approach the exact solution in a finite number of points $x_j = j\Delta x$ and $y_l = l\Delta y$ with $(j, l) \in \mathbb{Z}^2$ in space and a finite number of time steps $t_n = n\Delta t$ with $n \in \mathbb{N}$. The value at these points is noted

$$f^n_{j,l} = f(x_j, y_l, t_n) = f(j\Delta x, l\Delta y, n\Delta t)\,, \tag{5.7}$$

where Δx and Δy are the spatial sampling periods in respective direction x and y, while Δt is the time sampling step. Thus the method leads us to build an algorithm that compute an approximate value $\tilde{f}^n_{j,l}$ of $f^n_{j,l}$. However, in the following, we will not specify this distinction and the recurrence equations describing a FD time domain scheme for updating quantities of interest are written with index notation.

In order to derive a FD scheme, it may be convenient to define these approximations as *finite difference operators* as suggested by Bilbao (2009). For a multivariate function, the forward, backward and central time difference operators can be written respectively as

$$\delta_{t+} f^n_{j,l} \triangleq \frac{f^{n+1}_{j,l} - f^n_{j,l}}{\Delta t} = \left.\frac{\partial f}{\partial t}\right|_{x_j, y_l, t_n} + \mathcal{O}(\Delta t)\,, \tag{5.8a}$$

$$\delta_{t-} f^n_{j,l} \triangleq \frac{f^n_{j,l} - f^{n-1}_{j,l}}{\Delta t} = \left.\frac{\partial f}{\partial t}\right|_{x_j, y_l, t_n} + \mathcal{O}(\Delta t)\,, \tag{5.8b}$$

$$\delta_{t\cdot} f^n_{j,l} \triangleq \frac{f^{n+1}_{j,l} - f^{n-1}_{j,l}}{2\Delta t} = \left.\frac{\partial f}{\partial t}\right|_{x_j, y_l, t_n} + \mathcal{O}(\Delta t^2)\,. \tag{5.8c}$$

As mentioned above, the second order operator can be constructed by composition of the non-centered first order operators as

$$\delta_{tt} f^n_{j,l} \triangleq \frac{f^{n+1}_{j,l} - 2f^n_{j,l} + 2f^{n-1}_{j,l}}{\Delta t^2} = \delta_{t+}\delta_{t-} f^n_{j,l} = \left.\frac{\partial^2 f}{\partial t^2}\right|_{x_j, y_l, t_n} + \mathcal{O}(\Delta t^2)\,. \tag{5.9}$$

Similarly, the first order spatial difference operators for forward, backward and central differences with regards to the x-axis can be written respectively as

$$\delta_{x+} f^n_{j,l} \triangleq \frac{f^n_{j+1,l} - f^n_{j,l}}{\Delta x} = \left.\frac{\partial f}{\partial x}\right|_{x_j, y_l, t_n} + \mathcal{O}(\Delta x)\,, \tag{5.10a}$$

$$\delta_{x-} f^n_{j,l} \triangleq \frac{f^n_{j,l} - f^n_{j,l-1}}{\Delta x} = \left.\frac{\partial f}{\partial x}\right|_{x_j, y_l, t_n} + \mathcal{O}(\Delta x)\,, \tag{5.10b}$$

$$\delta_{x\cdot} f^n_{j,l} \triangleq \frac{f^n_{j+1,l} - f^n_{j-1,l}}{2\Delta x} = \left.\frac{\partial f}{\partial t}\right|_{x_j, y_l, t_n} + \mathcal{O}(\Delta x^2) \tag{5.10c}$$

and also

$$\delta_{xx} f^n_{j,l} \triangleq \frac{f^n_{j+1,l} - 2f^n_{j,l} + 2f^n_{j-1,l}}{\Delta x^2} = \delta_{x+}\delta_{x-} f^n_{j,l} = \left.\frac{\partial^2 f}{\partial x^2}\right|_{x_j, y_l, t_n} + \mathcal{O}(\Delta x^2)\,. \tag{5.11}$$

5.1.1 Yee's algorithm for linear acoustics

Yee (1966) is commonly cited as the first to implement a scheme for solving initial boundary value problems involving Maxwell's equations. This time stepping numerical scheme is usually referred as Yee's algorithm (Taflove et al., 2005) or Yee's scheme. It

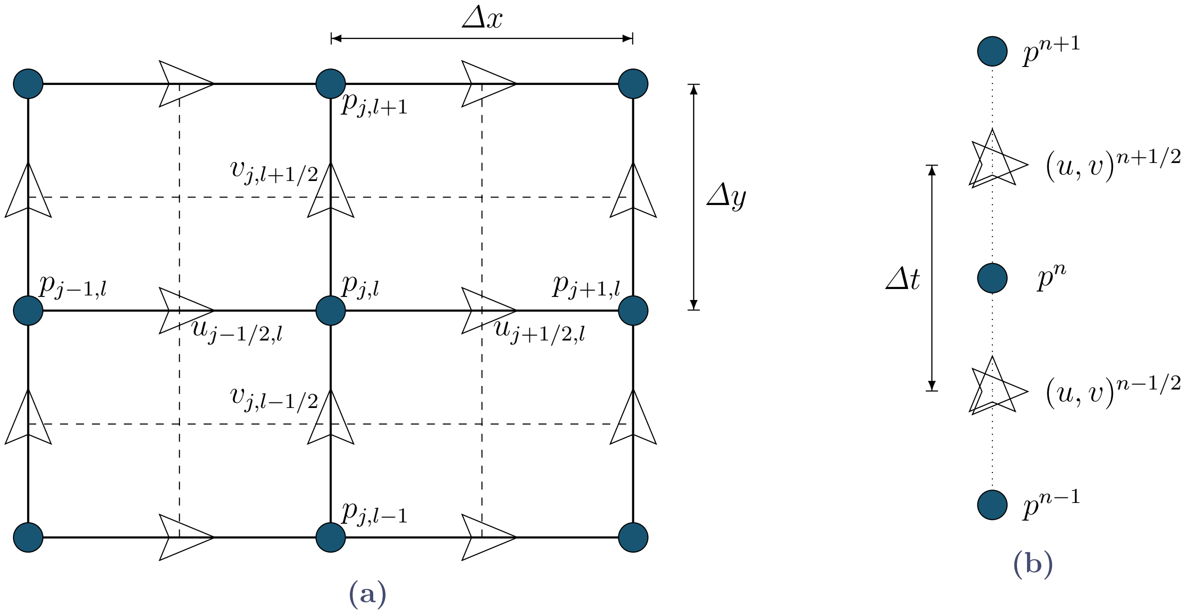

Figure 5.1 Yee lattice adapted to linear acoustics. Staggered in **(a)** space and **(b)** time.

has been since adapted to linear acoustics by several authors (Botteldooren, 1995; Schady et al., 2014; Wang, 1996). They solve the system of partial differential equations derived from the conservation of momentum and mass giving respectively

$$\rho \frac{\partial \mathbf{v}}{\partial t} = -\boldsymbol{\nabla} p \,, \tag{5.12a}$$

$$\frac{1}{\rho c^2} \frac{\partial p}{\partial t} = -\boldsymbol{\nabla} \cdot \mathbf{v} \,, \tag{5.12b}$$

with $\mathbf{v}$ and p the acoustic velocity and pressure fields, respectively, ρ the density of the propagation medium, and c the speed of sound. $\boldsymbol{\nabla}$ and $\boldsymbol{\nabla}\cdot$ are respectively the gradient and divergence operators. The analogy with electric and magnetic fields is clear. In a two dimensional space, this system can be written

$$\rho \frac{\partial u}{\partial t} = -\frac{\partial p}{\partial x} \,, \tag{5.13a}$$

$$\rho \frac{\partial v}{\partial t} = -\frac{\partial p}{\partial y} \,, \tag{5.13b}$$

$$\frac{1}{\rho c^2} \frac{\partial p}{\partial t} = -\left(\frac{\partial u}{\partial x} + \frac{\partial v}{\partial y} \right) \,, \tag{5.13c}$$

with x and y the Cartesian coordinates, u and v the velocity components. The space is dicretized using a Yee lattice as shown in fig. 5.1 where p, u and v are evaluated on staggered grids in space (fig. 5.1a) and time (fig. 5.1b). Using the difference operators introduced earlier, the system can be approximated by

$$\rho \delta_{t-} u^{n+1/2}_{j+1/2,l} = -\delta_{x+} p^n_{j,l} \,, \tag{5.14a}$$

$$\rho \delta_{t-} v^{n+1/2}_{j,l+1/2} = -\delta_{y+} p^n_{j,l} \,, \tag{5.14b}$$

$$\frac{1}{\rho c^2} \delta_{t+} p^n_{j,l} = -\left(\delta_{x-} u^{n+1/2}_{j+1/2,l} + \delta_{y-} v^{n+1/2}_{j,l+1/2} \right) \,. \tag{5.14c}$$

That leads to the following updates equations

$$u^{n+1/2}_{j+1/2,l} = u^{n-1/2}_{j+1/2,l} - \frac{\Delta t}{\rho} \frac{p^n_{j+1,l} - p^n_{j,l}}{\Delta x}\,, \tag{5.15a}$$

$$v^{n+1/2}_{j,l+1/2} = v^{n-1/2}_{j,l+1/2} - \frac{\Delta t}{\rho} \frac{p^n_{j,l+1} - p^n_{j,l}}{\Delta y}\,, \tag{5.15b}$$

$$p^{n+1}_{j,l} = p^n_{j,l} - \rho c^2 \Delta t \left(\frac{u^{n+1/2}_{j+1/2,l} - u^{n+1/2}_{j-1/2,l}}{\Delta x} + \frac{v^{n+1/2}_{j,l+1/2} - v^{n+1/2}_{j,l-1/2}}{\Delta y} \right)\,. \tag{5.15c}$$

The staggering in time is represented by the fractional part in the time index, but in practice the operations are performed at the same time when the recursion is implemented.

5.1.1.1 Numerical dispersion

The inherent approximations of the method introduce what is called numerical dispersion in the sense that, in the discretized problem, the phase velocity of the wave will depend on its frequency. The common way to analyze this dispersion is to consider monochromatic traveling plane waves. In the discrete space-time domain, such waves can be expressed

$$p^n_{j,l} = p_0 e^{i(\hat{k}_x j \Delta x + \hat{k}_y l \Delta y - \omega n \Delta t)}, \tag{5.16a}$$

$$u^n_{j,l} = u_0 e^{i(\hat{k}_x j \Delta x + \hat{k}_y l \Delta y - \omega n \Delta t)}, \tag{5.16b}$$

$$v^n_{j,l} = v_0 e^{i(\hat{k}_x j \Delta x + \hat{k}_y l \Delta y - \omega n \Delta t)}\,, \tag{5.16c}$$

where p_0, u_0, and v_0 are real-valued amplitudes. $\hat{k}_x = \hat{k}\cos(\theta)$ and $\hat{k}_y = \hat{k}\sin(\theta)$ are the components of the effective numerical wave vector $\hat{k}$ and θ is the angle between the direction of propagation and the x-axis.

After substituting the plane waves expressions eq. (5.16) into the system of discrete equations eq. (5.15) and applying the correct substitutions in the resulting system of equations, we obtain the numerical dispersion relation for this scheme :

$$\left[\frac{1}{c\Delta t} \sin\left(\frac{\omega \Delta t}{2}\right)\right]^2 = \left[\frac{1}{\Delta x} \sin\left(\frac{\hat{k}_x \Delta x}{2}\right)\right]^2 + \left[\frac{1}{\Delta y} \sin\left(\frac{\hat{k}_y \Delta y}{2}\right)\right]^2. \tag{5.17}$$

On a regular grid, with a square lattice ($\Delta x = \Delta y$), the dispersion relation may be written

$$\sin^2\left(\frac{\omega \Delta t}{2}\right) = C_r^2 \left[\sin^2\left(\frac{\hat{k}\cos(\theta)\Delta x}{2}\right) + \sin^2\left(\frac{\hat{k}\sin(\theta)\Delta x}{2}\right)\right]^2, \tag{5.18}$$

with $C_r = c\Delta t/\Delta x$ known as the *Courant number*. This number is dimensionless and, in section 5.1.1.2, we will apply a similar method to deduce a condition on it that ensure the stability of the scheme.

In addition to being frequency dependent, eq. (5.18) shows that the numerical phase velocity varies with the propagation angle. To inspect this effect, it is possible to write $\hat{k}$ as function of ω and θ, and thus calculate the ratio between the numerical phase speed $\hat{c} = \omega/\hat{k}$ and the real wave speed c. One may refer to van Walstijn et al. (2008) for details of the calculation. To illustrate this, we evaluate this ratio for Yee's scheme on a square grid with $C_r = \sqrt{2}/2$. Figure 5.2 shows the real part, noted with Re($\cdot$), and imaginary

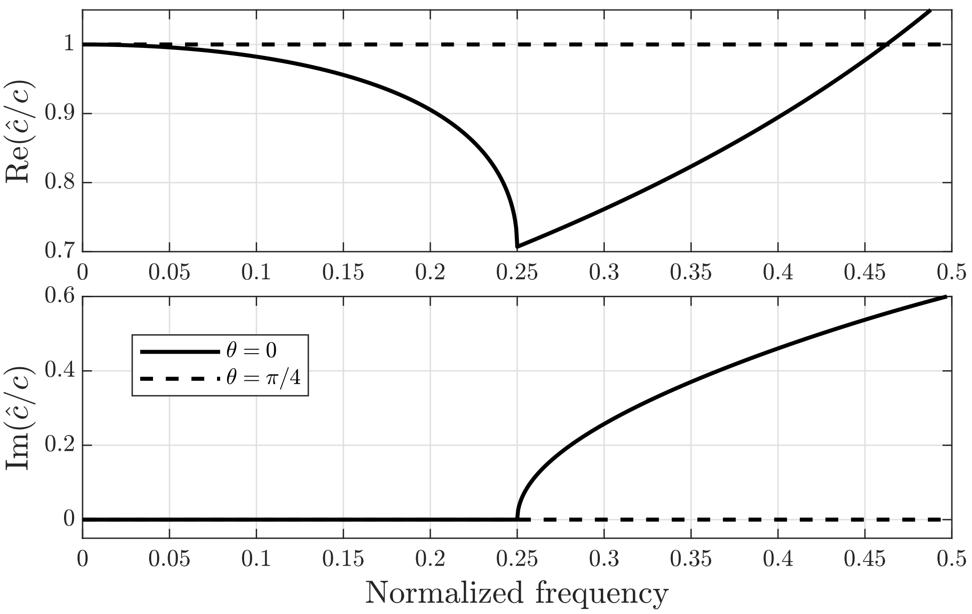

Figure 5.2 Real and imaginary parts of relative phase velocities in diagonal ($\theta = \pi/4$) and axial ($\theta = 0$) directions for Yee's scheme.

part, noted with Im($\cdot$), for the relative phase velocities in function of the normalized frequency. They have been calculated for two propagation angles : $\theta = 0$ being the axial direction and $\theta = \pi/4$ being the diagonal one.

For the diagonal direction, represented in dashed lines, the numerical wave speed is purely real and and the effective numerical phase velocity equals the expected wave speed. This is not the case for the axial direction. We observe that the curve has a discontinuity at one point. Below this point, the effective phase velocity is real but the ratio decreases with frequency. Beyond, it becomes complex and both real and imaginary parts increase. The frequency where this occurs is defined as the numerical cutoff frequency (Kowalczyk et al., 2010) from which the wave becomes evanescent. Although the real part increases until it exceeds the real speed, at the same time, its imaginary part also increases, implying an increasing attenuation (Schneider et al., 2001).

As a result, the FD method introduces a numerical anisotropy of the propagation medium. In practice, the rule of thumb for Yee's scheme often encountered is that the shortest wavelength of interest should approximately be equal to one-tenth the spatial step (Botteldooren, 1995). It actually comes from the limitation of the relative phase velocity admissible error to 2 %. Thus, despite a normalized cutoff frequency equal to $0.25/\Delta t$ as shown in fig. 5.2, the scheme is in fact considered accurate up to $0.1/\Delta t$. Since the phase velocity is exact in the diagonal directions for this scheme with $C_r = \sqrt{2}/2$, this rule is the same for considering the scheme as isotropic according to the definition of Kowalczyk et al. (2010), limiting the relative difference between the phase velocities for the "best" and "worst" directions of propagation to 2 %.

5.1.1.2 Stability condition

The stability condition can be derived in a similar way, assuming a propagating discrete plane wave, but with the difference that the pulsation ω can be complex-valued : $\omega = \omega_{real} + i\omega_{imag}$. Similarly to eq. (5.16), the discrete waves are thus written

$$p^n_{j,l} = p_0 \xi e^{i(\hat{k}_x j \Delta x + \hat{k}_y l \Delta y)}, \tag{5.19a}$$

$$u^n_{j,l} = u_0 \xi e^{i(\hat{k}_x j \Delta x + \hat{k}_y l \Delta y)}, \tag{5.19b}$$

$$v^n_{j,l} = v_0 \xi e^{i(\hat{k}_x j \Delta x + \hat{k}_y l \Delta y)}, \tag{5.19c}$$

where $\xi = e^{-i\omega n \Delta t}$. With this notation, we can write the relation

$$p^{n+1}_{j,l} = \xi p^n_{j,l}, \tag{5.20}$$

that shows that advancing by one time step in the numerical scheme is equivalent to multiplying the solution by ξ. For this reason, it is called the amplification factor (Strikwerda, 2004). The scheme will be unstable for $|\xi| > 1$, and so we are looking for a condition that leads to $|\xi| \leq 1$, ensuring its stability. Such a procedure is classically known as a von Neumann stability analysis.

Again, substituting eq. (5.19) into eq. (5.15) and after some manipulations leads to

$$\xi^2 + 2B\xi + 1 = 0, \tag{5.21}$$

where

$$B = 2\left[\left(\frac{c\Delta t}{\Delta x}\right)^2 \sin^2\left(\frac{\hat{k}_x \Delta x}{2}\right) + \left(\frac{c\Delta t}{\Delta y}\right)^2 \sin^2\left(\frac{\hat{k}_y \Delta y}{2}\right)\right] - 1. \tag{5.22}$$

The solutions of the polynomial eq. (5.21) are

$$\xi = B \pm \sqrt{B^2 - 1}, \tag{5.23}$$

whose moduli are bounded by 1 if and only if $B^2 \leq 1$. This leads to the stability condition

$$c\Delta t \leq \frac{1}{\sqrt{(\frac{1}{\Delta x})^2 + (\frac{1}{\Delta y})^2}}, \tag{5.24}$$

known as the Courant-Friedrichs-Lewy condition (Courant et al., 1928), linking the spatial and temporal steps in order to ensure the stability of the numerical scheme. Considering a regular grid with $h = \Delta x = \Delta y$, the stability condition for Yee's scheme is reduced to

$$C_r \leq \frac{1}{\sqrt{2}}, \tag{5.25}$$

with $C_r = c\Delta t/h$, the Courant number. This is consistent with the principle of causality, *i.e.* the wave can not go faster than c, since the criterion indicates that the time step must be less than the time required for the wave to travel a distance $h/\sqrt{2}$ in the diagonal on a square lattice. In the previous example, we have shown the numerical dispersion when the parameters are optimal, *i.e.* C_r is equal to the stability limit. If C_r is lower then it also affects the dispersion of the scheme.

5.1.2 Schemes for the scalar wave equation

5.1.2.1 Cartesian grid

Yee's algorithm provides a method to calculate the pressure and particle velocity at uncollocated grid points. If one is interested in calculating only the pressure then it seems appropriate to construct a numerical scheme to solve the scalar wave equation. Such a scheme can also be adapted to compute the acoustic velocity potential. With the knowledge of this potential, it becomes more convenient to calculate, in a second step, the pressure and the particle velocity at collocated points.

The homogeneous linear scalar wave equation in a two dimensional space for the velocity potential $\varPhi(\mathbf{x}, t)$ is

$$\nabla^2 \varPhi - \frac{1}{c^2}\frac{\partial^2 \varPhi}{\partial t^2} = 0\,, \tag{5.26}$$

with $\nabla^2 = \frac{\partial^2}{\partial x^2} + \frac{\partial^2}{\partial y^2}$ the 2D Laplacian operator in a Cartesian coordinate system. Replacing the derivatives by their corresponding difference operator leads to the approximation

$$\left(\frac{\partial^2}{\partial t^2} - c^2\nabla^2\right)\varPhi^n_{j,l} = \left[\delta_{tt} - c^2\left(\delta_{xx} + \delta_{yy}\right)\right]\varPhi^n_{j,l} + \mathcal{O}(h^2) + \mathcal{O}(\varDelta t^2)\,. \tag{5.27}$$

The update recursion is eventually

$$\varPhi^{n+1}_{j,l} = 2\left(1 - 2C_r^2\right)\varPhi^n_{j,l} + C_r^2\left(\varPhi^n_{j+1,l} + \varPhi^n_{j-1,l} + \varPhi^n_{j,l+1} + \varPhi^n_{j,l-1}\right) - \varPhi^{n-1}_{j,l}\,. \tag{5.28}$$

This second order accurate scheme is usually referred as Standard Leap-Frog or Standard Rectilinear. It is equivalent to Yee's scheme in terms of stability condition and numerical dispersion but more computationally efficient as, overall, less variables need to be stored.

It has been seen that dispersion limits the useful frequency bandwidth. A family of explicit schemes, referred as compact-explicit (Kowalczyk et al., 2010) or interpolated (Bilbao, 2004b), has been proposed that approximates the Laplacian by extending the spatial stencil and allowing the use of the first diagonal points. By introducing a parameter $b \in \mathbb{R}^+$, the Laplacian may be approximated with

$$\nabla^2 \approx \delta_{xx} + \delta_{yy} + b\delta_{xx}\delta_{yy}\,, \tag{5.29}$$

leading to the following update recursion :

$$\begin{aligned}\varPhi^{n+1}_{j,l} = {} & C_r^2\left(1 - 2b\right)\left(\varPhi^n_{j+1,l} + \varPhi^n_{j-1,l} + \varPhi^n_{j,l+1} + \varPhi^n_{j,l-1}\right) \\ & + C_r^2 b\left(\varPhi^n_{j+1,l+1} + \varPhi^n_{j+1,l-1} + \varPhi^n_{j-1,l+1} + \varPhi^n_{j-1,l-1}\right) \\ & + 2\left(1 - 2C_r^2 + 2C_r^2 b\right)\varPhi^n_{j,l} - \varPhi^{n-1}_{j,l}\,.\end{aligned} \tag{5.30}$$

They are stable for

$$C_r \leq \sqrt{\frac{1}{2 - 4b}}\,, \tag{5.31}$$

and their accuracy, dispersion and efficiency in the context of room acoustics simulation has been studied deeply by Kowalczyk et al. (2010). For $b = 1/4$, the resulting scheme is called Interpolated Wideband and constitutes a good compromise between isotropy and cutoff frequency. It is accurate and isotropic up to $0.23/\varDelta t$ according to the 2 % error criterion. Other schemes can be more isotropic but less accurate such as the Interpolated Isotropic for $b = 1/6$, accurate and isotropic up to $0.18/\varDelta t$ and $0.27/\varDelta t$, respectively. This

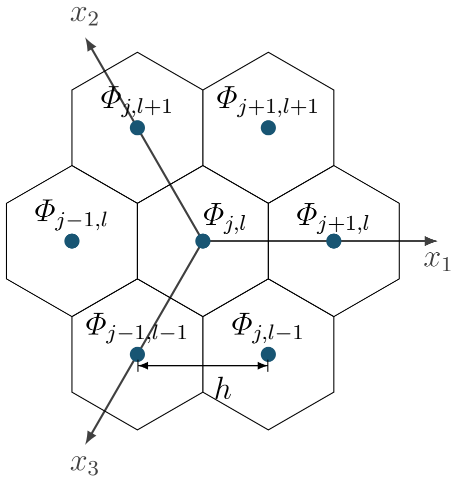

Figure 5.3 Hexagonal grid with indexing.

family provides a way to mitigate numerical dispersion using a 9-point spatial stencil and can be adapted with regards to the intended application. Other ways are to use implicit formulations such as the alternating-direction implicit method (Bilbao, 2004a), wider stencils (Dablain, 1986; Liu et al., 2009), or compact higher order schemes (Tuomela, 1994) but these come at the cost of increased complexity and memory requirements.

5.1.2.2 Hexagonal grid

As advised by Taflove et al. (2005), another strategy is to use the hexagonal spatial grid. Triangular or hexagonal tilings are, with the square one, the only other two regular tessellations of the plane and they are linked by reciprocity, one being the dual of the other as shown in fig. 5.3. By connecting the center of each hexagon with the centers of its neighbors, we obtain the triangular tilling. Thus the grid used for the scheme presented here is sometimes described as triangular (Zingg et al., 1993) but more often as hexagonal (Hamilton et al., 2013). On such a grid, it is more convenient to use the three linearly dependent axes x_1, x_2 and x_3 of respective unit vector

$$\mathbf{e_1} = \begin{bmatrix} 1 \\ 0 \end{bmatrix} = \mathbf{e_x} \,, \quad \mathbf{e_2} = \begin{bmatrix} -1/2 \\ \sqrt{3}/2 \end{bmatrix} \,, \quad \mathbf{e_3} = \begin{bmatrix} -1/2 \\ -\sqrt{3}/2 \end{bmatrix} = -\left(\mathbf{e_1} + \mathbf{e_2}\right) \,, \tag{5.32}$$

whose components are given with respect to the Cartesian coordinate system. The 2D Laplacian operator can then be expressed

$$\nabla^2 = \frac{2}{3}\left(\frac{\partial^2}{\partial x_1^2} + \frac{\partial^2}{\partial x_2^2} + \frac{\partial^2}{\partial x_3^2}\right) . \tag{5.33}$$

A second order accurate approximation $\triangle_{hex}$ of the Laplacian can be constructed by using a 7-point spatial stencil (Kantorovich et al., 1958), *i.e.* the center point and its six nearest neighbors, resulting in

$$\triangle_{hex} = \frac{2}{3}\left(\delta_{x_1x_1} + \delta_{x_2x_2} + \delta_{x_3x_3}\right) = \nabla^2 + \frac{h^2}{16}\left(\nabla^2\right)^2 + \mathcal{O}(h^4) \tag{5.34}$$

and showing that this difference operator is also isotropic to the fourth order as the second-order error term is independent of any direction of space. The update equation for $\varPhi^n_{j,l}$, $(j,l) \in \mathbb{Z}^2$, $n \in \mathbb{N}$, approximating $\varPhi\left(jh\mathbf{e_1}, lh\mathbf{e_2}, n\varDelta t\right)$ with $\varDelta t$ the time step, h the grid spacing, is eventually

$$\begin{aligned}\varPhi^{n+1}_{j,l} = {} & 2\left(1 - 2C_r^2\right)\varPhi^n_{j,l} - \varPhi^{n-1}_{j,l} \\ & + \frac{2}{3}C_r^2\left(\varPhi^n_{j+1,l} + \varPhi^n_{j-1,l} + \varPhi^n_{j,l+1} + \varPhi^n_{j,l-1} + \varPhi^n_{j+1,l+1} + \varPhi^n_{j-1,l-1}\right) .\end{aligned} \tag{5.35}$$

This scheme is stable for

$$C_r \leq \sqrt{\frac{2}{3}} \tag{5.36}$$

as derived by Fabero et al. (2001). Its dispersion properties has been studied by Liu (1996). The 2 % error is reached at about $0.25/\varDelta t$ in accuracy and isotropy at the stability limit. It has also been compared to the Interpolated Wideband scheme by Hamilton et al. (2013) and it has been found to be more than 3 times more efficient when less than 1 % relative wave speed error is required using a relative computational efficiency measure proposed by van Walstijn et al. (2008).

The grid points can be generated from a square grid whose coordinates are transformed with a generator matrix $\mathbf{G_{hex}}$ for the hexagonal lattice composed here of the unit vectors $\mathbf{e_1}$ and $\mathbf{e_2}$ as

$$\mathbf{G_{hex}} = \begin{bmatrix} 1 & -1/2 \\ 0 & \sqrt{3}/2 \end{bmatrix} \tag{5.37}$$

having the effect to skew the starting grid. Its has the advantage to give a natural indexing to the grid points has shown in fig. 5.3. In practice, $\triangle_{hex}$ can then be computed as a spatial convolution with the appropriate stencil.

The gradient for such a grid can be computed at each time step using the second-order accurate central differences

$$\boldsymbol{\nabla}_{hex,x}\varPhi^n_{j,l} = \frac{\varPhi^n_{j+1,l+1} - \varPhi^n_{j,l+1} + 2\varPhi^n_{j+1,l} - 2\varPhi^n_{j-1,l} + \varPhi^n_{j,l-1} - \varPhi^n_{j-1,l-1}}{6h} , \tag{5.38a}$$

$$\boldsymbol{\nabla}_{hex,y}\varPhi^n_{j,l} = \frac{\sqrt{3}\left(\varPhi^n_{j+1,l+1} + \varPhi^n_{j,l+1} - \varPhi^n_{j,l-1} - \varPhi^n_{j-1,l-1}\right)}{6h} , \tag{5.38b}$$

for a unstaggered, collocated hexagonal grid (Taflove et al., 2005).

5.1.3 Sources and grid excitation

We have derived the schemes for the homogeneous wave equations. When sources are present, the inhomogeneous wave equation is

$$\frac{1}{c^2}\frac{\partial^2 \varPhi}{\partial t^2} - \nabla^2 \varPhi = q_s(t)\delta(\mathbf{x} - \mathbf{x}_s) , \tag{5.39}$$

where $q_s(t)$ is the added mass rate of the volume source at a point $\mathbf{x}_s$. More generally, there are also external volume forces that can be a source of acoustic pressure, however they are not considered here.

This can be modeled as a *hard* source, *i.e.* the source signal is imposed on the source node

$$\varPhi^{n+1}_{j_s,l_s} = s^{n+1}_p , \tag{5.40}$$

where $(j_s, l_s) \in \mathbb{Z}^2$ are the indexes of the source node and s^{n+1}_p is a source signal discretized in time. This type of source have the disadvantage to scatter any wave that pass through the source node.

To prevent that, another type of grid excitation is the *soft* source. In this case the driving function is added at the source node after it has been updated. This can be written

$$\Phi^{n+1}_{j_s,l_s} = \left\{\Phi^{n+1}_{j_s,l_s}\right\} + s^{n+1}_p \,, \tag{5.41}$$

where $\{\cdot\}$ on the right-hand side denotes the result after that the node has been updated with one of the schemes for the homogeneous wave equation (eqs. (5.28), (5.30) and (5.35)).

When a soft source is used, the driving signal is modified by the grid's response after injection (Jeong et al., 2012). An approach to overcome that and prevent scattering at the source node too is the *transparent* source model (Schneider et al., 1998). The field at this node is updated with

$$\Phi^{n+1}_{j_s,l_s} = \left\{\Phi^{n+1}_{j_s,l_s}\right\} + s^{n+1}_p - \sum_{p=0}^{n} I^{n-p+1} s^p_p \,, \tag{5.42}$$

where I^n is the grid impulse response obtained by exciting it with a unit pulse. In order to characterize sound scattering, slight frequency shift between the injected signal and the signal actually propagating on the grid is not particularly limiting, so a soft source can be used.

Sheaffer et al. (2014) proposed a unified approach of these types of grid excitation in the context of room acoustics, employing cascade filters, each of them addressing a particular constraint required for these models, that are derived in part from the discretization of eq. (5.39). A unit pulse is first filtered to limit its bandwidth, then a filter based on the mechanics of a pulsating sphere is used as a DC blocker, finally the signal is introduced at the node source using an injection filter meeting the scaling and superposition constraints.

As pulse-shaping filters, they proposed several types to design Blackman-Harris, Gaussian, sine-modulated Gaussian, or Ricker pulses. This latter is particularly interesting as it has a rather large bandwidth and it is time compact at the same time, which is useful for the visualization of transient fields and scattering events.

Another approach to account for sources is to consider a Cauchy initial value problem. For a second-order in time partial differential equation, such as the homogeneous scalar wave equation, the initial conditions of the field and its first derivative are specified,

$$\Phi(\mathbf{x}, t = 0) = \mu(\mathbf{x}) \,, \quad \frac{\partial \Phi}{\partial t} = \nu(\mathbf{x}) \,. \tag{5.43}$$

For example, the scheme eq. (5.35) requires the two first states $\Phi^0_{j,l}$ and $\Phi^1_{j,l}$ to be specified. The first one can be determined by the initial condition μ, discretized on the grid as

$$\Phi^0_{j,l} = \mu_{j,l} \,, \tag{5.44}$$

and the second one can be estimated with an initialization scheme that is also second-order in time (Strikwerda, 2004), but only requires the first time step, such as

$$\Phi^1_{j,l} = \Phi^0_{j,l} + \Delta t \nu_{j,l} + \frac{c^2 \Delta t^2}{2} \triangle_{hex} \Phi^0_{j,l} \,. \tag{5.45}$$

This can be used for the other second-order schemes eqs. (5.28) and (5.30) by substituting the Laplacian difference operator with the appropriate one.

5.1.4 Boundary conditions

A boundary value problem requires a boundary condition to be well posed. In rooms acoustics, the locally reactive boundary condition assumption is often used because the propagation inside walls and obstacles can be neglected as soon as the impedance contrast between air and wall material is important. However, if these elements are too thin, the fluid-structure coupling can be strong and then the assumption in no longer valid, requiring to solve the coupled problem (Junger et al., 1986). In the context of problems of airborne sound scattering by immovable obstacles that interest us, the hypothesis seems reasonable given the dense rocky materials constituting them. It is therefore not necessary to discretize their interior but only the boundaries.

Examples of such boundary conditions often encountered are the Dirichlet condition where the value of the field is known on the boundary contours $\partial\mathcal{D}$. For a pressure field, if

$$p(\mathbf{x}) = 0\,, \qquad \mathbf{x} \in \partial\mathcal{D} \tag{5.46}$$

then the boundary condition is said *soft* or *pressure-release*. If the derivative of the field is known then it is a Neumann condition. This results in a condition on the normal velocity and if

$$\mathbf{v}(\mathbf{x}) \cdot \mathbf{n}(\mathbf{x}) = 0\,, \qquad \mathbf{x} \in \partial\mathcal{D}\,, \tag{5.47}$$

with $\mathbf{n}(\mathbf{x})$ the outward normal vector at $\mathbf{x}$ on $\partial\mathcal{D}$, then the boundary is *hard* or *rigid*. The admittance boundary condition

$$\mathbf{v}(\mathbf{x}) \cdot \mathbf{n}(\mathbf{x}) = Y(\mathbf{x})p(\mathbf{x})\,, \qquad \mathbf{x} \in \partial\mathcal{D}\,, \tag{5.48}$$

where

$$Y(\mathbf{x}) = Y_0\gamma(\mathbf{x}) \tag{5.49}$$

is the specific acoustic admittance, with $Y_0 = 1/\rho c$ the characteristic specific acoustic admittance of air and $\gamma(\mathbf{x}) \in \mathbb{R}^+$ the normalized specific acoustic admittance. If $Y = 0$, the rigid case is retrieved.

The reciprocal impedance condition is

$$p(\mathbf{x}) = Z(\mathbf{x})\mathbf{v}(\mathbf{x}) \cdot \mathbf{n}(\mathbf{x})\,, \qquad \mathbf{x} \in \partial\mathcal{D}\,, \tag{5.50}$$

where

$$Z(\mathbf{x}) = Z_0\xi(\mathbf{x}) \tag{5.51}$$

is the specific acoustic impedance, with $Z_0 = \rho c$ the characteristic specific acoustic impedance of air and $\xi = 1/\gamma$ the normalized specific acoustic impedance. The pressure-release condition is then retrieved with $Z = 0$.

The case $\xi = \gamma = 1$ gives the Enquist-Majda first-order absorbing boundary condition (Engquist et al., 1977), theoretically fully absorbing at normal incidence, that can be used to terminate a computational domain. Another approach to mitigate the effect of reflections from the computational domain boundaries, and thus allowing to reduce the grid size needed for the scattering simulation, is the perfectly matched layer (PML) proposed by Berenger (1994).

With γ or ξ, a fixed positive real value, the behavior of the boundaries is independent of the frequency. Kowalczyk et al. (2008) proposed a method to include complex frequency behavior, *e.g.* as exhibited by porous materials. Locally reacting boundaries are modeled with digital impedance filter included in the recursion with the help of auxiliary update equations. On a regular grid, the objects are described by a staircase approximation, similarly to rasterization in computer graphics with the difference that only the border is necessary here. It results different update equations regarding the boundary node configuration, derived from the elimination of "ghost" points located on the interior of the boundaries. They latter derived them for the compact interpolated schemes (Kowalczyk et al., 2010).

Tornberg et al. (2008) inspected the effects of staircase approximation on reflection of waves solved with 2D Yee's scheme through numerical experiments on a tilted rigid boundary and a circular cylinder. They found that the accuracy of the scheme is degraded and local errors propagate in the domain. This has been confirmed by others (Häggblad et al., 2014). Yamashita et al. (2015) evaluated the approximation on a rigid sphere with the Interpolated Wideband scheme and centered boundary conditions. They found large deviations compared to the theory. This was explained by the fact that a rasterized sphere converges to the expected value in volume but not in surface area at the limit of small spatial steps (Bilbao et al., 2016).

5.2 Finite Volume Method

Botteldooren (1994) extended the FD time domain method to what he called a quasi-Cartesian grid, allowing to overcome the staircase approximation of boundaries. He applied it to the modeling of low frequency in room acoustic modeling (Botteldooren, 1995). It has been further formalized in this context and termed the FV method (Bilbao, 2013). The formulation employs an orthogonal unstructured mesh that restores the consistency of the schemes when boundaries are involved and allows to model complex geometries. We present in this section the method using the formalism developed along the last decade by Bilbao et al. (2017, 2019).

5.2.1 Grid definition

The main advantage of the FV method is that it is formulated to accommodate unstructured meshes. Figure 5.4 shows a part of a region of interest $\mathcal{D}$ and an object defining a region ν. The boundary between the two is noted $\partial\mathcal{D} = \mathcal{D} \cap \nu$. The domain $\mathcal{D}$ is decomposed into N polygons (in 2D) or polyhedra (in 3D), called cells in the following, $\bar{\varOmega}_i$, with the associated index $i = 1, \ldots, N$. Each cell has an interior $\varOmega_i$ and a boundary $\partial\varOmega_i$, such that $\bar{\varOmega}_i = \varOmega_i \cup \partial\varOmega_i$. The set of cells forms a tiling or tessellation of $\mathcal{D}$. Formally, it means that there is not any gap between the cells and their union is equal to the domain of interest :

$$\bigcup_{i=1}^{N} \bar{\varOmega}_i = \mathcal{D}, \tag{5.52}$$

and, furthermore, the cells do not overlap :

$$\varOmega_i \cup \varOmega_j = \emptyset \qquad \forall\, (i,j) \in [1, \ldots, N]^2 \,, \, i \neq j. \tag{5.53}$$

Such a tiling can be obtained from the Voronoi diagram of a set of points then called sites or seeds. To each of them is associated a Voronoi cell, containing a single site, defined as the set of points closer to it than any other. The tessellation in fig. 5.4 has been obtain from the Voronoi diagram of the points represented with black dots. It results that the boundaries between the cells are straight lines, each of which has the property of being on

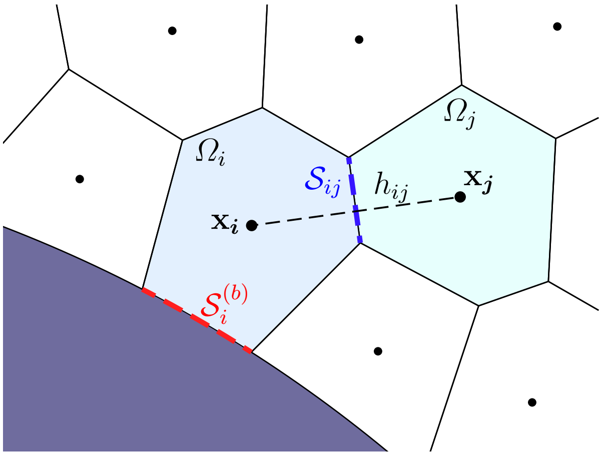

Figure 5.4 Part of an orthogonal unstructured grid near a scatterer with variable definitions for a cell Ω_i on a boundary and an adjacent cell Ω_j.

the bisector of the segment formed by two neighboring sites generating it. It also results that the Voronoi cell of a site surrounded by other ones is a convex polygon such as Ω_j. A Voronoi cell such as Ω_i may be concave as it is bounded by ν.

Each cell $\bar{\Omega}_i$ with its sites of coordinates $\mathbf{x_i}$ has an associated surface (in 2D) or volume (in 3D) noted $V_i = |\Omega_i|$. When a cell $\bar{\Omega}_i$ is adjacent to a cell $\bar{\Omega}_j$, the shared edge or surface is said internal noted $\mathcal{S}_{ij} = \bar{\Omega}_i \cap \bar{\Omega}_j$. Its length or surface area is $S_{ij} = |\mathcal{S}_{ij}|$ and $\bar{\Omega}_i$ has N_i such edges. The inter-cell distance between the two associated sites is noted $h_{ij} = \|\mathbf{x_i} - \mathbf{x_j}\|$. A cell $\bar{\Omega}_i$ in contact with the boundary $\partial\mathcal{D}$ is called a boundary cell and the shared edge or surface is noted $\mathcal{S}_i^{(b)} = \bar{\Omega}_i \cap \partial\mathcal{D}$. Similarly, its associated length or area is noted $S_i^{(b)} = \left|\mathcal{S}_i^{(b)}\right|$. A cell where $\bar{\Omega}_j \cap \partial\mathcal{D} = \emptyset$ is called an interior cell.

5.2.2 Finite Volume formulation

The principle of the method consists in approximating the integral forms of the conservation equations forming our problem. In the case of linear acoustics, these partial differential equations are the conservation of momentum eq. (5.12a) and the conservation of mass eq. (5.12b). Integrating the latter on cell $\bar{\Omega}_i$ gives

$$\frac{1}{\rho c^2} \int_{\bar{\Omega}_i} \frac{\partial p}{\partial t} \, d\mathbf{x} + \int_{\bar{\Omega}_i} \boldsymbol{\nabla} \cdot \mathbf{v} \, d\mathbf{x} = 0 \, . \tag{5.54}$$

Using the divergence theorem, the second term may be written

$$\int_{\bar{\Omega}_i} \boldsymbol{\nabla} \cdot \mathbf{v} \, d\mathbf{x} = \int_{\partial\Omega_i} \mathbf{v} \cdot \mathbf{n} \, d\mathbf{x} \, , \tag{5.55}$$

with $\mathbf{n}$ the outward normal on $\partial\Omega_i$. In order to arrive at a numerical scheme operating over a finite set of discrete values of pressure and velocities, we define the discrete pressure of cell Ω_i at its associated point $\mathbf{x_i}$ as the spatial average pressure over its volume (or surface) :

$$p_i^n = p(\mathbf{x_i}, n\Delta t) \approx \frac{1}{V_i} \int_{\bar{\Omega}_i} p(\mathbf{x}, n\Delta t) \, d\mathbf{x} \, . \tag{5.56}$$

The time is discretized with a regular time step $\mathit{\Delta} t$. To approximate the right-hand term in eq. (5.55), we must discretize the normal velocity at edges of the cell. From the perspective of cell $\bar{\mathit{\Omega}}_i$, the normal velocity associated with $\mathcal{S}_{ij}$ is approximated as

$$v_{ij}^n \approx \frac{1}{S_{ij}} \int_{\mathcal{S}_{ij}} \mathbf{v}(\mathbf{x}, n\mathit{\Delta} t) \cdot \mathbf{n}_{ij} \, d\mathbf{x} \,, \tag{5.57}$$

where $\mathbf{n}_{ij}$ is the outward normal on $\mathcal{S}_{ij}$. Note that, from the perspective of the adjacent cell $\bar{\mathit{\Omega}}_j$, we have the symmetry

$$v_{ji} = -v_{ij}. \tag{5.58}$$

Similarly, the velocity over $\mathcal{S}_i^{(b)}$ is approximated as

$$v_{(b),i}^n \approx \frac{1}{S_i^{(b)}} \int_{\mathcal{S}_i^{(b)}} \mathbf{v}(\mathbf{x}, n\mathit{\Delta} t) \cdot \mathbf{n}(\mathbf{x}) \, d\mathbf{x} \,, \tag{5.59}$$

where the normal may vary on the boundary. $\mathcal{S}_i^{(b)}$ in fig. 5.4 appears curved but, in practice, it is approximated by a set of $N_i^{(b)}$ straight edges $\mathcal{S}_{il}^{(b)}$, with $l = 1, \ldots, N_i^{(b)}$. The approximate normal velocity $v_{(b),il}^n$ of one subdividing edge is obtain from

$$v_{(b),il}^n \approx \frac{1}{S_{il}^{(b)}} \int_{\mathcal{S}_{il}^{(b)}} \mathbf{v}(\mathbf{x}, n\mathit{\Delta} t) \cdot \mathbf{n}_{il} \, d\mathbf{x} \,, \tag{5.60}$$

with $\mathbf{n}_{il}$ the outward normal on $\mathcal{S}_{il}^{(b)}$, and thus

$$v_{(b),i}^n = \frac{1}{S_i^{(b)}} \sum_{l=1}^{N_i^{(b)}} S_{il}^{(b)} v_{(b),il}^n. \tag{5.61}$$

With these approximations, it is now possible to write eq. (5.54) in discrete form for a cell $\bar{\mathit{\Omega}}_i$:

$$\frac{V_i}{\rho c^2} \delta_{t+} p_i^n = -\sum_{j=1}^{N_i} S_{ij} v_{ij}^{n+\frac{1}{2}} - S_i^{(b)} v_{(b),i}^{n+\frac{1}{2}} \,. \tag{5.62}$$

We used a forward difference in time similarly to eq. (5.14c), but other choices are possible. The gradient required in eq. (5.12a) is approximated by the following operator

$$\delta_{ij} p_i^n = \frac{p_j^n - p_i^n}{h_{ij}} \approx \nabla p(\mathbf{x}_i + \mathbf{n}_{ij} h_{ij}/2, n\mathit{\Delta} t) \,. \tag{5.63}$$

The second equation of the scheme is then

$$\rho \delta_{t-} v_{ij}^{n+\frac{1}{2}} = -\delta_{ij} p_i^n \,. \tag{5.64}$$

Alternatively, a FV scheme for the second order wave equation may be formulated using the relations for the velocity potential. In discrete form, they may be written

$$p_i^n = \rho \delta_{t-} \mathit{\Phi}_i^n, \qquad v_{ij}^{n+\frac{1}{2}} = -\delta_{ij} \mathit{\Phi}_i^n \,. \tag{5.65}$$

Substituting them in eq. (5.62) gives

$$\frac{V_i}{c^2} \delta_{tt} \mathit{\Phi}_i^n = \sum_{j=1}^{N_i} S_{ij} \delta_{ij} \mathit{\Phi}_i^n - S_i^{(b)} v_{(b),i}^{n+\frac{1}{2}} \,. \tag{5.66}$$

5.2.3 Matrix form

The implementation of the scheme is done in practice using the matrix form as proposed by Bilbao et al. (2019), where several tensors formalizing the adjacency relations between the cells and their boundaries are introduced. The set of N cells tessellating the domain has a finite number N_e of internal edges (for a two dimensional space) and a finite number N_b of boundary cells. Thus, we assign to these geometric quantities, already introduced as h_{ij}, $S_{ij} = |\mathcal{S}_{ij}|$ or $S_i^{(b)}$, an index $e = 1, \ldots, N_e$ for variables associated to internal edges and new variables $R_b = |\mathcal{R}_b|$ with index $b = 1, \ldots, N_b$ for boundary edges. For variables referring to cell quantities, we assign an index $l = 1, \ldots, N$.

A given internal edge with index e is shared by two and only two adjacent cells $\bar{\Omega}_i$ and $\bar{\Omega}_j$ with $i > j$. We define then the oriented adjacency tensor Q_{le} as

$$Q_{le} = \begin{cases} 1 & \text{if } l = i \quad , \\ -1 & \text{if } l = j \quad , \\ 0 & \text{otherwise}, \end{cases} \tag{5.67}$$

where $l = 1, \ldots, N$ and $e = 1, \ldots, N_e$. Moreover, as a boundary edge $\mathcal{R}_b$ is a part of only one cell $\bar{\Omega}_{l_b}$, we define similarly a non-oriented adjacency tensor W_{lb} as

$$W_{lb} = \begin{cases} 1 & \text{if } l = l_b \quad , \\ 0 & \text{otherwise}, \end{cases} \tag{5.68}$$

where $l = 1, \ldots, N$ and $b = 1, \ldots, N_b$. In matrix notation, they are noted $\mathbf{Q}$ and $\mathbf{W}$ of sizes $N \times N_e$ and $N \times N_b$, respectively.

We also define the following vectors for the discrete pressures and velocities at discrete time $n\Delta t$:

$$\mathbf{p}^n = \begin{bmatrix} p_1^n \\ \vdots \\ p_N^n \end{bmatrix}, \qquad \mathbf{v}^n = \begin{bmatrix} v_1^n \\ \vdots \\ v_{N_e}^n \end{bmatrix}, \qquad (\mathbf{v}')^n = \begin{bmatrix} (v')_1^n \\ \vdots \\ (v')_{N_b}^n \end{bmatrix}, \tag{5.69}$$

associated with the N cells sites, the N_e internal edges, and the N_b boundary edges, respectively.

It is now possible to write eq. (5.62) and eq. (5.64) in matrix form as

$$\frac{1}{\rho c^2}\mathbf{V}\delta_{t+}\mathbf{p}^n - \mathbf{Q}\mathbf{S}\mathbf{v}^{n+\frac{1}{2}} + \mathbf{W}\mathbf{R}(\mathbf{v}')^{n+\frac{1}{2}} = \mathbf{0}\,, \tag{5.70}$$

$$\rho\mathbf{H}\delta_{t-}\mathbf{v}^{n+\frac{1}{2}} + \mathbf{Q}^T\mathbf{p}^n = \mathbf{0}\,, \tag{5.71}$$

where $\mathbf{V}$ is a diagonal matrix of size $N \times N$ with the cell areas V_l, $l = 1, \ldots, N$ as elements. $\mathbf{S}$ and $\mathbf{H}$ are diagonal matrices of size $N_e \times N_e$ with the internal edge lengths S_e and inter-cell distances h_e, $e = 1, \ldots, N_e$ as elements, respectively. Similarly, $\mathbf{R}$ is a diagonal matrix of size $N_b \times N_b$ with the boundary edge lengths R_b, $b = 1, \ldots, N_b$ as elements.

This system can be rewritten under a more tractable form

$$\delta_{t+}\tilde{\mathbf{p}}^n - c\mathbf{D}^T\tilde{\mathbf{v}}^{n+\frac{1}{2}} + c\mathbf{B}^T\left(\tilde{\mathbf{v}'}\right)^{n+\frac{1}{2}} = \mathbf{0}\,, \tag{5.72}$$

$$\delta_{t-}\tilde{\mathbf{v}}^{n+\frac{1}{2}} + c\mathbf{D}\tilde{\mathbf{p}}^n = \mathbf{0}\,, \tag{5.73}$$

introducing the scaled variables

$$\tilde{\mathbf{p}} = \frac{1}{\sqrt{\rho}c}\mathbf{V}^{1/2}\mathbf{p}\,, \quad \tilde{\mathbf{v}} = \sqrt{\rho}\mathbf{S}^{1/2}\mathbf{H}^{1/2}\mathbf{v}\,, \tag{5.74}$$

and the scaled boundary variables

$$\tilde{\mathbf{p}'} = \frac{1}{\sqrt{\rho}c}\mathbf{R}^{1/2}\mathbf{p}'\,, \quad \tilde{\mathbf{v}'} = \sqrt{\rho}\mathbf{R}^{1/2}\mathbf{v}'\,, \tag{5.75}$$

with

$$\mathbf{D} = \mathbf{S}^{1/2}\mathbf{H}^{-1/2}\mathbf{Q}^T\mathbf{V}^{-1/2} \quad , \quad \mathbf{B} = \mathbf{R}^{1/2}\mathbf{W}^T\mathbf{V}^{-1/2}\,. \tag{5.76}$$

Similarly to eq. (5.66), this can be expressed under second-order form

$$\delta_{tt}\tilde{\mathbf{\Phi}}^n + c^2\mathbf{D}^T\mathbf{D}\tilde{\mathbf{\Phi}}^n + c\mathbf{B}^T\left(\tilde{\mathbf{v}'}\right)^{n+\frac{1}{2}} = \mathbf{0} \tag{5.77}$$

solving the scaled velocity potential $\tilde{\mathbf{\Phi}}$, linked respectively to $\tilde{\mathbf{p}}$ and $\tilde{\mathbf{v}}$ by

$$\tilde{\mathbf{p}}^n = \delta_{t-}\tilde{\mathbf{\Phi}}^n\,, \quad \tilde{\mathbf{v}}^{n+\frac{1}{2}} = -c\mathbf{D}\tilde{\mathbf{\Phi}}^n\,. \tag{5.78}$$

The matrices $\mathbf{D}$ and $-\mathbf{D}^T\mathbf{D}$ are ultimately the gradient and Laplacian approximations in this formulation. It is straightforward to verify that eq. (5.77) simplifies to eq. (5.28) or eq. (5.35) considering the Cartesian grid (Botteldooren, 1994) or the hexagonal grid, respectively.

5.2.4 Stability condition

A detailed stability analysis has been realized for this scheme by Bilbao et al. (2019). The stability condition they found is

$$\Delta t \leq \frac{2}{\sqrt{\beta_{\max}}c}\,, \tag{5.79}$$

where $\beta_{\max}$ is the largest eigenvalue of $\mathbf{D}^T\mathbf{D}$. Previously, Bilbao (2013) derived the condition for non-negative internal stored energy and found

$$\Delta t^2 \leq \min_{\forall i\in[1,\ldots,N]} \frac{2V_i}{c^2\sum_{j=1}^{N_i} S_{ij}/h_{ij}}\,. \tag{5.80}$$

These conditions are equivalent to eq. (5.25) obtained through von Neumann stability analysis for a square grid.

However, this is not the case for the hexagonal scheme whose von Neumann condition is given by eq. (5.36). The eigen-decomposition for such a discrete operator gives a maximum eigenvalue $\beta_{\max} = 16/3h^2$ (Sun, 2004), resulting in a less strict condition, $C_r \leq \sqrt{3}/2$, using the first inequality. Surprisingly, it results in the unattainable value required to obtain a fourth-order isotropic scheme (Tuomela, 1990). The second gives the same condition as the Standard Rectilinear scheme, stricter than the one obtained by von Neumann analysis for such a scheme.

Therefore, the condition used in a two-dimensional space is

$$\Delta t \leq \min\left\{\frac{2}{\sqrt{\beta_{\max}}c}, \sqrt{\frac{2}{3}}\frac{h}{c}\right\}\,, \tag{5.81}$$

where h is the spatial step of the regular grid used to generate the FV mesh as it will be seen in section 5.3.

5.2.5 Boundary conditions

The boundary condition in this formulation are locally reactive since the velocity $v_{(b),i}$ is only dependent on the potential or pressure of Ω_i during the recursion. In the case of rigid boundaries, eq. (5.47), $\tilde{\mathbf{v}}' = \mathbf{0}$ and thus the recursion reduces to

$$\tilde{\mathbf{\Phi}}^{n+1} = 2\tilde{\mathbf{\Phi}}^{n} - \tilde{\mathbf{\Phi}}^{n-1} - c^2\Delta t^2 \mathbf{D}^T\mathbf{D}\tilde{\mathbf{\Phi}}^{n}\,, \tag{5.82}$$

where the matrix $\mathbf{R}$ no longer intervenes.

The admittance boundary condition given eq. (5.48) can be written

$$\left(\tilde{\mathbf{v}}'\right)^{n+\frac{1}{2}} = \mathbf{\Gamma}\tilde{\mathbf{p}}'^{\,n+\frac{1}{2}} \tag{5.83}$$

where $\mathbf{\Gamma}$ is a $N_b \times N_b$ diagonal matrix with γ_b the normalized specific admittance for each boundary edge $b = 1, \ldots, N_b$ on its diagonal. Using the time averaging operator $\mu_+ = (e_+ + 1)/2$, such that $e_+\tilde{\mathbf{\Phi}}^n = \tilde{\mathbf{\Phi}}^{n+1}$ and $\mu_+\tilde{\mathbf{\Phi}}^n = \tilde{\mathbf{\Phi}}^{n+\frac{1}{2}}$, this can be further expressed

$$\left(\tilde{\mathbf{v}}'\right)^{n+\frac{1}{2}} = \mu_+\delta_{t-}\mathbf{\Gamma}\mathbf{B}\tilde{\mathbf{\Phi}}^{n}\,. \tag{5.84}$$

Substituting eq. (5.84) in eq. (5.77) results in the update for frequency-independent impedance boundaries

$$\left(\mathbf{I}_N + \frac{c\Delta t}{2}\mathbf{B}^T\mathbf{\Gamma}\mathbf{B}\right)\tilde{\mathbf{\Phi}}^{n+1} = 2\tilde{\mathbf{\Phi}}^{n} + \left(\frac{c\Delta t}{2}\mathbf{B}^T\mathbf{\Gamma}\mathbf{B} - \mathbf{I}_N\right)\tilde{\mathbf{\Phi}}^{n-1} - c^2\Delta t^2\mathbf{D}^T\mathbf{D}\tilde{\mathbf{\Phi}}^{n}\,, \tag{5.85}$$

where $\mathbf{I}_N$ is the identity matrix of size N. Although the recursion is presented as a linear system to be solved to determine $\tilde{\mathbf{\Phi}}^{n+1}$, the matrix in factor is actually diagonal. It is thus possible to multiply this update equation by the inverse matrix, precomputed only once (Bilbao et al., 2019).

Frequency-dependent boundaries can be implemented similarly to the digital impedance filters approach already mentioned in section 5.1.4, through auxiliary relations linking the derivatives of $\tilde{\mathbf{v}}'$ and $\tilde{\mathbf{p}}'$. Details are given by Bilbao (2013) and Bilbao et al. (2017, 2016), where a given complex frequency behavior can be prescribed estimating the coefficients of the auxiliary equations with the Nelder-Mead simplex method.

Ultimately, a complete analogy can be made with RLC circuits of electronics or mass-spring-damper systems of mechanics. Therefore, the stability condition given eq. (5.81) holds if the boundary models are passive (Bilbao et al., 2019), *i.e.* they can not create energy.

5.3 Hybridation

It has been seen that the FV formulation reduces to the FD one when applied on regular grids. We propose here to use the two methods conjointly through the generation of hybrid meshes. A regular grid is modified in close proximity to the boundaries of the objects, resulting in an unstructured grid where the FV method is applied. The rest of the domain is computed with the FD method that arises by simplification.

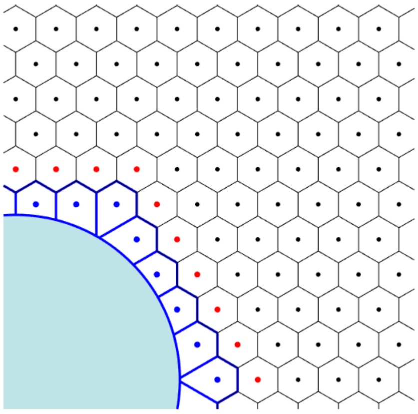

Figure 5.5 Example of hybrid mesh in proximity to a curved boundary with the Bounded Voronoi diagram method. FV cells and their corresponding generating sites are represented with blue edges and dots, respectively. They are clipped by the boundary of the object shown in cyan and bounded in the outer direction by the regular grid points enclosing them shown with red dots. Regular hexagonal grid is shown in black.

5.3.1 Bounded Voronoi diagram

The first approach is to modify only the grid points that enclose the object completely as shown in fig. 5.5. The FV mesh is obtained from the Voronoi diagram of this set of points represented by blue dots. The achieved polygons are, in a second step, clipped by the boundaries of the scatterer represented in cyan. It results the Voronoi cells represented with blue edges. The red dots, located on the hexagonal grid, are used to bound the Voronoi diagram in the outer direction to the scattering object. Computing the Voronoi diagram of both sets of points gives their adjacency relation. It is then possible to establish the discrete Laplacian to link the two meshes when updating the equations. This method is equivalent to other conformal methods already proposed, validated in the case of soft and hard boundaries (Häggblad et al., 2012; Tolan et al., 2003).

It is worth noting that with this approach the inter-cell distance stays equal to the regular grid spacing. The example is given with a hexagonal grid but it also applies to rectilinear grids and probably others. All the other geometrical quantities necessary to construct the discrete Laplacian are computed from the Voronoi cells obtained from this bounded Voronoi diagram (BVD). In practice, it is interesting, when simulating a scattering problem, to have the unperturbed incident field to normalize and take into account the magnitude and phase of the source signal. Moreover, by subtracting it from the total field, we obtain the scattered field in the time domain. For this, a simulation is performed in parallel on the regular FD grid used at the beginning with strictly identical parameters.

In the following, the boundaries of the cross section are discretized by a set of linear elements using GMSH version 4.7.1 (Geuzaine et al., 2009) so that the error on the perimeter is less than 0.1 %.

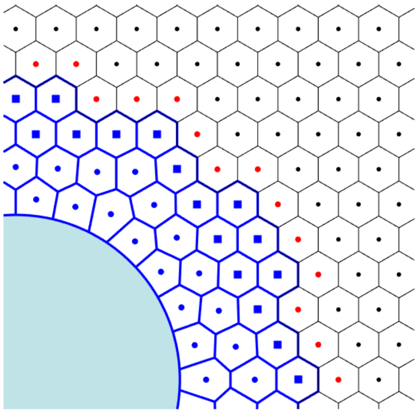

Figure 5.6 Centroidal Voronoi diagram after 10 iterations of Lloyd's method. Voronoi cells are shown with blue edges and their corresponding generating sites with blue dots and square.

5.3.2 Centroidal Voronoi diagram

Depending on the geometry of the scatterer, *i.e.* whether it is smooth with respect to the spatial step or sharp with re-entrant corners, the mesh with the BVD method can result in very strict stability condition in the second case (Hamilton, 2014), which is not computationally efficient. Therefore, if necessary, a new mesh can be generated from the Voronoi diagram of the centroids of the previously obtained Voronoi cells and clipped as before. This process is repeated to approximate a centroidal Voronoi diagram (CVD) with Lloyd's method (Du et al., 1999). Moreover, the locally reactive boundary conditions imply that the normal velocity at a boundary cell is aligned with the generating site. This approach is supposed to improve locally this requirement.

Figure 5.6 shows the FV mesh obtained after 10 iterations. Here, Lloyd's method is only applied on the points less than two spatial steps away from the boundary at the first iteration and not on the sites marked with a blue square. In other words, these points remain at their original position on the regular grid, ensuring complete regularity beyond where the FD method applies. In practice, it is desirable that the spatial step is not much larger than the smallest geometrical detail to avoid meshing errors. In our applications, a spatial step of about 5 mm is used, representing 10 points per wavelength at 7 kHz, which is sufficient for the geometries of interest.

5.4 Verification

According to the Lax-Richtmyer theorem, the stability of the scheme is a necessary and sufficient condition to guarantee its convergence, assuming that it is consistent with the well-posed problem (Lax et al., 1956). The stability of the proposed method is validated by verifying that the total acoustic energy is conserved in a closed system with lossless boundaries.

Then, the convergence of the scheme is investigated by comparison with the series solutions for sound scattering by rigid and impedance circular cylinders. It is also compared with another computational code, already validated, that solves multiple scattering problems (Rohfritsch et al., 2019), applied to one of the geometries of interest with this feature.

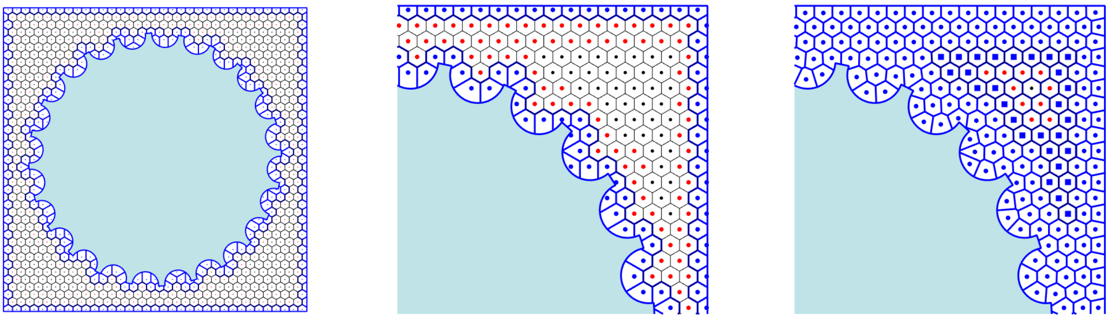

(a) (b) (c)

Figure 5.7 Hybrid meshes for energy conservation verification. **(a)** Full view of the domain. **(b)** Details of BVD mesh. **(c)** Details of CVD mesh.

The far field is computationally expensive to simulate with FD methods. We use here a method that extrapolate it from the near field. The method is validated by comparisons with analytic solutions for a circular cylinder and a BEM code simulating the far field of one of our geometries of interest.

5.4.1 Energy conservation

Stability is verified through conservation of energy. Even if the FV method is conservative by construction, it is a good way to verify the implementation. For that, a closed domain is meshed using the proposed methods, the BVD and the CVD. The boundaries are considered rigid, allowing to verify that the numerical acoustic energy, computed at each time step with

$$E_{int}^{n} = \frac{1}{2}\left(\left(\tilde{\mathbf{p}}^{n}\right)^{T}\tilde{\mathbf{p}}^{n} + \left(\tilde{\mathbf{v}}^{n+\frac{1}{2}}\right)^{T}\tilde{\mathbf{v}}^{n-\frac{1}{2}}\right), \tag{5.86}$$

is constant over time after that the source signal is fully injected (Bilbao, 2013).

Figure 5.7a shows the domain considered. It consists of a closed square with 1.1 m sides with one of the scatterer of interest at its center. This geometry has been chosen because of its convexity and, therefore, it is considered as the most problematic regarding the BVD mesh with potential unstable boundary cells (Hamilton, 2014). The speed of sound is set at $c = 344\,\mathrm{m\,s^{-1}}$ and the spatial step is $h = 34.4\,\mathrm{mm}$. After generating a mesh from the BVD method (fig. 5.7b), the time step is set to meet the stability condition eq. (5.81), resulting here in $dT = h/c\sqrt{2/3} \approx 8.09 \times 10^{-5}\,\mathrm{s}$. For the CVD method (fig. 5.7c), the resulting time step is $dT \approx 7.68 \times 10^{-5}\,\mathrm{s}$, slightly lower compared to the BVD. The grids are excited using the initial conditions $f = 1$ at a random point of a regular part of the domain and zero everywhere else, and $g = 0$ with the initialization scheme given eq. (5.45).

Figure 5.8 shows the variation of total internal acoustic energy $1 - E_{int}^{n}/E_{int}^{1}$ over time. It is calculated over 200 ms, or about 2470 and 2610 samples for the BVD (fig. 5.8a) and CVD (fig. 5.8b) mesh, respectively. The numerical energies appear to be conserved in both cases, as no increasing is observed on the time segment considered, and vary as integer multiples of machine epsilon, 2^{-53} here, as already observed on other cases (Bilbao, 2013; Hamilton, 2016). The amplitude of the variations is more important for the BVD compared to the CVD. This is attributed to the fact that Lloyd's algorithm will tend to subdivide the space more uniformly and thus each FV cell has more or less the same

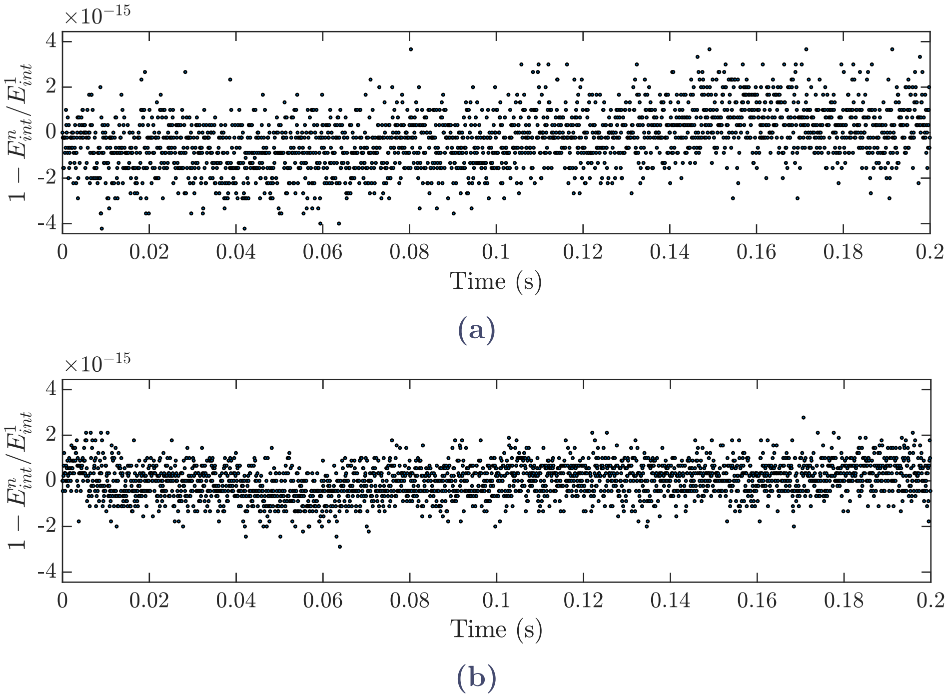

Figure 5.8 Normalized variation of numerical internal acoustic energy $1 - E_{int}^n/E_{int}^1$. **(a)** BVD. **(b)** CVD.

"weight" as the others, however it reduces the stability limit.

In the examples, the problem is treated entirely with the FV matrix formulation, which allows to compute E_{int}^n efficiently. In practice, the regular parts of a hybrid mesh are updated with the FD method, where the Laplacian can be computed using a spatial convolution with the appropriate stencil. Therefore, the discrete velocities are difficult to identify, especially at the junction of the grids. Nevertheless, it has been verified that the discrete Laplacian reduces well to the stencil for the hexagonal scheme with differences of the order of machine epsilon. Replacing them with the regular stencil, as we do for our scattering problems in an "open" domain, could result in instability at long time in a closed domain. However, it is verified in the convergence study and a cross validation case, that these differences do not have an impact for our objectives.

5.4.2 Convergence study

In order to validate the proposed hybrid finite difference finite volume (FDFV) methods, a second step is to verify their convergence. They are compared with the series solutions for sound scattering by circular cylinders under plane wave incidence given section 2.4.1.1. Rigid and admittance boundary conditions with $\gamma = 0$ and $\gamma = \rho c/10^3 \approx 0.42$, respectively, are investigated on a cylinder of 0.5 m radius. The speed of sound is $346\,\mathrm{m\,s^{-1}}$ and the air density is $\rho = 1.2\,\mathrm{kg\,m^{-3}}$.

The pressure is evaluated at $N_{rec} = 200$ points regularly spaced on a circle of radius 1 m centered on the axis of the cylinder. These positions on the discrete space are never exactly on this circle but the closest point is used for each and the analytic solutions will be calculated at these points. The source signal is a Ricker pulse with a center frequency of 500 Hz. It is injected as a soft source on a line of points located at the closest 1.1 m from the center of the cylinder. Periodic boundary conditions are used to extend the

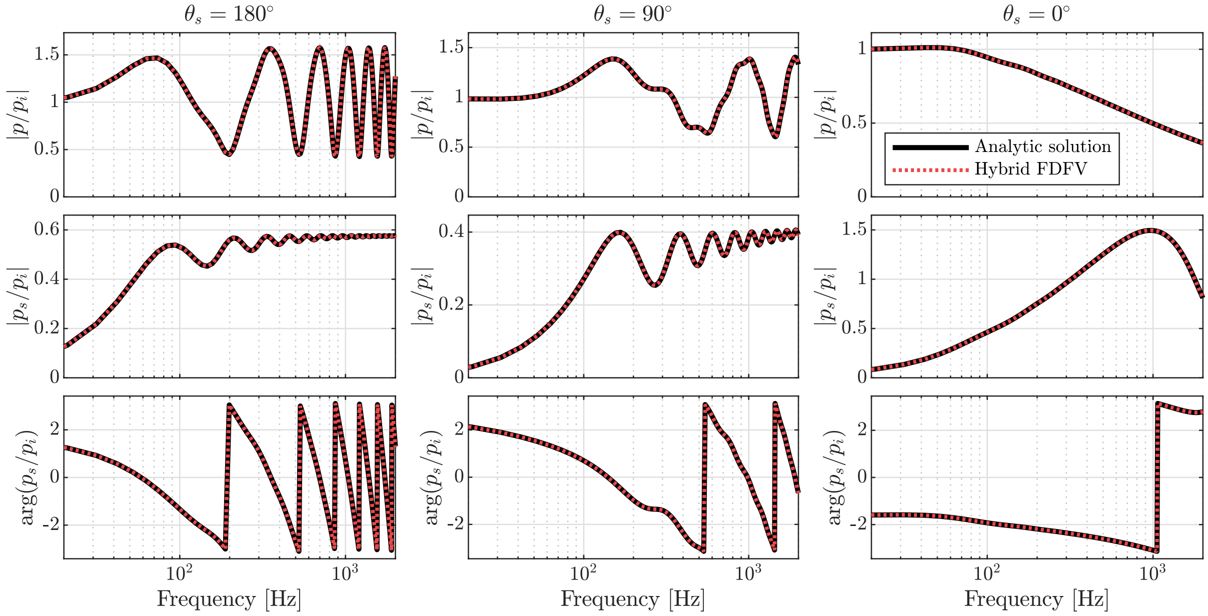

Figure 5.9 Magnitude of p/p_i (top row) and magnitude and phase of p_s/p_i (middle and bottom row) as functions of frequency for back, transverse, and forward scattering, *i.e.* $\theta_s = 180°$, $90°$ and $0°$, respectively, by a rigid cylinder for analytic and hybrid FDFV with BVD method with $h = 5\,\mathrm{mm}$.

domain infinitely in the directions perpendicular to that of the incident plane wave and thus prevent edge effects. Each simulation is stopped after the wave traveled 15 m, which is about 43 ms for a speed of sound fixed at $c = 346\,\mathrm{m\,s^{-1}}$. The two-dimensional domain is large enough that, during this time, only the scattering by the cylinder is recorded. The simulations are performed with 6 spatial steps ranging from $h = 5\,\mathrm{mm}$ to 17 mm and the time step is set using the condition given eq. (5.81).

The scattered field can be isolated by subtracting the incident field from the total field. For that, a simulation without the cylinder is run for each spatial step. They are performed in parallel to the total field simulation, on the regular grid used to generate the hybrid mesh with, consequently, strictly identical parameters. The comparison is done in the frequency domain. Each spectrum is calculated using the Fast Fourier Transform (FFT) on the signal with zero padding. Series solutions for the scattered pressure are calculated until double precision is reached. The incident plane wave is calculated with $p_i = e^{ikx}$.

Figures 5.9 and 5.10 show the magnitude and phase of normalized total and scattered pressures obtained with series solutions and the hybrid FDFV method with BVD for a rigid and an impedance circular cylinder from 20 Hz to 2000 Hz for the smallest spatial step $h = 5\,\mathrm{mm}$. This is the usable bandwidth for the Ricker pulse used. The results are shown for three directions of scattering: back on the left, transverse in the middle and forward on the right. Graphically, we find an excellent agreement between the two on the considered frequency range for both boundary conditions. Although, the lack of energy injected above 2 kHz is visible in fig. 5.10 where the magnitude ratio of back and transverse scattered pressures starts to deviate around this frequency.

To further compare the results spatially, figs. 5.11a and 5.11b are the polar diagrams of the magnitude ratios of total and scattered pressures, respectively, to the incident pressure

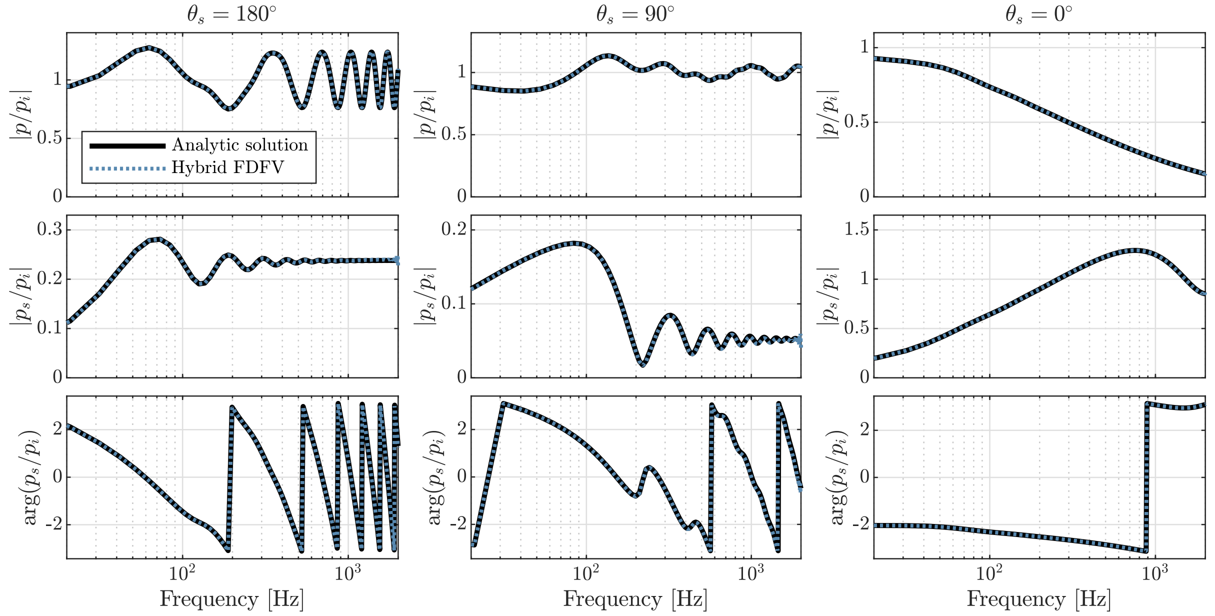

Figure 5.10 Magnitude of p/p_i (top row) and magnitude and phase of p_s/p_i (middle and bottom rows) as functions of frequency for back, transverse, and forward scattering, *i.e.* $\theta_s = 180°$, $90°$ and $0°$, respectively, by an impedance cylinder ($\gamma \approx 0.42$) for analytic and hybrid FDFV with BVD results with $h = 5\,\mathrm{mm}$.

in dB for the rigid cylinder. They are shown for the central frequencies of the octave bands from 63 Hz to 2000 Hz. The incident wave goes from the left to the right. Figures 5.11c and 5.11d show these results for the impedance cylinder. Again, the agreement between simulated and analytic results is also found on all positions for both boundary conditions with slight differences at 2 kHz for the impedance cylinder as already observed.

To quantify the convergence, we use the L_2-norm of the absolute errors on the normalized scattered pressures, evaluated on the N_{rec} positions, that is expressed

$$\|E\|_2 = \sqrt{\sum_{n=1}^{N_{rec}} \left| \frac{p_{s,sim}(r_n,\theta_n)}{p_{i,sim}(r_n,\theta_n)} - \frac{p_{s,ana}(r_n,\theta_n)}{p_{i,ana}(r_n,\theta_n)} \right|^2}, \tag{5.87}$$

calculated at the frequency 500 Hz, where the subscripts "*sim*" and "*ana*" stand for simulated and analytic results. This global error is calculated with a fixed number of positions. Note that if the function chosen to evaluate a global error considers an increasing number of points as the spatial step is reduced, an appropriate scaling by $\sqrt{h}$ should be applied (LeVeque, 2002, 2007). The values obtained for each spatial step, hybrid mesh and boundary condition are represented in fig. 5.12. The log-log linear fit for norms with the same boundary condition and hybrid mesh method are given, as well as the slopes for first and second-order convergence.

For all cases, the norm decreases with h showing that the proposed methods are convergent. With identical boundary conditions, the norms show a similar convergence. The slopes for rigid boundary conditions are about 1.7 and 1.1 for impedance boundaries. The global errors for the rigid cylinder are lower than the impedance cylinder. Moreover, the errors for the results with BVD are lower than with CVD. To examine if this is due to increased dispersion resulting from the stricter stability condition of the CVD

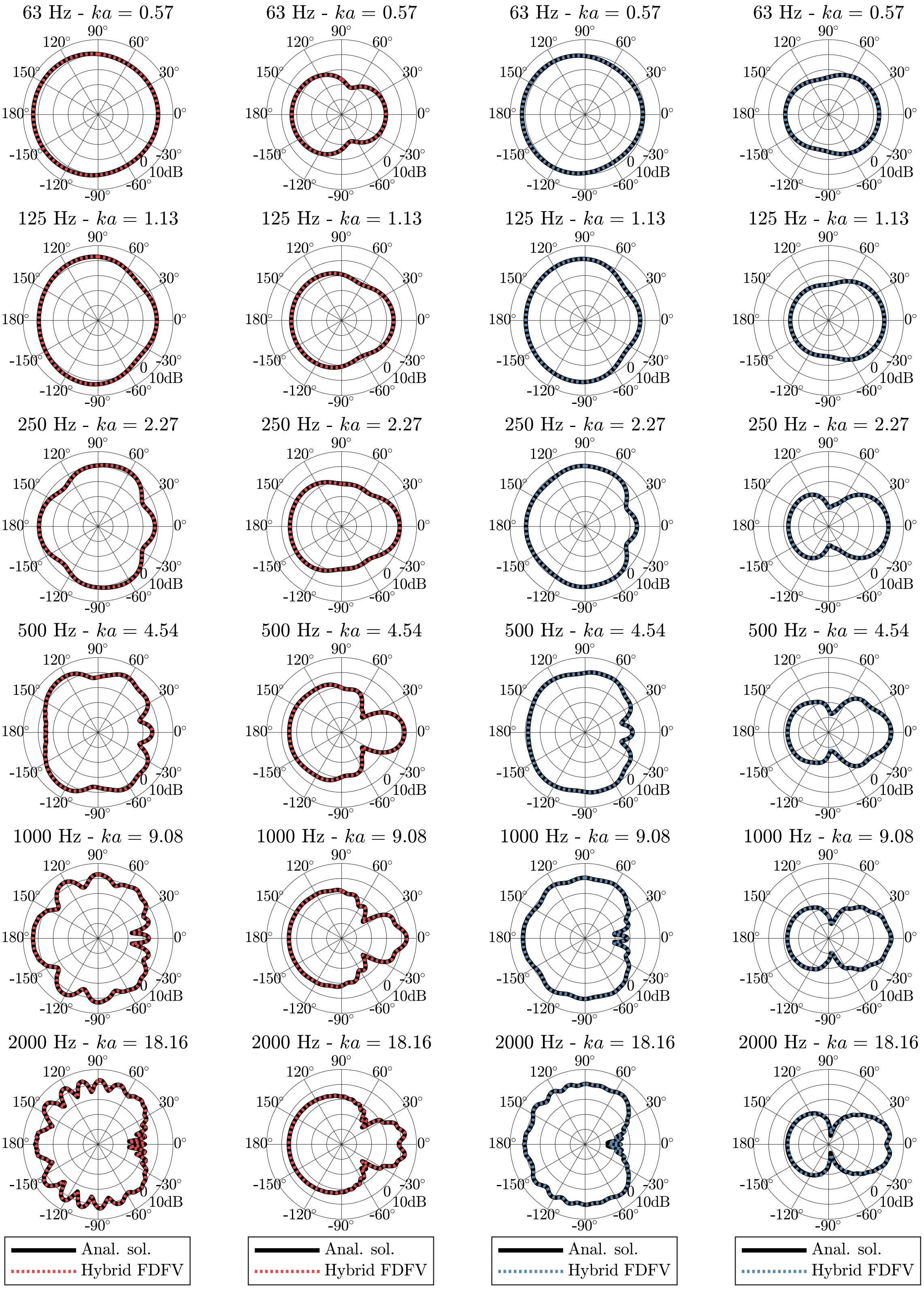

(a) **(b)** **(c)** **(d)**

Figure 5.11 Polar diagrams, as function of the scattering angle, of **(a, c)** $20 \log_{10} |p/p_i|$ and **(b, d)** $20 \log_{10} |p_s/p_i|$ for a **(a, b)** rigid and **(c, d)** impedance ($\gamma \approx 0.42$) cylinder at different central frequencies of octave bands. The corresponding Helmholtz number ka is also indicated with k the wavenumber and a the radius.

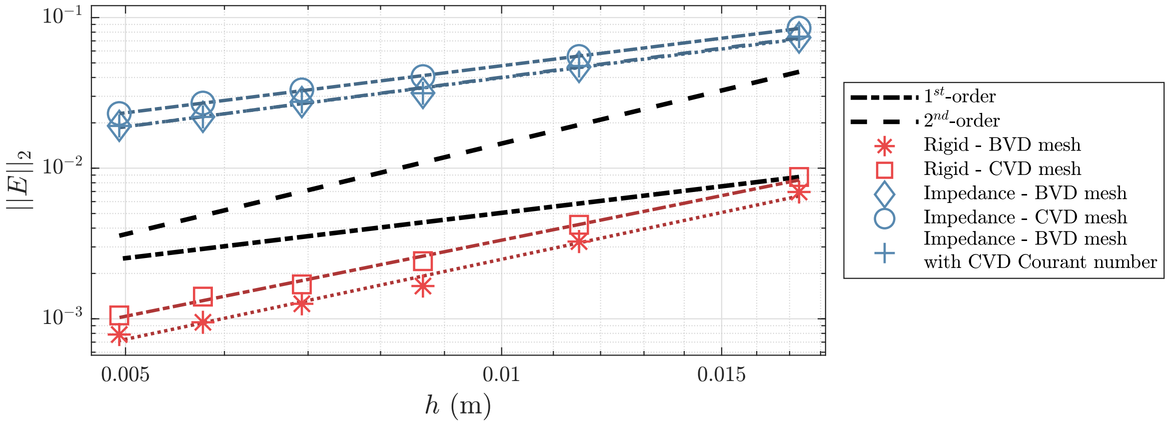

Figure 5.12 $\|E\|_2$ with log-log linear fits as functions of the spatial step h for convergence study for BVD and CVD meshes with rigid and impedance boundary conditions. First and second-order slopes are represented with black dash-dotted and dashed lines, respectively.

method or the unstructured mesh itself, simulations are performed with the BVD method and impedance boundaries setting the time step to match those resulting from the CVD method. Their norms are represented with "+" signs in fig. 5.12. They are approximately equal to those with an optimal Courant number, indicating that the CVD unstructured orthogonal mesh results in a slight reduction of accuracy. Nevertheless, the order of convergence is maintained between the two methods.

5.4.3 Multiple scattering

In order to verify that the method is suitable to simulate sound scattering by multiple cylindrical bodies, it is compared with MuScat (Rohfritsch et al., 2019), a frequency domain method developed to solve multiple scattering problems as described in section 2.4.3. The infinite linear system is truncated to a certain order and solved with iterative methods.

We compare the harmonic scattered field at 500 Hz and 950 Hz for one of our geometries of interest. It is a type of column shaft present in the *Cathédrale Notre-Dame de Paris*, formed by a circular cylinder surrounded by 12 relatively thin others, angularly evenly distributed, as shown later in fig. 6.5g. They are all rigid. The speed of sound was set at 346.6 m s^{-1}. For the hybrid method, the BVD mesh was employed with $h = 5$ mm. The excitation signal is a Ricker pulse with a central frequency of 1 kHz injected as a soft source on a line of grid points at 0.8 m from the cylinder axis at the closest.

Figure 5.13 shows snapshots of the simulated pressure field at different times. The scale is in dB and the total field is normalized to the peak value of the incident field. The last snapshot represents the state of the field at the end of simulation. This shows that the monochromatic pressure fields have been calculated with impulses with sufficient dynamics. Especially within the cluster where we can notice that the wave is in part almost trapped and released over a long time, appearing as low amplitude resonance tails in the pulse signals. At these positions, the ratios between the first and last peaks of the signal are at least 25 dB, while for positions on the edge of the domain presented, they are at least 45 dB.

Figure 5.14 shows the magnitude of the harmonic scattered pressure field relative to

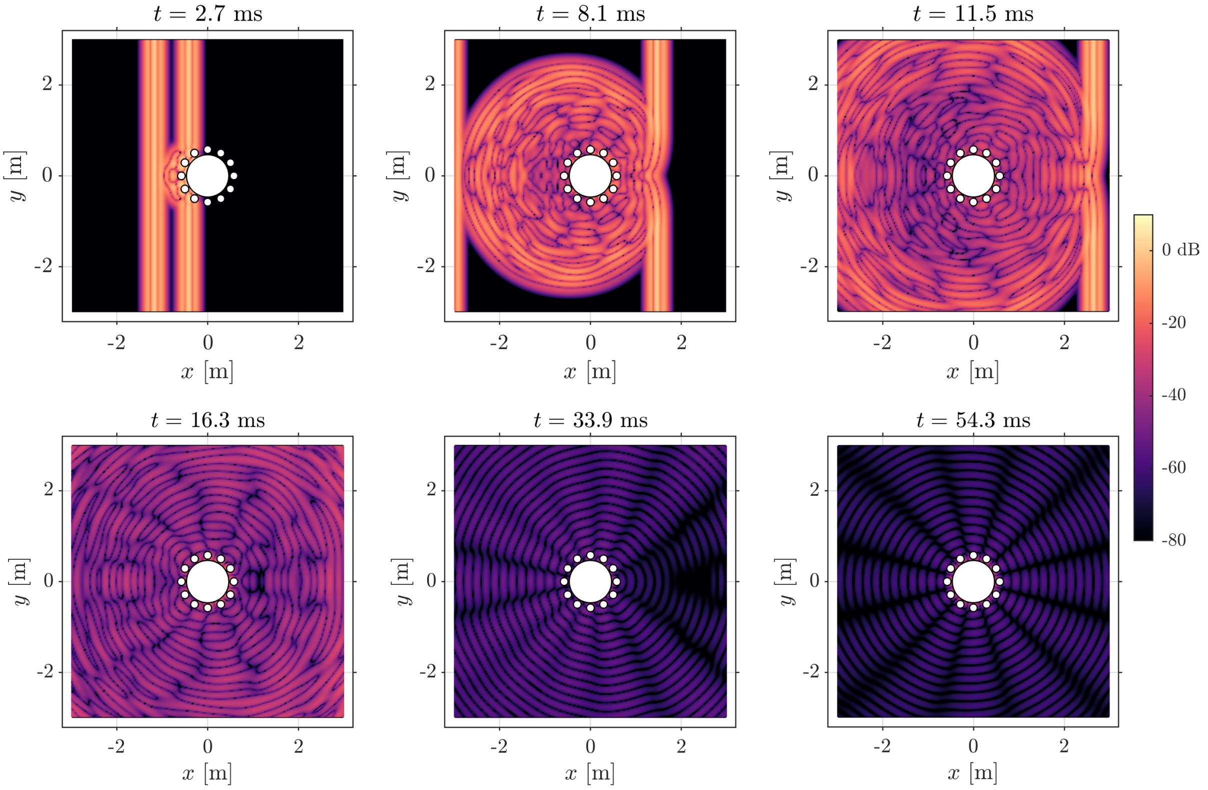

Figure 5.13 Snapshots of the total pressure field in time domain for a set of parallel circular cylinders under plane wave incidence.

the incident field, a plane wave traveling in the direction of the x-axis, at these frequencies for both methods in the near zone around the cluster. For the results figs. 5.14a and 5.14c from MuScat, the field is displayed from a polar grid with 300 radial and angular steps of about 10.4 mm and 1.2°, respectively. The field for the hybrid method uses 1:4 and 1:6 points in the horizontal and vertical directions of the hexagonal grid, resulting in a rectilinear grid with spatial steps 30 mm and 23 mm in the x and y-axis of figs. 5.14b and 5.14d. The figures show excellent agreement between the two methods. All the points in the FV mesh have been used for the maps, allowing to have the detailed field within the cluster. The BVD method allows to access the scattered field more easily in this part as the positions have their equivalent on the regular grid. If the CVD method is used, it requires to interpolate the field on the regular grid prior to subtraction. This can be achieved in time domain.

The polar diagrams shown in fig. 5.14e are derived from the positions represented by a dashed circle in fig. 5.14. For our method we used the closest points on the hexagonal grid. MuScat offers the possibility to compute the solution where the the wave scattered by a cylinder does not interact with the others, *i.e.* the single scattering (SS) represented by black dashed lines. The results for the multiple scattering (MS) are shown in black solid lines. Again, the two methods agree very well with slight differences where the scattered field is weak at 950 Hz between 40° and 60°. For these positions, the late resonances matter if an extreme accuracy is required.

This example provides eventually a cross-validation case of the two methods for the simulation of sound scattering by rigid circular cylinders. MuScat has already been compared to another method solving the wave equation in the case of scattering by soft cylinders and the results were in agreement too (Rohfritsch et al., 2019).

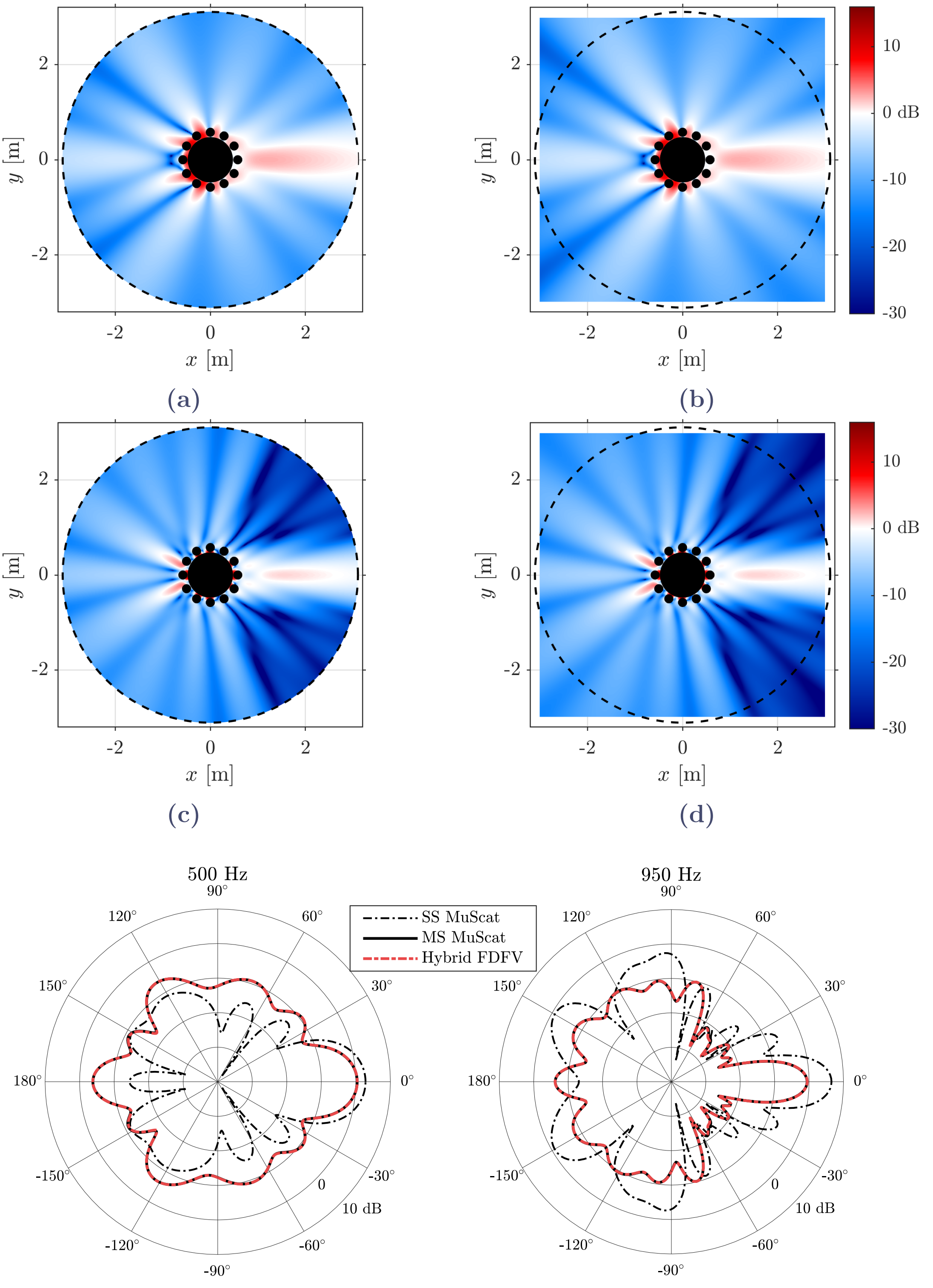

(a) (b)

(c) (d)

(e)

Figure 5.14 $20\log_{10}|p_s/p_i|$ at **(a, b)** 500 Hz and **(c, d)** 950 Hz for a cluster of circular cylinders obtained with **(a, c)** MuScat and **(b, d)** hybrid FDFV. The dashed circle represent the positions used for the polar diagrams **(e)** of $20\log_{10}|p_s/p_i|$ at 500 Hz and 950 Hz for MuScat with multiple (MS) and single (SS) scattering, shown with black solid and dashed lines, respectively, and hybrid method.

5.4.4 Far field and scattering cross sections

5.4.4.1 Near-Field to Far-Field Transformation

We recalled in section 2.4.2, eq. (2.52), that the scattered field due to the presence of an obstacle may be described by its scattering amplitude defined in the far field. To simulate directly the far-field propagation with a FD method, it would be necessary to discretize a large space which will increase the computational cost, moreover it suffers from numerical dispersion, as previously shown section 5.1.1.1, which deteriorates the signal as the propagation proceeds.

To avoid this and, nevertheless, benefit from one of the main advantages of the method which is the possibility to obtain results over a wide frequency range from a single simulation, there exist extrapolation methods for estimating the far field from knowledge of the near field. They are used in the field of electromagnetism for the characterization of antennas radiation in numerical simulations or physical measurements (Johnson et al., 1973) and are sometimes called near-field to far-field transform (NFFFT), *near-to-far-field* (Taflove et al., 2005), *near-field to far-field*, or *near-zone-to-far-zone* transformation (Luebbers et al., 1991) in the literature. In architectural acoustics, such method has been applied to characterize sound diffusers experimentally by Richard et al. (2019) or numerically, from simulation using a FDTD method, by Redondo et al. (2007).

These methods are usually based on the Kirchhoff-Helmholtz integral that relates the velocity potential at a given point to the velocity potential on a closed surface (or a closed contour in a two-dimensional space) that does not contain any source, which is the case for the scattered field. In this case

$$\mathit{\Phi}_s(\mathbf{r}) = \oint_{\mathit{\Gamma}} \left(\mathit{\Phi}_s(\mathbf{r}') \frac{\partial G(\mathbf{r}, \mathbf{r}')}{\partial \mathbf{n}} - \frac{\partial \mathit{\Phi}_s(\mathbf{r}')}{\partial \mathbf{n}} G(\mathbf{r}, \mathbf{r}') \right) d\mathit{\Gamma}(\mathbf{r}') \tag{5.88}$$

where $\mathbf{r}'$ is a point on the closed contour $\mathit{\Gamma}$, G is the Green's function to the Helmholtz equation, $\partial/\partial\mathbf{n}$ denotes directional derivative in the normal direction $\mathbf{n}$ to the closed surface.

5.4.4.2 Scattering cross sections

To validate the suitability and accuracy of the NFFFT to calculate differential scattering cross sections, we compare the results obtained by transformation with analytic solutions for a rigid circular cylinder.

The domain is similar to the one used in the convergence study, with the difference that in this case we record pressures and velocities at positions localized on a closed hexagonal contour centered on the axis of the cylinder. It is hexagonal here because the regular grid is also hexagonal, and therefore it is the simplest closed contour if it is build with adjacent points. Moreover, its roundness is higher than a equilateral triangle, which is the other simple regular closed contour on such a grid. Figure 5.15 shows a schemtatic of the computational setup used. The spatial step is $h = 5\,\mathrm{mm}$ and $c = 346\,\mathrm{m\,s^{-1}}$. The domain is meshed using the BVD method, resulting in a Courant number $C_r = \sqrt{2/3}$. The grid is excited with a Ricker pulse of central frenquency 2 kHz injected as a soft source on a line of nodes represented by red dots. PMLs are used along the x-axis, in the directions of propagation of the incident wave, and periodic boundaries are used to have a plane wave of infinite extension and prevent edge effects. With such boundaries, the domain can be seen as a flat torus. In the directions of the line of source nodes, along the y-axis, we do

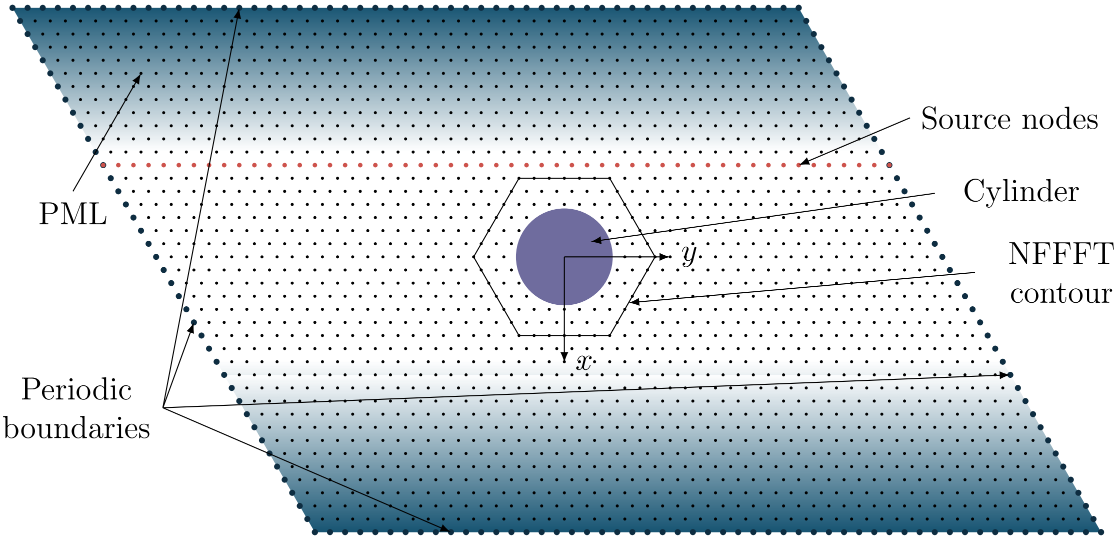

Figure 5.15 Computational setup for the numerical calculation of differential scattering cross sections via NFFFT.

not use any PML. Therefore, the length of the signals is controlled by the domain width, as the scattering event comes back from the other side when it encounters one where a PML is absent. On the contrary, with these periodic boundaries, it is theoretically possible to deal with periodic configurations of identical obstacles (Taflove et al., 2005), whose period is controlled by the width in this case. We make sure that the domain is long enough to record only one scattering event with sufficient dynamics on the contour nodes.

The gradient required for the transformation and to calculate the total scattering cross section σ by integrating the scattered intensity over a closed contour in near field, as given eqs. (2.55) and (2.59) is computed using eq. (5.38) at each time step. The pressure at 200 m around the cylinder is used to estimate the target strength.

Figure 5.16a shows the comparison of total scattering cross sections computed with the series solution and by integrating the time-averaged scattered intensities on the hexagonal closed contour. Graphically, the results are in agreement. Even with a band-limited pulse, the method seems able to estimate σ at the limits of the bandwidth. Figure 5.16b shows the relative absolute error of the hybrid method. Above 70 Hz, the error is less than 1 %. At 20 Hz, the relative error is about 33 %, which is due to the too short length of the signals to account for the complete scattering process at low frequency. However, this is in part where humans are less perceptually sensitive and where the scattering is weak, which make the characterization at these frequencies less critical for applications in room acoustics.

Figure 5.17 shows the comparisons of target strengths obtained with series solutions and the hybrid FDFV method via NFFFT. As the setup is symmetric, they are presented on a semicircle only, as functions of the scattering angle θ_s from 0° to 180°, divided in 200 positions. From 63 Hz to 2000 Hz, the results are in strong agreement with the theory. Consistently with the results for σ, we find some deviations at 32 Hz, especially at the minimum around $\theta = 62°$ where the difference is 0.9 dB. Similarly, at 4 kHz, 6 kHz, and 8 kHz, we find some differences at the minima up to 3 dB for the highest frequency. For the latter two, the monostatic target strengths ($\theta_s = 180°$) are poorly reproduced compared to the other directions that do not coincide with a notch, with underestimations of 0.7 dB

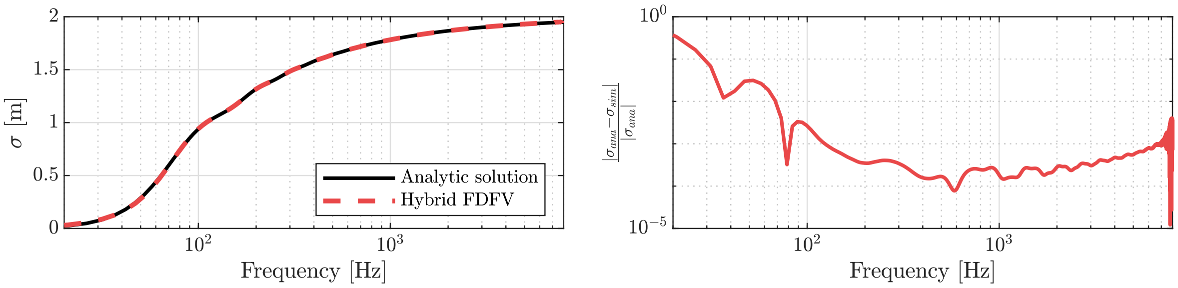

(a) **(b)**

Figure 5.16 Total scattering cross section σ for a rigid circular cylinder. **(a)** Comparison between series solution and hybrid FDFV. **(b)** Relative absolute error.

and 1.8 dB, respectively.

Li et al. (2005) also observed such reduction of accuracy for strongly forward scattering objects that they attributed to the fact that small numerical errors in these directions can pollute the results in the backscattering region. We examine to what extent this effect is present when NFFFT is applied to non-circular geometries that interest us here. For this, the monostatic target strengths of one of the studied cylinders are estimated as before and compared to those obtained using BEM in the frequency domain, that has the advantage of being able to simulate the far field directly without any impact on the computational cost. The implementation used is openBEM (update 5-2020) (Henriquez et al., 2010), a collection of open-source MATLAB functions allowing in particular to solve two-dimensional problems. The cross section of the cylinder is composed of two intersecting cylinders, one being smaller than the other, described in more detail in chapter 6 and represented in fig. 6.5b. The simulation parameters and the excitation source for the hybrid FDFV method are identical to those for the circular cylinder case. The domain is meshed using the CVD method resulting in a Courant number $C_r = 0.75$. NFFFT is applied to extrapolate the backscattered pressure at 100 m with respect to the centroid of the cross section. For the BEM, the boundary is discretized with at least 6 points per wavelength using linear elements. The pressure is simulated at the same distance as the one extrapolated via NFFFT, at the central frequencies of octave-bands from 63 Hz to 4000 Hz and at 5657 Hz, the upper band-edge frequency of the latter.

Figure 5.18 shows the monostatic target strengths obtained for two incidence angles $\theta_0 = 90°$ and 0° as functions of frequency. The results are in excellent agreement for both methods with differences lower than 0.1 dB below 4000 Hz for both incidences. For the highest frequency considered, the results obtained via NFFFT are slightly lower than those obtained with BEM with differences of 0.8 dB and 0.4 dB for $\theta_0 = 90°$ and 0°, respectively. Therefore, the proposed method with the chosen parameters allows to estimate far-field quantities with a certain confidence on the considered frequency range.

5.5 Discussions and conclusion

This chapter presented a time domain method to study the scattering by cylindrical obstacles in the context of airborne sound. The method is based on the joint use of FD and FV through hybrid meshes. An explicit FD scheme operating on a hexagonal grid is used for the main part of the domain for its good numerical performance in terms of

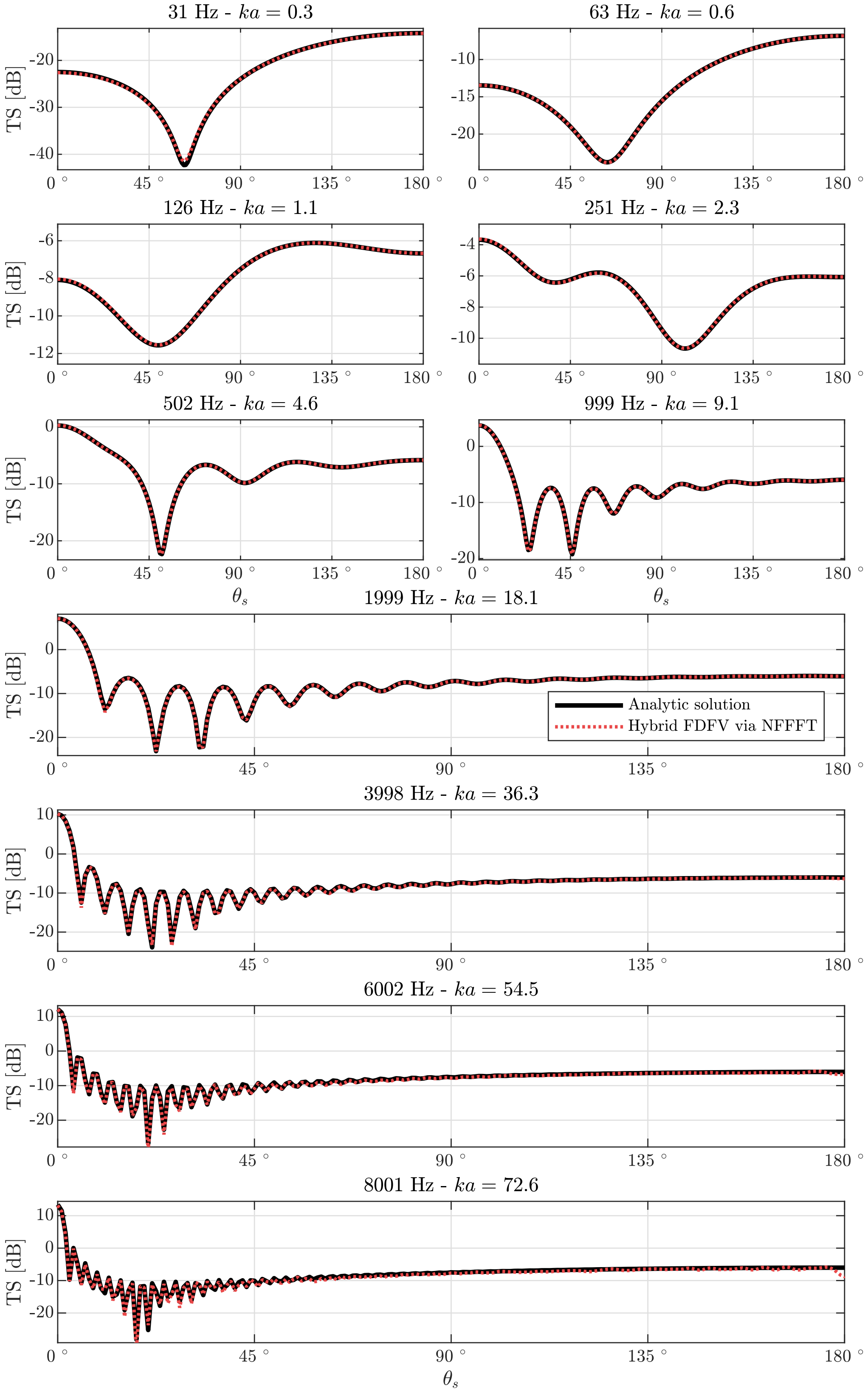

Figure 5.17 Target strengths as functions of the scattering angle θ_s at several frequencies for a rigid circular cylinder computed with series solution and hybrid FDFV via NFFFT.

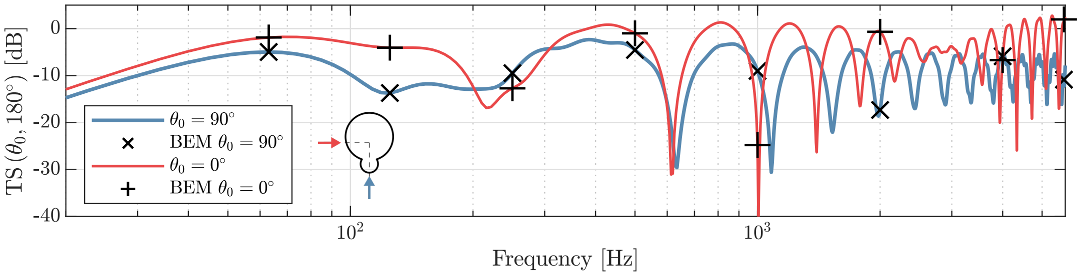

Figure 5.18 Monostatic target strengths as functions of frequency

dispersion and isotropy for a reasonable computational cost. The grid is modified in close vicinity of the obstacles to conform them, resulting in an unstructured mesh handled using the FV method, allowing to overcome the staircase approximation.

Two meshing methods have been tested. They are based on the Voronoi diagrams of the grid points surrounding the studied objects, bounded by their boundaries. To obtain a more homogeneous orthogonal mesh, it was proposed to apply Lloyd's algorithm to approximate a CVD. The method is able to relax the stability condition to the expected one if some cells of the mesh generated with the BVD method result in a stricter condition.

The methods were validated by comparisons with analytic solutions from scattering theory in the case of rigid and impedance circular cylinders. In addition, one of our geometries of interest, consisting of a cluster of parallel circular cylinders, served as a model for cross-validation in the context of multiple scattering problems. Furthermore, NFFFT was evaluated for the calculation of target strengths by comparison with analytic results for a rigid circular cylinder and with BEM for a more complex geometry, whose cross section consists of two intersecting circles, part of the cylinders studied in a more complete way in the following chapter.

Chapter 6

Sound scattering by Gothic piers and Classical columns

In old buildings, columns and piers[1] can be present in a large number for structural reasons. The elements that constitute them such as the capital and the shape of their shafts are often representative of an architectural style. In this chapter, we are interested in the sound scattering by different columns representative of two styles that have strongly marked the history of Western architecture: Classical and Gothic architecture.

Classical architecture is divided into several orders. The Doric and Ionic orders are studied to investigate the influence of the typical patterns they display on the column shafts. They are the first two orders that appeared in ancient Greece, and, therefore, these patterns are found in the later orders. The study of Gothic piers and columns is restricted to a selection among those found in the *Cathédrale Notre-Dame de Paris*, France, following historical-architectural criteria, since its construction lasted for several centuries. This is reflected in the shafts of various geometries that constitute it, representative of different styles following the long evolution of this architecture. They are also chosen for reasons of room acoustics, depending on their positions in relation to a listener and a source, or their frequency. This is further detailed in section 6.1, as well as background information on Classical architecture and the history of Notre-Dame construction.

The study of the sound scattering they induce is restricted to that of the shaft, being the major part of a column. They are considered to be rigid, which is consistent with the strong impedance contrast that exists between the air and the rocky materials that constitute the historic buildings. Measurements on scale models representing some of the selected geometries, are conducted and presented in section 6.2. They are long cylinders with scale factors ranging from 1:8.5 to 1:12. A subtraction method is used to isolate the scattered pressure for positions completely surrounding the obstacle, validated by comparisons with measurements on a rigid circular cylinder and the analytic solutions presented in section 2.4.1. The results for the geometries of interest are compared with that of simulations conducted with the numerical method presented in chapter 5. In section 6.3, the objects are numerically characterized in the far field using the scattering quantities to evaluate the scattering strength and its directionality. Eventually, the results obtained are compared to the thresholds of audibility for single reflections that have been reported in the literature in section 6.4.

6.1 Architectural cases

6.1.1 Classical columns

Classical architecture is derived from the architecture of ancient Greece and ancient Rome. During the Renaissance, the work of the Roman architect Vitruvius (1999) has

---

[1] In art history, a column refers to a support based on a circular section, while a pier is a generic term.

been rediscovered by Italian architects such as Alberti (2004) during the 15th century. It is divided into several orders that are distinguished according to the proportions used, but also by the type of column employed. In this work, to assess the influence of shapes on the sound scattering by such columns, we are interested in the Doric and the Ionic orders, as the particular patterns on the shafts of their columns, called the fluting, with grooves or channels extending along the height, known as flutes, can be found in the other later Classical orders.

In the Doric order, there are 20 flutes meeting continuously along an edge called the *arris* as represented in figs. 6.1a and 6.1b. Different rules can be found for their shape. Vitruvius (1999) indicates that the flutes describe arcs constructed as shown in fig. 6.1b at right, *i.e.* from the quarter of the circle inscribed in the square of side equal to the width of the fluting. This fluting is labeled **D2** in this manuscript. Alberti (2004) reports that this rule is more of a limit for the depth of the flutes. The flutes drawn in Vignola's plates are indeed less deep (Vignola et al., 2011). They are built from an arc of 60° as shown in fig. 6.1a. This rule is found in other latter architectural handbooks (Nicholson, 1823; Ware, 1904). It is labeled **D1**.

Ionic columns' shaft is characterized by its 24 *flutes* separated by a *fillet* as shown in figs. 6.1c and 6.1d. The shape of these grooves according to Vitruvius (1999) is a semicircle. He describes in fact Thales's theorem as represented in fig. 6.1d. This fluting is labeled **I2**. Plate 69 of Field et al. (1922) and Plate XV of Ware (1904) represent the Ionic columns of the Temple of Ilissus (Barrett et al., 1975). The drawing method described is the same that for a three-centered arch (Adams, 2015) as shown is fig. 6.1d. This shape is sometimes qualified as pseudo-semielliptic even though the intention of such a design was probably not to approach an elliptical arc (Huerta, 2007). It is labeled **I1**. The angular sector occupied by a fillet is fixed to be equal to a quarter of that occupied by a groove for both designs, but they can be found wider with a limit of one-third (Alberti, 2004; Perrault, 1996).

We give in the following some additional information on the history of these orders with examples of use to demonstrate that these particular patterns have crossed the millennia. The origins of the Greek Doric architecture, the oldest order, are a topic of debate that has been present for a long time and is still ongoing among archaeologists and art historians (Barletta, 2001; Howe, 2018; Jones, 2014). Influences from Egyptian architecture have been advanced (Betts, 1936). Similarities are found with polygonal columns such as those found at the site of Beni Hasan, which Champollion called proto-Doric, suggesting this link (Rosellini et al., 2003). However, it is more likely that each of the civilizations reached these patterns independently (Jones, 2014; Pratt, 1879).

Originally, these columns are present in the temples of ancient Greece, forming the outer part, the peristyle, with their colonnades but also in the inner parts, the naos and the sekos, of the largest temples. They were made from local stones, most often with limestones and rarely in marble (Wycherley, 1974). We can mention the *Parthenon*, representing the apogee of the Doric order, built around 440 BC, or any other temple of the Athenian Acropolis such as the *Erechtheion* and the *Temple of Athena Nike*, which are of Ionic style. The Romans were largely inspired by these orders to form their own, the Tuscan and the Composite orders (Chitham, 2014; Ware, 1904). Beyond the temples, others buildings integrated colonnades in their structure like the civil basilicas, multi-purpose public buildings installed near a forum serving as a gathering place, business negotiations, and the administration of justice in particular (Ginouvès et al., 1998). We can give the example of the one of Aphrodisias (fig. 6.2), an archaeological site in Caria,

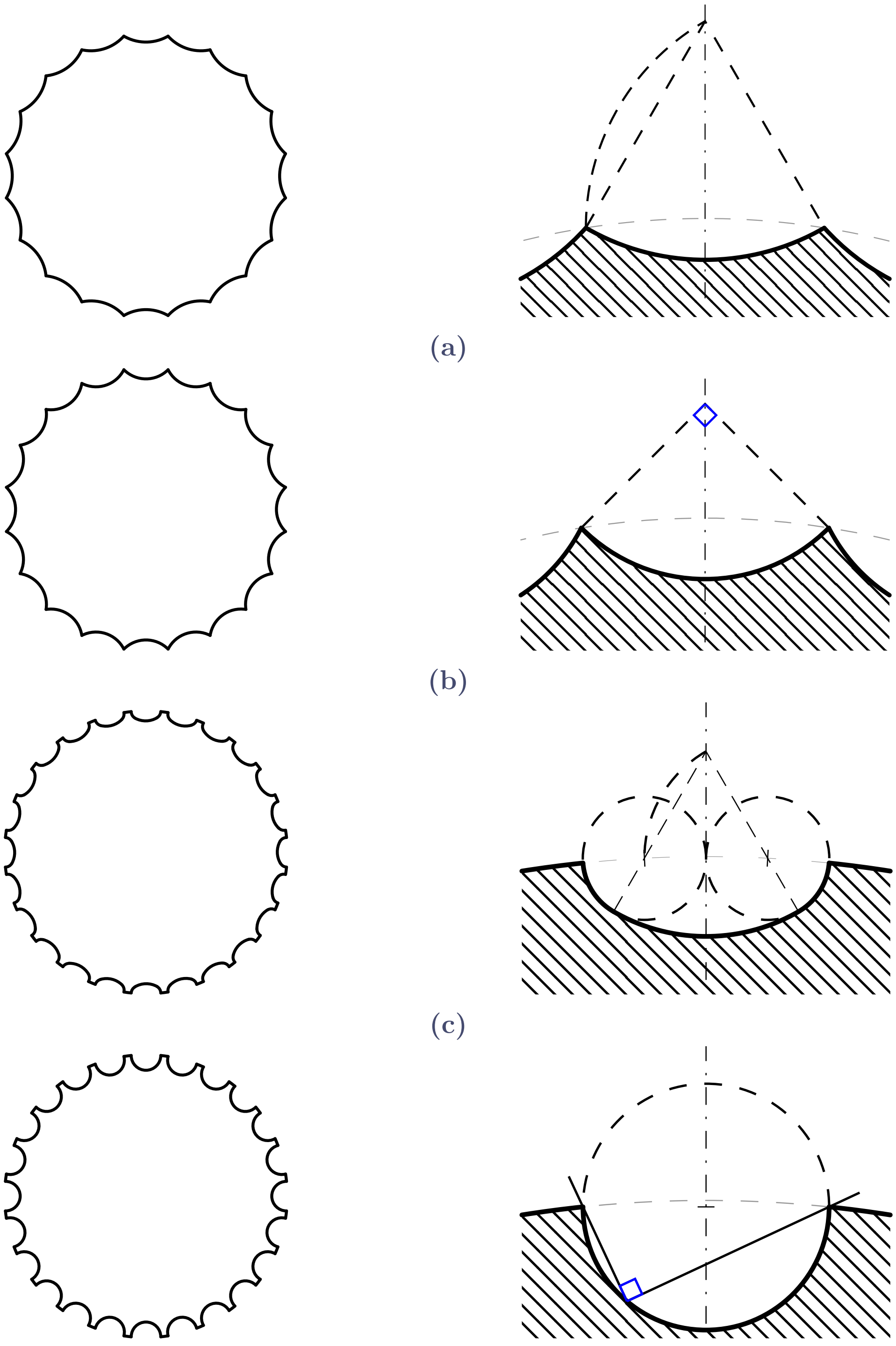
(a)

(b)

(c)

(d)

Figure 6.1 Cross sections (left) and method of drawing for the fluting (right) for (a) **D1**, (b) **D2**, (c) **I1**, and (d) **I2**.

Turkey, inscribed on the UNESCO World Heritage List in 2017 (Erim, 1988; Smith, 2019; Stinson, 2016). The building was about 145 m long in total and 30 m large, with a long main hall covering more than three quarters of the length composed of a central nave and two side aisles separated by two-storey colonnades from Ionic and Corinthian orders.

The Renaissance is a period of transition between the Middle Ages and the modern era in Europe, which began in Italy during the 14th century. The scholars rediscovered the

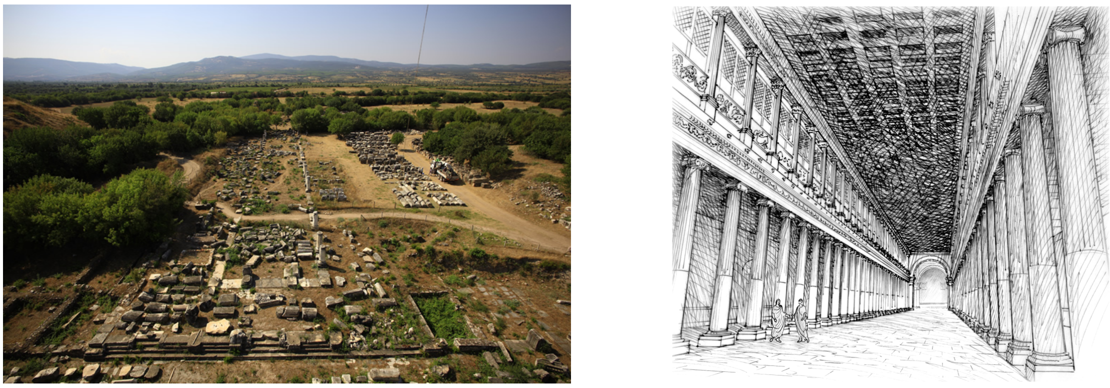

(a) (b)

Figure 6.2 Civil basilica of Aphrodisias. **(a)** Photograph by E. Küçük of the site *ca.* 2012, reprinted with permission of New York University Excavations at Aphrodisias. **(b)** Reconstruction by Stinson (2016), reprinted with his permission.

philosophy and the arts of the Greek and Roman Antiquity, which appeared to them as a golden age. Its architecture succeeded the Gothic style and integrated the principles of the ancient classical orders, interpreted and theorized by Alberti (2004) and Serlio (1560), in particular. One of the most emblematic buildings is the *Papal Basilica of Saint Peter* in the Vatican, whose construction began in 1506. It has Ionic columns in its narthex, but not in its nave, however, Corinthian pilasters, that have the same fluting, are used to decorate the piers and the responds[2] (Lotz et al., 1995). Overall, this period participated in the development of what is formally called Classical architecture that occupied the 17th and 18th centuries.

This style reappeared again in the second half of the 18th century in the form of what is called Neoclassical architecture, succeeding the Baroque and Rococo styles. As famous examples, there are the *Pantheon* and *Église Sainte-Marie-Madeleine (La Madeleine)* in Paris, France, which both have Corinthian columns and pilasters. *Église Saint-Philippe-du-Roule* was built at the end of the 18th century. It is designed according to a basilica layout with a central nave covered by a barrel vault supported by Ionic colonnades. The *Église Saint-Symphorien* in Versailles, France, was build during the same time and has a similar design but with Doric colonnades. It is interesting to mention that many cathedrals or churches renovated during this period incorporated fluted columns. The *Nikolaikirche* in Leipzig, Germany was built in 1165 in a Romanesque style, but its interior was fully redesigned in 1795 by the architect Johann Carl Friedricg Dauthe, who integrated Ionic colonnades in the nave. The *Catedral de la Santa Cruz de Cádiz* in Spain was originally designed in the Baroque style, but many Rococo and Neoclassical elements were added during its construction from 1722 to 1838. In Paris, France, the *Église Saint-Nicolas-des-Champs* was built during the 15th century in a Gothic style qualified as *flamboyant*, but during the 18th century, Ionic columns replaced those of the choir, and some were surmounted with Ionic pilasters. The *Protestant Temple of Saint-Eloi of Rouen* in France, was a former Catholic church built in the 13th century in Gothic style. Its interior was redesigned in a Baroque style by the architect Jean-Jacques Martinet, who changed the nave columns with Doric ones during the 18th century. Beyond Europe, this style was

---

[2] Respond: Half-pier or half-column embedded in a wall.

exported to the United States of America with a great success and gave birth to what is sometimes referred to as the Federal order. References to antiquity are found in official buildings, *e.g.* the *Lincoln Memorial* inaugurated in 1922 or the *Capitol* in Washington D.C. The columns could then be immense and wide such as in the interior of the *Old Pennsylvania Railroad Station* in New-York City, where Madison Square Garden is now located.

6.1.2 Gothic columns of Notre-Dame de Paris

The Gothic piers and columns are studied through the *Cathédrale Notre-Dame de Paris* that is of particular importance for the history of music. It was the cradle of what is called by the historians the "École de Notre-Dame", a polyphonic singing style that was developed between 1170 and 1250 by various composers (Duhamel, 2010). Musical manuscripts such as the *Magnus Liber Organi* (Roesner, 1993) or texts (Anonymous IV et al., 1985) testify to this intense musical activity. The following period known as the *Ars Antiqua*, until 1320, corresponds to the moment when it gradually lost its musical supremacy to other places that were more attractive to the talented composers of the time. During the *Ars Nova*, the period that followed until 1380, the episcopal school refocused on teaching the liturgy and maintained eight choirboys to restore a certain level of musical quality. A permanent choir organ was installed around 1334 according to a historical document citing the name of Jean de Bruges as the first organist (Wright, 2008). The first tribune organ was built between 1403 and 1415 by Frederic Schambantz. The choirmasters enjoyed a growing reputation, notably Antoine Brumel nominated in 1498, bringing with him Flamish influences. Moreover, the choirboys were increased to 12 members in 1550. Their reputation was such that the Cardinal of Guise tried to kidnap the student Claude Ruffin in 1576, moved by his voice (Chartier, 1897). In the centuries that followed, the reform of the liturgy relaxed the musical rules of the services. It allowed the masters and the organists a freedom of style and creation. In the modern era, the reigns of Louis XIII and Louis XIV were a period of prosperity for the arts in which the cathedral was strongly involved. It offered musicians a listening space open to all, at a time when public halls did not exist.

6.1.2.1 Architectural-historical description

The construction of the *Cathédrale Notre-Dame de Paris* began in 1163 under the responsibility of Maurice de Sully, bishop of Paris. Figure 6.3 shows the principal phases of construction. The first part to be built was the choir, completed in 1182. At this date, the western wall of the transept was already erected. The choir had a double ambulatory and tribunes like nowadays, but did not have its radiating chapels yet. The elevation of the nave started in 1180 while the vaults were missing in the choir. Several construction campaigns will have been necessary for the western part of the cathedral to be completed. The first bay of the nave, connecting it to the facade composed of the bases of the towers, was completed around 1220. While the construction of the towers continued, changes were made to the building from 1225, following a fire between the roof and the vaults according to Viollet-le-Duc (Sandron et al., 2020). At that time, the work had already been going on for more than 60 years, a period during which the techniques of masonry were refined at other sites. Thus, the hypothesis that, by rivalry with other dioceses building cathedrals at the same time, the bishop would have decided to bring it up-to-date has also been advanced (Sandron et al., 2020). The main roof was raised with the

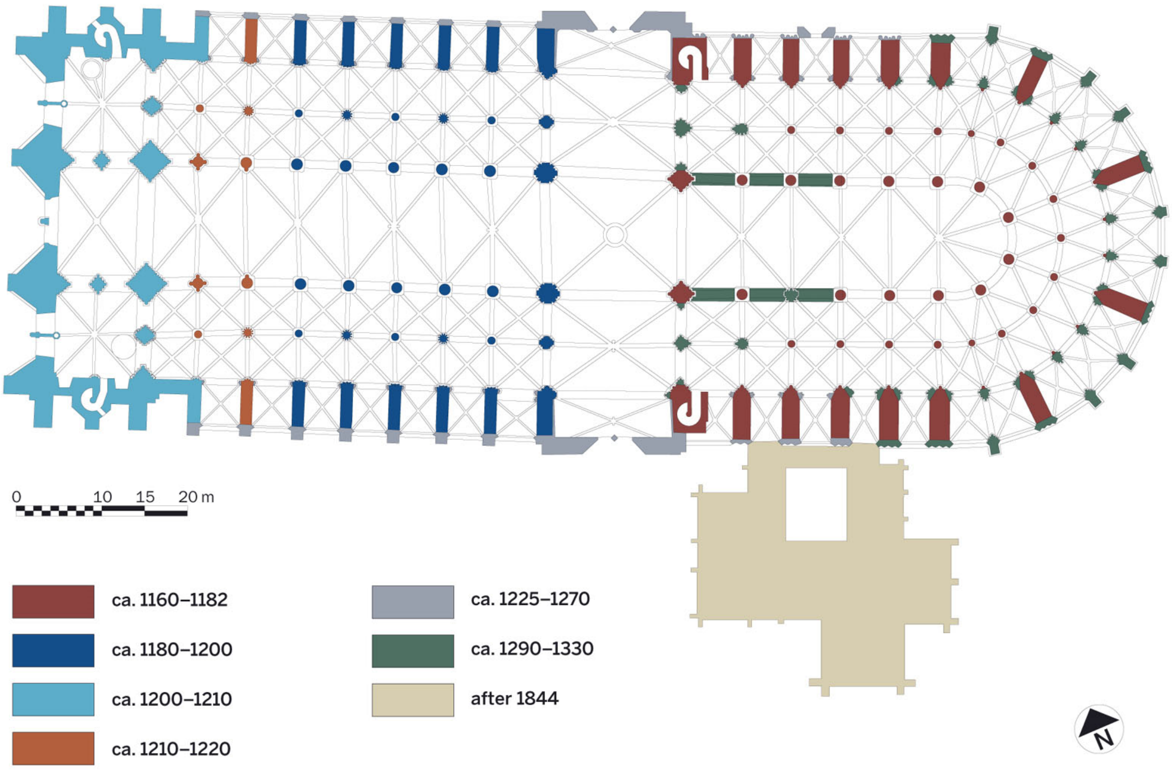

Figure 6.3 Plan of Notre-Dame de Paris with principal phases of construction. Retrieved from Sandron et al. (2020).

addition of a wall around the entire perimeter, allowing a uniform height from the choir to the nave and the windows of the clerestory[3] were doubled in height. The towers were completed around 1240, at the same time that the lateral chapels were added to the nave. Around 1250, the rose window of the north arm of the transept, extended by one bay, was built by the master mason Jean de Chelles and that of the south, added 10 years latter, is attributed to his successor, Pierre de Montreuil. In the meantime, a wooden spire was added above the crossing. The radiating chapels were built between 1290 and 1330 under the supervision of Pierre de Chelles and his successor, Jean Ravy. The latter was responsible for the construction of the jubé surrounding the liturgical choir, later completed by his nephew and successor, Jean le Bouteiller.

It took almost two centuries for the cathedral to reach a shape close to the one we know today and it is only from the seventeenth century that modifications were made to the interior, except maintenance operations. In 1622, Paris became a archbishopric and for the occasion, Queen Anne of Austria commissioned François Mansart, king's architect, to rework the jubé with marble and include a Virgin and Child in niches. During the Vow of Louis XIII in 1638, it was announced that the choir would be restored. It was only from 1708, under the reign of Louis XIV, that this work began. The design is attributed to the king's chief architect, Jules Hardouin-Mansart, but dying in 1709, the construction was mostly undertaken by his successor and brother-in-law, Robert de Cotte who completed it by 1723. The stone jubé was replaced by a gilded forged-iron fence. The piers of the hemicycle were covered with panels of colored marble and the pointed arches were transformed in round ones. The still present polychromatic marble pavement, Pietà and

---

[3] Clerestory: Upper row of bays of a nave located above the triforium and the tribunes.

oak stalls are also from this period sometimes qualified as Baroque transformation.

After the French Revolution, the building was requisitioned and rededicated Temple of Reason on November 10, 1793. It returned to the clergy less than 10 years later, on April 10, 1802, in a more deteriorated state than it already was. During the 1830's, the historian and politician, François Guizot, aware that national history could be a powerful means to federate the population, initiated a cultural heritage policy. He created the position of inspector general of historical monuments. The inspector appointed in 1834, Prosper Mérimée, entrusted the prefects to establish a list of historic buildings that they considered to be priorities for protection and renovations in their department. In this context, the Minister of Religious Affairs, Pierre Dessauret, received a petition to preserve the cathedral which led to a tender for a renovation project. In 1843, Lassus and Viollet-le-Duc won (Lassus et al., 1843), being the only ones to submit on time. Their wish was to return to a state closer to the cathedral's origins. They removed some of the additions from the Baroque period but renovated some of them, such as the pavement. They rebuilt a spire above the crossing in imitation of the 13th century one that had to be dismantled at the end of the 18th century because it showed signs of fragility and was in danger of collapsing. Oculi were introduced at the level of the triforium[4] on the walls of the transept, on the last bay of the nave and the first of the choir. These renovations, lasting for almost 20 years, were conscientiously consigned in a daily work journal (MPP, 2021).

6.1.2.2 General acoustics

The cathedral suffered a major fire in April 2019. However, measurements were taken almost 4 years earlier (Postma et al., 2016). The reverberation time T_{20} measured at that time was about 7 s at 500 Hz. We conducted additional measurements after the fire in 2020 (Katz et al., 2020b). Among the damages, several vaults collapsed, including the one at the crossing, leaving large openings. The reduction in reverberation time was estimated to be 20 % on average. These measurements have allowed the calibration of a geometrical acoustic model that can be modified with historically informed data to estimate the acoustics of the building in past states (Canfield-Dafilou et al., 2022; Mullins et al., 2022), allowing then to study the influence that these could have on the musical practices.

6.1.2.3 Columns and piers of interest

The many successive construction and renovation campaigns can be seen in part through the geometry of the many piers and columns in the cathedral (fig. 6.3). The study of the plinths, bases, and capitals contributed notably to the sequencing of the building site (Bruzelius, 1987). In total, 7 geometries were retained according to architectural criteria such as their location or frequency and historical criteria such as their place among the different Gothic styles or their links of influence with later or earlier architectural styles. The groups of columns they define are shown in fig. 6.4 with a label attributed to each. There are 5 compound piers, consisting of a core flanked by engaged columns and/or pilasters. These elements extend the arches and ribs to take some of their loads and articulate the structure vertically. These principles were already used in Romanesque architecture (Hoey, 1989; Thurlby, 1998). Their section is formed of a single closed shape. This distinguishes them from the piers with *colonnettes* where long thin

---

[4] Triforium: Narrow level below the clerestory.

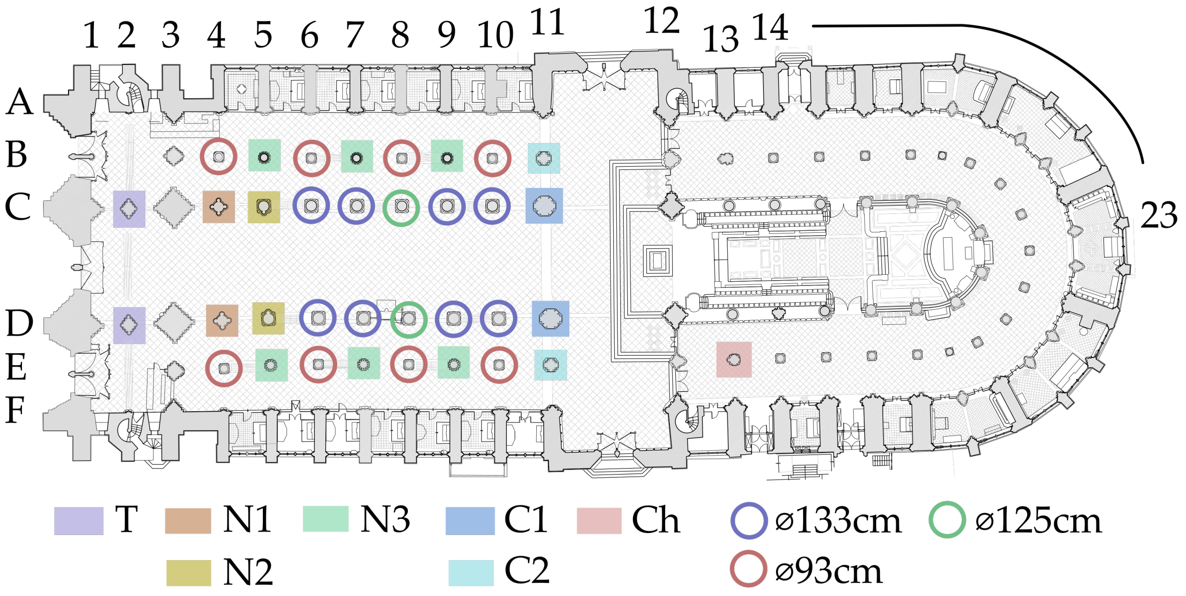

Figure 6.4 Floor plan with piers, columns, and responds locations indicated by the row (A-F) and column (1-23) grid. The shafts of identical cross section from the selection are highlighted with a common color. The columns of the nave with circular shafts are indicated with a circle.

en-délit circular columns flank without contact a central part, in this case they have a decorative function; 2 were selected. They are all located in the nave, except one. The columns with circular sections present in this part of the cathedral are also indicated in fig. 6.4 with their diameters. The piers that are not retained, *i.e.* not colored, are globally formed with shafts of similar geometries. Their cross sections are included in appendix C.

The shafts are in Lutetian limestone. Although not perfectly smooth, Vázquez et al. (2016) measured an average surface roughness of 40 µm on a sample from the Gothic church *Notre-Dame de Vetheuil*, whose construction began in the 12th century. In the cathedral, while the stones were bare during the first centuries like today, they were actually painted from the middle of the 14th century until the end of the Baroque period (Sandron et al., 2020), probably leading to an even smoother surface.

Figure 6.5 shows the cross sections of the studied shafts with their dimensions given in cm. They were drawn based on orthoimages extracted from the interactive 3D visualization environment developed by the working group of the scientific project for the restoration of the cathedral[5]. This numerical tool integrates the 3D point clouds obtained by several laser survey campaigns conducted notably by Andrew Tallon in 2010 (Sandron et al., 2020) and also by the company Art Graphique et Patrimoine (AGP) just after the fire of April 15, 2019.

Compound piers The first bay of the nave, connecting it with the frontispiece, was built last (see fig. 6.3). It resulted in specificity on its columns because more stiffness was needed in this part according to Bruzelius (1987). The shafts **N1**, located at C/D4,

---

[5] This tool was developed by members of the *Modèles et simulations pour l'architecture et le patrimoine* (MAP) laboratory in the framework of the *Données numériques* working group of the scientific project, supported by the *Centre National de Recherche Scientifique* (CNRS) and the *Ministère de la Culture* (CNRS/MC, 2019).

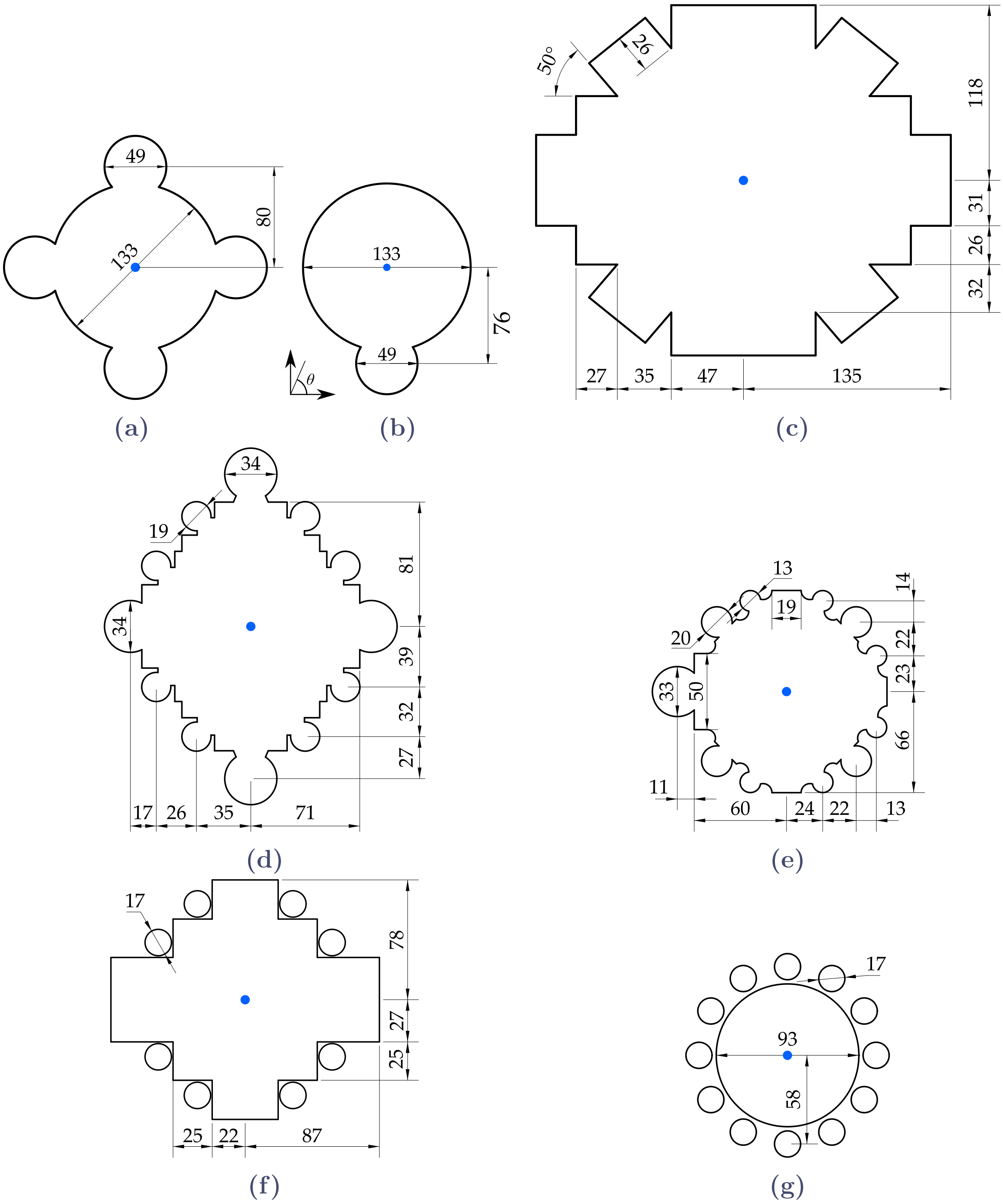

(a) (b) (c) (d) (e) (f) (g)

Figure 6.5 Cross sections of the selected shafts. Piers of the western bay of the nave, **(a)** **N1**, **(b)** **N2**. Western crossing piers **(c)** **C1** at the arcade level. Piers **(d)** **T**, supporting the tribune between the towers. Pier **(e)** **Ch** in the southern ambulatory. Piers with detached colonnettes **(f)** **C2**, western wall of the transept, and **(g)** **N3**, nave aisles. Dimensions are given in cm.

are engaged with four circular colonnettes on a circular core as shown in fig. 6.5a. Just besides, the piers **N2**, located at C/D5, are engaged with a single one (fig. 6.5b). Their central parts are of the same diameter as the other columns of the nave arcades, except the columns at C/D8 that follow the principle of strong and weak piers as their diameter is

125 cm. The colonnettes are engaged by less than a quarter of their diameter, penetrating 11 cm and 15 cm, respectively. This type of circular lobe shaft is also found engaged in every responds. They are *piliers cantonnés*, a type of pier already used in Romanesque architecture where massive rectangular piers are flanked by semicircular columns as with *Église Saint-Étienne de Caen* in France, *Catedral de Santiago de Compostela* in Spain, or *Hohe Dom St. Martin zu Mainz* in Germany. Geometries similar to these two couples may be found in other High Gothic cathedrals as with the naves of *Notre-Dame de Chartres* and *Notre-Dame de Reims*, or in the choir of *Notre-Dame de Noyon*. They are more robust variations of the columns known as "*soissonnaises*", which first appeared in the *Cathédrale de Soissons*, where a single colonnette is engaged in a circular core on the part facing the nave and rises to the vault (Klein, 1999).

The transept crossing piers on the nave side **C1**, located at C/D11, are among the selected geometries. They are actually the union of several pilasters, each one receiving a transverse or diagonal rib of the nave or crossing vaults. At the arcade level, this results in an asterisk-shaped section as shown in fig. 6.5c. They are the largest piers of the selection, and, with the two previous ones, they directly surround the nave where listeners are located.

Typical of Gothic architecture, it is also found in the cathedral, compound piers formed by a cluster of coursed shafts shaped with relatively thin engaged circular parts that extend vertically the arcs and the ribs of the vaults. The supports of the towers, located at C/D3, are built with this method. Their sides facing the central vessel extend up to high capitals at the base of the sexpartite vaults, forming a diffusing surface close to the Grand Organ. This is also the case for its intermediate piers. The piers **T**, located at C/D2, are selected to study the influence of such shafts. Figure 6.5d shows the cross section. At each corner of the diamond shape is engaged a wider column of diameter 34 cm and, on the sides, there are alternately right corners and engaged colonnettes of diameter 19 cm. This pattern is repeated on the wall and outer aisle responds, between each chapels, of the choir (Murray, 1998).

The eastern transept crossing piers, located at C12 and D12, on either side of the current altar, are the oldest of the building with such shafts. When the chapels of the choir were nearly completed, Pierre de Chelles renewed the eastern wall of the transept around 1315 (Davis, 1998), introducing foliate gables to the arcades of the ambulatory entrance and the piers located at B12 and E12 were modified. The North and South parts are different, the second, probably built in first, is less massive and less prismatic. Their shapes are similar to those of the intermediate piers of the chapels, located from A18 to A23, as well as the responds located in the outer direction to them, at the back of the chapels, and their couterpart in the southern half. As in Early Gothic, the shafts have engaged columns and colonnettes. However, we find some cross sections that reveal a more advanced Gothic style, closer to the *flamboyant* Gothic style. Here the corners are no longer all straight as de Chelles introduced curved faces between the flanking colonnettes. The piers, located at B13 and E13 in the ambulatory, and the second one of the south side arcade, located at D14, were also built around this moment, and are similar. Around this time, structural problems led to ruptures in this region and circular piers were replaced. It is not clear who led these repairs (Davis, 1998). The pier in the southern part of the ambulatory is selected to study a shaft more representative of a latter Gothic style. It is labeled **Ch** and its cross section is shown in fig. 6.5e.

Piers with detached colonnettes en délit The use of *colonnettes en délit* is widespread in the cathedral. They divide the tribune openings, in two in the choir and in three in the nave, except in the first bay. They are in the responds of the nave, in the central vessel from the clerestory to the tribunes, extending in a uniform way the ribs of the sexpartite vaults and in the outer aisles. They are 17 cm in diameter. This principle is found at the arcade level on the columns **C2**, located at B/E11, at the entrance of the double aisles at the western wall of the transept. Their cross section is represented in fig. 6.5f. The prismatic piers formed by the union of the arcades and vaults dosserets[6] are supplemented by detached colonnettes at each re-entrant corner separated by a distance of 1 cm.

Separating the double aisles, every other circular pier **N3**, located at B/E5/7/9, is surrounded by 12 detached colonnettes as shown in fig. 6.5g. Viollet-le-Duc (1859) explained this difference with the single circular cylinder neighbors by considerations of structural strength and stability. In particular, since these piers are in line with the most heavily loaded columns of the nave, they had to take the load of the buttresses which existed before 1220 and allowed to counter the thrust from the sexpartite vaults. However, this has been challenged by Murray (1998), and Viollet-le-Duc (1859) himself acknowledged that they have a decorative function when installed at the responds after settlement of the building. A couple are also included among the coursed shafts that form the piers supporting the towers located at B/E3. Many examples of such elements can be found in other cathedrals at the time, including, not exhaustively, the cathedrals *Notre-Dame de Noyon*, *Saint-Étienne de Bourges*, *Notre-Dame de Dijon*, and *Notre-Dame de Laon* (Fernie, 1987). Their use facilitated the way in which the walls are vertically articulated with the vaults compared to coursed shafts with circular shapes as in the choir responds. They could be manufactured in mass by standard processes while the walls were built with stones cut in regular rectangular shape (Olson, 2004). The piers surrounded by colonnettes are also at the origin of a whole architectural style in England (Bony, 1949). We can give the examples of the Canterbury Cathedral, the Lincoln Cathedral, or the Salisbury Cathedral where the colonnettes are in marble of a different color from the central part (Hoey, 1987).

6.2 Experimental measurements of scattering

We have seen in part I that physical scale modeling is a very useful tool for the validation of numerical methods. The different geometries of interest have been reproduced to measure experimentally their scattering.

6.2.1 Methods

6.2.1.1 Scale models

The scattering of the different geometries was measured experimentally on 1:12 to 1:8.5 scale models. They are for the most part made of an assembly of long rigid PVC tubes and/or dense wooden boards and cleats as shown in figs. 6.6c to 6.6f. The detached colonnettes are positioned at the right distance from their core with the help of wedges. Their total length is about 2 m. Both models of compound piers with clustered engaged

---

[6] Dosseret: Pilaster used as a straight jamb for an arch.

shafts, as well as the fluted columns, are made of staff. The fresh material is spread in successive layers with a comb whose shape is the negative of one symmetric part of the section. These parts are attached together to form the cylinder as shown in figs. 6.6a and 6.6b. They are eventually painted to protect them from desiccation and crumbling, as well as to further decrease the surface roughness. Those are 1 m long. The scale of the fluted columns is set so that the circle circumscribing their cross section is 1 m in diameter at full scale. The resulting scale factors for each is given in table 6.1. **D2** has not been built as it is not very different from **D1**, but it is numerically characterized.

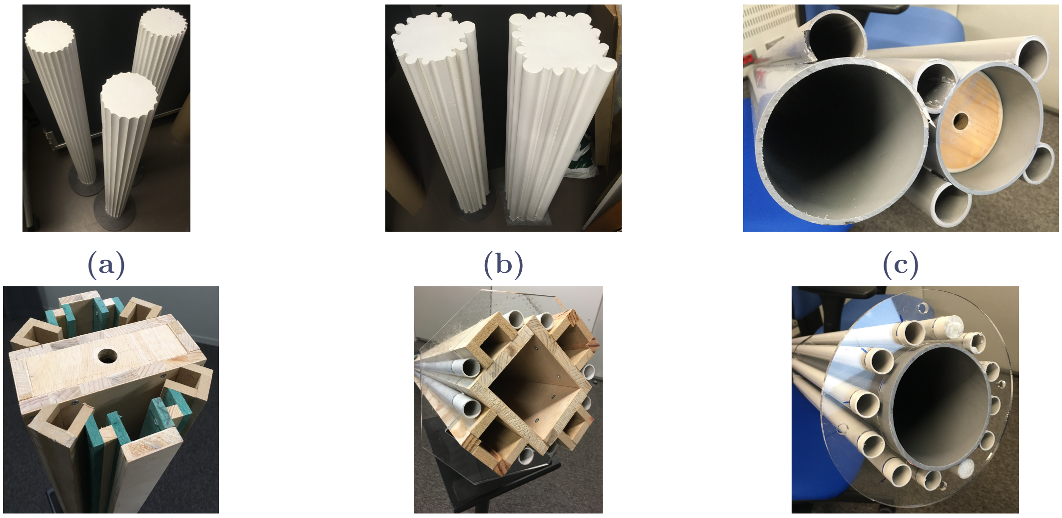
(a) (b) (c)
(d) (e) (f)

Figure 6.6 Photographs of scale models of the piers and columns. From left to right: (a) **I2**, **D1**, and **I1**. (b) **Ch**, and **T**. (c) **N2**, and **N1**. (d) **C1**. (e) **C2**, (f) **N3**.

6.2.1.2 Measurements

The scattered pressure they induce is measured experimentally with a subtraction method similarly to the procedure used to characterize surface diffusers. For each configuration tested, involving a geometry and an angle of incidence θ_0, a series of measurements with then without the cylinder have been made taking care not to change the positions of the source and the receiver during the removal.

The measurements were carried out in the anechoic chamber of Sorbonne Université (fig. 6.7). The sound field was measured on a circular arc around the cylinder. For that, a microphone was attached to an articulated arm allowing for positioning in space, which was mounted on a turntable (Brüel & Kjær Turntable System Type 9640). The cylinders were positioned on a platform above the turntable that was not in contact with it to allow the arm with the microphone to rotate around. In practice, the legs of the support platform prevented measurement for about a quarter of a circle (fig. 6.7b). Since all diffusers have at least one plane of symmetry, recording the signals on an arc greater than a semicircle that includes the forward and backscattering positions allows for full measurement of the scattering in the case where the source is included in this plane of symmetry and orientated towards the center of the scatterer.

The source was a 20 mm diameter dome tweeter (Audax TM020G3) driven by an amplifier (Samson Servo 120a) positioned at a corner of the chamber as may be seen on

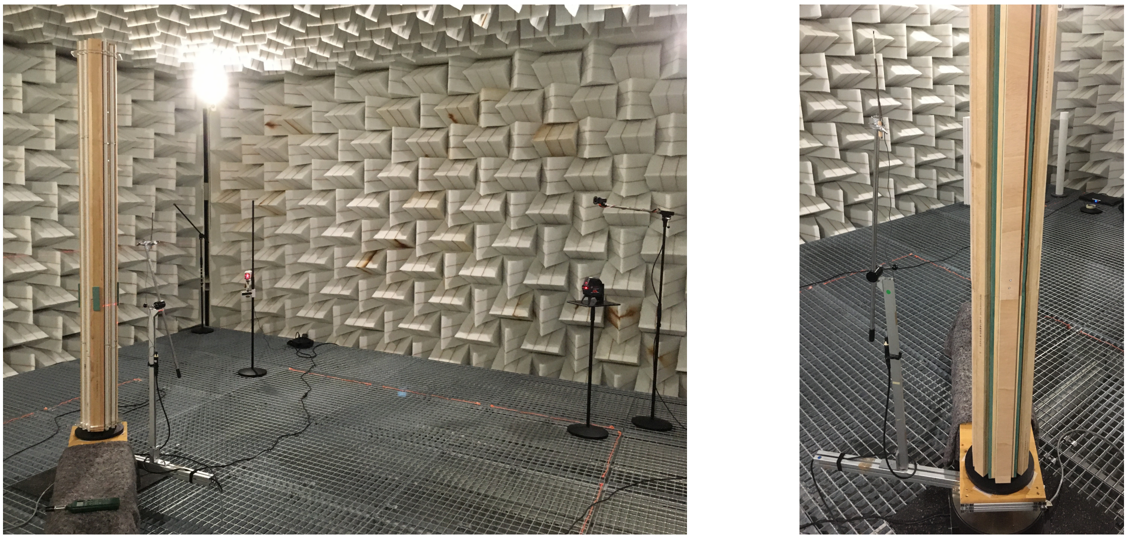
(a) (b)

Figure 6.7 Photographs of the experimental set-up. **(a)** Overview with the sound source on the right. **(b)** Close view with the platform, the turntable and the microphone mounted on an articulated arm.

the right of fig. 6.7a. The signals were recorded using a miniature microphone (Feichter Audio M1). Its axis was parallel to the cylinder axis to minimize variations due to its directivity. All were connected to an audio interface (RME Babyface) configured at a sample rate of 192 kHz. The exponential swept sine method (Müller et al., 2001) was used with signal spanning frequencies from 2 kHz to 95 kHz over 3 s. The exploitable frequency band has been identified from 2 kHz to 30 kHz, limited by the source, with a drop in SNR at 20 kHz. The measurements were carried out with an angular step of 5° and the emission and acquisition of signals as well as the control of the turntable were performed with MATLAB 2020a through an automatic procedure. The source, the microphone and the cylinder were positioned with the help of laser levels visible in fig. 6.7a. The temperature and humidity have been measured in the experimental room for each series to estimate the speed of sound using the formula of Rasmussen (1997). The different set-ups and the estimated c are summarized in table 6.1. The shortest distance from the source to the columns is nearly 3 m, well beyond the Rayleigh distance of the source, $\pi a_{\mathrm{source}}^2 f/c$, where a_{source} is the source radius, at any frequency f.

6.2.1.3 Post-processing

For each configuration tested, involving a geometry and an angle of incidence, a series of measurements with then without the cylinder have been made taking care not to change the positions of the source and the receiver during the removal. Figure 6.8a shows the impulse responses obtained for one position for a rigid circular cylinder present and absent. It is then possible to isolate the scattered pressure by subtracting the incident pressure to the total pressure recorded respectively without and with the cylinder present. This method is very sensitive to variations of environmental conditions. Changes in temperature and humidity in the chamber, microphone positioning or response of the equipment due to electrical deviations and Joule heating cause disparities in time and

---

[1] Represented by a blue dot in figs. 6.5a to 6.5g

Table 6.1 Experimental set-ups and parameters for the measurements on scale models with the Courant number λ used in each corresponding simulation.

Label (fig.)	**Scale factor**	**Incidence angle** θ_0	**Distance from center**[1] **Source** [cm]	**Receiver** [cm]	c [m s^{-1}]	λ
D1 (6.1a)	1:10	9°	31	291	346.0	0.746
I1 (6.1c)	1:10	0°	31	296	346.0	0.761
I2 (6.1d)	1:10	0°	31	289	346.2	0.744
N1 (6.5a)	1:12	90°	32	307	345.7	0.751
		45°	32	307	345.8	0.731
N2 (6.5b)	1:12	90°	31	307	346.2	0.755
C1 (6.5c)	1:12	0°	32	306	345.7	0.753
		90°	32	306	346.2	0.742
T (6.5d)	1:10	90°	31	319	346.1	0.744
Ch (6.5e)	1:10	0°	31	319	346.5	0.743
C2 (6.5f)	1:8.5	90°	33	307	346.1	0.753
		0°	33	307	345.9	0.739
N3 (6.5g)	1:8.5	0°	33	338	346.6	0.745
		15°	37	317	346.6	0.762

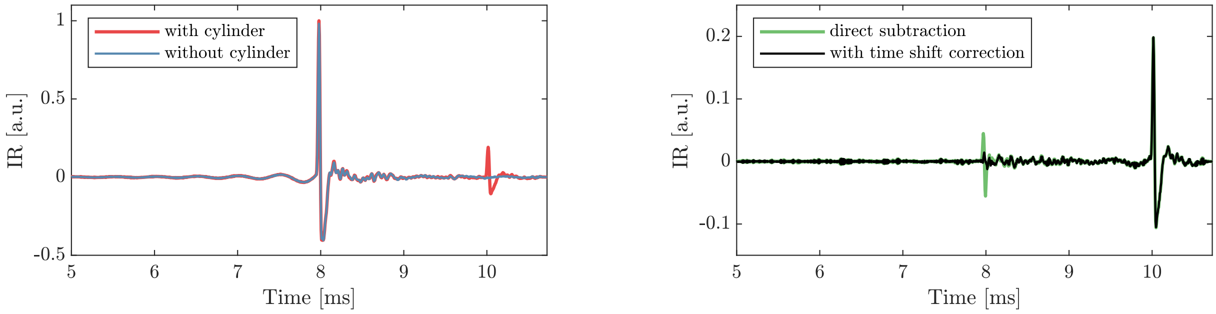

(a) (b)

Figure 6.8 Examples of impulse responses obtained for one position. **(a)** With and without the cylinder. **(b)** Signals obtained by direct subtraction and with the proposed time shift correction. Note that the range of the vertical axis is different.

amplitude between measurements. Several methods have been proposed to compensate for them in post-processing (Robinson et al., 2010). At low frequency, amplitude variation is the dominant error factor, while at high frequency it is the time shift. Here, we compensate only for difference of time of arrival. It is obtained by cross-correlation between the free-field signal and the total pressure signal. As it is generally fractions of a sample, the estimation is refined by interpolation on a Gaussian curve as proposed by Zhang et al. (2005). The free-field signal is delayed using the MATLAB function `delayseq` with the estimated time shift and it is subtracted to the total pressure signal to obtain eventually

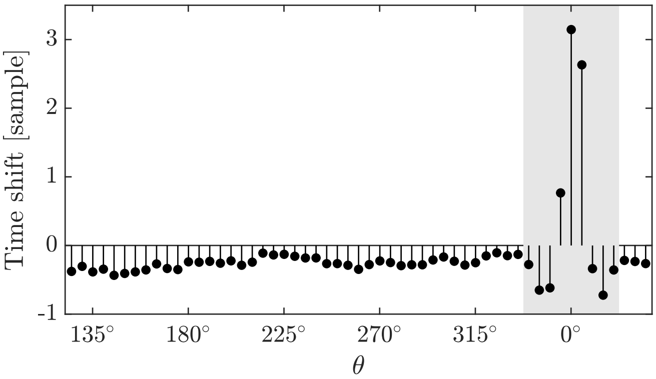

Figure 6.9 Example of estimated time shifts expressed in number of samples as a function of the angular position. The positions in shadow zone are shaded in gray.

the scattered pressure signal.

The measurements are compared to analytic solutions or simulations in the frequency domain. The spectra of the scattered and free-field pressure signals are obtained by Fast Fourier Transform with windowing to exclude any unwanted reflections, especially from the metal grid forming the floor of the chamber (see fig. 6.7), and zero-padding to increase the frequency resolution. No correction is made for excessive high-frequency air absorption, as the scattering happens over a short time, but it is partly taken into account and compensated for that occurring during the direct sound propagation when normalizing by the free-field pressure signal for each position. Figure 6.9 shows the time shift expressed in number of samples for each angular position estimated with the proposed method. The positions in the shadow zone are shaded in gray. It is clear that this method is not applicable to signals measured in this zone. These are therefore corrected using an average of the estimated time shifts for the neighboring visible positions of the same series.

The signals obtained with direct subtraction and with the correction method proposed, for the total and free-field signals shown in fig. 6.8a. A residual part of the direct sound is clearly visible if simple direct subtraction is employed, while using the proposed method results in a significant reduction of the direct sound in comparison.

6.2.2 Validation using a rigid circular cylinder

In order to validate the proposed measuring system and post-processing to obtain the scattered pressure, measurements have been made with a PVC tube of outer diameter 110 mm to model an infinite rigid circular cylinder. The thickness of the pipe is 3.2 mm, which is sufficient to assume such a boundary condition in the case of airborne propagation (Krynkin et al., 2011). The scale factor is set to 1:9.1 in order that it represents a cylinder of $2a = 1\,\mathrm{m}$ in diameter at full scale. Three repetitions of the same measurement have been made. The source and microphone positions are not changed between them. They are at 310 cm and 42 cm from the cylinder axis, respectively. The humidity and room temperature have been measured for each series. The average estimated speed of sound for the three series was $345.47\,\mathrm{m\,s^{-1}}$, with $\pm 0.10\,\mathrm{m\,s^{-1}}$ absolute differences. The variations of c between the repeated series are small, so they are compared to the analytic solutions for plane and spherical incidences presented in chapter 2 calculated using this average value.

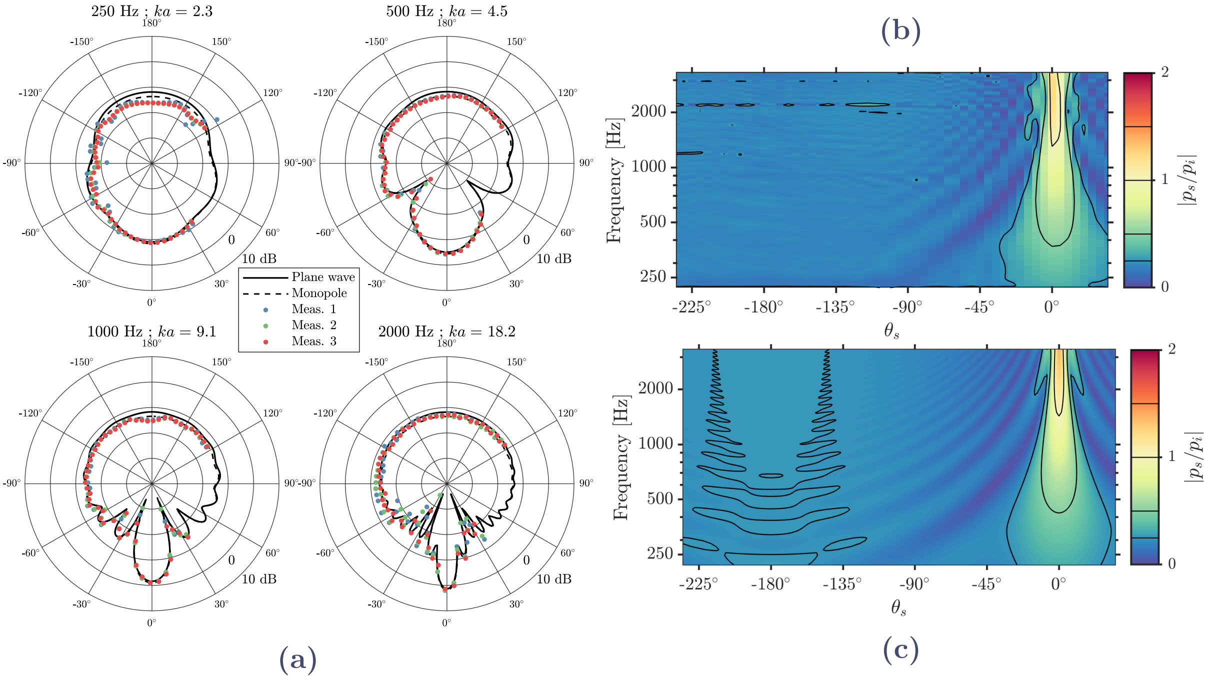

(a) (b) (c)

Figure 6.10 Measured scattered fields (3 repetitions) for a rigid cylinder compared to analytic solutions. **(a)** Polar diagrams $20\log_{10}|p_s/p_i|$ as functions of the scattering angle θ_s at different central frequencies of octave bands with the corresponding Helmholtz numbers ka indicated, where k is the wavenumber and a the radius. $|p_s/p_i|$ from **(b)** measurements (Meas. 3) with scaled frequency and **(c)** series solutions with plane wave incidence.

Figure 6.10 compares measured and analytic results for the scattered sound in the frequency domain. Figure 6.10a shows the polar diagrams as functions of the scattering angle, $\theta_s = \theta - \theta_0$, of scattered pressure levels relative to the incident field at the discrete scaled frequencies 250 Hz, 500 Hz, 1000 Hz, and 2000 Hz, compared to analytic solutions with plane wave and spherical incidence. The corresponding Helmholtz number ka is also indicated for generalization, where k is the wavenumber and a the cylinder radius. For the source distance chosen, the scattered relative level for the plane wave incidence is about 1.8 dB higher than the spherical incidence in the backscattering direction for all the frequencies considered here. For other angular positions, the differences are lower. In the forward scattering direction, the plane wave incidence leads to a relative scattered level about 0.6 dB lower than the monopole source. Overall, the measurements are in a better agreement with spherical incidence than the plane wave. A very good agreement is observed at 500 Hz and 1000 Hz. At 250 Hz, the back and transverse relative scattered pressure levels are lower than the analytic solutions and the variations between series are high. This is also the case at 2000 Hz in the transverse direction. These frequencies are close to the limit of the sound source where the signal-to-noise ratio is lower, degrading the accuracy. Additionally, the proposed correction for positions in the shadow zone leads to a good estimate, given the excellent agreement found for the forward scattering peak and the observed repeatability between the series. Finally, the rigidity hypothesis for this scale model seems acceptable.

Figure 6.10b shows the magnitude of the measured scattered pressure relative to the incident pressure for Meas. 3 over all the available frequency range, scaled according to

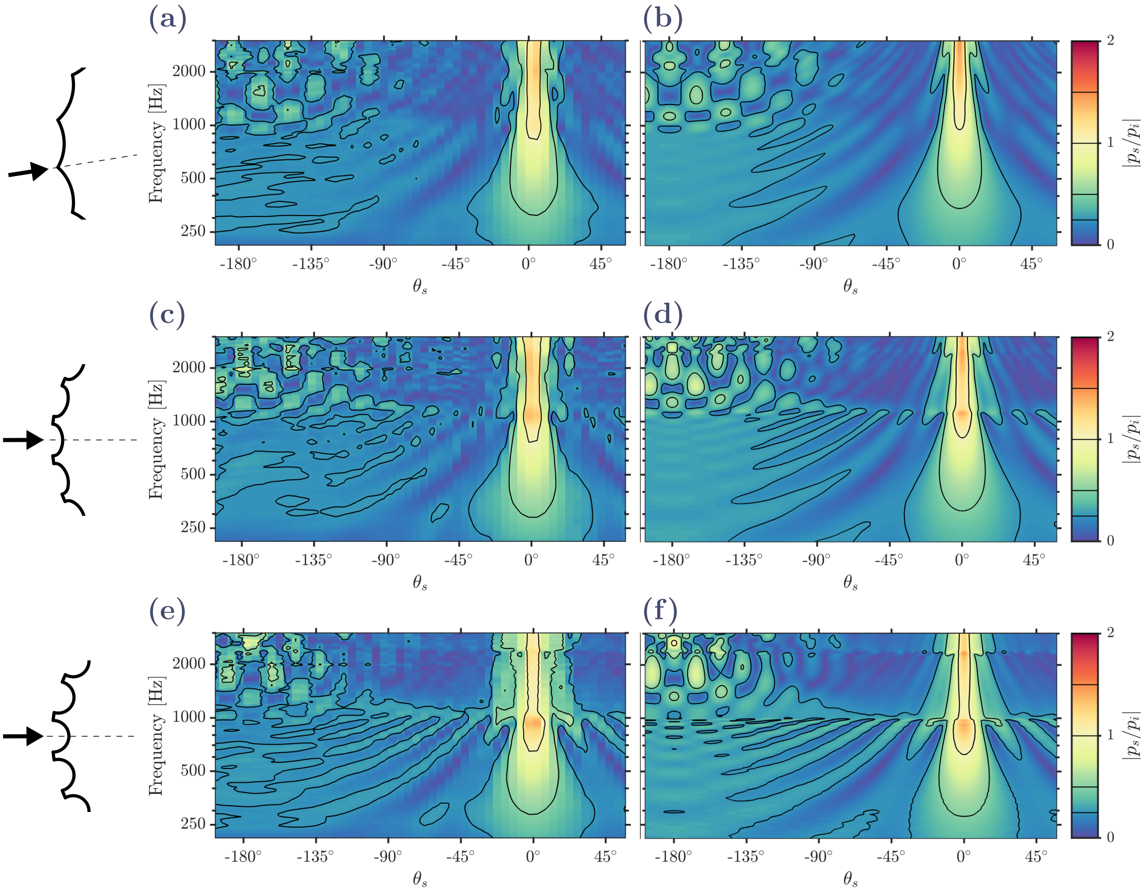

Figure 6.11 $|p_s/p_i|$ for the fluted columns: **D1** (**a**, **b**) with $\theta_0 = 9°$, **I1** (**c**, **d**) with $\theta_0 = 0°$, and **I2** (**e**, **f**) with $\theta_0 = 0°$. Scale model measurements (left) compared to simulations (right). The frequency axis of the measurements is scaled according to the factors given in table 6.1.

the factor, for each angular position. Comparing it to the plane wave solution represented in fig. 6.10c confirms the underestimation in the backscattering region, and the slight overestimation in the forward direction. The interference pattern in the transverse direction is less visible at high frequency in fig. 6.10b compared due to the low angular sampling. The drop of signal-to-noise ratio around 20 kHz is visible at the scaled frequency of 2200 Hz, manifested by an horizontal line of high values, mainly over the backscattering positions of the arc. The proposed method for time shift correction seems to be suitable for visible and shaded positions. In the following, the measurements on the columns of interest are compared to simulation results where the source is a plane wave. The present results show that this assumption is likely to affect mainly the backscattering region.

6.2.3 Results and comparisons with numerical simulations

The measurements on the different scale models of the selected scatterer are compared to simulations carried out with the hybrid method presented in chapter 5. They are performed with a grid spacing about $h = 5\,\mathrm{mm}$ in the regular part, corresponding to 10 points per wavelength at 7 kHz. The hybrid mesh is obtained with the CVD method with 5 iterations of Lloyd's algorithm. The speed of sound c is matched to that estimated for

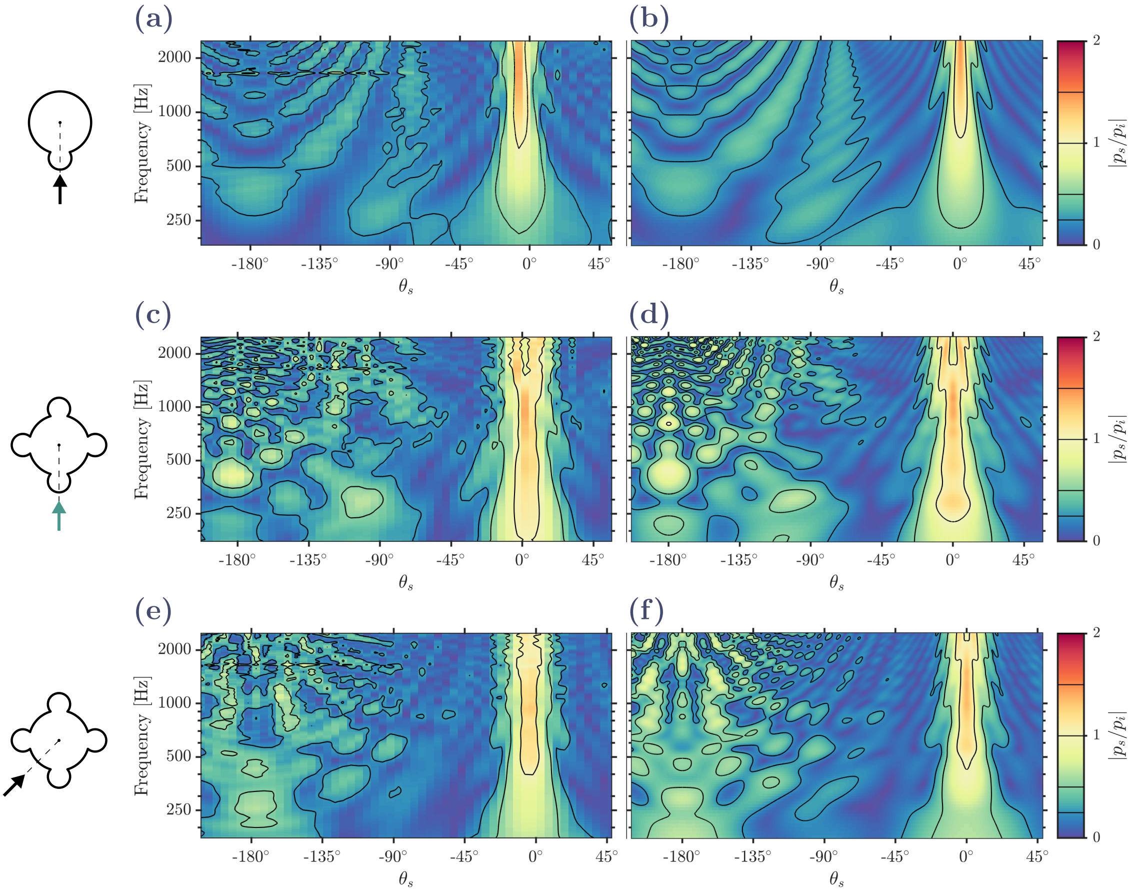

Figure 6.12 $|p_s/p_i|$ for the compound piers of the western bay of the nave: **N2** (**a**, **b**) with $\theta_0 = 90°$, **N1** with $\theta_0 = 90°$ (**c**, **d**), and $\theta_0 = 45°$ (**e**, **f**). Scale model measurements (left) compared to simulations (right). The frequency axis of the measurements is scaled according to the factors given in table 6.1.

each cylinder and configuration, reported in table 6.1. The time step Δt is set by the limit value determined by the stability condition eq. (5.81). The resulting Courant number λ of each simulation is given in table 6.1. The source signal is a Ricker wavelet with a central frequency of 2 kHz injected as a soft source over a line of grid points to have a plane wave incidence. The boundary conditions are considered to be rigid. The simulated total and incident pressure fields are recorded on the grid positions closest to the circle describing the arc of the microphone positions in the physical measurements, whose radius is given in table 6.1.

Figures 6.11 to 6.14 show the magnitude ratio between the scattered pressure and the incident pressure measured experimentally for each setup and their numerically simulated counterpart. The results are compared in the frequency domain and the vertical axis of the surface plots of the experimental results has been scaled according to the factor of each given table 6.1. Overall, a good agreement between measurements and simulations can be observed, with constructive and destructive interference appearing within the scattered pressure in steady state match in frequency and space. In particular, the post-processing method for obtaining the scattered pressure in the shadow area, based on neighboring positions, is suitable as shown by the comparison of the figures around the direction $\theta_s = 0°$. In the backscattering region, the magnitude ratios are systematically slightly

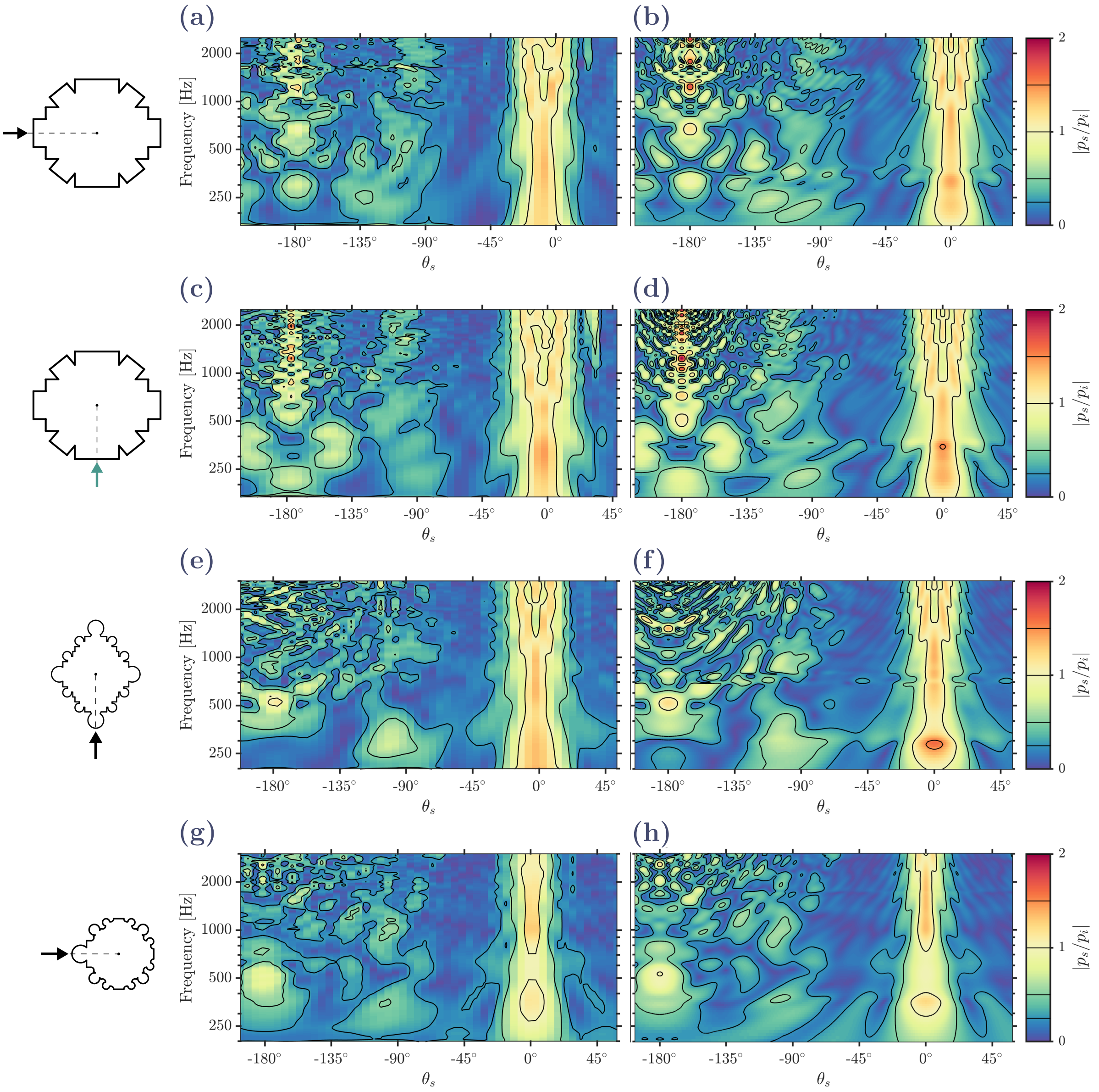

Figure 6.13 $|p_s/p_i|$ for the western crossing piers **C1** with $\theta_0 = 0°$ (**a**, **b**), and $\theta_0 = 90°$ (**c**, **d**), tower piers **T** with $\theta_0 = 90°$ (**e**, **f**), and choir pier **Ch** with $\theta_0 = 0°$ (**g**, **h**). Scale model measurements (left) compared to simulations (right). The frequency axis of the measurements is scaled according to the factors given in table 6.1.

lower for the measurements on scale models compared to simulations, in agreement with the difference expected between a plane and a spherical incidence. The drop of SNR around 20 kHz is visible in some of the measurement results, *e.g.* in fig. 6.12a around 2400 Hz, or in fig. 6.14a around 1700 Hz.

In addition to the error due to the nature of the incident field, other sources are that, for certain configurations, the centering of the cylinder and the perpendicularity of the measurement plane to the cylinder axis are not perfectly achieved. For this latter, a part of the wave is thus scattered out of the plane corresponding to oblique incidence. This can be seen when the measured backscattered and forward scattered pressures do not exactly match the expected diametrically opposite directions $\theta_s = -180°$ and $\theta_s = 0°$,

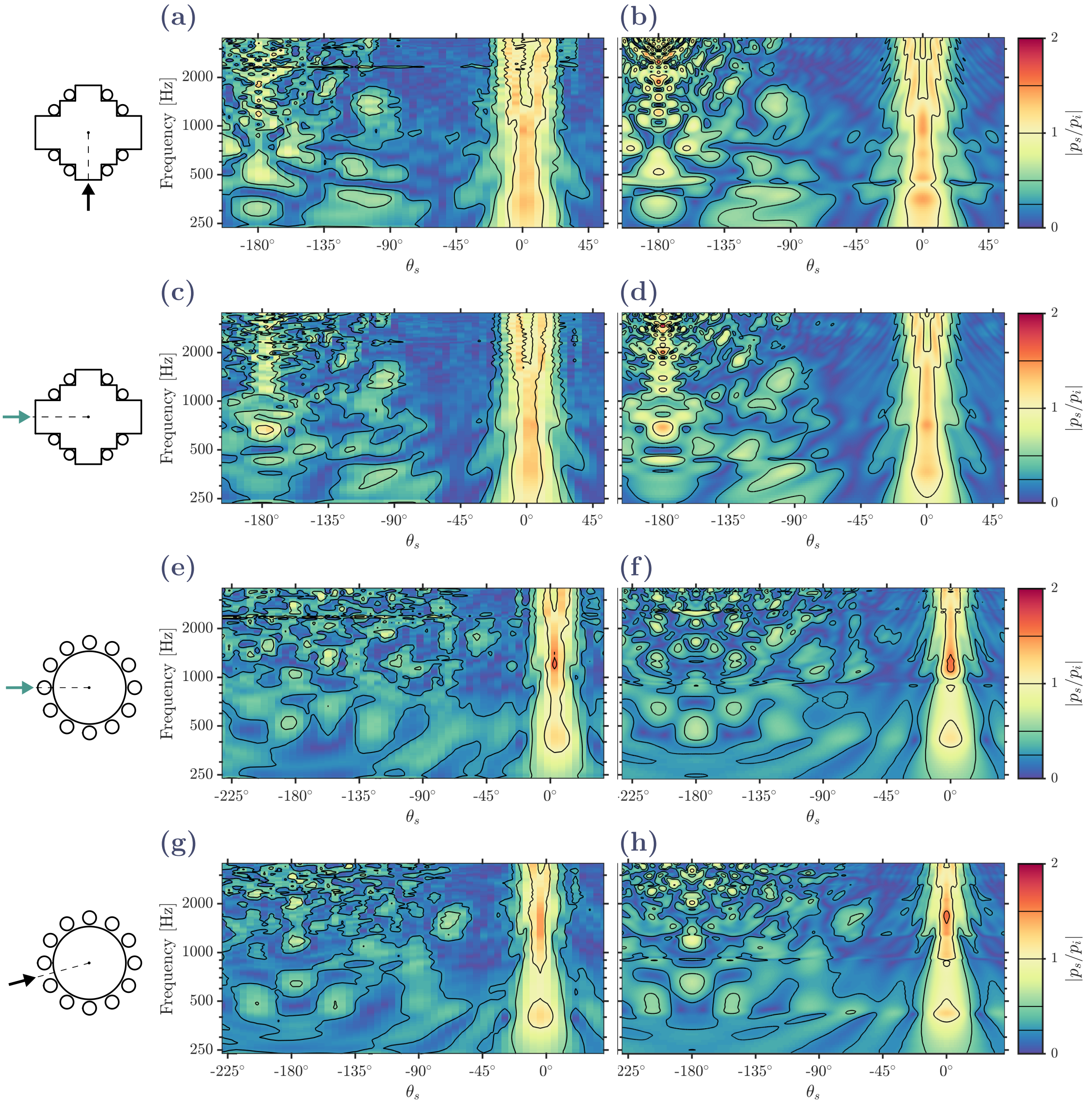

Figure 6.14 $|p_s/p_i|$ for the piers with *colonnettes*: **C2** with $\theta_0 = 0°$ **(a, b)** and $\theta_0 = 90°$ **(c, d)**, and **N3** with $\theta_0 = 0°$ **(e, f)** and $\theta_0 = 15°$ **(g, h)**. Scale model measurements (left) compared to simulations (right). The frequency axis of the measurements is scaled according to the factors given in table 6.1.

respectively, that are supposed to be symmetry lines in the figures for such configurations as shown in the simulated results. This is particularly striking in fig. 6.13a compared to fig. 6.13b where the cylinder is probably leaning in the transverse direction. If the cylinder is slightly tilted forward or backward from the source then it is not visible in this way but the deflection is still present.

Another one is the geometrical differences that can exist between a hand-made physical model and a perfect numerical model. For geometries with outward or inward corners, the scale models will have rounded corners compared to their digital counterparts where no rounding was introduced afterwards. The effect of rounding corners on the scattered field by concave cylinders with one, two or four corners has been studied numerically by Markowskei et al. (2017) and they found that maximum differences occurred in the backscattering region with expected dependencies on the radius of curvature, the wavelength and the angle of incidence with respect to the position of the corners. Here, the scale models made of staff (figs. 6.6a and 6.6b) have more rounded edges compared to wooden models because of the viscosity of the material having a surface tension, also affecting both outer and re-entrant corners. For manufacturing reasons, the angles existing at the intersections of the circles for **N2** and **N1** (fig. 6.6c) are also rounded. In addition, for geometries with several elements, a bad straightness and, therefore, positioning of the small cylinders leads to a different scattering, such as in fig. 6.14e in comparison to fig. 6.14f.

6.2.3.1 Fluted columns

The fluted columns are circular cylinders with parallel regular grooves on their surface in the axial direction. It can be observed that below a certain frequency, approximately 1000 Hz for the three tested fluting, the scattering is similar to that of a circular cylinder, while lobes appear beyond. The backscattering is increased and the scattered pressures in the forward region on both sides of the peak decrease. This is more pronounced for the Ionic flutes, *i.e.* **I1** and **I2** as shown in figs. 6.11d and 6.11f, respectively, compared to the Doric fluting shown in fig. 6.11b.

The first strong backscattering peak ($\theta_s = -180°$) for **D1**, **I1**, and **I2** is found at about 1130 Hz, 1280 Hz, and 1320 Hz with a simulated magnitude ratio of 0.56, 0.57, and 0.55, respectively. It also appear in the measurements with respective differences of about −1.6 dB, −1.9 dB, and −2.5 dB, in the range of what is expected given the spherical incidence. A better agreement is overall observed on the forward scattering region, especially around the forward scattering peak, for $-90° \leq \theta_s \leq -30°$.

The positioning of the cylinders, *i.e.* their perpendicularity and centering, is less ensured for **D1**, and **I2**, compared to **I1**, visible through the slight angular shifts for the forward and backward directions supposed to be symmetry lines for these incidences, clearly visible in the simulations. The arc angle between the maximum found in the backward and forward peaks in the measurements is about 5° larger than a semicircle for **D1** and about 3° smaller for **I2**, and the difference is less than 1° for **I1**.

6.2.3.2 Compound piers

Figure 6.12 shows the comparisons for the columns **N2** and **N1**, located at the western bay of the nave. These cross sections are formed by intersecting circles. We observe that the pressure they scatter has more peaks and notches of interference compared to a simple circular cylinder, and even more so for **N1** comprising four engaged circles on its core against only one for **N2**. For this latter, the wave travel along the symmetry axis of the cross section, hitting the small circle first. We observe that part of the wave is scattered in the transverse directions, with high magnitude ratios for $-135° \leq \theta_s \leq -45°$. The differences between the measurements (fig. 6.12a) and the simulations (fig. 6.12b) are less than 1 dB in this region. In the backscattering direction, peaks and notches appear. They are regularly spaced in frequency, indicating interference between several reflected sound paths. For **N1**, two incidence angles have been tested that correspond to plane wave traveling along the symmetry axes of this cross section: $\theta_0 = 90°$ (figs. 6.12c and 6.12d) corresponding to a plane wave hitting a small engaged cylinder, and $\theta_0 = 0°$ (figs. 6.12e and 6.12f) corresponding to a plane wave hitting two engaged circular cylinders simultaneously. For both incidences, less energy is scattered in the transverse directions, around $\theta_s = -60°$, in comparison to **N1**, especially at low frequency around 250 Hz. Comparing the two incidences, we observe that for $\theta_0 = 45°$, more energy is backscattered at low frequency, around 200 Hz than for $\theta_0 = 90°$. On the other hand, a lobe is found in the transverse directions for the latter, around $\theta_s = -100°$, which does not appear for the other incidence.

The results for the other compound piers are shown in fig. 6.13. The western crossing piers **C1** were measured and simulated for two angles of incidence normal to a flat face of the cylinder. An increase in backscattering is observed as the frequency increases for both in the simulations figs. 6.13b and 6.13d, and to a lesser extent in the measurements figs. 6.13a and 6.13c. This is shown here with peaks and notches indicating interference between the reflections from the different parts. The scattering in the transverse direction, comparing the two incidence angles, seems similar up to about 1000 Hz, beyond that the tilted faces reflect the wave in the respective specular directions.

The tower piers **T** are measured and simulated for $\theta_0 = 90°$ and the results are shown in figs. 6.13e and 6.13f, respectively. We observe a good agreement up to 800 Hz for all directions. However, the simulation predicts a strong forward scattered pressure ($\theta_s = 0°$) around 290 Hz with a magnitude approximately equal to 1.6 times that of the incident pressure, while the measure gives a ratio of about 1.3. Beyond 800 Hz, the agreement remains good except for the backscattering region where the symmetry with respect to $\theta_s = -180°$ is not visible unlike the simulation. For the pier **Ch** of the south ambulatory of the choir, considering the remarks already made about the difference in the nature of the sources, the agreement is good between the measurement and the simulation shown in figs. 6.13g and 6.13h, respectively, over the envisaged frequency range, and a good symmetry is observed in relation to the median plane.

6.2.3.3 Piers with *colonnettes en délit*

Figure 6.14 shows the comparisons for the piers **C2** and **N3** that include *colonnettes en délit*. The piers **C2** were measured and simulated for two angles of incidence normal to a flat face of the cylinder, similarly to **C1**. The increase of backscattering is also observed as the frequency increases for both in the simulations figs. 6.14b and 6.14d. In the measurement results, the maxima are more visible for $\theta_0 = 90°$ in fig. 6.14a than for $\theta_0 = 0°$ in fig. 6.14c. These maxima are spatially localized and we can observe in the simulations that for the distance of the receiver, they occupy a small angular sector, less than 5°, so a very good relative positioning of the different elements is necessary to capture them. The results are overall similar comparing the two incidence angles, with a weak scattering for $-90° \leq \theta_s \leq -30°$ above 2000 Hz.

The piers **N3** of the nave aisles have been measured and simulated for $\theta_0 = 0°$ shown in figs. 6.14e and 6.14f, respectively. We find a general agreement, *e.g.* the maximum of forward scattering around 1300 Hz present in both with a relative difference of less than 5 %. For $\theta_0 = 15°$ shown in figs. 6.14g and 6.14h, the measurements appear more symmetric with respect to the median plane compared to the other incidence angle.

6.2.4 Discussion

The comparisons between the measurements on scale model of the different architectural columns and their simulated counterpart with the hybrid time domain method have shown that both models are in general agreement, visible in particular through the interference patterns appearing in the scattered pressure which correspond in frequency. The magnitude ratios in the backscattering region are slightly higher for the simulation results. This is mainly explained by the nature of the sources, an infinite plane wave compared to a single tweeter in the measurements. They are in better agreement for the transverse directions. The other sources of error identified are the positioning of the cylinder, and the geometrical differences existing in the scale models due to manufacturing constraints. Differences are observed between the geometries of interest, and the scattering depends strongly on the incidence angle.

Finally, these are other cases of cross-validation of the numerical method presented in chapter 5. It allows us in the following to further characterize the geometries of interest in far and near field on a wider frequency band, and other incidence angles with some confidence, free from any experimental error.

6.3 Numerical characterization

To better identify the reasons for the observed differences, the columns and piers are characterized in the far field using numerical simulations only. The quantities calculated are those usually used in scattering studies, presented in section 2.4.2, namely the total scattering cross section (TSCS) $\sigma(\theta_0)$, the monostatic target strength $\mathrm{TS}(\theta_0, 180°)$, that measure the overall scattered power and the backscattered one, and the asymmetry factor $g(\theta_0)$ to quantify globally preferential scattering directions.

The latter focus on the forward and backward directions. To account for transverse directions, we propose to calculate the transverse anisotropy factor $g_\perp$ conjointly that is defined as

$$g_\perp(\theta_0) = \int_0^{2\pi} P(\theta_0, \theta_s) \sin(\theta_s)^2 \, d\theta_s \,, \tag{6.1}$$

where P is the scattering phase function defined eq. (2.61). It is comprised between 0 and 1. Values close to 0 indicate that the scattering is mainly distributed on the forward and backward directions, while values close to 1 indicate full transverse scattering in the perpendicular directions to the incidence. Moreover, if g and $g_\perp$ are close to 0 and 0.5, respectively, then it indicates isotropic scattering.

The average octave-band target strength $10\log_{10} < |f|^2 >$ are also calculated with the discrete equivalent of

$$< |f_\infty|^2 >= \frac{1}{f_2 - f_1} \int_{f_1}^{f_2} |f_\infty(\omega)|^2 \, d\omega \,, \tag{6.2}$$

where f_1 and f_2 are the edge frequencies of an octave band. We recall that $|f_\infty|^2$ is the differential scattering cross section.

6.3.1 Simulation parameters

The numerical characterizations are performed using the same parameters as for the comparisons with the measurements, with the exception of the speed of sound c, which is the same for all in this section, set at $344\,\mathrm{m\,s^{-1}}$. As before, an incident plane wave is used to model a far field wave, to get rid of the effect of the distance from the source. The scattered far field is estimated using NFFFT presented and validated in chapter 5, on a circle of 100 m radius centered on the centroid of each cross section at 300 regularly spaced angular positions. A Ricker pulse of center frequency 2 kHz is also used here. These parameters allow us to have results with a good accuracy from 20 Hz to the limit of the 4 kHz octave band, *i.e.* around 5700 Hz.

6.3.2 Results

Figures 6.15 to 6.25 show TSCSs $\sigma(\theta_0)$, the monostatic target strength $\mathrm{TS}(\theta_0, 180°)$, defined as the differential basckscattering cross section expressed in dB, and the two anisotropy factors for the geometries of interest and different angles of incidence θ_0 as functions of the frequency. They are compared with that of the circular cylinder of equivalent cross-sectional area determined with classical series expansion (Morse et al., 1986) and represented by a solid black line in each figure. The upper horizontal axis shows the Helmholtz number ka_{eq} with k the wave number and a_{eq} the radius of the equivalent cylinder. They allow comparison with scattering theory with a geometry independent of the angle of incidence and supposed to exhibit a similar behavior at low frequency.

When the circular cylinder is small compared to the wavelength, scattering can be modeled with Rayleigh scattering, dependent on the volume of the scatterer. TSCS and the target strength are low, the scattering happens more in the backward direction as g is negative and $g_\perp$ is low. Then a resonant regime when it is of comparable dimensions. TSCS increases and oscillations are observed in the target strength, due to the interference with the Franz waves traveling around the boundary (Bowman et al., 1988). The anisotropy factors increase, with g approaching 0 to become positive and $g_\perp$ has its maximum value around 0.56 at $ka_{eq} = 1.4$. Eventually, a geometric regime at high frequency where σ tends to $4a_{eq}$, *i.e.* twice the shadow length. The Franz waves are attenuated and become negligible. The target strength tends to the geometrical limit $10\log_{10}(a_{eq}/2)$. The scattering happens more in the forward direction as a shadow beam is formed, g increases and $g_\perp$ decreases to the asymptotic values about 0.32 and 0.27, respectively.

6.3.2.1 Fluted columns

The results for the Doric columns **D1** and **D2** are shown in figs. 6.15 and 6.16 with their respective mean octave-band target strengths in figs. 6.15e and 6.16e.

Their scattering behavior is very close to that of their equivalent circular cylinder below 700 Hz for both Doric flute depths. Above, TSCSs are not monotonic anymore and local maxima appear. The first maxima for the shaft with 60°-arc flutes are at about 1040 Hz and 1100 Hz for the incidence on arris and on flute, respectively, as shown in fig. 6.15a. They are approximately at the value of the geometrical limit. On the considered frequency range, maxima are found at higher frequencies, at about 2200 Hz and 4330 Hz for $\theta_0 = 0°$ representing slight overshoots of 3 % and 5 %, approximately, and at about 3230 Hz and 5510 Hz for $\theta_0 = 9°$ representing lower overshoots of 2 % and 2.5 %, respectively. For the other Doric fluting, the first maxima appear for slightly lower frequencies, at about 1000 Hz for both incidence, and represent the highest values for the frequency range considered, overshooting the geometrical limit by 17 % and 11 % for the incidence on arris and on flute, respectively, as shown in fig. 6.16a. Above, TSCSs vary more than the other fluting with comparable incidence. The equivalent cylinder and the real geometry are overall less in agreement at high frequency as, in this case, the cross section is more concave and, therefore, the difference between the shadow length and the equivalent radius is increased.

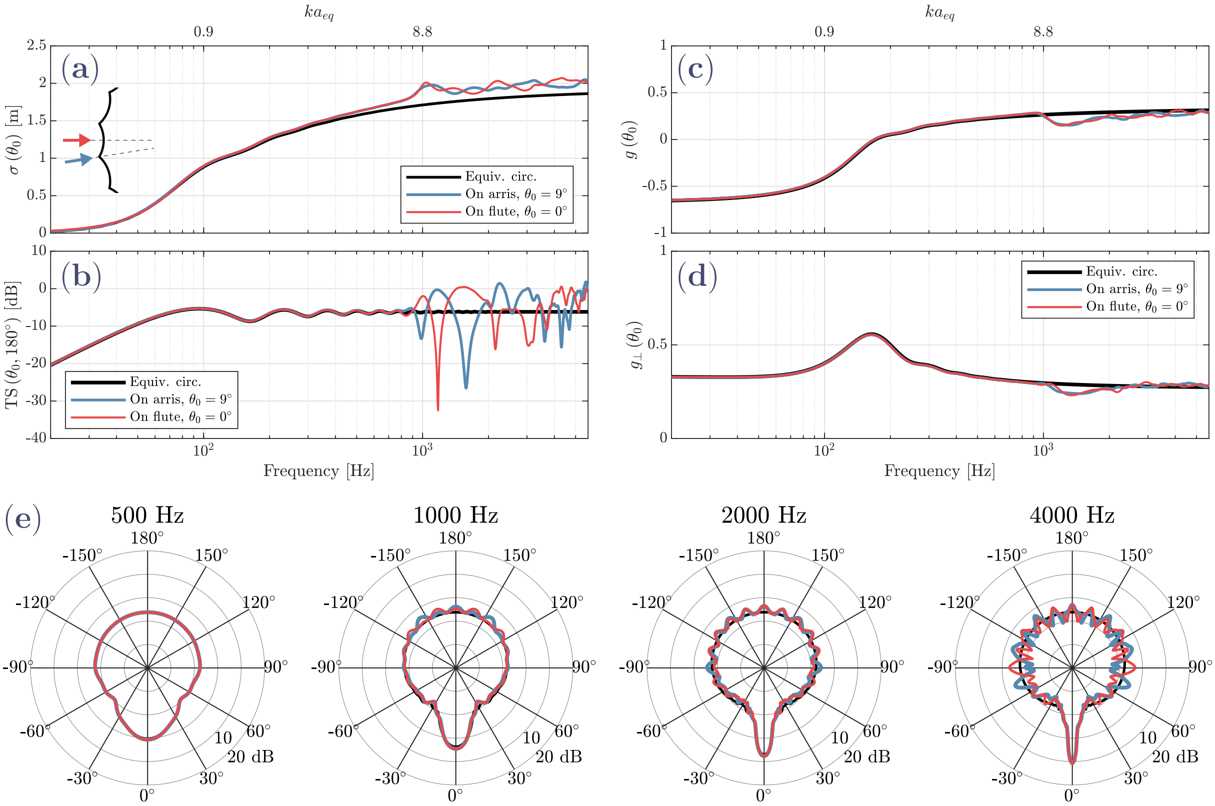

Figure 6.15 Total scattering cross section σ **(a)**, monostatic target strength $\mathrm{TS}(\theta_0, 180°)$ **(b)**, and anisotropy factors g **(c)** and $g_\perp$ **(d)** as functions of frequency, and average octave-band target strengths **(e)** as function of scattering angle, for different incidence angles θ_0 for the Doric shaft **D1** compared to its equivalent cylinder with $a_{eq} = 48.2\,\mathrm{cm}$.

The monostatic target strengths represented in figs. 6.15b and 6.16b are very close to that of the equivalent cylinder below 800 Hz for both incidences and both flutings. Above, large differences appear with maximum values of 1.4 dB and 2.8 dB for **D1** and **D2**, respectively, for the incidence on the arris. The peaks and notches appearing for one incidence are in opposition to that of the other tested incidence. This tendency is globally visible until the upper frequency considered, except one notch at 3750 Hz that exist for **D2** presents for both incidences.

The asymmetry factors g represented in figs. 6.15c and 6.16c show that the existing similarities with the equivalent cylinder in terms of strength are also found in the scattering directions. The variations of g are overall correlated with that of σ. Above 1000 Hz, the values of g indicate that, overall, the increase of strength happens in the backscattering direction, with slightly lower values for **D2** of 0.1 at minimum compared to 0.15 for **D1**, around 1300 Hz. The ascending parts of σ, where they strongly differ from the equivalent cylinder is reflected in a slight increase of the forward scattering, especially visible for **D2** around 900 Hz.

In terms of transverse directions, $g_\perp$ represented in figs. 6.15d and 6.16d present lower values compared to the equivalent cylinder between 1000 Hz to 2500 Hz approximately. Similarly to g, the values are lower for **D2**, and the minimum is about 0.2 around the same frequency. Above, the values are close to the equivalent cylinder with variations comprised between 0.25 and 0.31 for **D2**, and 0.27 and 0.30 for **D1**, considering both

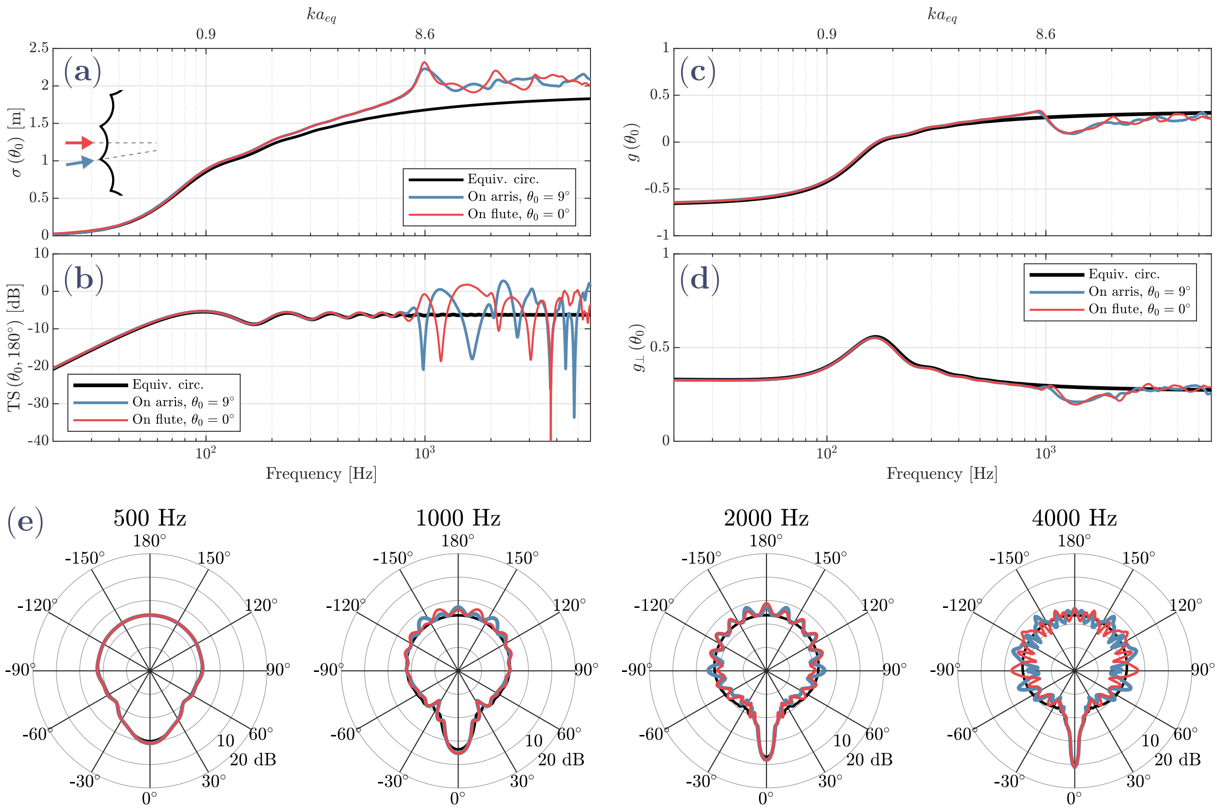

Figure 6.16 Total scattering cross section σ **(a)**, monostatic target strength $\mathrm{TS}(\theta_0, 180°)$ **(b)**, and anisotropy factors g **(c)** and $g_\perp$ **(d)** as functions of frequency, and average octave-band target strengths **(e)** represented with the plane wave coming from the top, for different incidence angles θ_0 for the Doric shaft **D2** compared to its equivalent cylinder with $a_{eq} = 47.3\,\mathrm{cm}$.

incidences.

Figures 6.15e and 6.16e show the average octave-band target strengths from 500 Hz to 4000 Hz. They are not represented for the lower ones as we have seen that differences with regards to the incidence or comparing with the equivalent cylinder are not expected there.

Figure 6.17 show the scattering results for **I1**. Globally, the behavior observed with the Doric flutings is also found for this Ionic shaft in an even more visible way. The first maxima are found around the same frequency for both tested incidences, at about 1100 Hz, representing higher overshoots of the geometrical limit of 39 % and 33 % for the incidence on a flute and a fillet, respectively, as shown in fig. 6.17a. At high frequency, TSCSs remain above their geometric limit in contrast to the Doric shafts. The backscattering is even more increased as shown in fig. 6.17b, with a maximum value of 4.2 dB found in this case for the normal incidence to a flute around 2700 Hz. The anisotropy factors shown in figs. 6.17c and 6.17d seem to be less dependent on the angle of incidence compared to the Doric shafts. The increase of g correlated with the increasing part of TSCS before they reach their maximum is more visible compared to the Doric flutings. Above, the local minima are also present and lower, with values about 0.06 around 1600 Hz for both incidences. Similarly, the decrease of transverse scattering is also observed with lower values of $g_\perp$ compared to the equivalent cylinder from 1200 Hz to 3000 Hz, approximately.

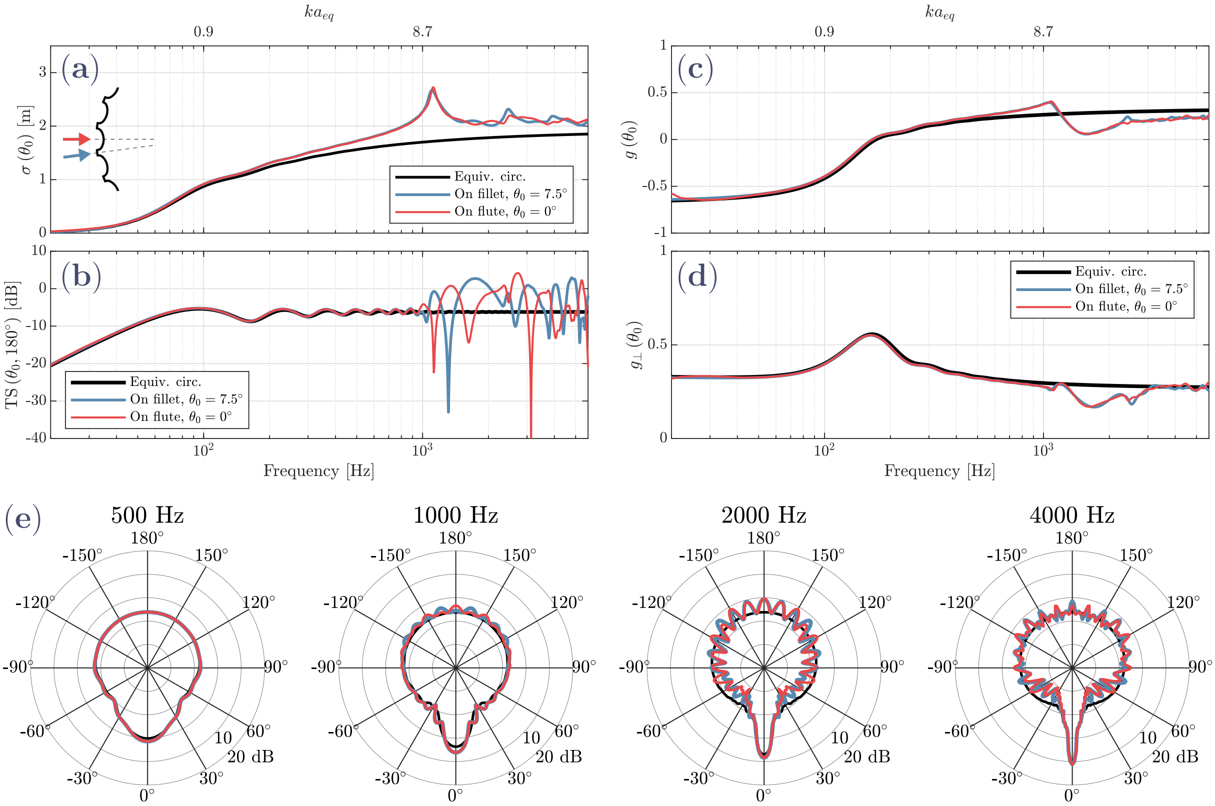

Figure 6.17 Total scattering cross section σ **(a)**, monostatic target strength TS$(\theta_0, 180°)$ **(b)**, and anisotropy factors g **(c)** and $g_\perp$ **(d)** as functions of frequency, and average octave-band target strengths **(e)** with the plane wave coming from the top, for different incidence angles θ_0 for the Ionic shaft **I1** compared to its equivalent cylinder with $a_{eq} = 47.9\,\text{cm}$.

For the Ionic shaft with semicircular fluting **I2**, TSCSs shown in fig. 6.18a are globally the highest among the tested Classical columns. They differ more strongly from the equivalent cylinder and deviations appear visibly at lower frequencies. Around 150 Hz, TSCSs are approximately 10 % higher than that of the equivalent cylinder. The global maxima are around 960 Hz for both incidences representing the highest overshoots of about 68 % and 63 % for $\theta_0 = 7.5°$ and 0°, respectively. Local maxima can be observed around 2340 Hz, representing in this case respective overshoots of 21 % and 24 %. Similarly to **I1**, TSCSs remain above their geometrical limit after 500 Hz. A second minimum can be observed around 2340 Hz, with 2 local minima of values 0.15 and 0.14 at 1750 Hz and 2400 Hz present for both incidences.

The monostatic target strengths represented in fig. 6.18b show also a substantial increase in backscattering beyond the frequency of the global maxima of TSCS. The maximum value of 5.5 dB is found at about 2800 Hz for the incidence on the flute. Below 900 Hz, the oscillations representing interference with the Franz waves do not decrease in amplitude as the frequency increases, unlike the circular cylinder.

We find a similar behavior to the other sections in terms of angular distribution but even more accentuated. Figure 6.18c shows that g are higher than that of the equivalent cylinder from 250 Hz to 1200 Hz with maximum values of 0.45 for both incidences, approximately, representing the highest values among the Classical shafts. Above, g are

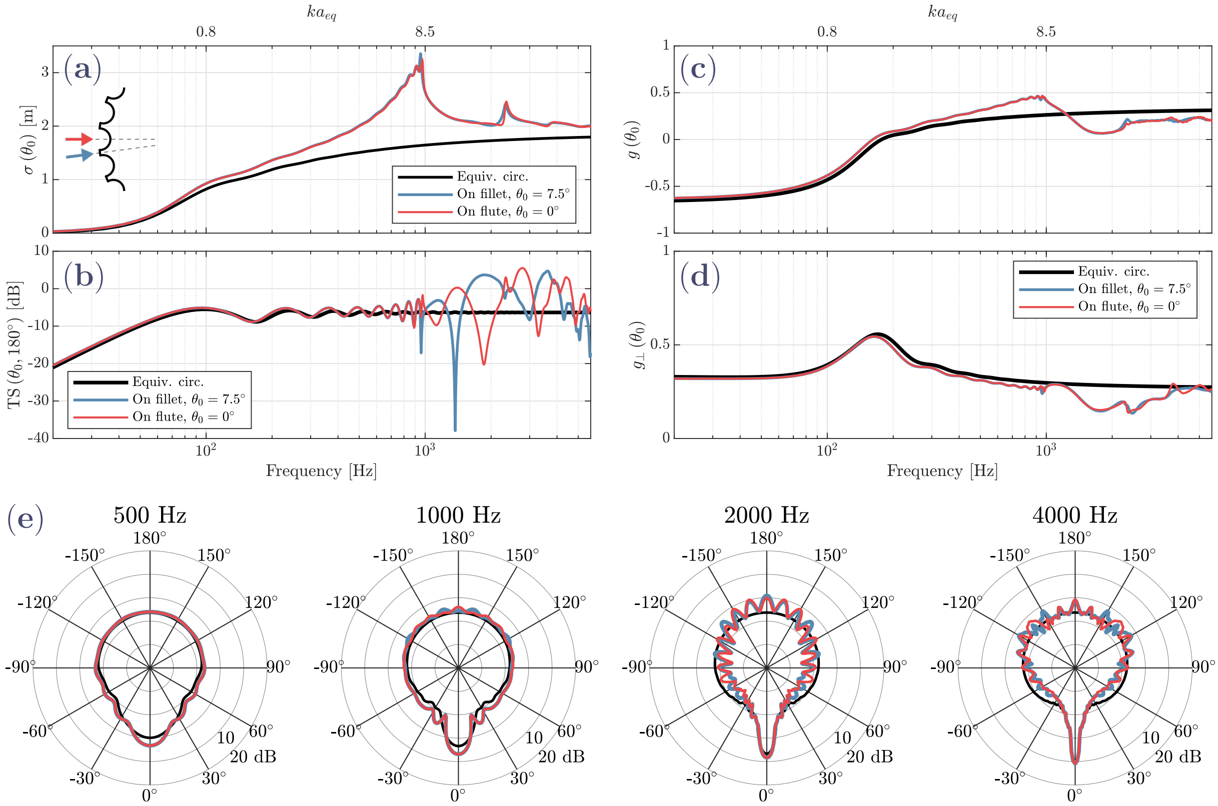

Figure 6.18 Total scattering cross section σ (a), monostatic target strength TS$(\theta_0, 180°)$ (b), and anisotropy factors g (c) and $g_\perp$ (d) as functions of frequency, and average octave-band target strengths (e) represented with the plane wave coming from the top, for different incidence angles θ_0 for the Ionic shaft **I2** compared to its equivalent cylinder with $a_{eq} = 46.5\,\text{cm}$.

lower with minimum values of about 0.07. Figure 6.18d shows that $g_\perp$ is overall very similar to that of **I1** with lower values compared to the equivalent cylinder over a slightly wider frequency range until 3800 Hz.

6.3.2.2 Compound piers

TSCSs for **N2** shown in fig. 6.19a are also compared with that of the inscribed circular cylinder, *i.e.* the core alone represented with a dash-dotted line. For $\theta_0 = 90°$, a plane wave traveling along its symmetry axis hitting first the smaller of the two arcs, σ is smaller than that of the equivalent cylinder, especially under 250 Hz with a maximum relative difference of $-24\,\%$ at 141 Hz corresponding to $ka = 0.63$ with respect to the small engaged circle. Above 250 Hz, TSCSs are comparable, with relative differences between $\pm 2\,\%$. The wave is thus partly deflected by scattering in the transverse directions prior to its interaction with the large arc resulting in even less overall scattered energy compared to the inscribed cylinder. This is also visible in the low target strength shown in fig. 6.19b on this frequency range, as well as in fig. 6.12b. The peaks and notches above 400 Hz are explained by the constructive and destructive interference with the second wave front due to the reflection on the core similarly to Varadan et al. (1982). The path difference for a plane wave reflected on the small circle and at the intersection points of the circles is about

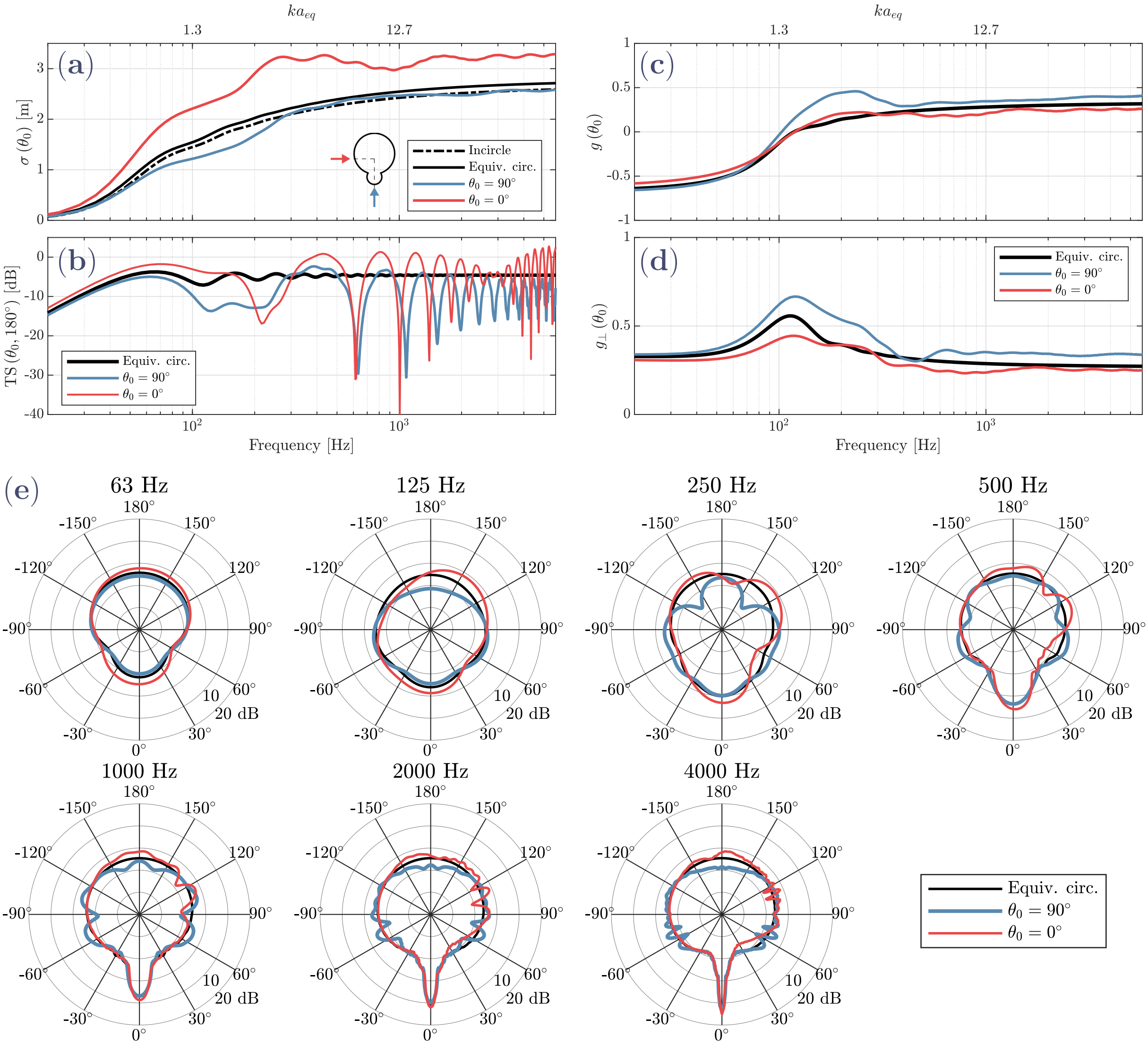

Figure 6.19 Total scattering cross section σ **(a)**, monostatic target strength TS$(\theta_0, 180°)$ **(b)**, and anisotropy factors g **(c)** and $g_\perp$ **(d)** as functions of frequency, and average octave-band target strengths **(e)** represented with the plane wave coming from the top, for different incidence angles θ_0 for **N2** compared to its equivalent cylinder with $a_{eq} = 70\,\text{cm}$.

76 cm, which is in agreement with the frequency spacing of notches about 450 Hz. The deflection in the transverse directions is confirmed by the high values of $g_\perp$ at frequencies corresponding to the resonant regime of the small intersecting cylinder as shown fig. 6.19d, accompanied by a maximum in g in fig. 6.19c, overshooting the asymptotic value.

For $\theta_0 = 0°$, the plane wave travels perpendicularly to the symmetry axis and scattering is increased over the whole frequency range considered compared to the other configuration and the equivalent cylinder. The target strength presents also peaks and notches above 300 Hz that can also be explained by geometrical considerations. The path difference between the reflection on the core and at the re-entrant corner formed at the intersection is about 3.4 m for this incidence, which agrees with the frequency spacing of notches which is about 400 Hz. The peaks are higher than the other angle of incidence or the equivalent

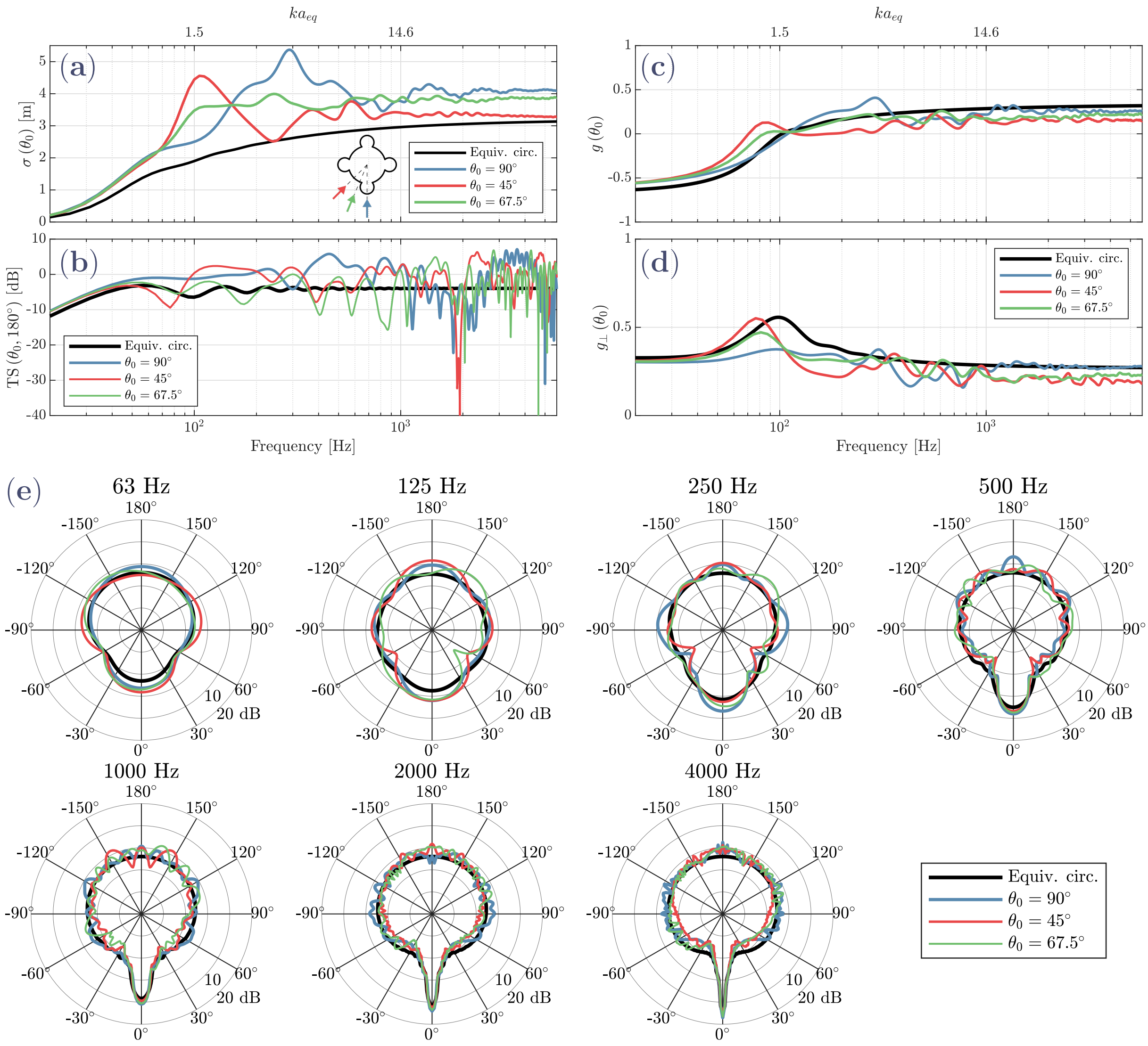

Figure 6.20 Total scattering cross section σ **(a)**, monostatic target strength $\mathrm{TS}(\theta_0, 180^\circ)$ **(b)**, and anisotropy factors g **(c)** and $g_\perp$ **(d)** as functions of frequency, and average octave-band target strengths **(e)** represented with the plane wave coming from the top, for different incidence angles θ_0 for **N1** compared to its equivalent cylinder with $a_{eq} = 80\,\mathrm{cm}$.

cylinder with a value of about 1.3 dB around 800 Hz, as the intersection acts more as a retroreflector, *i.e.* a dihedral corner reflector facing the plane wave. The asymmetry factor g is quite close to that of the equivalent cylinder, while $g_\perp$ appears flatter with a lower maximum value of about 0.44 and an increase around the resonant regime of the small intersecting cylinder. The scattering directions are overall constant above 600 Hz for both angles.

N1 exhibits greater scattering than its equivalent cylinder for any of the three incidences considered as shown in fig. 6.20a. At 20 Hz, the relative differences are around 43 % showing that Rayleigh scattering is not suitable for such geometry. At low frequencies, the three curves are close but they separate beyond 65 Hz and they converge to different values at high frequencies in agreement with the respective lengths of the cast shadows.

For $\theta_0 = 90°$, σ presents a large peak of value 5.4 m at 288 Hz, corresponding to an overshoot of 29 % compared to the geometrical limit. The wave deflection is still present but the additional engaged circles extend the geometry and interact with it eventually as we have seen that forward and transverse directions were favored (figs. 6.19c and 6.19d). For $\theta_0 = 45°$, σ has a maximum of value 4.6 m at 106 Hz, corresponding to a higher overshoot of 41 %. For the angle $\theta_0 = 67.5°$, σ appears as an intermediate value except from 570 Hz to 1100 Hz.

As the geometries become more complicated, it becomes harder to explain the target strength curves with geometrical considerations due to the overlapping of interference from multiple path differences. Nevertheless, for $\theta_0 = 90°$, the target strength shown in fig. 6.20b is high around 440 Hz similarly to **N2** for $\theta_0 = 0°$ (fig. 6.19b), where the 4 corners at the intersections increase the basckscattering. The average value for the 500 Hz octave band is 3.2 dB against −4 dB for the equivalent cylinder. In contrast, for $\theta_0 = 45°$, the overall geometry forms a larger retroreflector having more effect on the low frequency, with an average value of 1.5 dB on the 125 Hz octave band compared to −4.7 dB for the equivalent cylinder. This is further confirmed by a low value of $g_\perp$ shown in fig. 6.20d, and a value close to 0 for g as shown in fig. 6.19c, as well as in the simulations comparing figs. 6.12d and 6.12f. For $\theta_0 = 90°$, g and $g_\perp$ have peak values at the same frequency than σ. For $\theta_0 = 0°$, $g_\perp$ appears flat compared to the resonance region of the equivalent cylinder and **N2**. The scattering directions are overall constant above around 1200 Hz indicating the geometrical limit, yet they are dependent on the incident direction as expected.

Figure 6.21 shows the scattering cross sections and the anisotropy factors for **C1** for three different angles of incidence. They are compared with the results obtained for a geometry where the 40° and 50° angle V-grooves are occluded to investigate the effect of such features. Among the three incident directions tested, $\theta_0 = 90°$ results the highest value for σ as shown in fig. 6.21a of 7.1 m at 360 Hz or 32 % more than the asymptotic value. Moreover, σ is relatively high compared to the equivalent cylinder. For $\theta_0 = 45°$, σ is maximum around 370 Hz with a value of 7.0 m, which corresponds to an overshoot of 38 %. For $\theta_0 = 0°$, σ has two maxima at 220 Hz and 320 Hz of similar values about 5.7 m, representing overshoots of about 21 %. In comparison, the maximum overshoot when the V-grooves are occluded happens for $\theta_0 = 90°$ at 320 Hz with a value of 12 %.

At low frequency, the target strengths shown in fig. 6.21b have average values of -2.5 ± 0.7 dB for the 63 Hz octave band, close to that of the equivalent cylinder about −2.7 dB. When the V-grooves are occluded, the average values are -2.6 ± 0.5 dB. For $\theta_0 = 90°$ and 0°, the target strength increases linearly as the frequency doubles, while it is not observed for $\theta_0 = 45°$ on the frequency range considered. For the formers, the differences of the averages on the 2 kHz and 4 kHz octave bands between the geometry with and without grooves of are less than ±0.5 dB, compared to 2.5 dB and 3.1 dB for the latter, indicating that, at high frequency, the backscattering is dominated by the reflections on the flat sides normal to the propagation in these cases. The frequency spacing of the notches for $\theta_0 = 90°$ is approximately 200 Hz, which is in agreement with the path differences between a reflection on the long side and the other planar surfaces at 87 cm in the direction of propagation. Similarly, for $\theta_0 = 0°$ the spacing between notches is about 660 Hz, which is consistent with the distance of 26 cm separating the sides normal to the propagation. These observations hold when the V-grooves are occluded as these sides are not modified. The highest difference between the actual and the simplified cross section is found for $\theta_0 = 0°$ on the 250 Hz octave band with average values of 0.8 dB and −6.5 dB, respectively.

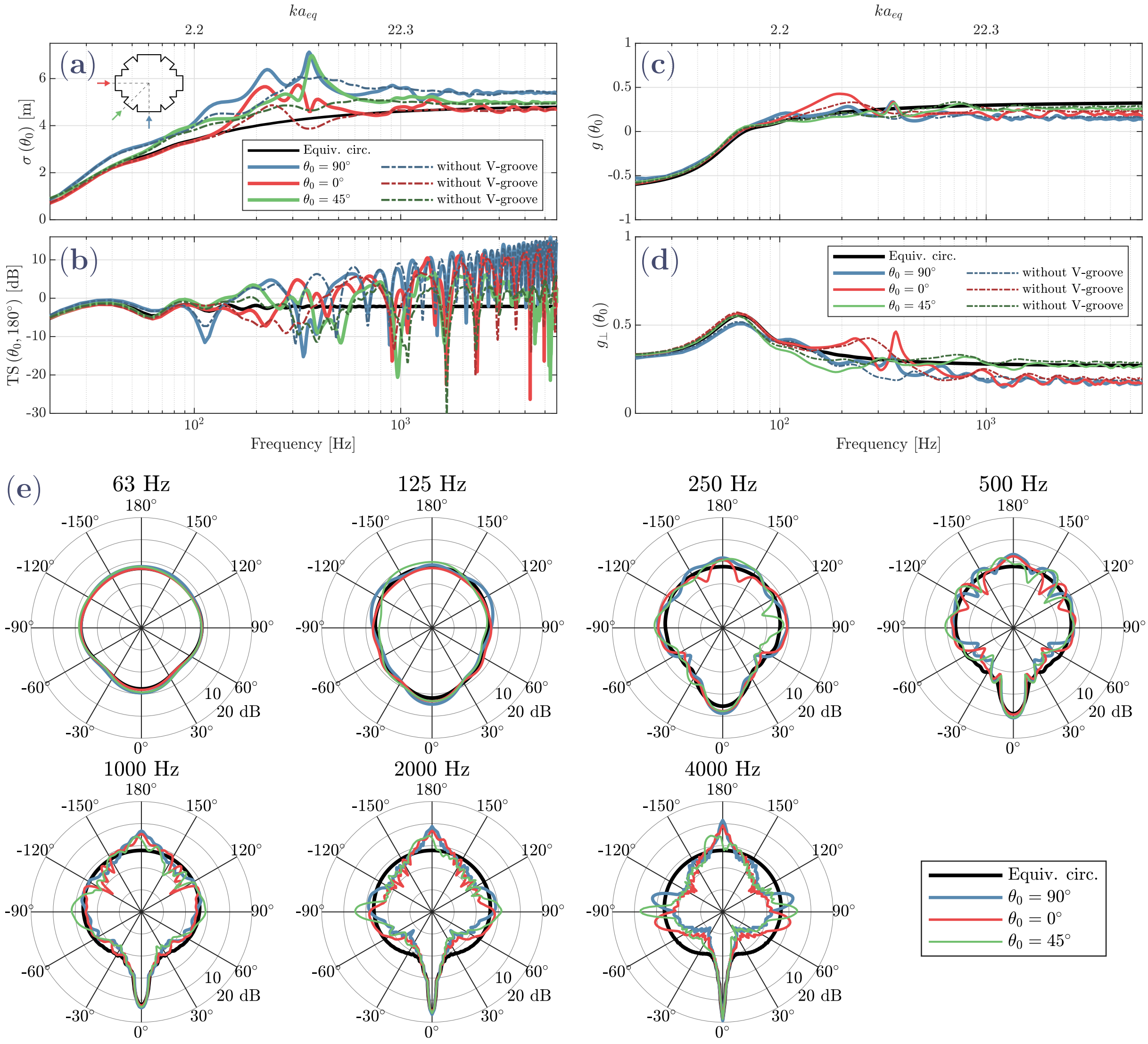

Figure 6.21 Total scattering cross section σ **(a)**, monostatic target strength $\mathrm{TS}(\theta_0, 180°)$ **(b)**, and anisotropy factors g **(c)** and $g_\perp$ **(d)** as functions of frequency, and average octave-band target strengths **(e)** represented with the plane wave coming from the top, for different incidence angles θ_0 for **C1** (solid lines) and with the V-grooves occluded (dash-dotted) compared to its equivalent cylinder with $a_{eq} = 122\,\mathrm{cm}$.

At low frequency, the asymmetry factors shown in fig. 6.21c are comparable to that of the equivalent cylinder. For $\theta_0 = 0°$, g is maximum around 200 Hz and has a local maximum at 350 Hz, also appearing for the other angles. They are accompanied by local increases in transverse scattering as shown in fig. 6.21d, with a local minimum around 310 Hz. $g_\perp$ is flatten around the resonant regime for $\theta_0 = 90°$. Above 100 Hz, the anisotropy factors g and $g_\perp$ vary less overall for the geometry without V-grooves. At high frequency, the incidence $\theta_0 = 45°$ is overall more scattered in the forward and transverse directions compared to the other angles, as the large flat sides reflect the wave in these directions. Moreover, $g_\perp$ varies around the equivalent cylinder values. The scattering directions are influenced by the grooves from 100 Hz to 1600 Hz, above, the reflections from the flat sides dominate overall. This is confirmed by the peaks appearing in the

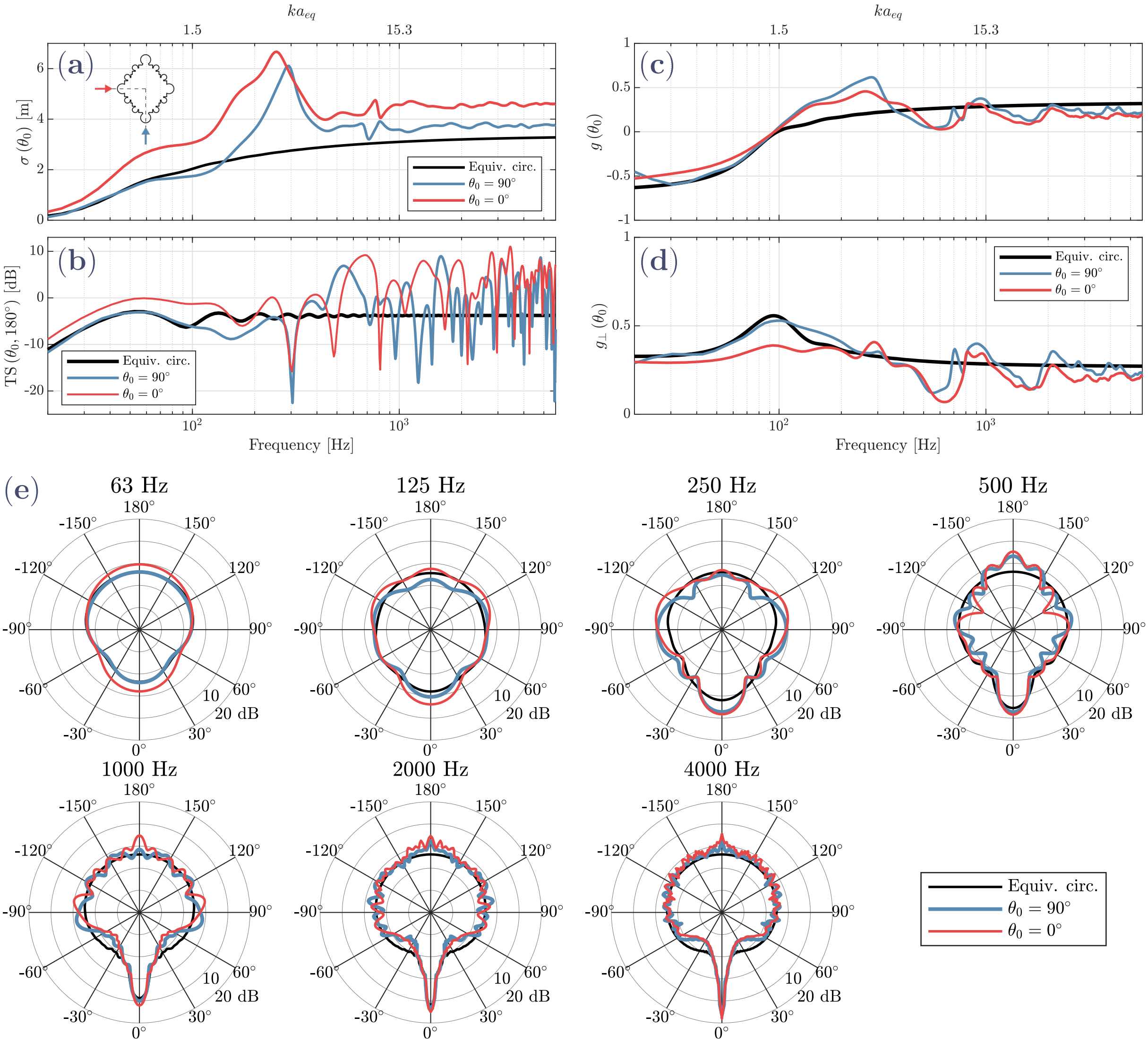

Figure 6.22 Total scattering cross section σ **(a)**, monostatic target strength $\mathrm{TS}(\theta_0, 180°)$ **(b)**, and anisotropy factors g **(c)** and $g_\perp$ **(d)** as functions of frequency, and average octave-band target strengths **(e)** represented with the plane wave coming from the top, for different incidence angles θ_0 for **T** compared to its equivalent cylinder with $a_{eq} = 84\,\mathrm{cm}$.

average octave-band bistatic target strengths. The directions of scattering appear to be globally constant. Nevertheless, oscillations are observed for $\theta_0 = 90°$ and $0°$ in g and in $g_\perp$ for the latter, revealing the influence of the grooves at high frequency with oblique incidence.

The scattering results for **T** are shown in fig. 6.22. For $\theta_0 = 90°$, σ, shown in fig. 6.22a, is overall greater than the equivalent cylinder, with a maximum value of 6.7 m at 256 Hz, representing an overshoot of 44 %. For $\theta_0 = 0°$, σ follows the curve of the equivalent cylinder at low frequency, then appears slightly smaller from 70 Hz to 150 Hz, to reach its maximum of about 6.1 m at 293 Hz, representing an overshoot of 60 % compared to the geometrical limit. This is in agreement with the previous results where the effect of the aspect ratio is similar, the wave will be globally more scattered for the configuration where the cast shadow is the longest.

The target strength shown in fig. 6.22b is higher for $\theta_0 = 0°$ at low frequency, with average values of -0.5 dB and -2.5 dB for the 63 Hz and 125 Hz octave bands, respectively. In comparison, the respective average values are -3.9 dB and -7.3 dB for $\theta_0 = 90°$ and -3.9 dB and -4.5 dB for the equivalent cylinder. For both angles, a notch is present at 305 Hz. At high frequency, the average values are increased. For the frequency range covered by the 500 Hz to 4000 Hz octave bands, they are 2.0 ± 1.4 dB and 5.1 ± 0.5 dB for $\theta_0 = 90°$ and 0°, respectively, compared to -3.8 dB for the equivalent cylinder.

For frequencies above 400 Hz, the anisotropy factors g and $g_\perp$ shown in figs. 6.22c and 6.22d are similar for the two angles. At low frequency, $g_\perp$ appears flatter for $\theta_0 = 0°$. This can be explained by the diamond shape of the geometry that can deflect more energy in the transverse directions when the wave hits the acute angle and visible in fig. 6.13f. Around the frequency range where TSCSs are maximum, *i.e.* from 150 Hz to 350 Hz, g is increased for both angles, indicating an increase of forward scattering. This is accompanied by a slight increase in $g_\perp$. This is attributed to the four circular cylinders engaged at the corner of the cross section, increasing forward-transverse scattering as already observed for **N2** and **N1**.

The results for **Ch** are shown in fig. 6.23 for two angles $\theta_0 = 90°$ and 0° and further compared, for this latter, with the scattering simulated for the convex hull of the cross section, represented with dash-dotted lines. As previously observed, σ is greater overall for $\theta_0 = 90°$ except around 450 Hz as shown in fig. 6.23a, as it casts the longest shadow. Its maximum value is 4.3 m at 340 Hz, representing an overshoot of 41 %. For $\theta_0 = 0°$, the maximum is 4.1 m at 355 Hz, representing an overshoot of 55 %. The convex hull has a TSCS very close to that of the equivalent cylinder.

At low frequency, below 150 Hz, the target strengths represented in fig. 6.23b are overall similar, with average values for the 63 Hz and 125 Hz octave bands of -3.9 ± 0.7 dB and -5.7 ± 0.3 dB for **Ch**, respectively, compared to -4.5 dB and -5.6 dB for the equivalent cylinder and -5.1 dB and -6.5 dB for the convex hull. In comparison to **T**, the shape of **Ch** is rounder so the increase for $\theta_0 = 0°$ compared to $\theta_0 = 90°$ is smaller. At high frequency, the backscattering is on average increased, compared to the equivalent cylinder and the convex hull. This latter presents a obtuse wedge where the plane wave hits, therefore, backward and transverse directions are favored in the geometrical limit. On average, the target strength is -0.3 ± 1.4 dB on the 500 Hz to 4000 Hz octave bands for $\theta_0 = 0°$, compared to -11.3 ± 1.5 dB for the convex hull.

This is confirmed by the higher values of g and $g_\perp$ represented in figs. 6.23c and 6.23d, respectively. The convex hull case appears almost as a bounding value compared to the actual cross section with the same θ_0. The curves separate at 350 Hz and g has a local minimum close to zero around 500 Hz. On the other hand, $g_\perp$ has also a minimum on this frequency range, indicating an increase of backscattering, further confirmed by the peak in target strength and visible in fig. 6.13h. This is not found for $\theta_0 = 90°$. Above 600 Hz, the anisotropy factors are comparable for both incidence angles and varies in a similar fashion and amplitudes compared to the equivalent cylinder, similarly to **T** (figs. 6.22c and 6.22d).

6.3.2.3 Piers with *colonnettes en délit*

Figure 6.24 shows the results for **C2**. They are compared additionally with the results where the small circular cylinders are removed. TSCSs shown in fig. 6.24a are greater without *colonnettes* compared to the actual geometry, except at very low frequency in

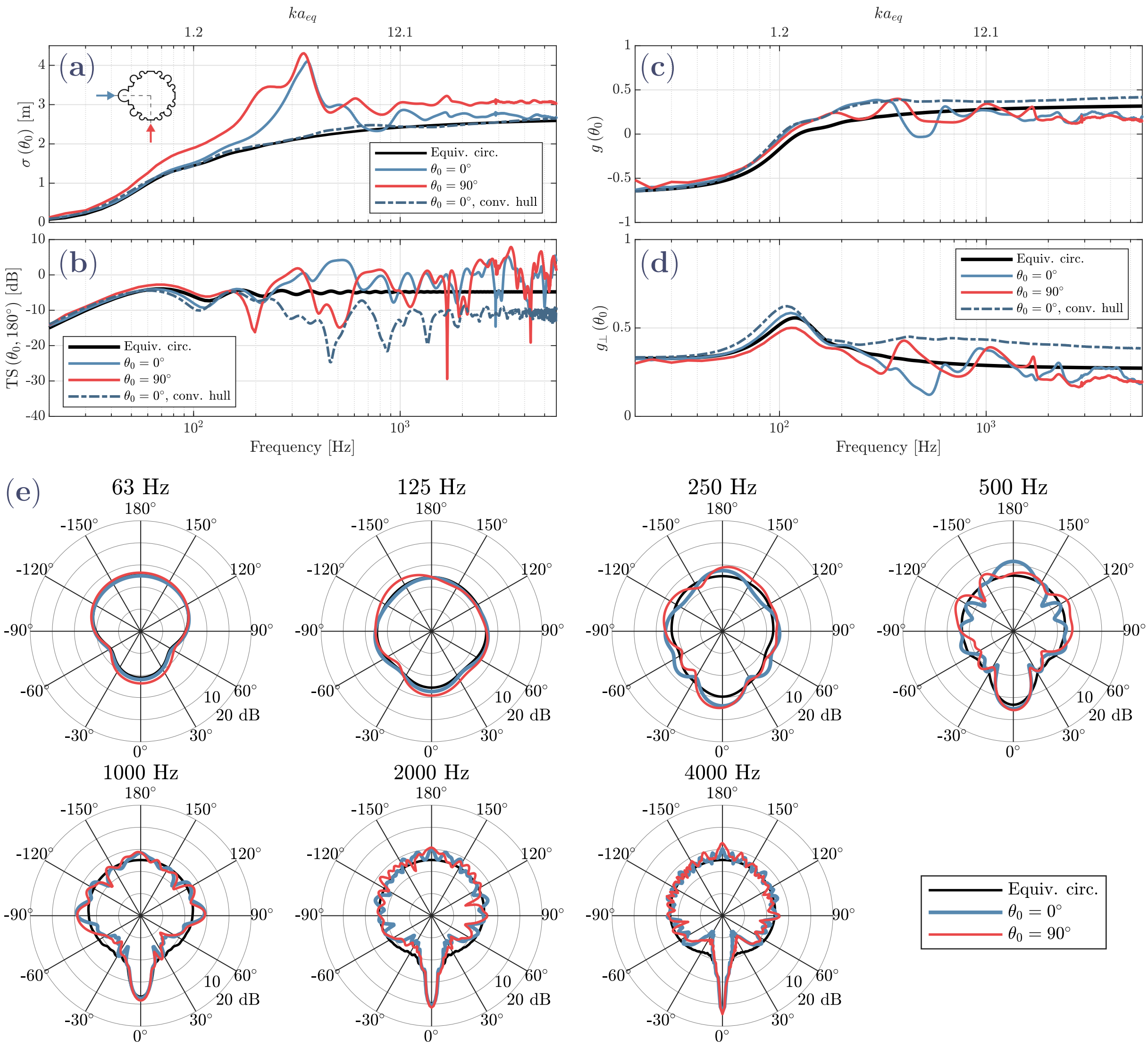

Figure 6.23 Total scattering cross section σ **(a)**, monostatic target strength TS$(\theta_0, 180°)$ **(b)**, and anisotropy factors g **(c)** and $g_\perp$ **(d)** as functions of frequency, and average octave-band target strengths **(e)** represented with the plane wave coming from the top, for different incidence angles θ_0 for **Ch** (solid lines) compared to its equivalent cylinder with $a_{eq} = 66$ cm, and its convex hull (dash-dotted line).

agreement with Rayleigh scattering with a crossing of curves at different frequencies depending on the angle of incidence; about 40 Hz, 70 Hz, and 130 Hz for $\theta_0 = 90°$, 45° and 0°, respectively. This trend is reversed above approximately 350 Hz. For $\theta_0 = 45°$, TSCSs are similar around 200 Hz with or without cylinders. At low frequency, similarly to previous results, σ is higher for the propagation along the small axis, *i.e.* for $\theta_0 = 90°$, and lower than the equivalent cylinder for the propagation along the long axis, *i.e.* for $\theta_0 = 0°$ below 170 Hz. TSCSs are overall constant above 1700 Hz.

The target strengths at low frequency are comparable to that of the equivalent cylinder as show in fig. 6.24b. The average for the 63 Hz octave band are −4.3 dB and −4.6 dB for $\theta_0 = 0°$ and 45°, respectively, compared to −4.0 dB and −4.9 dB without cylinders, and −4.2 dB for the equivalent cylinder. The highest average values are found for $\theta_0 = 90°$ with

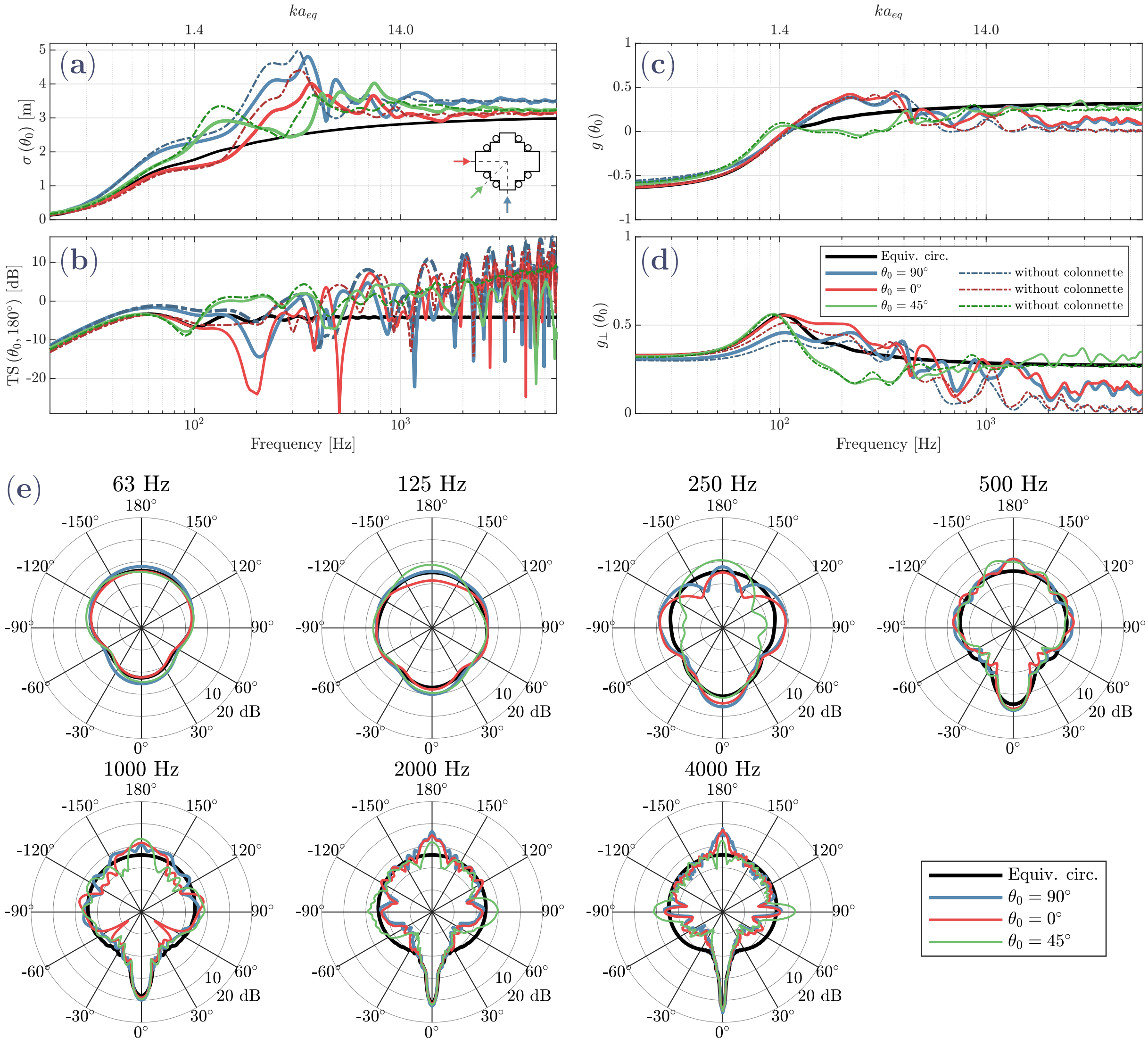

Figure 6.24 Total scattering cross section σ **(a)**, monostatic target strength $\mathrm{TS}(\theta_0, 180°)$ **(b)**, and anisotropy factors g **(c)** and $g_\perp$ **(d)** as functions of frequency, and average octave-band target strengths **(e)** represented with the plane wave coming from the top, for different incidence angles θ_0 for **C2** (solid lines) compared to its equivalent cylinder with $a_{eq} = 76\,\mathrm{cm}$, and without *colonnettes* (dash-dotted line).

$-2.2\,\mathrm{dB}$ and $-1.7\,\mathrm{dB}$ with and without cylinders, similarly to previous results. Around 200 Hz, the target strengths are low for $\theta_0 = 90°$ and $0°$ compared to their counterpart without cylinders. The average values for the 125 Hz and 250 Hz octave bands are $-4.3\,\mathrm{dB}$ and $-2.3\,\mathrm{dB}$ for $\theta_0 = 90°$, respectively, compared to $-2.6\,\mathrm{dB}$ and $-1.0\,\mathrm{dB}$ without cylinders, and $-8.5\,\mathrm{dB}$ and $-4.9\,\mathrm{dB}$ for $\theta_0 = 0°$, compared to $-5.9\,\mathrm{dB}$ and $-3.8\,\mathrm{dB}$. The values are greater for $\theta_0 = 45°$, with averages of $-1.4\,\mathrm{dB}$ and $0.7\,\mathrm{dB}$ for these octave bands, similar to the case without cylinders of averages $-0.4\,\mathrm{dB}$ and $1.9\,\mathrm{dB}$. The presence of the cylinders increase the backscattering for $\theta_0 = 45°$ on the 1 kHz octave band, with average values of 3.1 dB and 1.5 dB with and without, respectively. This corresponds to $ka \approx 1.5$ with respect to the small cylinder radii, that falls in a peak region in the form function amplitudes reported by (Hasheminejad et al., 2006). The target strengths increase linearly on average above 600 Hz as the frequency doubles, except for $\theta_0 = 45°$, reflecting the dominance of the flat normal sides similarly to **C1**.

The asymmetry factors represented in fig. 6.24c are similar for $\theta_0 = 90°$ and 0° above 70 Hz. They are greater than the equivalent cylinder between 110 Hz and 410 Hz, and lower above. On average, the values are higher for the geometry with the cylinders compared to without, especially at high frequency. The similarity between $\theta_0 = 90°$ and 0° is also found for $g_\perp$ represented in fig. 6.24d, with the difference that the curve is flatter compared to the resonant regime of the equivalent cylinder, as already observed on previous results. In contrast, g is greater than the equivalent cylinder for $\theta_0 = 45°$ at low frequency, below 110 Hz, and lower above. This is accompanied by a plateau of minimum values for $g_\perp$, confirming an increase in backscattering attributed in this case to the dihedral corners. Compared to **C1**, the effect is greater since they both have right angles and the incidence is normal on both for this angle. At high frequency, the cylinders increase transverse scattering and they induce more oscillations in g and $g_\perp$. This is attributed to the multiple interactions of the scattered waves resulting in a more variable directionality (Hasheminejad et al., 2006), or resonances of the volumes between the core and the *colonnettes*.

Figure 6.25 shows the results for **N3** for $\theta_0 = 15°$, *i.e.* the wave hits two colonnettes simultaneously first, and for $\theta_0 = 0°$, the other symmetric setup. TSCSs shown in fig. 6.25a are similar for both angles at low frequency, below 850 Hz. Above, they vary in opposite ways. They are maximum around the same frequency at 430 Hz, corresponding to $ka = 1.3$ with a the small cylinder radius. For $\theta_0 = 0°$ and 15°, the values are 3.9 m and 3.6 m, representing overshoots of 90 % and 70 %, respectively. This is the highest ones of all the geometries and incidence angles considered, as this particular one is propitious to multiple scattering, having several cylinders and therefore more boundaries to interact with the wave over a restricted area compared to the others. They are overall greater than that of the equivalent cylinder, except for $\theta_0 = 0°$ from 900 Hz to 990 Hz. Other plateau values, overshooting the geometrical limit, are found on overlapping frequency ranges, from 1050 Hz to 1600 Hz and from 1280 Hz to 2160 Hz for $\theta_0 = 0°$ and 15°, respectively.

The target strengths shown in fig. 6.25b are similar to the equivalent cylinder below 300 Hz for both angles, with average values of −6.0 dB and −6.1 dB on the 63 Hz to 125 Hz octave-band frequency range for $\theta_0 = 0°$ and 15°, respectively, compared to −6.3 dB. Above the peaks and notches of respective curves appear in opposition. This is also visible in figs. 6.14f and 6.14h for the backscattering over a rather large angular portion. The average values for the 500 Hz, 1000 Hz, and 2000 Hz octave bands are −3.1 dB, −0.6 dB, and −0.4 dB for $\theta_0 = 0°$, and −0.9 dB, −5.2 dB, and 0.7 dB for $\theta_0 = 15°$, respectively.

The variations of g represented in fig. 6.25c are strongly correlated with those of σ (fig. 6.25a). The peak and plateau values found in σ appear to be associated with an increase of forward scattering. They are not correlated with an increase of $g_\perp$ as shown in fig. 6.25d, indicating transmission of sound in the shadow region. This is further confirmed by the peak values found in figs. 6.14f and 6.14h in the direction θ_0. At low frequency, the factors are very similar to the equivalent cylinder as already seen for TSCSs and the target strengths. Local increases of $g_\perp$ are observed from 750 Hz to 1100 Hz for both angles.

6.3.3 Influence of the geometrical features

The scattering is influenced at different frequencies depending on the scales of the geometrical features. At low frequency, the roundness or the elongation of the cross

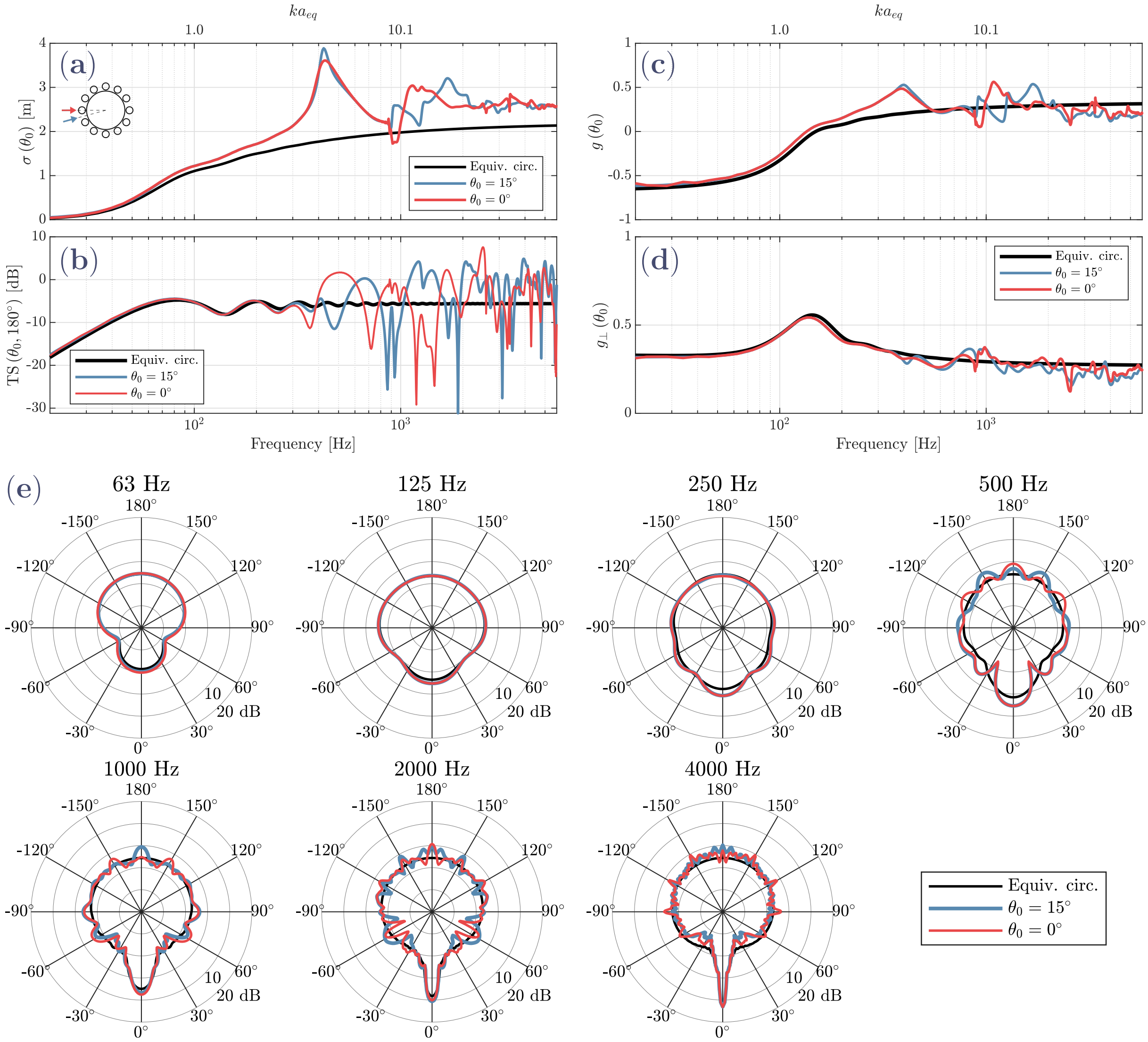

Figure 6.25 Total scattering cross section σ **(a)**, monostatic target strength TS$(\theta_0, 180°)$ **(b)**, and anisotropy factors g **(c)** and $g_\perp$ **(d)** as functions of frequency, and average octave-band target strengths **(e)** represented with the plane wave coming from the top, for different incidence angles θ_0 for **N3** compared to its equivalent cylinder with $a_{eq} = 76\,\text{cm}$.

sections are important factors for the strength and the directionality. The backscattering will be increased when the incidence is normal to the long axis, reflected by higher TSCS and target strength, and lower $g_\perp$. The more it is elongated, the higher g is and $g_\perp$ does not grow as much in its ascending phase compared to equivalent cylinder and other angles of incidence. For **N1**, the section is not elongated but it is not round. In this case, g is not different but the observation for $g_\perp$ holds. On the contrary, as expected, the sections that are rounder are well modeled by their equivalent cylinder as seen for the fluted columns or **N3**.

For wavelengths close to the characteristic size of a geometrical element of a section, be it the radius of a circle, the distance between two corners or discontinuities in a general way or the opening length of locally concave parts, the scattered wave will be the most impacted. Since it corresponds to the frequency band of the resonant regime of these smaller elements where the direction of scattering varies strongly and its amplitude increases, the wave scattered by one will interact with its neighbors and this multiple times. In general, TSCS reaches its maximum and exceeds the geometric limit. Of course for this to be true it is necessary that several size scales are identifiable. **N2** for example has a rather defined cross section, the reflected wave fronts have a clear origin and the multiple interactions are limited. **N1** has a few of the rather large engaged circles, therefore the scattering will depend on the incidence angle. The maxima of TSCS seem to be less dependent on this parameter when the geometrical details of a cross section are numerous and, therefore, smaller, as seen for the fluted columns, and the Gothic piers **T**, **Ch**, and **N3**, yet local features on the section can have an influence depending on their size and their relative position to the incident wave.

At high frequency, the geometrical regime is reached if the wavelength is small compared to the smallest element. But at the same time, the smaller it is and the less energy is scattered. For example, **N2** and **N1** have a constant scattering behavior at high frequency, while this is not the case for the others to some extent, nevertheless the oscillations seems to decrease in amplitude. The scattering strength and its direction is overall dominated by the larger elements, especially flat sides when they are under incidence and large compared to the other elements, as seen for **C1**. For **C2**, the particular positions of the *colonnettes*, near re-entrant corners, result in variations of scattering angular distribution even at relatively small wavelengths. This is also observed for **N3** and the geometries with cavities formed by the multiple intersecting circles and corners such as **Ch**, and **T**.

The cross sections studied have relatively different geometrical features overall, nevertheless comparisons with simplified or elementary geometries have allowed us to propose some explanations and to evaluate the differences with such approximations. It would be necessary to conduct further scattering characterizations on parametric geometries to better identify some mechanisms and verify some of our speculations.

6.4 Audibility of the scattering

In this section, the simulations results are presented in a perceptually relevant way to discuss the audibility of the scattering from the obstacles with respect to the results of the literature presented in section 2.5.3. The impulses are analyzed in time-frequency domain using the continuous wavelet transform. This allows to compare the time spreading of the reflections, restricted in the following to the backscattering direction. They are then expressed in terms of reflected to direct level ratios, to be compared with the audibility thresholds reported in the literature.

6.4.1 Time-frequency analysis

Figures 6.26 and 6.27 show the simulated pressure signals for some piers of Notre-Dame de Paris and the fluted columns, respectively, at 4 m from the centroid of different cylinders in the backscattering direction and their wavelet scalograms in dB where each scale has been normalized by the maximum value obtained for the incident pulse. The continuous wavelet transform has been performed using the function `cwt` implemented in the Wavelet Toolbox version 5.5 of MATLAB 2020a. It has been computed using Morse

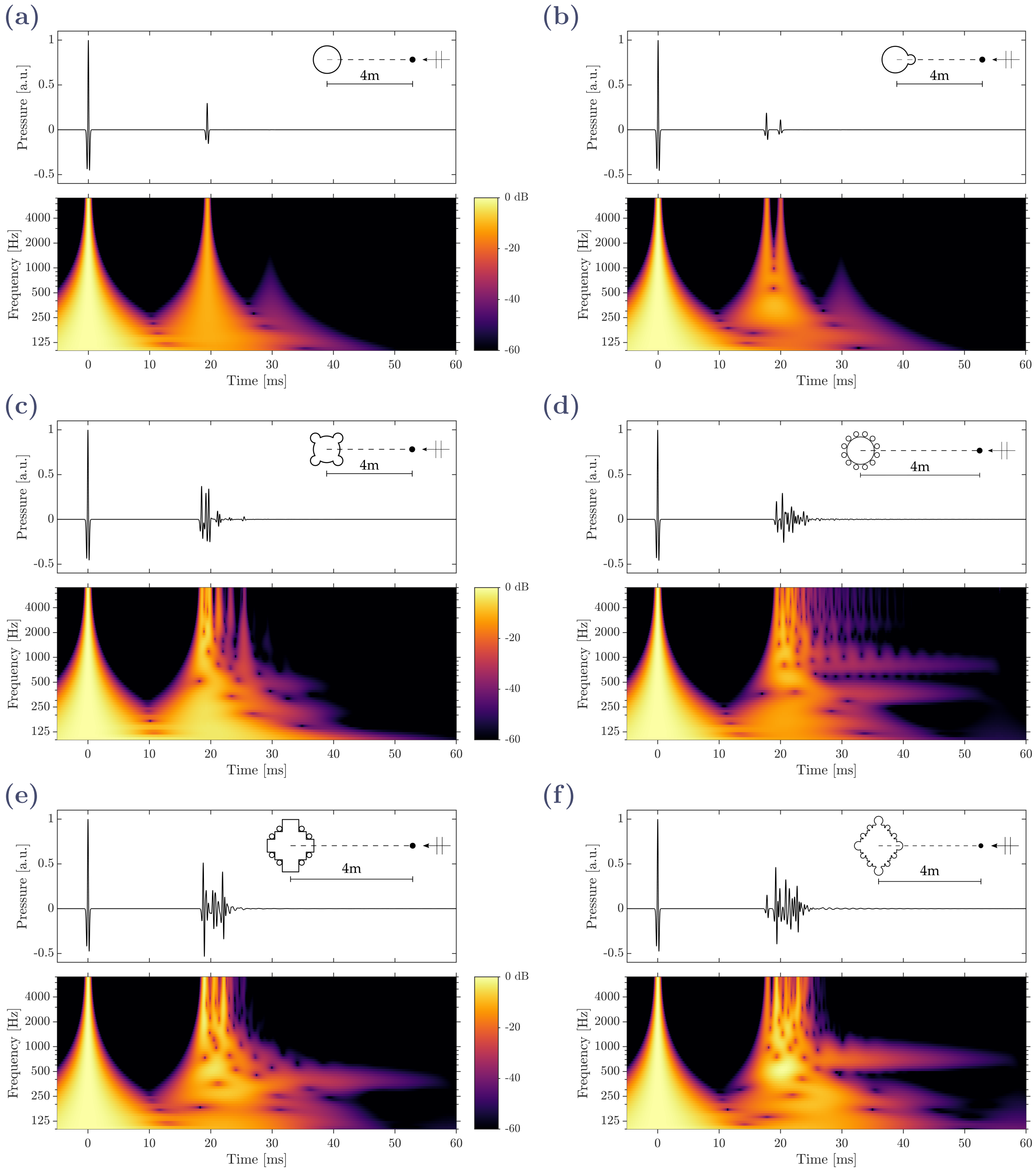

Figure 6.26 Pressure signal and corresponding wavelet scalogram normalized with the maximum of that of the free-field for **(c)** **N1** with $\theta_0 = 45^\circ$, **(d)** **N3** with $\theta_0 = 15^\circ$, **(e)** **C2** with $\theta_0 = 90^\circ$, and **(f)** **T** with $\theta_0 = 0^\circ$ at 4 m from their center in the backscattering direction.

wavelets which can be expressed in the frequency domain

$$\Psi_{\beta,\gamma}(\omega) = H(\omega) a_{\beta,\gamma} \omega^{\beta} e^{-\omega^{\gamma}} , \tag{6.3}$$

where H is the Heaviside step function, ω is the angular frequency, $a_{\beta,\gamma}$ is a normalizing constant, β is a compactness parameter, and γ characterizes the symmetry (Lilly et al., 2009). The signals are transformed using 10 voices per octave with parameters set to $\beta\gamma = 25$ and $\gamma = 3$.

As expected, the temporal structure of the backscattered pulses depends strongly on

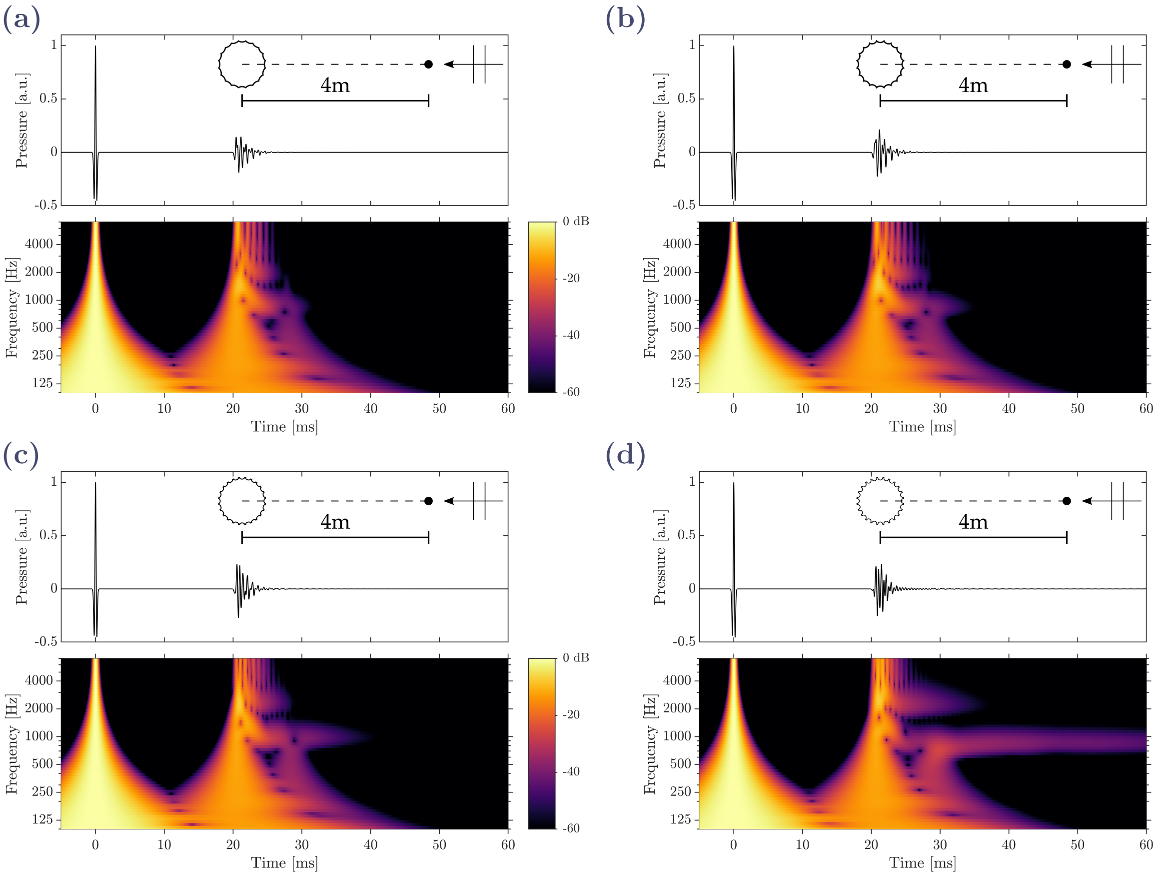

Figure 6.27 Pressure signal and corresponding wavelet scalogram normalized with the maximum of that of the free field for **(a) D1**, **(b) D2**, **(c) I1**, and **(d) I2** with $\theta_0 = 0°$ at 4 m from their center in the backscattering direction.

the geometry of the diffuser. Figure 6.26a represents the results obtained for a circular cylinder of diameter 133 cm, corresponding to the columns of the nave arcade columns, and to the central part of **N1** and **N2**. In the time domain, the first arrival after the direct sound has a relative peak level of -10.5 dB, which is approximately the value found in the scalogram. A second arrival is visible in the scalogram at low frequency, 30 ms after the direct sound, corresponding to the creeping waves circumventing the cylinder that are strongly attenuated at high frequency. It is not visible in the signal as its relative peak level is -62 dB. For **N2** with $\theta_0 = 90°$ (fig. 6.26b), there are two visible arrivals, corresponding to the reflections on the two circular parts constituting the cross section, with relative peak levels of -14.5 dB and -18.9 dB. The arrival due to the creeping waves is still visible in the scalogram and has a level and frequency range similar to the circular cylinder. For **N1** with $\theta_0 = 45°$ (fig. 6.26c), the pressure signal is composed of a three localized pulses between 18 ms to 20 ms after the direct sound with -9.5 ± 1.1 dB relative peak levels. The latter arrivals are due to higher order reflections between the different part of the cross section that account for about 4 % of the cumulative energy of the backscattered pulse. Its normalized wavelet scalogram also shows spreading of low frequency similarly to the previous geometries. For **C2** with $\theta_0 = 90°$ (fig. 6.26e), the wave packet has visible pulses at its onset and offset. They are attributed to the reflections on the plane faces of the cylinder whose normal is colinear with the direction of propagation. In comparison, those of **N3** (fig. 6.26d) and **T** (fig. 6.26f) look more like diffuse reflections (Robinson et al., 2011).

This is also the case for the fluted columns shown in fig. 6.27, where their envelope describes a fast growth followed by a slower decay like a reflection on a Lambertian surface (Wendt et al., 2021) or the model using a Gamma function proposed by Robinson et al. (2013a). As already observed in the previous section, **D2** in fig. 6.27b backscatters more than **D1** in fig. 6.27a with respective maximum peak levels of −12.9 dB and −14.4 dB. Comparing **I1** in fig. 6.27c and **I2** in fig. 6.27d, their maximum peak levels are closer and respectively equal to −11.3 dB and −11.9 dB, however more energy seems to be concentrated around the maximum of the envelope for the latter. The low-frequency creeping waves are observable in each scalogram. At 500 Hz, the maximum relative level for these waves is −38.5 dB at 28.1 ms after the direct sound for **D1** compared to −29.4 dB at 28.9 ms for**I2**, in agreement with the observations made in the previous section.

Resonance tails are visible in the scalograms of the sections with smaller scale geometrical features, *i.e.* for **N3**, **C2**, **T**, and **I2** thus favoring multiple interactions during scattering. The column **N3** in fig. 6.26d has two resonances over the considered frequency range. The first one occurs at around the same frequency as **C2** in fig. 6.26e, around 400 Hz. The second one is around 850 Hz and seems to decay slightly slower. The resonance of **T** in fig. 6.26f is around 700 Hz. For **I2** in fig. 6.27d, a first resonance is around 900 Hz and second one seems to appear around 2500 Hz. A resonance around 1000 Hz can also be observed for **I1** in fig. 6.27c but it decreases faster than that of **I2** and hardly appears for the considered range. They all have low amplitudes, so they hardly appear on the linear scale of the pressure signals and account for a very small part of the cumulative energy of the backscattered pulses, less than 0.2 % for **T** for instance.

6.4.2 Reflected-to-Direct Level Difference

To analyze the reflected signals in a way that is relevant to our perception of sound, the Reflected-to-Direct Level Differences (RDLDs) proposed by Pelegrín-García et al. (2016) are calculated for each one-third octave band in order to better observed the spectral and strength differences depending on the geometry of the cylindrical obstacle, the incidence angle, and the direction of scattering. They are calculated in the frequency domain with the discrete equivalent of

$$\mathrm{RDLD}_f = 20\log_{10}\sqrt{\frac{1}{f_2 - f_1}\int_{f_1}^{f_2}\left|\frac{p_s(\omega)}{p_i(\omega)}\right|^2 d\omega}\,, \tag{6.4}$$

where f_1 and f_2 are the edge frequencies of the fractional octave band f. Moreover, to be compared with the audibility thresholds reported in the literature, a single-number RDLD (Pelegrín-García et al., 2016) is also calculated, taking into account the spectral sensitivity of the ear, with

$$\mathrm{RDLD} = 10\log_{10}\left(\frac{\sum_{f=1}^{N} 10^{\frac{\mathrm{RDLD}_f + T_{W,f}}{10}}}{\sum_{f=1}^{N} 10^{\frac{T_{W,f}}{10}}}\right)\,, \tag{6.5}$$

where RDLD_f are the one-third octave-band RDLDs, $f = 1, \ldots, N$, and $T_{W,f}$ are the weights obtained by inverting the equal loudness curve at 40 phons according to ISO 226:2003. Note that no additional weighting is applied, contrary to Pelegrín-García et al. (2016), which is equivalent to considering a flat source magnitude spectrum.

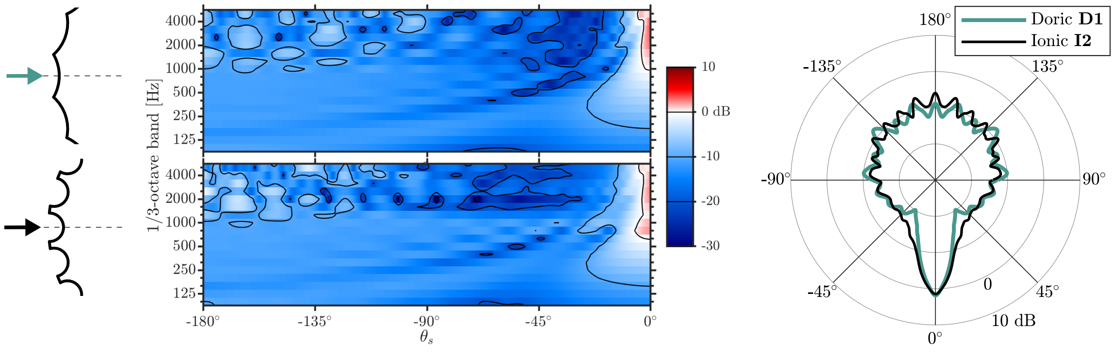

(a)

(b)

Figure 6.28 One-third octave-band (a) and overall (b) RDLDs for **D1** and **I2** for receivers at 3.1 m from their center.

Figures 6.28 and 6.29 represent the results obtained for the fluted columns **D1** and **I2** for $\theta_0 = 0°$, and the Gothic piers **N2**, **C1**, **C2**, and **N3** for two incidence angles for each one, respectively. We recall that they are derived from simulations representing the experimental set-ups reported in table 6.1 where the distances of the receivers to the center of the section are indicated for each one. The one-third octave-band RDLDs are shown on a semicircle only, since the configurations are symmetrical. Moreover, RDLDs for the positions located in shadow zone are also represented, however, they can not be interpreted as such because of the interference between the incident and scattered pressures occurring in this region.

We have noticed that among the fluted columns, **D1** and **I2** differ the most, so we compare only these two in fig. 6.28. The RDLDs in fig. 6.28a in the bascattering region are quite similar below the 800 Hz one-third octave band with values around -11 dB. In the transverse region, **I2** seems to scatter more than **D1**, especially around $\theta_s = -45°$ and the 630 Hz one-third octave band. At high frequency, beyond the 800 Hz one-third octave band, this behavior is reversed. **I2** scatters more in the backward directions and less in the transverse directions compared to **D1**. This is also visible in fig. 6.28b as the overall value weights favorably the high frequencies.

For the piers **N2**, the two incidence angles considered result in strong spectral and strength differences across the scattering directions as shown in fig. 6.29a. For $\theta_0 = 90°$, the overall RDLDs represented in fig. 6.29b are around 3 dB higher in the transverse directions compared to $\theta_0 = 45°$. For the piers **C1**, the RDLDs are very similar up to 1 kHz as shown in fig. 6.29c. Above, the large planar parts of the section favor some directions according to ray acoustics. These particular directions are therefore highlighted in the overall RDLDs, represented in fig. 6.29d, where they found their second maximum around -4 dB and -6 dB for $\theta_0 = 90°$ and 0°, respectively. Their maximum of about 2 dB is found in the backscattering direction as these incidences are normal to large plane faces of the cylinders. This is also the case for **C2** as shown in fig. 6.29e where a positive value of nearly 1 dB is found in the backscattering direction for $\theta_0 = 0°$. For the two incidences considered, the overall RDLDs, represented in fig. 6.29f, differ mainly in this region, for $\theta_s \geq 150°$. Compared to the other section, RDLDs for **N3** seems to depend less on the incidence angle as shown in fig. 6.29g.

Figures 6.30 and 6.31 represent the octave-band RDLDs from 63 Hz to 4000 Hz spatially for **D1** and **I2**, as well as **N1** and **C1**. The delay between a reflection and the direct sound is an important parameter to determine its audibility. The isochrones of

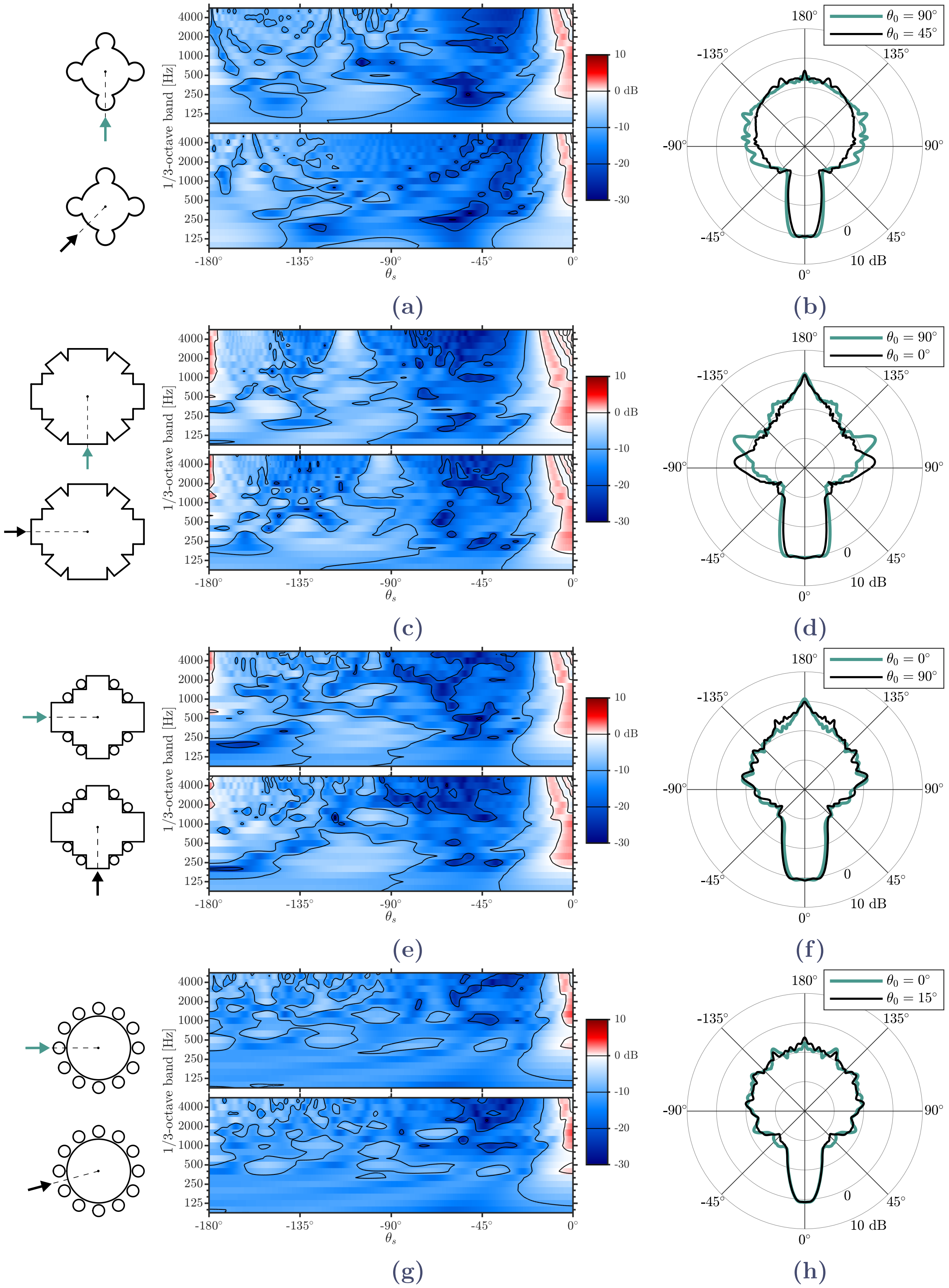

Figure 6.29 One-third octave-band (left) and overall (right) RDLDs for **N2** (a, b), **C1** (c, d), **C2** (e, f), and **N3** (g, h) for different plane wave incidence angles θ_0 as functions of the scattering angle θ_s. The receiver positions are reported in table 6.1.

time difference of arrival are thus represented with green dotted lines and are calculated as the difference between the arrival time of the first reflection and that of the plane wave, assuming that it can penetrate the obstacle at the same speed and when it has reached a point on the boundary, it radiates as a monopole, resulting in the lowest estimate.

The similarity of the low frequency scattering behavior up to the 250 Hz octave band already observed for the fluted columns in fig. 6.30 is confirmed here. The influence of the creeping waves is visible over the 500 Hz and 1000 Hz octave bands where higher levels are found in the transverse-forward regions for **I2** in fig. 6.30b compared to **D1** in fig. 6.30a. At high frequency, over the 1000 Hz octave band and beyond, the backscattering is increased for **I2** as already observed.

The scattered near field of **N1** is visibly high for the 250 Hz octave band in fig. 6.31a, between the engaged shafts, and this can also be observed for **C1** in fig. 6.31b. Strong specular reflections dominate for the latter at higher frequencies, as observed previously.

6.4.3 Discussions

6.4.3.1 Piers and columns as volumetric diffusers

The function of a surface diffuser is to redirect a sound wave in directions other than the specular one and to spread it out in time. From these perspectives, a simple circular cylinder alone achieve the spatial spreading but is not really a good diffuser as it produces a high-pass strongly correlated reflection in the backscattering region (Cox et al., 2016). Moreover, its finite size allows it to interact only in a limited way with the wave that impinges on it. Even in its resonant regime, we have seen that the circumferential waves have a very low level and only exist at low frequency. But as soon as discontinuities are included in the geometry, they are potential sources of scattering that produce additional wavefronts.

The compound piers and fluted columns studied here are all concave and some of them are star-shaped. This allows potentially several interactions of a wave scattered by a part of a shape with another of these parts. This is also true for the piers with *colonnettes* **C2** and **N3**, especially as the small cylinders are close to the central part and to each other. This effect is particularly visible through the existence of resonance frequencies revealed for the latter, as well as for the compound piers with geometric elements of small size such as **T** and the Ionic column **I2**. They are probably the result of coupling between the small cavities formed on the surface of the cylinders creating surface waves as described by Berry et al. (2019) and Farhat et al. (2016). They are by definition localized in frequency and in the cases studied here count very little for the total energy of the reflections. However, around these frequencies, where the wavelengths are of the order of magnitude of the geometrical elements, *i.e.* up to about 1 kHz for the geometries considered here, the scattered power is increased without strongly favoring any particular direction. Contrary to beyond, in the limit of small wavelengths, the scattering directions can be determined according to the acoustic ray model and the overall scattered power is related to the size of the shadow.

We have considered here the obstacles alone, but one may wonder if volumetric diffusion could be possible by multiple scattering between columns. In the cathedral Notre-Dame de Paris, the piers of the nave are approximately 5.5 m between centers. Therefore, based on the RDLDs obtained, following the decreasing of intensity of a spherical wavefront, the level of a re-scattered wave would be too low compared to the other wall reflections. However, this is valid for a far field source and it would be interesting to study

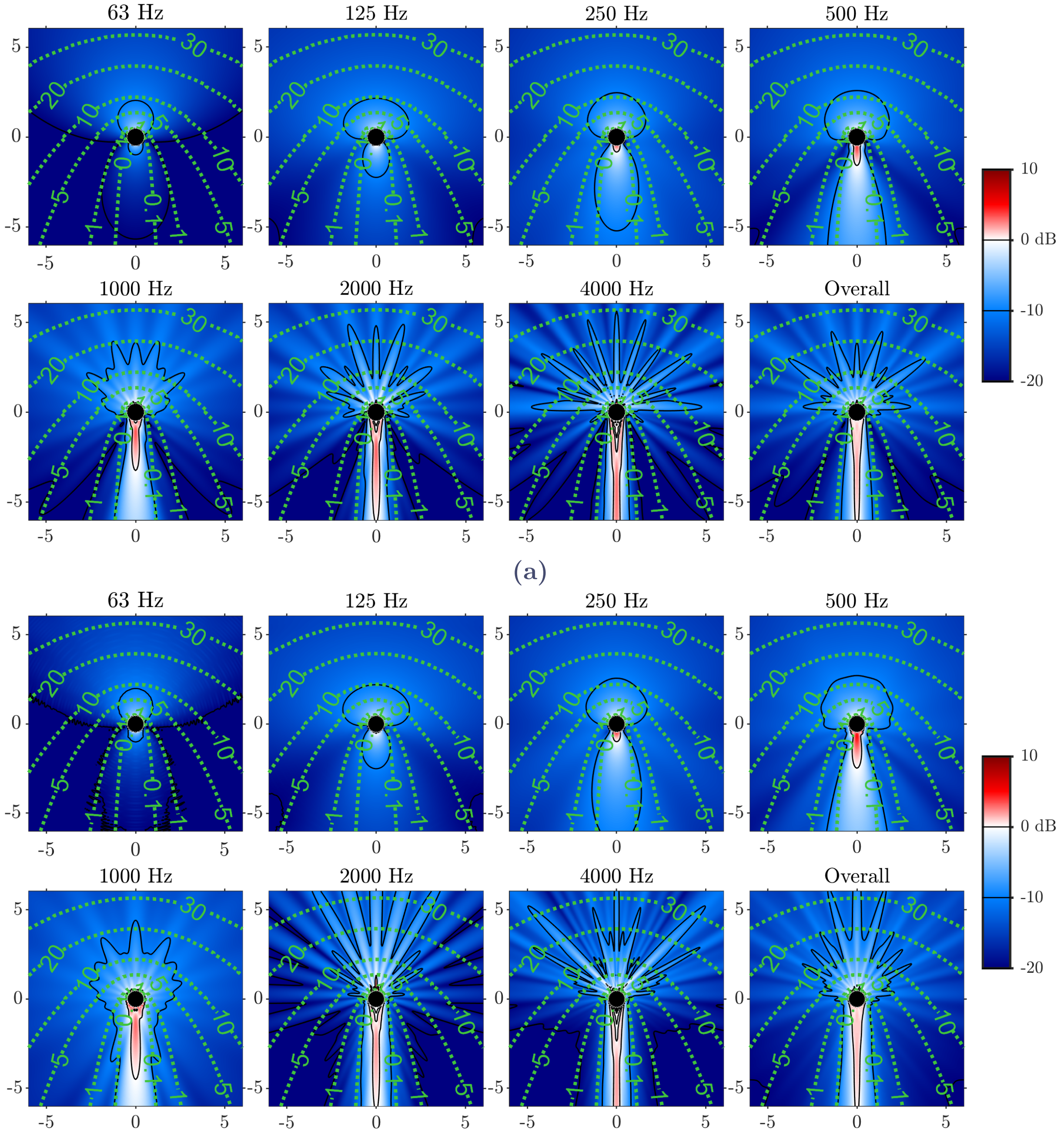

(a)

(b)

Figure 6.30 Octave-band RDLDs in dB for a plane wave going from top to bottom for **D1** (a) and **I2** (b) for $\theta_0 = 0°$. Isochrones of time difference of arrival in ms are represented with green dotted lines.

the effect of an obstacle near a source for a distant listener. Moreover, their influence on the late reverberation, especially on the modes at low frequency, considering that, in this case, an image-source of a high order of reflections has interacted with a lot of small obstacles, similar to the propagation within a sonic crystal, could be a topic for future investigations.

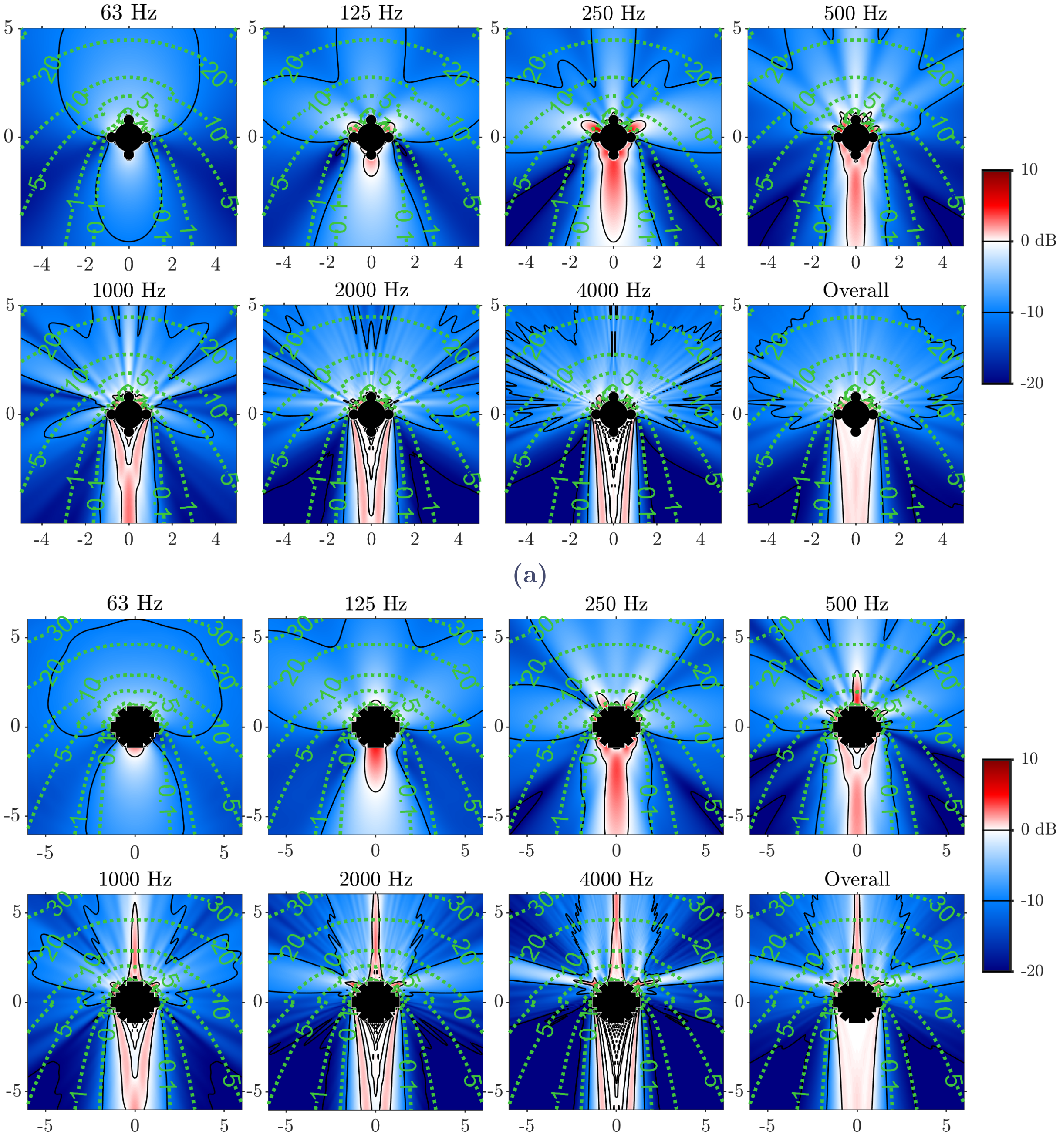

(a)

(b)

Figure 6.31 Octave-band RDLDs in dB for a plane wave going from top to bottom for **N1** (a) and **C1** (b). Isochrones of time difference of arrival in ms are represented with green dotted lines.

6.4.3.2 Audibility of scattering by cylindrical obstacles

The simulations assumed a source positioned at infinity, however, they were shown to be equivalent to the experiments where the source was in the far field, at about 30 m at full scale, and as the receiver is near the obstacle, about 3 m from their center here. This is even more true for the transverse directions which better correspond to a listening situation with a listener facing the source and with an obstacle near him on its side. In this case, the results presented in figs. 6.28 to 6.31 indicate that the reflections have sufficient levels to be audible. For the geometries and configurations shown here, RDLDs

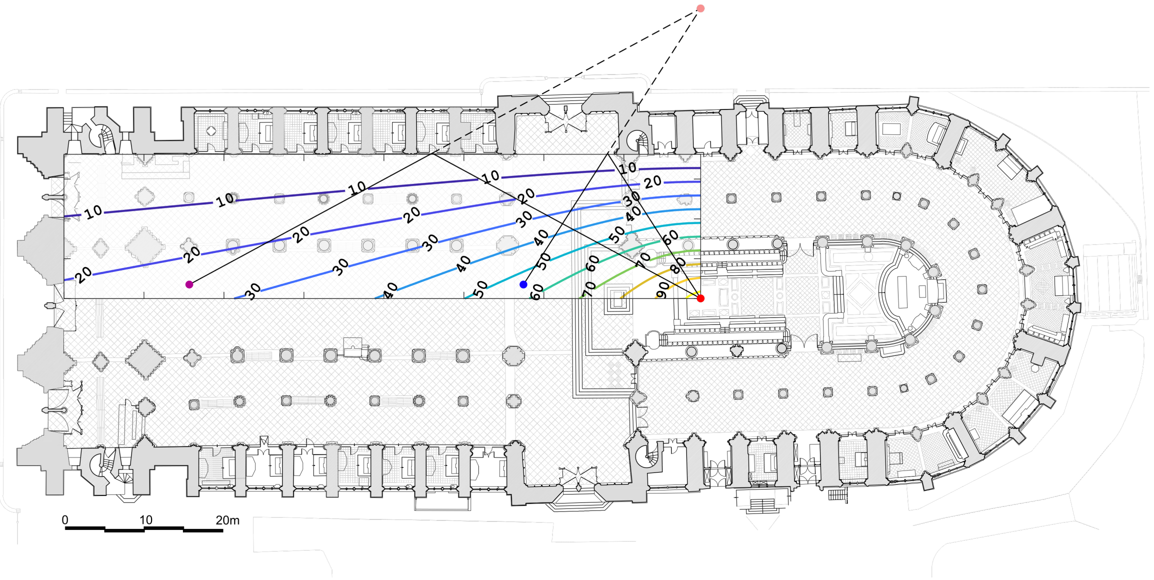

Figure 6.32 Floor plan of Notre-Dame de Paris with time delay in ms between direct sound and the reflection from a lateral wall for a source located in the choir represented by a red dot.

in the direction $\theta_s = 90°$ are greater than -20 dB, which is approximately the thresholds of audibility reported by Pelegrín-García et al. (2016) or the criterion used by Rathsam et al. (2010). They are between -15 dB and -10 dB, except for **C1**, where values exist up to -6 dB and -4 dB, for $\theta_0 = 0°$ and $90°$, and $\theta_s = 95°$ and $113°$, respectively.

For such levels, the reflections are audible through changes in coloration rather than loudness. Humans are more sensitive to spectral overlap below 1 kHz (Buchholz, 2011), which is the range that is best scattered in all directions. Furthermore, in a binaural context, it has been shown that a reflection coming from a lateral direction was more audible than if it came from the same direction or from behind (Begault et al., 2003; Olive et al., 1988; Zhong et al., 2018). However, as already mention, for positions more distant in the transverse directions, the decreasing of intensity becomes important enough so that the reflected wave becomes undetectable. Comparing the one-third octave-band RDLDs between piers, the spectral differences seem significant enough to discriminate between these reflections. With preliminary listening of the impulse responses, columns inducing diffuse reflections are discernible from a simple circular cylinder, in agreement with the results of Kritly et al. (2021), but these are monoaural responses and further perceptual studies, *e.g.* using measurements on scale models or three-dimensional simulations of the binaural responses, would be necessary to be able to conclude as to the other shapes between them in scenarios approaching real conditions for isolated columns.

A listener in the cathedral receives several early reflections, from the columns but also from the walls. The question arises of a possible masking happening systematically for the positions considered here. For a source located in the choir between the stalls, the reflection off the side wall arrives between approximately 25 ms to 55 ms for the receivers located respectively from the back to the front of the nave as shown in fig. 6.32. This leaves an interval before which these early column reflections can be significant if we consider the isochrone values in the transverse directions for the corresponding piers **N1** and **C1** represented in fig. 6.31. Furthermore, if we consider a realistic source, the relative positions will be decisive. Based on scattering theory, a spherical or cylindrical source will be scattered more in the forward and backward and less transversely compared to a plane wave incidence, and the closer it is the greater the effect (Zitron et al., 1966). However, such sources also imply a decay of intensity due to the spatial spread of their wavefront, which could result in a lower relative level of the reflections (Rathsam et al., 2010). Further investigations on RIRs and simulations could evaluate these effects.

6.5 Conclusion

The purpose of this chapter was to investigate the sound scattering by obstacles of complex geometries that are the typical fluted columns of Classical architecture and the Gothic piers of the *Cathédrale Notre-Dame de Paris*. This heritage monument has evolved across the centuries and is marked by several Gothic styles, which allowed us to select typical geometries relatively different, reflecting the evolution of this medieval architecture. Their scattering has been simulated up to 6 kHz using a low dispersion and anisotropy finite difference scheme with a pulse excitation presented in chapter 5. It is modified according to the formalism of finite volumes around the boundaries to conform to it and avoid the staircase approximation. The geometries have been reproduced in scale models allowing to physically measure their scattering to be compared with the simulation method. A plane wave incidence has been considered in the simulations and has been shown to be close to the experimental measurements in the case of a far field source and a receiver close to the cylinder.

The simulated scattered fields were consequently characterized in far field using the NFFFT and analyzed in terms of perceptually relevant quantities. The main observations from the numerical characterization could be summarized as follows:

- At low frequency, the scattering is well modeled by that of the circular cylinder with equal cross-sectional area for geometries with a high roundness. For elongated geometries or with a large scale concavity, high deviations in strength and angular distribution are observed depending on the incidence angle;
- The scattering strength is greatly increased for wavelengths close to the sizes of the smaller geometrical features of a cross section. When they are numerous, multiple scattering between them result in a large overshoot of the geometrical limit of the total scattering cross section;
- A geometric acoustic behavior is observed when the angular distribution does not vary, for wavelengths sufficiently small compared to the smaller geometrical features. For geometries with boundaries that form cavities due to a low convexity or the presence of additional cylinders, the anisotropy factors nevertheless shows relatively large variations at high frequency;

Similarly to reflectors, the reflections from columns and piers are limited by their finite size. However, due to their early arrival before most wall reflection, the scattered field at the evaluated positions revealed that these obstacles could produce audible reflections over all scattering directions based on thresholds reported in the literature. The temporal spreading strongly depend on the scatterer, *i.e.* the piers' form. Those with small geometrical features have the ability to produce diffuse reflections similarly to surface diffusers. Low level resonances have also been revealed, however, they represent a very small part of the total reflected energy. Strong spectral differences were observed between piers, such that it is likely possible to be able to discriminate between their reflections. Further studies could evaluate more realistic scenarios with a spherical source and different relative distances between the latter, the obstacle and the listener, numerically and with perceptual testings.

Chapter 7

Conclusions and future works

7.1 Room acoustic scale modeling & coupled volumes

The study of the acoustics of historic buildings relies on modeling to study those that have disappeared or past states, which can not be measured in-situ.

Physical methods such as acoustic scale models are a very powerful tool in the sense that they can account for the same phenomena as at full scale. Nevertheless, this implies experimental difficulties such as a larger frequency range to cover, partly extending over the ultrasound domain. In chapter 3, we were then interested in two elements of the measurement chain: the sources and the receivers.

We evaluated in terms of omnidirectionality three sources designed for scale factors ranging from 1:10 to 1:20. Two of them are tweeter arrays, one is tetrahedral with 4 dome tweeters and the other is cuboidal with 4 super tweeters, able to cover respectively low-mid and high frequencies. They remain limited with deviations exceeding the limits of the standard but reasonable such that it is possible to consider rotations to mitigate this. A third design used an inverted horn on a tweeter inspired by existing full-scale proposals. It strongly improves the omnidirectionality compared to the tweeter alone but introduces resonances producing a detrimental coloration for the auralizations and for the temporal compactness of the impulse.

On the receiving side, we adapted two methods used at full scale to capture the spatiality of the sound field from a listener's point of view: binaural recordings with artificial head and the Spatial Decomposition Method (SDM). The proposed artificial head was a 1:8 scale version of the popular Neumann KU 100 model. The design integrated two miniature microphones usually used for HRTF measurements. The measurements showed that it globally reproduced the ILDs and ITDs of the full scale model, nevertheless limited at high frequencies due to the equipment. It was used for measurements in a 1:10 scale model of a future concert hall, unfortunately not directly adapted to the dimensions. In order to propose a method that could be used at different scale factors, SDM was also tested in this model. From the results obtained, restricted to the lateral plane, the method seemed to be able to localize satisfactorily different source positions on stage, as well as the early reflections.

The interest of this type of modeling was demonstrated in chapter 4 where a round robin study was performed to evaluate the ability of different numerical methods used today to model the phenomenon of coupled volumes in room acoustics. Measurements in a 1:10 scale model of a concert hall with a reverberation chamber and a single aperture were used as references for comparison with the simulations. In order to focus on the phenomenon to be evaluated, the participants had to calibrate their simulations in decoupled configurations to match the reverberation times with corresponding measurements, thus ensuring a common basis for the late field decays. Although globally respected, the results of this calibration procedure showed that it would be necessary to provide the participants with a common tool to estimate the reverberation time and thus minimize this source of variation. In the end, 11 participants sent us their simulated RIRs with 7 geometrical acoustic software and 3 FD time-domain methods. All exhibited the expected double-slope decay, quantified using several suitable indicators. Compared to a previous study (Luizard et al., 2013) using the same system and comparing similar methods, we could show a clear improvement. Despite the calibration procedure and homogeneous surfaces in both rooms, the results of the methods still differed significantly between them spatially.

7.2 Sound scattering by architectural piers and columns

In part II we were interested in the study of the scattered reflections from columns and piers of two architectural styles: Gothic and Greek-Roman, as these elements can appear in large numbers in historic buildings for structural reasons.

For this purpose, a numerical simulation tool has been developed, presented and validated in chapter 5. The method employed the finite difference method in the time domain and was restricted to two space dimensions, given the geometry of the problems, discretized with a hexagonal grid. The studied sections being of complex geometry, the method employed jointly the finite volume formalism on an unstructured mesh in the vicinity of the boundaries, thus allowing to overcome the staircase approximation. It was validated by comparisons with analytic solutions of the circular cylinder with rigid and impedance boundary conditions, and also with a frequency method developed for multiple scattering problems. In order to characterize our objects in the far field and to not simulate it directly for computational reasons, a near-field to far-field transform (NFFFT) has been implemented and validated by comparisons with analytic solutions and BEM.

In addition to this method, the different architectonic elements studied in chapter 6 have also been reproduced at reduced scales (1:8.5 to 1:12). Comparisons with measurements showed that for distances close to the obstacle and a far field source, our two dimensional numerical model reproduces satisfactorily the reflection levels relative to the direct sound, especially for the transverse directions. For the fluted columns, it was revealed that they could be the support of circumventing surface waves especially for the one with the deepest grooves. In a similar way, Gothic piers with small geometrical elements of smaller scales on their cross section also presented such waves that manifested themselves as resonance tails in the time domain. For the source pulse used, however, they constituted only a small part of the total backscattered energy. Otherwise, the reflected pulses had envelopes close to what has been described for diffuse reflections. Beyond the localized resonances, around them, where the wavelengths are of comparable size to that of the smaller geometric features, the scattering strength is increased without strongly favoring any direction. It could be estimated that the reflections are likely to be heard with respect to the reported reflection audibility thresholds considering a listening situation in a cathedral, *e.g.* where the time interval between the direct sound and the first reflection from the side walls is large enough to not be masked.

7.3 Future works

7.3.1 Room acoustic scale modeling

Regarding the miniaturization of sources for scale models, the solution involving an inverted horn is promising but requires future investigations to attenuate the resonances. It could be by signal processing techniques in the manner of Cobo et al. (2013). Preliminary tests showed that the inverse filter method had a limited effect on directions other than the one used to build it. The dimensions of the cone could be optimized and other profiles considered.

Regarding the solutions tested to extend the scale model measurements for directional parameters or auralizations, the artificial head still requires methods to extrapolate the frequency band to obtain a satisfactory rendering for future perceptual studies. The same is true for the fact that we are also limited by the 192 kHz sampling frequency of the audio equipment used. For SDM, we were limited to visualizations in the lateral plane. Future studies are planned to include the third axis. The two techniques could also be the object of perceptual validation after frequency extrapolation, including the latest improvements for the latter (Amengual Garí et al., 2021).

7.3.2 Coupled volumes

The round robin on numerical simulations was limited to the 1 kHz octave band so that the procedure did not take too much time for the participants. It would be interesting to evaluate a wider range of frequencies. Otherwise, it is regrettable that some of the methods such as the diffusion equation or acoustic radiosity methods did not participate to the round robin as they are particularly suitable for modeling the late field.

7.3.3 Sound scattering by architectural piers and columns

Our numerical method is limited to a two-dimensional space, and although similar relative levels were measured in our cases, this does not correspond to the real situation. An implementation of the code for three-dimensional spaces might then be necessary for more faithful perceptual studies. Otherwise, it would be possible to use the method described by Duhamel (1996), using the invariance of the problem along a direction of space to transform the solutions of the 2D problem into that of the 3D problem. The method was rather used in the frequency domain being derived from the Helmholtz equation (Hornikx et al., 2007; Salomons et al., 1997), but it has also been adapted for transient time solutions obtained by the finite difference method (Sakamoto, 2009).

We estimated that the reflections from the obstacles could be audible and that from preliminary listening that was done through the perception of a coloration. Only in this case we are limited to a dichotic listening, with monaural impulse responses. Thus it seems relevant to carry out future perceptual tests to determine if the obstacles are audible in a binaural context, where it would be interesting to study the impact of the orientation of the head with respect to the source and the obstacle. This could be achieved through physical measurements using the scale models and the scale artificial head, similarly to Kleiner et al. (1992), or with simulations using our numerical tools, similarly to Meyer et al. (2019). Otherwise, it would also be interesting to determine if it is possible to perceptually discriminate these different reflections and under what conditions, similarly to Kritly et al. (2021).

Beyond their study in isolation, it would also be relevant to study objectively and perceptually their collective effects on the room acoustics as it has been done in several studies for diffusing surfaces (Jeon et al., 2020; Kim et al., 2011; Ryu et al., 2008) but also for columns (Suzumura et al., 2000) in concert halls using scale models, where the variation of the room acoustics parameters was observed. Shtrepi et al. (2015, 2017) also studied the impact of surface diffusers with geometrical acoustics software.

Finally, we studied the columns with solutions giving physically accurate results, and the geometries were very detailed. In a context of numerical simulations of a full room, such a level of detail will not be directly included in the geometrical model used in the geometrical or wave-based methods. Our results are thus references for the validation of modeling strategies for such finite objects, as it has been done for surfaces (Kowalczyk et al., 2011). Another strategy to take into account finite objects for virtual acoustic applications is to encode its scattering in a basis such as spherical harmonics to reduce computational costs while ensuring some physical accuracy (Gonzalez et al., 2022; Gonzalez, 2021; Rungta et al., 2018). Our simulation method could then provide the solutions before encoding. This strategy could also have an interest in perceptual tests which could then be conducted using an interactive virtual environment where the object or the scene could be more easily manipulated using the transformations (rotation, translation, scaling) that this decomposition allows.

Bibliography

Adams, H. (2015). *Adams' Building Construction.* Taylor & Francis. ISBN: 9781317742913.

Alberdi, E., F. Martellotta, M. Galindo, and Á. L. León (2019). "Dome sound effect in the church of San Luis de los Franceses". In: *Applied Acoustics* 156, pp. 56–65. ISSN: 0003-682X. DOI: 10.1016/j.apacoust.2019.06.030.

Alberti, L. (2004). *L'art d'édifier.* Trans. by P. Caye and F. Choay. Sources du savoir. Seuil.

Aletta, F. and J. Kang (2020). "Historical Acoustics: Relationships between People and Sound over Time". In: *Acoustics* 2.1, pp. 128–130. ISSN: 2624-599X. DOI: 10.3390/acoustics2010009.

Allen, J. B. and D. A. Berkley (1979). "Image method for efficiently simulating small-room acoustics". In: *The Journal of the Acoustical Society of America* 65.4, pp. 943–950. DOI: 10.1121/1.382599.

Álvarez-Morales, L., M. Lopez, and Á. Álvarez-Corbacho (2019). "Cathedral Acoustics: Bristol Cathedral as a Case Study". In: *INTER-NOISE and NOISE-CON Congress and Conference Proceedings.* Vol. 259. 3. Institute of Noise Control Engineering, pp. 6457–6468.

Amengual Garí, S. V., J. M. Arend, P. T. Calamia, and P. W. Robinson (2021). "Optimizations of the Spatial Decomposition Method for Binaural Reproduction". In: *Journal of the Audio Engineering Society* 68.12, pp. 959–976. DOI: 10.17743/jaes.2020.0063.

Anderson, J. and M. Bratos-Anderson (2000). "Acoustic Coupling Effects in St Paul's Cathedral, London". In: *Journal of Sound and Vibration* 236.2, pp. 209–225. ISSN: 0022-460X. DOI: 10.1006/jsvi.1999.2988.

Andreopoulou, A., D. R. Begault, and B. F. G. Katz (2015). "Inter-Laboratory Round Robin HRTF Measurement Comparison". In: *IEEE Journal of Selected Topics in Signal Processing* 9.5, pp. 895–906. DOI: 10.1109/JSTSP.2015.2400417.

Anonymous IV and J. Yudkin (1985). *The Music Treatise of Anonymous IV: A New Translation.* Musicological studies and documents. American Institute of Musicology.

Antani, L., A. Chandak, M. Wilkinson, A. A. Bassuet, and D. Manocha (2013). "Validation of adaptive rectangular decomposition for three-dimensional wave-based acoustic simulation in architectural models". In: *Proceedings of Meetings on Acoustics* 19.1, p. 015099. DOI: 10.1121/1.4800221.

Antoine, X., C. Chniti, and K. Ramdani (2008). "On the numerical approximation of high-frequency acoustic multiple scattering problems by circular cylinders". In: *Journal of Computational Physics* 227.3, pp. 1754–1771. ISSN: 0021-9991. DOI: 10.1016/j.jcp.2007.09.030.

Aretz, M., R. Nöthen, M. Vorländer, and D. Schröder (2009). "Combined Broadband Impulse Responses Using FEM and Hybrid Ray-Based Methods". In: *EAA Auralization Symposium 2009.* URL: https://publications.rwth-aachen.de/record/97789.

Aspöck, L. and M. Vorländer (2019). "Simulation of a coupled room scenario based on geometrical acoustics simulation models". In: *Proceedings of Meetings on Acoustics* 36.1, p. 015002. DOI: 10.1121/2.0001041.

Ayrault, C., P. Béquin, and S. Baudin (2012). "Characteristics of a spark discharge as an adjustable acoustic source for scale model measurements". In: *Proceedings of Acoustics 2012*. Ed. by S. F. d'Acoustique. Nantes, France, pp. 3555–3559. URL: https://hal.archives-ouvertes.fr/hal-00810828.

Balanis, C. (2012). *Advanced Engineering Electromagnetics*. Wiley.

Barletta, B. (2001). *The Origins of the Greek Architectural Orders*. Cambridge University Press.

Barrett, A. A. and M. Vickers (1975). "Columns in Antis in the Temple on the Ilissus". In: *The Annual of the British School at Athens* 70, pp. 11–16. DOI: 10.1017/S0068245400006493.

Barron, M. (1997). "Acoustic Scale Model Testing over 21 Years". English. In: *Acoustics Bulletin* 22.3, pp. 5–12.

Barron, M. and C. Chinoy (1979). "1:50 scale acoustic models for objective testing of auditoria". In: *Applied Acoustics* 12.5, pp. 361–375. ISSN: 0003-682X. DOI: 10.1016/0003-682X(79)90015-X.

Barron, M. and L.-J. Lee (1988). "Energy relations in concert auditoriums. I". In: *The Journal of the Acoustical Society of America* 84.2, pp. 618–628. DOI: 10.1121/1.396840.

Barron, M. and A. Marshall (1981). "Spatial impression due to early lateral reflections in concert halls: The derivation of a physical measure". In: *Journal of Sound and Vibration* 77.2, pp. 211–232. ISSN: 0022-460X. DOI: 10.1016/S0022-460X(81)80020-X.

Begault, D. R., B. U. McClain, and M. R. Anderson (2001). "Early Reflection Thresholds For Virtual Sound Sources". In: *Proceedings of the 2001 International Workshop on Spatial Media*. Aizu-Wakamatsu, Japan.

— (2003). "Early Reflection Thresholds for Anechoic and Reverberant Stimuli within a 3-D Sound Display". In.

Beranek, L. L. (2004). *Concert Halls and Opera Houses: Music, Acoustics, and Architecture*. Springer New York. ISBN: 9780387216362. DOI: 10.1007/978-0-387-21636-2.

— (2008). "Concert Hall Acoustics – 2008". In: *Journal of the Audio Engineering Society* 56.7/8, pp. 532–544.

Berenger, J.-P. (1994). "A perfectly matched layer for the absorption of electromagnetic waves". In: *Journal of Computational Physics* 114.2, pp. 185–200. ISSN: 0021-9991. DOI: 10.1006/jcph.1994.1159.

Bernschütz, B. (2013). "A spherical far field HRIR/HRTF compilation of the Neumann KU 100". In: *Proceedings of the 40th Italian (AIA) annual conference on acoustics and the 39th German annual conference on acoustics (DAGA) conference on acoustics*. German Acoustical Society (DEGA), pp. 592–595. URL: http://audiogroup.web.th-koeln.de/PUBLIKATIONEN/Bernschuetz_DAGA2013.pdf.

Berry, D. L., S. Taherzadeh, and K. Attenborough (2019). "Acoustic surface wave generation over rigid cylinder arrays on a rigid plane". In: *The Journal of the Acoustical Society of America* 146.4, pp. 2137–2144. DOI: 10.1121/1.5126856.

Bertrand, J. C. and J. W. Young (1976). "Multiple scattering between a cylinder and a plane". In: *The Journal of the Acoustical Society of America* 60.6, pp. 1265–1269. DOI: 10.1121/1.381239.

Betts, A. D. (1936). "Origin of Fluted Doric Columns". In: *Nature* 137, p. 180. DOI: 10.1038/137180b0.

Bilbao, S. (2004a). “Parameterized families of finite difference schemes for the wave equation”. In: *Numerical Methods for Partial Differential Equations* 20.3, pp. 463–480. DOI: `10.1002/num.10101`.

— (2004b). *Wave and Scattering Methods for Numerical Simulation*. John Wiley & Sons. ISBN: 9780470870181.

— (2009). *Numerical Sound Synthesis: Finite Difference Schemes and Simulation in Musical Acoustics*. John Wiley & Sons. ISBN: 0470510463.

— (2013). “Modeling of Complex Geometries and Boundary Conditions in Finite Difference/Finite Volume Time Domain Room Acoustics Simulation”. In: *IEEE Transactions on Audio, Speech, and Language Processing* 21.7, pp. 1524–1533. ISSN: 1558-7924. DOI: `10.1109/TASL.2013.2256897`.

Bilbao, S. and B. Hamilton (2017). “Wave-Based Room Acoustics Simulation: Explicit/Implicit Finite Volume Modeling of Viscothermal Losses and Frequency-Dependent Boundaries”. In: *Journal of the Audio Engineering Society* 65.1/2, pp. 78–89. DOI: `10.17743/jaes.2016.0057`.

— (2019). “Passive volumetric time domain simulation for room acoustics applications”. In: *The Journal of the Acoustical Society of America* 145.4, pp. 2613–2624. DOI: `10.1121/1.5095876`.

Bilbao, S., B. Hamilton, J. Botts, and L. Savioja (2016). “Finite Volume Time Domain Room Acoustics Simulation under General Impedance Boundary Conditions”. In: *IEEE/ACM Transactions on Audio, Speech, and Language Processing* 24.1, pp. 161–173. ISSN: 2329-9304. DOI: `10.1109/TASLP.2015.2500018`.

Blake, E. C. and I. Cross (2015). “The Acoustic and Auditory Contexts of Human Behavior”. In: *Current Anthropology* 56.1, pp. 81–103. DOI: `10.1086/679445`.

Bomhardt, R. (2017). *Anthropometric Individualization of Head-Related Transfer Functions Analysis and Modeling*. Aachener Beiträge zur Akustik. Logos Verlag Berlin. ISBN: 9783832545437.

Bony, J. (1949). “French Influences on the Origins of English Gothic Architecture”. In: *Journal of the Warburg and Courtauld Institutes* 12, pp. 1–15. ISSN: 00754390. DOI: `10.2307/750252`.

Boole, G. (2009). *A Treatise on the Calculus of Finite Differences*. Cambridge Library Collection - Mathematics. Cambridge University Press. DOI: `10.1017/CBO9780511693014`.

Boone, M. M. and E. Braat-Eggen (1994). “Room acoustic parameters in a physical scale model of the new Music Centre in Eindhoven: Measurement method and results”. In: *Applied Acoustics* 42.1, pp. 13–28. ISSN: 0003-682X. DOI: `10.1016/0003-682X(94)90121-X`.

Boone, V. and T. Wulfrank (2008). “Acoustique variable”. In: *A+* 213, pp. 132–137.

Boren, B. B., M. Longair, and R. Orlowski (2013). “Acoustic simulation of renaissance Venetian churches”. In: *Acoustics in Practice* 1.2, pp. 17–28.

Bork, I. (2000). “A Comparison of Room Simulation Software - The 2nd Round Robin on Room Acoustical Computer Simulation”. In: *Acta Acustica united with Acustica* 86, pp. 943–956.

— (2005a). “Report on the 3rd Round Robin on Room Acoustical Computer Simulation – Part I: Measurements”. In: *Acta Acustica united with Acustica* 91, pp. 740–752.

— (2005b). “Report on the 3rd Round Robin on Room Acoustical Computer Simulation – Part II: Calculations”. In: *Acta Acustica united with Acustica* 91, pp. 753–763.

Botteldooren, D. (1994). “Acoustical finite-difference time-domain simulation in a quasi-Cartesian grid”. In: *The Journal of the Acoustical Society of America* 95.5, pp. 2313–2319. DOI: `10.1121/1.409866`.

— (1995). “Finite-difference time-domain simulation of low-frequency room acoustic problems”. In: *The Journal of the Acoustical Society of America* 98.6, pp. 3302–3308. DOI: `10.1121/1.413817`.

Bowman, J., T. Senior, P. Uslenghi, and J. Asvestas (1988). *Electromagnetic and Acoustic Scattering by Simple Shapes*. Taylor & Francis. ISBN: 9780891168850.

Bradley, D. T., M. Müller-Trapet, J. Adelgren, and M. Vorländer (2014). “Comparison of Hanging Panels and Boundary Diffusers in a Reverberation Chamber”. In: *Building Acoustics* 21.2, pp. 145–152. DOI: `10.1260/1351-010X.21.2.145`.

Bradley, D. T. and L. M. Wang (2005). “The effects of simple coupled volume geometry on the objective and subjective results from nonexponential decay”. In: *The Journal of the Acoustical Society of America* 118.3, pp. 1480–1490. DOI: `10.1121/1.1984892`.

— (2009). “Quantifying the Double Slope Effect in Coupled Volume Room Systems”. In: *Building Acoustics* 16.2, pp. 105–123. DOI: `10.1260/135101009788913275`.

— (2010). “Optimum absorption and aperture parameters for realistic coupled volume spaces determined from computational analysis and subjective testing results”. In: *The Journal of the Acoustical Society of America* 127.1, pp. 223–232. DOI: `10.1121/1.3268604`.

Braun, R. (1984). “Aufbau, Eigenschaften und Anwendungen einer Dodekaederförmigen Modellschallquelle aus PVDF-Schalen”. In: *Fortschritte der Akustik - DAGA ’84*. Darmstadt, Germany.

Brebeck, D., R. Bücklein, E. Krauth, and F. Spandöck (1967). “Akustisch ähnliche Modelle als Hilfsmittel für die Raumakustik”. In: *Acustica* 18.4, pp. 213–226.

Brinkmann, F., L. Aspöck, D. Ackermann, S. Lepa, M. Vorländer, and S. Weinzierl (2019). “A round robin on room acoustical simulation and auralization”. In: *The Journal of the Acoustical Society of America* 145, pp. 2746–2760. DOI: `10.1121/1.5096178`.

Brunner, S., H.-J. Maempel, and S. Weinzierl (2007). “On the Audibility of Comb Filter Distortions”. In: *122nd AES Convention*. Vienna, Austria: Audio Engineering Society.

Bruzelius, C. (1987). “The Construction of Notre-Dame in Paris”. In: *The Art Bulletin* 69.4, pp. 540–569. ISSN: 00043079. DOI: `10.2307/3050998`.

Buchholz, J. M. (2011). “A quantitative analysis of spectral mechanisms involved in auditory detection of coloration by a single wall reflection”. In: *Hearing Research* 277.1, pp. 192–203. ISSN: 0378-5955. DOI: `10.1016/j.heares.2011.01.002`.

Burgtorf, W. (1961). “Untersuchungen zur Wahrnehmbarkeit verzögerter Schallsignale”. In: *Acta Acustica united with Acustica* 11.2, pp. 97–111. ISSN: 1610-1928. URL: `https://www.ingentaconnect.com/content/dav/aaua/1961/00000011/00000002/art00006`.

— (1967). “Room-Acoustical Experiments on Models Using Ultrasonics”. In: *Acta Acustica united with Acustica* 18.6, pp. 323–333. ISSN: 1610-1928. URL: `https://www.ingentaconnect.com/content/dav/aaua/1967/00000018/00000006/art00004`.

Burgtorf, W. and H. K. Oehlschlägel (1964). “Untersuchungen über die richtungsabhängige Wahrnehmbarkeit verzögerter Schallsignale”. In: *Acta Acustica united with Acustica* 14.5, pp. 254–266. ISSN: 1610-1928. URL: `https://www.ingentaconnect.com/content/dav/aaua/1964/00000014/00000005/art00005`.

Cabrera, D., J. Xun, and M. Guski (2016). “Calculating Reverberation Time from Impulse Responses: A Comparison of Software Implementations”. In: *Acoustics Australia* 44, pp. 369–378.

Calamia, P. (2009). “Advances in Edge-Diffraction Modeling for Virtual-Acoustic Simulations”. PhD thesis. Princeton University.

Canac, F. (1967). *L’acoustique des théâtres antiques : ses enseignements*. Paris: Editions du Centre national de la recherche scientifique.

Canfield-Dafilou, E. K., S. S. Mullins, and B. F. G. Katz (2022). “Opening the Lateral Chapels and the Acoustics of Notre-Dame de Paris: 1225–1320”. en. In: *Symp The Acoustics of Ancient Theatres*. Verona. URL: `https://hal.archives-ouvertes.fr/hal-03724948`.

Carvalho, A. P. O. (1995). “The use of the Sabine and Eyring reverberation time equations to churches”. In: *The Journal of the Acoustical Society of America* 97.5, pp. 3319–3319. DOI: `10.1121/1.412850`.

CATT-Acoustic/TUCT (2016). *CATT-Acoustic, TUCT^{TM} v2.0a User’s manual*. English.

Chartier, F. (1897). *L’ancien Chapitre de Notre-Dame de Paris et sa maîtrise d’après les documents capitulaires (1326-1790), avec un appendice musical comprenant plusieurs fragments d’oeuvres des anciens maîtres de chapelle*. Perrin.

Chitham, R. (2014). *The Classical Orders of Architecture*. Elsevier Science. ISBN: 9781483278230.

Chojnacki, B., J. Rubacha, and M. Ziobro (2016). “Piezoelektryczne wszechkierunkowe źródło dźwięku do akustycznych badań w skali w zakresie ultradźwięków”. In: *Studium badawcze młodych naukowców*. Ed. by A. Pilch. Wydawnictwo AGH.

Chu, Y. and C. Mak (2009). “Early energy decays in two churches in Hong Kong”. In: *Applied Acoustics* 70.4, pp. 579–587. ISSN: 0003-682X. DOI: `10.1016/j.apacoust.2008.07.004`.

Ćirić, D. and A. Pantić (2012). “Numerical Compensation of Air Absorption of Sound in Scale Model Measurements”. In: *Archives of Acoustics* 37.2, pp. 219–225. DOI: `10.2478/v10168-012-0029-0`.

CNRS/MC (2019). *Chantier scientifique Notre-Dame de Paris*. URL: `https://www.notre-dame.science/` (visited on 11/01/2021).

Cobo, P., S. Ortiz, D. Ibarra, and C. de la Colina (2013). “Point source equalised by inverse filtering for measuring ground impedance”. In: *Applied Acoustics* 74.4, pp. 561–565. ISSN: 0003-682X. DOI: `10.1016/j.apacoust.2012.10.003`.

Colton, D. and R. Kress (2013). “The Helmholtz Equation”. In: *Inverse Acoustic and Electromagnetic Scattering Theory*. New York, NY: Springer New York, pp. 13–38. ISBN: 978-1-4614-4942-3. DOI: `10.1007/978-1-4614-4942-3_2`.

Core Sound (2022). *OctoMic® 2nd-order Ambisonic Microphone*. URL: `https://www.core-sound.com/products/octomic` (visited on 04/28/2022).

Courant, R., K. Friedrichs, and H. Lewy (1928). “Über die partiellen Differenzengleichungen der mathematischen Physik”. In: *Mathematische Annalen* 100.1, pp. 32–74. DOI: `10.1007/bf01448839`.

Cox, T. and P. D’Antonio (2016). *Acoustic Absorbers and Diffusers: Theory, Design and Application*. CRC Press. ISBN: 9781498741002. DOI: `10.1201/9781315369211`.

Cox, T. J., B. M. Fazenda, and S. E. Greaney (2020). “Using scale modelling to assess the prehistoric acoustics of Stonehenge”. In: *Journal of Archaeological Science* 122, p. 105218. ISSN: 0305-4403. DOI: `10.1016/j.jas.2020.105218`.

Cremer, L. and H. A. Müller (1982). *Principles and Applications of Room Acoustics - Vol 1*. Vol. Vol 1. Applied Science Publishers.

Dablain, M. A. (1986). "The application of high-order differencing to the scalar wave equation". In: *GEOPHYSICS* 51.1, pp. 54–66. DOI: `10.1190/1.1442040`.

Dalenbäck, B.-I. L. (1996). "Room acoustic prediction based on a unified treatment of diffuse and specular reflection". In: *The Journal of the Acoustical Society of America* 100.2, pp. 899–909. DOI: `10.1121/1.416249`.

Davis, A. H. and N. Fleming (1926). "Sound pulse photography as applied to the study of architectural acoustics". In: *Journal of Scientific Instruments* 3.12, pp. 393–398. DOI: `10.1088/0950-7671/3/12/301`.

Davis, A. (1925a). "The analogy between ripples and acoustical wave phenomena". In: *Proceedings of the Physical Society of London* 38.1, pp. 234–246. DOI: `10.1088/1478-7814/38/1/328`.

— (1925b). "VI. Reverberation equations for two adjacent rooms connected by an incompletely soundproof partition". In: *The London, Edinburgh, and Dublin Philosophical Magazine and Journal of Science* 50.295, pp. 75–80. DOI: `10.1080/14786442508634717`.

Davis, M. T. (1998). "Splendor and Peril: The Cathedral of Paris, 1290–1350". In: *The Art Bulletin* 80.1, pp. 34–66. URL: `https://www.tandfonline.com/doi/abs/10.1080/00043079.1998.10786818`.

Day, B. (1968). "A tenth-scale model audience". In: *Applied Acoustics* 1.2, pp. 121–135. ISSN: 0003-682X. DOI: `10.1016/0003-682X(68)90014-5`.

Driscoll, J. and D. Healy (1994). "Computing Fourier Transforms and Convolutions on the 2-Sphere". In: *Advances in Applied Mathematics* 15.2, pp. 202–250. ISSN: 0196-8858. DOI: `10.1006/aama.1994.1008`.

Du, Q., V. Faber, and M. Gunzburger (1999). "Centroidal Voronoi Tessellations: Applications and Algorithms". In: *SIAM Review* 41.4, pp. 637–676. DOI: `10.1137/S0036144599352836`.

Duhamel, D. (1996). "Efficient calculation of the three-dimensional sound pressure field around a noise barrier". In: *Journal of Sound and Vibration* 197, pp. 547–571. DOI: `10.1006/jsvi.1996.0548`.

Duhamel, P. (2010). *Polyphonie parisienne et architecture au temps de l'art gothique (1140-1240)*. Varia Musicologica Series. Lang. ISBN: 9783039116133.

Dungen, F.-H. van den (1933). "La similitude acoustique des Salles". In: *Bulletin de la Classe des sciences. Académie royale de Belgique.* 12, pp. 1299–1310.

Embrechts, J.-J. (2016). "Review on the Apllications of Directinal Impulse Responses in Room Acoustics". In: *13e Congrès Français d'Acoustique*. Le Mans, France, pp. 1621–1627. URL: `http://www.conforg.fr/cfa2016/cdrom/data/articles/000373.pdf`.

Engquist, B. and A. Majda (1977). "Absorbing Boundary Conditions for the Numerical Simulation of Waves". In: *Mathematics of Computation* 31.139, pp. 629–651. ISSN: 00255718, 10886842. DOI: `10.1090/S0025-5718-1977-0436612-4`.

Erim, K. T. (1988). "Recherches récentes et découvertes à Aphrodisias de Carie". In: *Comptes rendus des séances de l'Académie des Inscriptions et Belles-Lettres* 132.4, pp. 734–757. DOI: `10.3406/crai.1988.14666`.

Ermann, M. (2005). "Coupled Volumes: Aperture Size and the Double-Sloped Decay of Concert Halls". In: *Building Acoustics* 12.1, pp. 1–13. DOI: `10.1260/1351010053499252`.

Escolano, J., N. Xiang, J. M. Navarro, and Y. Jing (2013). “A diffusion equation model for investigations on acoustics in coupled-volume systems”. In: *Proceedings of Meetings on Acoustics* 19.1, p. 015102. DOI: 10.1121/1.4799421.

EVAA program (2021). *Experimental Virtual Archaeological-Acoustics*. Sorbonne Université, CNRS, Institut Jean Le Rond d’Alembert. URL: https://evaa.lam.jussieu.fr/.

Eyring, C. F. (1930). “Reverberation Time in “Dead” Rooms”. In: *The Journal of the Acoustical Society of America* 1.2A, pp. 168–168. DOI: 10.1121/1.1901884.

Fabero, J., A. Bautista, and L. Casasús (2001). “An explicit finite differences scheme over hexagonal tessellation”. In: *Applied Mathematics Letters* 14.5, pp. 593–598. ISSN: 0893-9659. DOI: 10.1016/S0893-9659(00)00199-3.

Farhat, M., P.-Y. Chen, and H. Bağcı (2016). “Localized acoustic surface modes”. In: *Applied Physics A* 122.4, pp. 1–8.

Farina, A. (1995). “RAMSETE - a new pyramid tracer for medium and large scale acoustic problems”. In: *Proceedings of the Euronoise*. Lyon, France.

Farnetani, A., F. Bettarello, N. Prodi, and R. Pompoli (2005). “Investigating the acoustics of ancient theatres by means of a modular scale model”. In: *Proceedings of the Forum Acusticum*. Budapest, Hungary, pp. 2185–2190.

Fernie, E. (1987). “La fonction liturgique des piliers cantonnés dans la nef de la cathédrale de Laon”. In: *Bulletin Monumental* 145, pp. 257–266. DOI: 10.3406/bulmo.1987.2963.

Field, W. and T. French (1922). *Architectural Drawing*. McGraw-Hill Book Company, Incorporated.

Foley, A. L. and W. H. Souder (1912). “A New Method of Photographic Sound Waves”. In: *Phys. Rev. (Series I)* 35 (5), pp. 373–386. DOI: 10.1103/PhysRevSeriesI.35.373.

Fuller, C. R. (1989). “Free-field correction factor for spherical acoustic waves impinging on cylinders”. In: *AIAA Journal* 27.12, pp. 1722–1726. DOI: 10.2514/3.10326.

Geuzaine, C. and J.-F. Remacle (2009). “Gmsh: A 3-D finite element mesh generator with built-in pre- and post-processing facilities”. In: *International Journal for Numerical Methods in Engineering* 79.11, pp. 1309–1331. DOI: 10.1002/nme.2579.

Ginouvès, R., A.-M. Guimier-Sorbets, C. Bouras, J. J. Coulton, Y. Morizot, F. Pesando, M. Kohl, V. Hadjimichali, M.-C. Hellmann, and P. Gros (1998). “Dictionnaire méthodique de l’architecture grecque et romaine. Tome III. Espaces architecturaux, bâtiments et ensembles”. In: *Publications de l’École Française de Rome* 84.3. URL: https://www.persee.fr/doc/efr_0000-0000_1998_dic_84_3.

Gómez Bolaños, J., V. Pulkki, P. Karppinen, and E. Hæggström (2013). “An optoacoustic point source for acoustic scale model measurements”. In: *The Journal of the Acoustical Society of America* 133.4, EL221–EL227. DOI: 10.1121/1.4793566.

Gonzalez, R., T. Lokki, and A. Politis (2022). “Functional Modelling of Scattering for Diffusive Geometries”. In: *AES 2022 International Audio for Virtual and Augmented Reality Conference*. Redmond, WA, USA, pp. 1–9.

Gonzalez, R. a. (2021). “Spherical Decomposition of Arbitrary Scattering Geometries for Virtual Acoustic Environments”. In: *2021 24th International Conference on Digital Audio Effects (DAFx)*, pp. 199–205. DOI: 10.23919/DAFx51585.2021.9768234.

Gradshteyn, I. S. and I. M. Ryzhik (2007). *Table of Integrals, Series, and Products*. Ed. by D. Zwillinger and A. Jeffrey. Seventh Edition. Academic Press.

Greff, R. and B. F. G. Katz (2007). “Round Robin Comparison of HRTF Simulation Systems: Preliminary Results”. In: *Journal of the Audio Engineering Society*.

Grillon, V., X. Meynial, and J.-D. Polack (1996). “What Can Auralisation in Small Scale Models Achieve?” In: *Acta Acustica united with Acustica* 82.2, pp. 362–364. ISSN: 1610-1928. URL: `https://www.ingentaconnect.com/content/dav/aaua/1996/00000082/00000002/art00024`.

Gumerov, N. A., A. E. O’Donovan, R. Duraiswami, and D. N. Zotkin (2010). “Computation of the head-related transfer function via the fast multipole accelerated boundary element method and its spherical harmonic representation”. In: *The Journal of the Acoustical Society of America* 127.1, pp. 370–386. DOI: `10.1121/1.3257598`.

Häggblad, J. and B. Engquist (2012). “Consistent modeling of boundaries in acoustic finite-difference time-domain simulations”. In: *The Journal of the Acoustical Society of America* 132.3, pp. 1303–1310. DOI: `10.1121/1.4740490`.

Häggblad, J. and O. Runborg (2014). “Accuracy of staircase approximations in finite-difference methods for wave propagation”. In: *Numerische Mathematik* 128, pp. 741–771.

Hak, C. and K. Bijsterbosch (2009). “Room Acoustic Scale Model Measurements using a "Spark Train"”. In: *NAG/DAGA 2009, International Conference on Acoustics*. Rotterdam, Netherlands: German Acoustical Society (DEGA), pp. 946–948. URL: `https://pub.dega-akustik.de/NAG_DAGA_2009/data/articles/000407.pdf`.

Hamilton, B. (2014). “Finite Volume Perspectives on Finite Difference Schemes and Boundary Formulations for Wave Simulation”. In: *DAFx-14*.

— (2016). “Finite Difference and Finite Volume Methods for Wave-based Modelling of Room Acoustics”. PhD thesis. University of Edinburgh.

Hamilton, B. and S. Bilbao (2013). “Hexagonal vs. rectilinear grids for explicit finite difference schemes for the two-dimensional wave equation”. In: *The Journal of the Acoustical Society of America* 133.5, pp. 3532–3532. DOI: `10.1121/1.4806369`.

Hargreaves, J. (2007). “Time domain boundary element method for room acoustics”. PhD thesis. University of Salford. URL: `http://usir.salford.ac.uk/id/eprint/16604/`.

Harwood, H. and A. Burd (1970). *Acoustic scaling: General outline*. Report 1970-13. BBC Research & Development. URL: `https://www.bbc.co.uk/rd/publications/rdreport_1970_13`.

Harwood, H., A. Burd, N. Spring, K. Randall, and M. Smith (1972). *Acoustic scaling: An evaluation of the proving experiment*. Report 1972-03. BBC Research & Development. URL: `https://www.bbc.co.uk/rd/publications/rdreport_1972_03`.

Harwood, H., K. Lansdowne, and K. Randall (1975). *Acoustic scaling: The design of a large music studio for Manchester: final report*. Report 1975-35. BBC Research & Development. URL: `https://www.bbc.co.uk/rd/publications/rdreport_1975_35`.

Hasheminejad, S. M. and M. A. Alibakhshi (2006). “Two-dimensional scattering from an impenetrable cylindrical obstacle in an acoustic quarterspace”. In: *Forschung im Ingenieurwesen* 70, pp. 179–186. DOI: `10.1007/s10010-006-0030-8`.

Heil, O. (1972). “Acoustic transducer with a diaphragm forming a plurality of adjacent narrow air spaces open only at one side with the open sides of adjacent air spaces alternatingly facing in opposite directions”. U.S. pat. 3636278.

Henriquez, V. C. and P. M. Juhl (2010). “OpenBEM — An open source boundary element method software in acoustics”. In: *Internoise 2010* 7, pp. 13–16.

Hidaka, T., K. Suzuki, and Y. Yamada (2010). “A New Miniature Loudspeaker For Room Acoustical Scale Model Experiment”. In: *20th International Congress on Acoustics, ICA 2010* (Aug. 23–27, 2010). Sydney, Australia.

Hidaka, Y., H. Yano, and H. Tachibana (1989). “Scale model experiment on room acoustics by hybrid simulation technique”. In: *The Journal of the Acoustical Society of Japan (E)* 10.2, pp. 111–117. DOI: 10.1250/ast.10.111.

Hoey, L. R. (1987). “Piers versus Vault Shafts in Early English Gothic Architecture”. In: *Journal of the Society of Architectural Historians* 46.3, pp. 241–264. ISSN: 00379808, 21505926. DOI: 10.2307/990229.

— (1989). “Pier Form and Vertical Wall Articulation in English Romanesque Architecture”. In: *Journal of the Society of Architectural Historians* 48.3, pp. 258–283. ISSN: 00379808, 21505926. DOI: 10.2307/990431.

Hornikx, M. and J. Forssén (2007). “The 2.5-dimensional equivalent sources method for directly exposed and shielded urban canyons”. In: *The Journal of the Acoustical Society of America* 122.5, pp. 2532–2541. DOI: 10.1121/1.2783197.

— (2008). “A Scale Model Study of Parallel Urban Canyons”. In: *Acta Acustica united with Acustica* 94.2, pp. 265–281. ISSN: 1610-1928. DOI: 10.3813/AAA.918030.

Howe, T. N. (2018). “Bold Imitator: Greek “Orders,” the Autodidact Polymath Architect and the Apollonion of Syracuse”. In: *The Many Faces of Mimesis: Selected Essays from the 2017 Symposium on the Hellenic Heritage of Western Greece*. Vol. 3. Parnassos Press – Fonte Aretusa, pp. 1–20. DOI: 10.2307/j.ctvbj7g5b.4.

Hu, Z., M. A. Ratner, and T. Seideman (2013). “Calculating scattering cross sections in the near field: Analytic proof and numerical verification”. In: *Chemical Physics* 415, pp. 14–17. ISSN: 0301-0104. DOI: 10.1016/j.chemphys.2013.01.033.

Huerta, S. (2007). “Oval Domes: History, Geometry and Mechanics”. In: *Nexus Network Journal* 9, pp. 211–248. DOI: 10.1007/s00004-007-0040-3.

Hughes, R. J., J. A. S. Angus, T. J. Cox, O. Umnova, G. A. Gehring, M. Pogson, and D. M. Whittaker (2010). “Volumetric diffusers: Pseudorandom cylinder arrays on a periodic lattice”. In: *The Journal of the Acoustical Society of America* 128.5, pp. 2847–2856. DOI: 10.1121/1.3493455.

Hyon, J. and D. Jeong (2021). “Variable Acoustics in performance venues- A review”. In: *The Journal of the Acoustical Society of Korea* 40.6, pp. 626–648. DOI: 10.7776/ASK.2021.40.6.626.

Ibarra, D., R. Ledesma, and E. Lopez (2018). “Design and construction of an omnidirectional sound source with inverse filtering approach for optimization”. In: *HardwareX* 4, e00033. ISSN: 2468-0672. DOI: 10.1016/j.ohx.2018.e00033.

ISO 17497-1 (2004). *Acoustics – Sound-Scattering properties of surfaces – Part 1: Measurement of the random-incidence scattering coefficient in a reverberation room*. standard. International Organization for Standardization.

ISO 17497-2 (2012). *Acoustics – Sound-Scattering properties of surfaces – Part 2: Measurement of the directional diffusion coefficient in a free field*. standard. International Organization for Standardization.

ISO 3382-1 (2009). *Acoustics - Measurement of room acoustic parameters – Part 1: Performance spaces*. standard. International Organization for Standardization.

Jeon, J. Y., H. I. Jo, R. Seo, and K. H. Kwak (2020). “Objective and subjective assessment of sound diffuseness in musical venues via computer simulations and a scale model”. In: *Building and Environment* 173, p. 106740. ISSN: 0360-1323. DOI: 10.1016/j.buildenv.2020.106740.

Jeon, J. Y., J. K. Ryu, Y. H. Kim, and S.-i. Sato (2009). “Influence of absorption properties of materials on the accuracy of simulated acoustical measures in 1:10 scale model test”.

In: *Applied Acoustics* 70.4, pp. 615–625. ISSN: 0003-682X. DOI: 10.1016/j.apacoust.2008.06.009.

Jeong, C.-H. (2012). “Absorption and impedance boundary conditions for phased geometrical-acoustics methods”. In: *The Journal of the Acoustical Society of America* 132.4, pp. 2347–2358. DOI: 10.1121/1.4740494.

Jeong, H. and Y. W. Lam (2012). “Source implementation to eliminate low-frequency artifacts in finite difference time domain room acoustic simulation”. In: *The Journal of the Acoustical Society of America* 131.1, pp. 258–268. DOI: 10.1121/1.3652886.

Jo, C., J. Jeong, B.-J. Kwon, K.-C. Park, and I.-K. Oh (2015). “Omnidirectional two-dimensional acoustic cloak by axisymmetric cylindrical lattices”. In: *Wave Motion* 54, pp. 157–169. ISSN: 0165-2125. DOI: 10.1016/j.wavemoti.2014.12.004.

Johnson, R., H. Ecker, and J. Hollis (1973). “Determination of far-field antenna patterns from near-field measurements”. In: *Proceedings of the IEEE* 61.12, pp. 1668–1694. DOI: 10.1109/PROC.1973.9358.

Johnson, R. and E. Kahle (1999). “The new Konzertsaal of the KKL Center, Lucerne, Switzerland. I. Acoustics design”. In: *The Journal of the Acoustical Society of America* 105.2, pp. 928–928. DOI: 10.1121/1.426283.

Jones, M. W. (2014). *Origins of Classical Architecture*. Yale University Press.

Jordan, V. L. (1973). “Acoustical Design Considerations of the Sydney Opera House”. In: *Journal and Proceedings of The Royal Society of New South Wales* 106, pp. 33–53. URL: https://royalsoc.org.au/images/pdf/journal/106_12_jordan.pdf.

Junger, M. and D. Feit (1986). *Sound, Structures, and Their Interaction*. Ed. by M. Press. Second. Acoustical Society of America. ISBN: 9780262100106.

Jurkiewicz, Y., E. Kahle, and B. F. G. Katz (2015). “Stavanger Concert Hall, acoustic design and measurement results”. In: *Intl. Conf. on Auditorium Acoustics*. Vol. 37. Paris, Unknown Region, pp. 300–307. URL: https://hal.archives-ouvertes.fr/hal-01789764.

Kantorovich, L. and V. Krylov (1958). *Approximate Methods of Higher Analysis*. Trans. by C. D. Benster. Interscience Publishers.

Katz, B. F. G. (2004). “International Round Robin on Room Acoustical Impulse Response Analysis Software 2004”. In: *Acoustics Research Letters Online* 5.4, pp. 158–164. DOI: 10.1121/1.1758239.

Katz, B. F. G., O. Delarozière, and P. Luizard (2011). “A ceiling case study inspired by an historical scale model”. In: *Intl. Conf. on Auditorium Acoustics*. Vol. 33. 2. Dublin, Ireland, pp. 314–321. URL: https://hal.archives-ouvertes.fr/hal-01789732.

Katz, B. F. G., Y. Jurkiewicz, T. Wulfrank, G. Parseihian, T. Scélo, and H. Marshall (2015). “La Philharmonie de Paris - Acoustic scale model study”. In: *Intl. Conf. on Auditorium Acoustics*. Vol. 37. Paris, Unknown Region, pp. 431–438. URL: https://hal.archives-ouvertes.fr/hal-01789762.

Katz, B. F. G., S. Leconte, and P. Stitt (2019). “EVAA: A platform for experimental virtual archeological-acoustics to study the influence of performance space”. In: *Intl Sym on Room Acoustics (ISRA)*. Amsterdam, Netherlands. DOI: 10.18154/RWTH-CONV-240136.

Katz, B. F. G., D. Murphy, and A. Farina (2020a). “The Past Has Ears (PHE): XR Explorations of Acoustic Spaces as Cultural Heritage”. In: *International Conference on Augmented Reality, Virtual Reality and Computer Graphics AVR 2020*. Vol. 12243. Lecture Notes in Computer Science book series. Salento, Italy, pp. 91–98. DOI: 10.1007/978-3-030-58468-9_7.

Katz, B. F. G. and A. Weber (2020b). “An acoustic survey of the Cathédrale Notre-Dame de Paris before and after the fire of 2019”. In: *Acoustics* 2.4. SI: Historical Acoustics, pp. 791–802. DOI: `10.3390/acoustics2040044`.

Kim, Y. H., J. H. Kim, and J. Y. Jeon (2011). “Scale Model Investigations of Diffuser Application Strategies for Acoustical Design of Performance Venues”. In: *Acta Acustica united with Acustica* 97.5, pp. 791–799. ISSN: 1610-1928. DOI: `10.3813/AAA.918459`.

Klein, B. (1999). “Naissance et formation de l’architecture gothique en France et dans les pays limitrophes”. In: *L’art gothique, Architecture - Sculpture - Peinture*. Ed. by R. Toman. Könemann. Chap. 3, pp. 28–114. ISBN: 9783833135132.

Kleiner, M., D. Klepper, and R. Torres (2010). *Worship Space Acoustics*. Acoustics/Architecture. J. Ross Publishing. ISBN: 9781604270372.

Kleiner, M., P. Svensson, and B.-I. Dalenbäck (1992). “Auralization of QRD and other diffusing surfaces using scale modelling”. In: *93rd AES Convention*. San Francisco, CA, USA: Audio Engineering Society.

Knudsen, V. O. (1932). *Architectural Acoustics*. J. Wiley & sons, Incorporated.

— (1970). “Model Testing of Auditoriums”. In: *The Journal of the Acoustical Society of America* 47.2A, pp. 401–407. DOI: `10.1121/1.1911533`.

Kowalczyk, K. and M. van Walstijn (2008). “Modeling Frequency-Dependent Boundaries as Digital Impedance Filters in FDTD and K-DWM Room Acoustics Simulations”. In: *Journal of the Audio Engineering Society* 56.7/8, pp. 569–583.

— (2010). “Wideband and Isotropic Room Acoustics Simulation Using 2-D Interpolated FDTD Schemes”. In: *IEEE Transactions on Audio, Speech, and Language Processing* 18.1, pp. 78–89. ISSN: 1558-7924. DOI: `10.1109/TASL.2009.2023645`.

Kowalczyk, K., M. van Walstijn, and D. Murphy (2011). “A Phase Grating Approach to Modeling Surface Diffusion in FDTD Room Acoustics Simulations”. In: *IEEE Transactions on Audio, Speech, and Language Processing* 19.3, pp. 528–537. DOI: `10.1109/TASL.2010.2051830`.

Krehl, P. and S. Engemann (1995). “August Toepler – The first who visualized shock waves”. In: *Shock Waves* 5, pp. 1–18. DOI: `10.1007/BF02425031`.

Kritly, L., Y. Sluyts, D. Pelegrín-García, C. Glorieux, and M. Rychtáriková (2021). “Discrimination of 2D wall textures by passive echolocation for different reflected-to-direct level difference configurations”. In: *PLOS ONE* 16.5, pp. 1–27. DOI: `10.1371/journal.pone.0251397`.

Krynkin, A., O. Umnova, J. V. Sánchez-Pérez, A. Yung Boon Chong, S. Taherzadeh, and K. Attenborough (2011). “Acoustic insertion loss due to two dimensional periodic arrays of circular cylinders parallel to a nearby surface”. In: *The Journal of the Acoustical Society of America* 130.6, pp. 3736–3745. DOI: `10.1121/1.3655880`.

Kuttruff, H. (2009). *Room Acoustics*. Fifth Edition. Taylor & Francis. ISBN: 9780203876374. DOI: `10.1201/9781482266450`.

— (2016). *Room Acoustics*. Sixth Edition. CRC Press. ISBN: 9781482260441. DOI: `10.1201/9781315372150`.

Lahti, U. I. (1985). “Inverted horn loudspeaker”. In: *The Journal of the Acoustical Society of America* 78.5, pp. 1932–1932. DOI: `10.1121/1.392690`.

Lam, Y. W. (1996). “The dependence of diffusion parameters in a room acoustics prediction model on auditorium sizes and shapes”. In: *The Journal of the Acoustical Society of America* 100.4, pp. 2193–2203. DOI: `10.1121/1.417928`.

Lam, Y. W. and J. Hargreaves (2012). “Time domain modelling of room acoustics”. In: *Acoustics 2012*. Ed. by S. F. d’Acoustique. Nantes, France. URL: `https://hal.archives-ouvertes.fr/hal-00811383`.

Lassus, J.-B. A. and E. E. Viollet-le-Duc (1843). *Projet de restauration de Notre-Dame de Paris par MM. Lassus et Viollet-Leduc: rapport...annexé au projet de restauration, remis le 31 janvier 1843*. imprimerie de Mme de Lacombe. URL: `https://gallica.bnf.fr/ark:/12148/bpt6k104823k`.

Lax, P. D. and R. D. Richtmyer (1956). “Survey of the stability of linear finite difference equations”. In: *Communications on Pure and Applied Mathematics* 9.2, pp. 267–293. DOI: `10.1002/cpa.3160090206`.

Leishman, T. W., S. Rollins, and H. M. Smith (2006). “An experimental evaluation of regular polyhedron loudspeakers as omnidirectional sources of sound”. In: *The Journal of the Acoustical Society of America* 120.3, pp. 1411–1422. DOI: `10.1121/1.2221552`.

LeVeque, R. J. (2002). *Finite Volume Methods for Hyperbolic Problems*. Cambridge Texts in Applied Mathematics. Cambridge University Press. DOI: `10.1017/CBO9780511791253`.

— (2007). *Finite Difference Methods for Ordinary and Partial Differential Equations: Steady-State and Time-Dependent Problems*. Other Titles in Applied Mathematics. Society for Industrial and Applied Mathematics. ISBN: 9780898717839. DOI: `10.1137/1.9780898717839`.

Li, X., A. Taflove, and V. Backman (2005). “Modified FDTD near-to-far-field transformation for improved backscattering calculation of strongly forward-scattering objects”. In: *IEEE Antennas and Wireless Propagation Letters* 4, pp. 35–38. DOI: `10.1109/LAWP.2005.845038`.

Li, Y., J. Meyer, T. Lokki, J. Cuenca, O. Atak, and W. Desmet (2022). “Benchmarking of finite-difference time-domain method and fast multipole boundary element method for room acoustics”. In: *Applied Acoustics* 191, p. 108662. ISSN: 0003-682X. DOI: `10.1016/j.apacoust.2022.108662`.

Lilly, J. and S. Olhede (2009). “Higher-Order Properties of Analytic Wavelets”. In: *IEEE Transactions on Signal Processing* 57.1, pp. 146–160. DOI: `10.1109/tsp.2008.2007607`.

Linton, C. M. and D. V. Evans (1990). “The interaction of waves with arrays of vertical circular cylinders”. In: *Journal of Fluid Mechanics* 215, pp. 549–569. DOI: `10.1017/S0022112090002750`.

Liu, Y. and M. K. Sen (2009). “A new time–space domain high-order finite-difference method for the acoustic wave equation”. In: *Journal of Computational Physics* 228.23, pp. 8779–8806. ISSN: 0021-9991. DOI: `10.1016/j.jcp.2009.08.027`.

Liu, Y. (1996). “Fourier Analysis of Numerical Algorithms for the Maxwell Equations”. In: *Journal of Computational Physics* 124, pp. 396–416. DOI: `10.1006/jcph.1996.0068`.

Liu, Y. (2019). “On the BEM for acoustic wave problems”. In: *Engineering Analysis with Boundary Elements* 107, pp. 53–62. ISSN: 0955-7997. DOI: `10.1016/j.enganabound.2019.07.002`.

Lorenzo, J. R. (2012). *Principles Of Diffuse Light Propagation: Light Propagation In Tissues With Applications In Biology And Medicine*. World Scientific. DOI: `10.1142/7609`.

Lotz, W., D. Howard, and M. Hottinger (1995). *Architecture in Italy, 1500-1600*. The Yale University Press Pelican History of Art Series. Yale University Press. ISBN: 9780300064698.

Luebbers, R., K. Kunz, M. Schneider, and F. Hunsberger (1991). "A finite-difference time-domain near zone to far zone transformation (electromagnetic scattering)". In: *IEEE Transactions on Antennas and Propagation* 39.4, pp. 429–433. DOI: `10.1109/8.81453`.

Lui, W. K. and K. M. Li (2010). "The scattering of sound by a long cylinder above an impedance boundary". In: *The Journal of the Acoustical Society of America* 127.2, pp. 664–674. DOI: `10.1121/1.3273891`.

Luizard, P. and B. F. G. Katz (2011). "Coupled volume multi-slope room impulse responses: a quantitative analysis method". In: *Intl. Conf. on Auditorium Acoustics*. Vol. 33. 2, pp. 169–176.

Luizard, P. (2013). "Les espaces couplés : comportement, conception et perception dans un contexte de salle de spectacle". Theses. Université Pierre et Marie Curie - Paris VI. URL: `https://tel.archives-ouvertes.fr/tel-00874238`.

Luizard, P. and B. F. G. Katz (2014a). "Investigation of the effective aperture area of sliding and hinged doors between coupled spaces". In: *The Journal of the Acoustical Society of America* 136.2, EL135–EL141. DOI: `10.1121/1.4890202`.

Luizard, P., B. F. G. Katz, and C. Guastavino (2015). "Perceptual thresholds for realistic double-slope decay reverberation in large coupled spaces". In: *The Journal of the Acoustical Society of America* 137.1, pp. 75–84. DOI: `10.1121/1.4904515`.

Luizard, P., M. Otani, J. Botts, L. Savioja, and B. F. G. Katz (2013). "Comparison of sound field measurements and predictions in coupled volumes between numerical methods and scale model measurements". In: *Proceedings of Meetings on Acoustics* 19.1, p. 015114. DOI: `10.1121/1.4799138`.

Luizard, P., J.-D. Polack, and B. F. G. Katz (2014b). "Sound energy decay in coupled spaces using a parametric analytical solution of a diffusion equation". In: *The Journal of the Acoustical Society of America* 135.5, pp. 2765–2776. DOI: `10.1121/1.4870706`.

Luizard, P., N. Xiang, and B. F. G. Katz (2012). "Coupled volumes and statistical acoustics: preliminary results of an improved analytical model". In: *The Journal of the Acoustical Society of America* 131.4, pp. 3245–3245. DOI: `10.1121/1.4708109`.

Magrini, A. and P. Ricciardi (2002). "Coupling effects in Christian churches: Preliminary analysis based on a simple theoretical model and some experimental results". In: *Proc. of Forum Acousticum, Sevilla.*

Markowskei, A. J. and P. D. Smith (2017). "Measuring the effect of rounding the corners of scattering structures". In: *Radio Science* 52.5, pp. 693–708. DOI: `10.1002/2017RS006276`.

Martellotta, F. (2009). "Identifying acoustical coupling by measurements and prediction-models for St. Peter's Basilica in Rome". In: *The Journal of the Acoustical Society of America* 126.3, pp. 1175–1186. DOI: `10.1121/1.3192346`.

— (2016). "Understanding the acoustics of Papal Basilicas in Rome by means of a coupled-volumes approach". In: *Journal of Sound and Vibration* 382, pp. 413–427. ISSN: 0022-460X. DOI: `10.1016/j.jsv.2016.07.007`.

Martellotta, F., L. Álvarez-Morales, S. Girón, and T. Zamarreño (2018). "An investigation of multi-rate sound decay under strongly non-diffuse conditions: The crypt of the Cathedral of Cadiz". In: *Journal of Sound and Vibration* 421, pp. 261–274. ISSN: 0022-460X. DOI: `10.1016/j.jsv.2018.02.011`.

Medwin, H. and C. S. Clay (1998). "Chapter 2 - Sound Propagation". In: *Fundamentals of Acoustical Oceanography*. Applications of Modern Acoustics. San Diego: Academic Press, pp. 17–69. DOI: `10.1016/B978-012487570-8/50004-0`.

Meyer, J., L. Savioja, and T. Lokki (2019). “A case study on the perceptual differences in finite-difference time-domain-simulated diffuser designs”. In.

mh acoustics LLC (2022). *Eigenmike® microphone*. URL: https://mhacoustics.com/products#eigenmike1 (visited on 04/28/2022).

Morse, P. M. and R. H. Bolt (1944). “Sound Waves in Rooms”. In: *Rev. Mod. Phys.* 16 (2), pp. 69–150. DOI: 10.1103/RevModPhys.16.69.

Morse, P. M. and K. U. Ingard (1986). *Theoretical Acoustics*. International series in pure and applied physics. Princeton University Press.

MPP (2021). *Travaux de Notre-Dame de Paris - Journal des travaux (1844-1865)*. URL: https://mediatheque-patrimoine.culture.gouv.fr/travaux-de-notre-dame-de-paris-1844-1865.

Müller, S. and P. Massarani (2001). “Transfer-Function Measurement with Sweeps”. In: *Journal of the Audio Engineering Society* 49.6, pp. 443–471.

Mullins, S. S., E. K. Canfield-Dafilou, and B. F. G. Katz (2022). “The development of the early acoustics of the chancel in Notre-Dame de Paris: 1160-1230”. In: *Symp The Acoustics of Ancient Theatres*. Verona.

Murray, S. (1998). “Notre-Dame of Paris and the Anticipation of Gothic”. In: *The Art Bulletin* 80.2, pp. 229–253. ISSN: 00043079. DOI: 10.2307/3051231.

Naylor, G. M. (1993). “ODEON—Another hybrid room acoustical model”. In: *Applied Acoustics* 38.2, pp. 131–143. ISSN: 0003-682X. DOI: 10.1016/0003-682X(93)90047-A.

Nicholson, P. (1823). *The Student’s Instructor in Drawing and Working the Five Orders of Architecture*. J. Taylor at the Architectural Library.

Noe, N., F. Gaudaire, P. Jean, and M. Vermet (2006). “A General Ray-Tracing Solution to Reflection on Curved Surfaces and Diffraction by their Bounding Edges”. In: *Proceedings of the 9th International Conference on Theoretical and Computational Acoustics*. Dresden, Germany, pp. 225–234.

Nørgaard, K. M., J. B. Allen, and S. T. Neely (2021). “On causality and aural impulse responses synthesized using the inverse discrete Fourier transform”. In: *The Journal of the Acoustical Society of America* 149.5, pp. 3524–3533. DOI: 10.1121/10.0005048.

ODEON (2018). *Odeon A/S, ODEON Room Acoustics Software User’s manual Version 15*. English.

Okuzono, T., T. Otsuru, R. Tomiku, and N. Okamoto (2010). “Fundamental accuracy of time domain finite element method for sound-field analysis of rooms”. In: *Applied Acoustics* 71.10, pp. 940–946. ISSN: 0003-682X. DOI: 10.1016/j.apacoust.2010.06.004.

Okuzono, T., T. Yoshida, K. Sakagami, and T. Otsuru (2016). “An explicit time-domain finite element method for room acoustics simulations: Comparison of the performance with implicit methods”. In: *Applied Acoustics* 104, pp. 76–84. ISSN: 0003-682X. DOI: 10.1016/j.apacoust.2015.10.027.

Olive, S. E. and F. E. Toole (1988). “The Detection of Reflections in Typical Rooms”. In: *Journal of the Audio Engineering Society* 37, pp. 539–553.

Olson, V. (2004). “Colonnette Production and the Advent of the Gothic Aesthetic”. In: *Gesta* 43.1, pp. 17–29. DOI: 10.2307/25067089.

Orlowski, R. (1981). “An eighth-scale speech source for subjective assessments in acoustic models”. In: *Journal of Sound and Vibration* 77.4, pp. 551–559. ISSN: 0022-460X. DOI: 10.1016/S0022-460X(81)80050-8.

Orlowski, R. (2020). “The historical use of models in the acoustic design of buildings”. In: *PHYSICAL MODELS*. John Wiley & Sons, Ltd. Chap. 26, pp. 762–792. ISBN: 9783433609613. DOI: `10.1002/9783433609613.ch26`.

Ortiz, S., B. Kolbrek, P. Cobo, L. M. González, and C. De La Colina (2014). “Point Source Loudspeaker Design: Advances on the Inverse Horn Approach”. In: *Journal of the Audio Engineering Society* 62.5, pp. 345–354. DOI: `10.17743/jaes.2014.0018`.

Osswald, F. (1930a). *Acoustic model test at the Institute for Applied Acoustics at ETH Zurich*. ETHZ. DOI: `10.3932/ethz-a-000986437`.

— (1930b). “Akustischer Konzert-und Vortragssaal mit veränderlichem Volumen”. In: *Schweizerische Bauzeitung* 96.18, pp. 224–225. DOI: `10.5169/seals-44077`.

Ouis, D. (1999). “Scattering by a barrier in a room”. In: *Applied Acoustics* 56.1, pp. 1–24. ISSN: 0003-682X. DOI: `10.1016/S0003-682X(98)00014-0`.

Pallett, D., E. Pierce, and D. Toth (1976). “A small-scale multi-purpose reverberation room”. In: *Applied Acoustics* 9.4, pp. 287–302. ISSN: 0003-682X. DOI: `10.1016/0003-682X(76)90010-4`.

Pätynen, J. and T. Lokki (2016). “Concert halls with strong and lateral sound increase the emotional impact of orchestra music”. In: *The Journal of the Acoustical Society of America* 139.3, pp. 1214–1224. DOI: `10.1121/1.4944038`.

Pätynen, J., S. Tervo, and T. Lokki (2013). “Analysis of concert hall acoustics via visualizations of time-frequency and spatiotemporal responses”. In: *The Journal of the Acoustical Society of America* 133.2, pp. 842–857. DOI: `10.1121/1.4770260`.

Pätynen, J. and T. Lokki (2010). “Directivities of Symphony Orchestra Instruments”. In: *Acta Acustica united with Acustica* 96.1, pp. 138–167. ISSN: 1610-1928. DOI: `10.3813/AAA.918265`.

Pedrero, A., R. Ruiz, A. Díaz-Chyla, and C. Díaz (2014). “Acoustical study of Toledo Cathedral according to its liturgical uses”. In: *Applied Acoustics* 85, pp. 23–33. ISSN: 0003-682X. DOI: `10.1016/j.apacoust.2014.04.004`.

Pelegrín-García, D., M. Rychtáriková, and Glorieux (2016). “Audibility Thresholds of a Sound Reflection in a Classical Human Echolocation Experiment”. In: *Acta Acustica united with Acustica* 102.3, pp. 530–539. ISSN: 1610-1928. DOI: `10.3813/AAA.918970`.

Perrault, C. (1996). *Ordonnance for the Five Kinds of Columns after the Method of the Ancients*. Texts & Documents. Getty Center for the History of Art and the Humanities. ISBN: 9780892362325.

PHE project (2021). *The Past Has Ears*. Sorbonne Université, CNRS, Institut Jean Le Rond d’Alembert. URL: `http://pasthasears.dalembert.upmc.fr/`.

Picaut, J. and N. Fortin (2012). “SPPS, a particle-tracing numerical code for indoor and outdoor sound propagation prediction”. In: *Acoustics 2012*. Ed. by S. F. d’Acoustique. Nantes, France. URL: `https://hal.archives-ouvertes.fr/hal-00810894`.

Pierce, A. (2019). *Acoustics: An Introduction to Its Physical Principles and Applications*. Springer International Publishing. DOI: `10.1007/978-3-030-11214-1`.

Pind, F., A. P. Engsig-Karup, C.-H. Jeong, J. S. Hesthaven, M. S. Mejling, and J. Strømann-Andersen (2019). “Time domain room acoustic simulations using the spectral element method”. In: *The Journal of the Acoustical Society of America* 145.6, pp. 3299–3310. DOI: `10.1121/1.5109396`.

Pogson, M. A., D. M. Whittaker, G. A. Gehring, R. J. Hughes, J. A. S. Angus, and T. J. Cox (2010). “Multiple Scattering Between Cylinders and a Schroeder Diffuser”. In: *Acta Acustica united with Acustica* 96.2, pp. 292–299. ISSN: 1610-1928. DOI: `10.3813/AAA.918278`.

Polack, J.-D. (1988). “La transmission de l’énergie sonore dans les salles”. 1988LEMA1011. PhD thesis. Université du Maine, p. 231. URL: http://www.theses.fr/1988LEMA1011.

Polack, J.-D., L. S. Christensen, and P. M. Juhl (2001). “An Innovative Design for Omnidirectional Sound Sources”. In: *Acta Acustica united with Acustica* 87.4, pp. 505–512. ISSN: 1610-1928. URL: https://www.ingentaconnect.com/content/dav/aaua/2001/00000087/00000004/art00010.

Polack, J.-D., A. H. Marshall, and G. Dodd (1989). “Digital evaluation of the acoustics of small models: The midas package”. In: *The Journal of the Acoustical Society of America* 85.1, pp. 185–193. DOI: 10.1121/1.397714.

Polack, J.-D., X. Meynial, and V. Grillon (1993). “Auralization in Scale Models: Processing of Impulse Response”. In: *Journal of the Audio Engineering Society* 41.11, pp. 939–945.

Poletti, M. A. (2013). “Active Acoustic Systems for the Control of Room Acoustics”. In: *Noise & Vibration Worldwide* 44.4, pp. 10–26. DOI: 10.1260/0957-4565.44.4.10.

Pörschmann, C. and J. M. Arend (2021). “Investigating phoneme-dependencies of spherical voice directivity patterns”. In: *The Journal of the Acoustical Society of America* 149.6, pp. 4553–4564. DOI: 10.1121/10.0005401.

Postma, B. N. and B. F. G. Katz (2016). “Acoustics of Notre-Dame Cathedral de Paris”. In: *Intl Cong on Acoustics (ICA)*. Buenos Aires, 0269:1–10. URL: http://www.ica2016.org.ar/ica2016proceedings/ica2016/ICA2016-0269.pdf.

Pracownia Tryktrak (2020). *Makieta akustyczna Sinfonia Varsovia*. URL: http://www.pracownia-tryktrak.pl/portfolio/makieta-akustyczna-sinfonia-varsovia/ (visited on 02/01/2020).

Pratt, W. S. (1879). “The Columnar Architecture of the Egyptians”. In: *Proceedings of the American Academy of Arts and Sciences* 15, pp. 313–365. ISSN: 01999818. DOI: 10.2307/25138580.

Pu, H., X. Qiu, and J. Wang (2011). “Different sound decay patterns and energy feedback in coupled volumes”. In: *The Journal of the Acoustical Society of America* 129.4, pp. 1972–1980. DOI: 10.1121/1.3553223.

Quiquerez, M., K. Oguchi, M. Komoda, D. Beckmann, and Y. Toyota (2018). “Acoustic tests with 1:10-scale model: Elbphilharmonie case study”. In: *Proceedings of the Institute of Acoustics*. Vol. 40, pp. 97–104.

Raghuvanshi, N., R. Narain, and M. C. Lin (2009). “Efficient and Accurate Sound Propagation Using Adaptive Rectangular Decomposition”. In: *IEEE Transactions on Visualization and Computer Graphics* 15.5, pp. 789–801. DOI: 10.1109/TVCG.2009.28.

Rasmussen, K. (1997). “Calculation methods for the physical properties of air used in the calibration of microphones”. In: *Report PL-11b*. Department of acoustical technology, Technical university of Denmark.

Rathsam, J. and L. M. Wang (2010). “Planar Reflector Panels with Convex Edges”. In: *Acta Acustica united with Acustica* 96.5, pp. 905–913. ISSN: 1610-1928. DOI: 10.3813/AAA.918349.

Redondo, J., R. Picó, B. Roig, and M. R. Avis (2007). “Time Domain Simulation of Sound Diffusers Using Finite-Difference Schemes”. In: *Acta Acustica united with Acustica* 93.4, pp. 611–622. ISSN: 1610-1928. URL: https://www.ingentaconnect.com/content/dav/aaua/2007/00000093/00000004/art00009.

Redondo, J., R. Picó, V. J. Sánchez-Morcillo, and W. Woszczyk (2013). “Sound diffusers based on sonic crystals”. In: *The Journal of the Acoustical Society of America* 134.6, pp. 4412–4417. DOI: 10.1121/1.4828826.

Richard, A., D. Fernández Comesaña, J. Brunskog, C.-H. Jeong, and E. Fernandez-Grande (2019). “Characterization of sound scattering using near-field pressure and particle velocity measurements”. In: *The Journal of the Acoustical Society of America* 146.4, pp. 2404–2414. DOI: 10.1121/1.5126942.

Rindel, J. (2011a). “The ERATO project and its contribution to our understanding of the acoustics of ancient theatres”. In: *The Acoustics of Ancient Theatres Conference*. Patras, Greece, pp. 1–10. URL: https://www.odeon.dk/pdf/AA2011_18_Rindel.pdf.

Rindel, J. H. (1986). “Attenuation of Sound Reflections due to Diffraction”. In: *Nordic Acoustical Meeting, Aalborg, Denmark, 20-22 August 1986*.

— (1991). “Design of new ceiling reflectors for improved ensemble in a concert hall”. In: *Applied Acoustics* 34.1, pp. 7–17. ISSN: 0003-682X. DOI: 10.1016/0003-682X(91)90043-E.

— (2002). “Modelling in auditorium acoustics. From ripple tank and scale models to computer simulations”. In: *Revista de Acústica* 33.3, pp. 31–35.

— (2011b). “Room Acoustic Modelling Techniques: A Comparison of a Scale Model and a Computer Model for a New Opera Theatre”. In: *Building Acoustics* 18. DOI: 10.1260/1351-010X.18.3-4.259.

Robinson, P. W., A. Walther, C. Faller, and J. Braasch (2013a). “Echo thresholds for reflections from acoustically diffusive architectural surfaces”. In: *The Journal of the Acoustical Society of America* 134.4, pp. 2755–2764. DOI: 10.1121/1.4820890.

Robinson, P. W. and N. Xiang (2010). “On the subtraction method for in-situ reflection and diffusion coefficient measurements”. In: *The Journal of the Acoustical Society of America* 127.3, EL99–EL104. DOI: 10.1121/1.3299064.

— (2013b). “Design, construction, and evaluation of a 1:8 scale model binaural manikin”. In: *The Journal of the Acoustical Society of America* 133.3, EL162–EL167. DOI: 10.1121/1.4789876.

Robinson, P. W., N. Xiang, and J. Braasch (2011). “Understanding the perceptual effects of diffuser application in rooms.” In: *Proceedings of Meetings on Acoustics* 12.1, p. 015002. DOI: 10.1121/1.3608405.

Roesner, E. H., ed. (1993). *Le Magnus liber organi de Notre-Dame de Paris*. Vol. 1, Les Quadrupla et Tripla de Paris. Musica Gallica. Monaco: Editions de l’Oiseau-Lyre.

Rohfritsch, A., J.-M. Conoir, R. Marchiano, and T. Valier-Brasier (2019). “Numerical simulation of two-dimensional multiple scattering of sound by a large number of circular cylinders”. In: *The Journal of the Acoustical Society of America* 145.6, pp. 3320–3329. DOI: 10.1121/1.5110310.

Rosellini, I. and F. Serino (2003). *The Monuments of Egypt and Nubia*. American University in Cairo Press. ISBN: 9789774247897.

Rungta, A., C. Schissler, N. Rewkowski, R. Mehra, and D. Manocha (2018). “Diffraction Kernels for Interactive Sound Propagation in Dynamic Environments”. In: *IEEE Transactions on Visualization and Computer Graphics* 24.4, pp. 1613–1622. DOI: 10.1109/TVCG.2018.2794098.

Ryu, J. K. and J. Y. Jeon (2008). “Subjective and objective evaluations of a scattered sound field in a scale model opera house”. In: *The Journal of the Acoustical Society of America* 124.3, pp. 1538–1549. DOI: 10.1121/1.2956474.

Sabine, W. (1922). *Collected Papers on Acoustics*. Harvard University Press.

Saffar, S. (2021). “Investigation and Comparison of Three Popular Ultrasonic Generators (PZT, PVDF, EMFi) for Employing in Acoustic Scaling”. In: *Iranian Journal of Mechanical Engineering Transactions of the ISME* 22.2, pp. 21–37. ISSN: 1605-9727. DOI: 10.30506/jmee.2021.128422.1231.

Sakamoto, S. (2009). “Calculation of sound propagation in three-dimensional field with constant cross section by Duhamel’s efficient method using transient solutions obtained by finite-difference time-domain method”. In: *Acoustical Science and Technology* 30.2, pp. 72–82. DOI: 10.1250/ast.30.72.

Salomons, E. M., A. C. Geerlings, and D. Duhamel (1997). “Comparison of a Ray Model and a Fourier-Boundary Element Method for Traffic Noise Situations with Multiple Diffractions and Reflections”. In: *Acta Acustica united with Acustica* 83.1, pp. 35–47. ISSN: 1610-1928. URL: https://www.ingentaconnect.com/content/dav/aaua/1997/00000083/00000001/art00009.

Sánchez-Pérez, J. V., C. Rubio, R. Martinez-Sala, R. Sanchez-Grandia, and V. Gomez (2002). “Acoustic barriers based on periodic arrays of scatterers”. In: *Applied Physics Letters* 81.27, pp. 5240–5242. DOI: 10.1063/1.1533112.

Sandron, D. and A. Tallon (2020). *Notre Dame Cathedral: Nine Centuries of History*. Trans. by A. Tallon and L. Cook. Penn State University Press. DOI: 10.1515/9780271087726.

Savioja, L. and U. P. Svensson (2015). “Overview of geometrical room acoustic modeling techniques”. In: *The Journal of the Acoustical Society of America* 138.2, pp. 708–730. DOI: 10.1121/1.4926438.

Scarre, C. and G. Lawson, eds. (2006). *Archaeoacoustics*. McDonald Institute for Archaeological Research, University of Cambridge.

Schady, A., D. Heimann, and J. Feng (2014). “Acoustic Effects of Trees Simulated by a Finite-Difference Time-Domain Model”. In: *Acta Acustica united with Acustica* 100.6, pp. 1112–1119. ISSN: 1610-1928. DOI: 10.3813/AAA.918790.

Schneider, J. B. and R. J. Kruhlak (2001). “Dispersion of homogeneous and inhomogeneous waves in the Yee finite-difference time-domain grid”. In: *IEEE Transactions on Microwave Theory and Techniques* 49.2, pp. 280–287. DOI: 10.1109/22.903087.

Schneider, J. B., C. L. Wagner, and S. L. Broschat (1998). “Implementation of transparent sources embedded in acoustic finite-difference time-domain grids”. In: *The Journal of the Acoustical Society of America* 103.1, pp. 136–142. DOI: 10.1121/1.421084.

Schröder, D. (2011). “Physically based real-time auralization of interactive virtual environments”. PhD thesis. Berlin, XVIII, 206 S. : Ill., graph. Darst. URL: https://publications.rwth-aachen.de/record/50580.

Schröder, D. and M. Vorländer (2011). “RAVEN: A real-time framework for the auralization of interactive virtual environments”. In: *Proceedings of Forum Acusticum 2011 : 27 June - 01 July, Aalborg, Denmark /ed. by Danish Acoustical Society (DAS) on behalf of European Acoustics Association (EAA)*. Madrid: Spanish Acoustical Society. URL: https://publications.rwth-aachen.de/record/127987.

Schroeder, M. R. (1965). “New Method of Measuring Reverberation Time”. In: *The Journal of the Acoustical Society of America* 37.3, pp. 409–412. DOI: 10.1121/1.1909343.

Serlio, S. (1560). *Tutte l’opere d’Architettura e prospettiva*. Appresso G. B. et M. Sessa fratelli.

Sheaffer, J., M. van Walstijn, and B. Fazenda (2014). “Physical and numerical constraints in source modeling for finite difference simulation of room acoustics”. In: *The Journal of the Acoustical Society of America* 135.1, pp. 251–261. DOI: 10.1121/1.4836355.

Shtrepi, L., A. Astolfi, S. Pelzer, R. Vitale, and M. Rychtáriková (2015). "Objective and perceptual assessment of the scattered sound field in a simulated concert hall". In: *The Journal of the Acoustical Society of America* 138.3, pp. 1485–1497. DOI: `10.1121/1.4929743`.

Shtrepi, L., A. Astolfi, G. E. Puglisi, and M. C. Masoero (2017). "Effects of the Distance from a Diffusive Surface on the Objective and Perceptual Evaluation of the Sound Field in a Small Simulated Variable-Acoustics Hall". In: *Applied Sciences* 7.3. ISSN: 2076-3417. DOI: `10.3390/app7030224`.

Siltanen, S., T. Lokki, S. Kiminki, and L. Savioja (2007). "The room acoustic rendering equation". In: *The Journal of the Acoustical Society of America* 122.3, pp. 1624–1635. DOI: `10.1121/1.2766781`.

Skelton, E. A. and J. H. James (1997). *Theoretical Acoustics of Underwater Structures*. Imperial College Press. DOI: `10.1142/p072`.

Smith, R. (2019). *A report on the Archeological Field Season*. Fieldwork report. Aphrodisias Excavations. URL: `http://aphrodisias.classics.ox.ac.uk/Aphrodisias-2019-report-c.pdf`.

Spa, C., A. Garriga, and J. Escolano (2010). "Impedance boundary conditions for pseudo-spectral time-domain methods in room acoustics". In: *Applied Acoustics* 71.5, pp. 402–410. ISSN: 0003-682X. DOI: `10.1016/j.apacoust.2009.11.015`.

Spandöck, F. (1934). "Akustische Modellversuche". In: *Annalen der Physik* 412.4, pp. 345–360. DOI: `https://doi.org/10.1002/andp.19344120402`.

Stephenson, U. M. (2010). "An Energetic Approach for the Simulation of Diffraction within Ray Tracing Based on the Uncertainty Relation". In: *Acta Acustica United With Acustica* 96.3, pp. 516–535. DOI: `10.3813/AAA.918304`.

— (2018). "Simulation of multiple Sound Particle Diffraction based on the Uncertainty Relation - a revolution in noise immission prognosis; Part I: Principle and Method". In: *Proceedings of the Euronoise 2018*. Heraklion, Greece, pp. 2063–2076. URL: `https://www.euronoise2018.eu/docs/papers/347_Euronoise2018.pdf`.

Stinson, P. (2016). *The Civil Basilica*. Vol. 7. Aphrodisias. Wiesbaden: Reichert Verlag. ISBN: 9783954901111. DOI: `10.29091/9783954909087`.

Strikwerda, J. C. (2004). *Finite Difference Schemes and Partial Differential Equations, Second Edition*. Society for Industrial and Applied Mathematics. DOI: `10.1137/1.9780898717938`.

Strutt, H. J. (1871). "XV. On the light from the sky, its polarization and colour". In: *The London, Edinburgh, and Dublin Philosophical Magazine and Journal of Science* 41.271, pp. 107–120. DOI: `10.1080/14786447108640452`.

Sü Gül, Z. (2021). "Exploration of room acoustics coupling in Hagia Sophia of İstanbul for its different states". In: *The Journal of the Acoustical Society of America* 149.1, pp. 320–339. DOI: `10.1121/10.0002971`.

Sü Gül, Z., M. Çalışkan, A. Tavukçuoğlu, and N. Xiang (2018). "Assessment of acoustical indicators in multi-domed historic structures by non-exponential energy decay analysis". In: *Acoustics Australia* 46.2, pp. 181–192.

Sü Gül, Z., N. Xiang, and M. Çalışkan (2016). "Investigations on sound energy decays and flows in a monumental mosque". In: *The Journal of the Acoustical Society of America* 140.1, pp. 344–355. DOI: `10.1121/1.4953691`.

Summers, J. E. (2005). "Technical Note: Remark on the Formal Identity of Two Statistical-Acoustics Models of Coupled Rooms". In: *Building Acoustics* 12.1, pp. 41–50. DOI: `10.1260/1351010053499225`.

Summers, J. E., R. R. Torres, and Y. Shimizu (2004). “Statistical-acoustics models of energy decay in systems of coupled rooms and their relation to geometrical acoustics”. In: *The Journal of the Acoustical Society of America* 116.2, pp. 958–969. DOI: 10.1121/1.1763974.

Sun, J.-c. (2004). “On Approximation of Laplacian Eigenproblem over a Regular Hexagon with Zero Boundary Conditions”. In: *Journal of Computational Mathematics* 22.2, pp. 275–286. ISSN: 1991-7139. URL: http://global-sci.org/intro/article_detail/jcm/10328.html.

Suzuki, K. and T. Hidaka (2019). “A study on precise measurement of room impulse response in a scale model and auralization”. In: *International Symposium on Room Acoustics, ISRA 2019* (Sept. 15–17, 2019). Amsterdam, Netherlands.

Suzuki, K., Y. Yamada, S. Koyanagi, and T. Hidaka (2018). “Basic study on improvement of precision of measurement of room acoustic characteristics using scale model and three-dimensioned (3D) sound field auralization”. In: *The Journal of the Acoustical Society of Japan* 74.5, pp. 244–253. DOI: 10.20697/jasj.74.5_244.

Suzumura, Y., M. Sakurai, Y. Ando, I. Yamamoto, T. Iizuka, and M. Oowaki (2000). “An evaluation of the effects of scattered reflections in a sound field”. In: *Journal of Sound and Vibration* 232.1, pp. 303–308. ISSN: 0022-460X. DOI: 10.1006/jsvi.1999.2822.

Svensson, U. P., R. I. Fred, and J. Vanderkooy (1999). “An analytic secondary source model of edge diffraction impulse responses”. In: *The Journal of the Acoustical Society of America* 106.5, pp. 2331–2344. DOI: 10.1121/1.428071.

Swearingen, M. E. and D. C. Swanson (2012). “A Numerical Model for Point Source Scattering from an Impedance Cylinder Placed Normal to an Impedance Plane”. In: *Acta Acustica united with Acustica* 98.4, pp. 523–533. ISSN: 1610-1928. DOI: 10.3813/AAA.918534.

Szeląg, A., T. Kamisiński, M. Lewińska, J. Rubacha, and A. Pilch (2014). “The Characteristic of Sound Reflections from Curved Reflective Panels”. In: *Archives of Acoustics* vol. 39.No 4, pp. 549–558. DOI: 10.2478/aoa-2014-0059.

Taflove, A. and S. Hagness (2005). *Computational Electrodynamics: The Finite-difference Time-domain Method*. Artech House antennas and propagation library. Artech House.

Tahara, Y., K. Ishikawa, H. Kawamura, S. Sasaki, and M. Nakamura (2003). “Acoustic scale model experiments using a piezoelectric dodecahedral speaker system”. In: *The Journal of the Acoustical Society of Japan* 59.10, pp. 614–621. DOI: 10.20697/jasj.59.10_614.

Tervo, S. (2020). *SDM Toolbox 1.3001, MATLAB Central File Exchange*. URL: https://www.mathworks.com/matlabcentral/fileexchange/56663-sdm-toolbox (visited on 09/01/2020).

Tervo, S., J. Pätynen, A. Kuusinen, and T. Lokki (2013a). “Spatial decomposition method for room impulse responses”. In: *The Journal of the Acoustical Society of America* 61.1/2, pp. 17–28.

Tervo, S., J. Pätynen, and T. Lokki (2013b). “Spatio-temporal energy measurements in renowned concert halls with a loudspeaker orchestra”. In: *Proceedings of Meetings on Acoustics* 19.1, p. 015019. DOI: 10.1121/1.4799424.

Thurlby, M. (1998). “Aspects of the architectural history of Kirkwall Cathedral”. In: *Proceedings of the Society of Antiquaries of Scotland* 127, pp. 855–888. URL: http://soas.is.ed.ac.uk/index.php/psas/article/view/9988.

Tolan, J. G. and J. B. Schneider (2003). “Locally conformal method for acoustic finite-difference time-domain modeling of rigid surfaces”. In: *The Journal of the Acoustical Society of America* 114.5, pp. 2575–2581. DOI: 10.1121/1.1616576.

Tornberg, A.-K. and B. Engquist (2008). “Consistent boundary conditions for the Yee scheme”. In: *Journal of Computational Physics* 227.14, pp. 6922–6943. ISSN: 0021-9991. DOI: 10.1016/j.jcp.2008.03.045.

Tuomela, J. (1990). *Fourth order schemes for wave equation Maxwell’s equations and linearized elastodynamic equations*. Tech. rep. RR-1337. Projet MENUSIN. INRIA. URL: https://hal.inria.fr/inria-00075222.

— (1994). “Fourth-order schemes for the wave equation, Maxwell equations, and linearized elastodynamic equations”. In: *Numerical Methods for Partial Differential Equations* 10.1, pp. 33–63. DOI: 10.1002/num.1690100104.

Twersky, V. (1952). “Multiple Scattering of Radiation by an Arbitrary Planar Configuration of Parallel Cylinders and by Two Parallel Cylinders”. In: *Journal of Applied Physics* 23.4, pp. 407–414. DOI: 10.1063/1.1702220.

Überall, H. (1985). “Acoustic scattering from elastic cylinders and spheres: surface waves (Watson transform) and transmitted waves”. In: *Diffusion et Diffraction* 2.5, pp. 353–387.

Umnova, O., K. Attenborough, and C. M. Linton (2006). “Effects of porous covering on sound attenuation by periodic arrays of cylinders”. In: *The Journal of the Acoustical Society of America* 119.1, pp. 278–284. DOI: 10.1121/1.2133715.

UNESCO (2003). *Text of the Convention for the Safeguarding of the Intangible Cultural Heritage*. Text of the Convention. UNESCO. URL: https://ich.unesco.org/en/convention.

— (2017). *The Importance of sound in today’s world: promoting best practices*. General Conference Resolution 39 C/49. UNESCO. URL: https://unesdoc.unesco.org/ark:/48223/pf0000259172.

Valier-Brasier, T. and D. Royer (2021). *Ondes élastiques dans les solides 2: Rayonnement, diffusion, génération*. Collection ondes vol. 2. ISTE Editions. ISBN: 9781784057671.

van der Aa, B. and J. Forssén (2015). “The 2.5D MST for sound propagation through an array of acoustically rigid cylinders perpendicular to an impedance surface”. In: *Journal of Physics D: Applied Physics* 48.29, p. 295501. DOI: 10.1088/0022-3727/48/29/295501.

van Walstijn, M. and K. Kowalczyk (2008). “On the numerical solution of the 2D wave equation with compact FDTD schemes”. In: *In Proc. Int. Conf. Digital Audio Effects (DAFx’08)*, pp. 205–212.

Varadan, V. K., V. V. Varadan, S. J. Tsao, and W. G. Neubauer (1982). “Scattering of acoustic waves by rigid cylindrical objects with sharp corners”. In: *The Journal of the Acoustical Society of America* 72.6, pp. 1957–1964. DOI: 10.1121/1.388627.

Vázquez, P., B. Menéndez, M. F. C. Denecker, and C. Thomachot-Schneider (2016). “Comparison between petrophysical properties, durability and use of two limestones of the Paris region”. In: *Sustainable Use of Traditional Geomaterials in Construction Practice*. Geological Society of London. ISBN: 9781862397255. DOI: 10.1144/SP416.15.

Vermeulen, R. and J. de Boer (1936). “Optical model experiments for studying the acoustics of theatres”. In: *Philips Technical Review* 1.2, pp. 46–52.

Vignola, G. da, J. Leeke, and D. Watkin (2011). *Canon of the Five Orders of Architecture*. Ed. and trans. by J. Leeke and D. Watkin. Dover Publications Inc.

Viollet-le-Duc, E. E. (1859). *Dictionnaire raisonné de l'architecture française du XIe au XVIe siècle*. B. Bance.

Vitruvius, P. (1999). *Vitruvius: 'Ten Books on Architecture'*. Ed. and trans. by I. D. Rowland and T. N. Howe. Cambridge University Press. DOI: `10.1017/CBO9780511840951`.

Vorländer, M. (1995). "International round robin on room acoustical computer simulations". In: *Proceedings of the 15th International Congress on Acoustics*. Trondheim, Norway, pp. 577–580.

Walther, A., P. W. Robinson, and O. Santala (2013). "Effect of spectral overlap on the echo suppression threshold for single reflection conditions". In: *The Journal of the Acoustical Society of America* 134.2, EL158–EL164. DOI: `10.1121/1.4812447`.

Wang, H., M. Cosnefroy, and M. Hornikx (2021). "An arbitrary high-order discontinuous Galerkin method with local time-stepping for linear acoustic wave propagation". In: *The Journal of the Acoustical Society of America* 149.1, pp. 569–580. DOI: `10.1121/10.0003340`.

Wang, S. (1996). "Finite-difference time-domain approach to underwater acoustic scattering problems". In: *The Journal of the Acoustical Society of America* 99.4, pp. 1924–1931. DOI: `10.1121/1.415375`.

Ware, W. (1904). *The American Vignola, Part I: The Five Orders*. International Textbook Company.

Weber, A. and B. F. G. Katz (2019). "Numerical simulation round robin of a coupled volume case: Preliminary results". In: *Proceedings of the 23rd International Congress on Acoustics : integrating 4th EAA Euroregio 2019*. 23rd International Congress on Acoustics, Aachen (Germany), 9 Sep 2019 - 13 Sep 2019. Berlin, Germany: Deutsche Gesellschaft für Akustik. DOI: `10.18154/RWTH-CONV-239933`.

— (2022). "Sound Scattering by Gothic Piers and Columns of the Cathédrale Notre-Dame de Paris". In: *Acoustics* 4.3, pp. 679–703. ISSN: 2624-599X. DOI: `10.3390/acoustics4030041`.

Wendt, F. and Höldrich, Robert (2021). "Precedence effect for specular and diffuse reflections". In: *Acta Acust.* 5, pp. 1–9. DOI: `10.1051/aacus/2020027`.

Wright, C. (2008). *Music and Ceremony at Notre Dame of Paris, 500-1550*. Cambridge Studies in Music. Cambridge University Press. ISBN: 9780521088343.

Wycherley, R. E. (1974). "The Stones of Athens". In: *Greece & Rome* 21.1, pp. 54–67. ISSN: 00173835, 14774550. URL: `http://www.jstor.org/stable/642554` (visited on 04/23/2022).

Xiang, N., A. Alamuru, I. B. Witew, and M. Vorländer (2018). "Experimental investigations on sound energy propagation in acoustically coupled volumes using a high-spatial resolution scanning system". In: *The Journal of the Acoustical Society of America* 143.6, EL437–EL442. DOI: `10.1121/1.5040886`.

Xiang, N. and J. Blauert (1991). "A miniature dummy head for binaural evaluation of tenth-scale acoustic models". In: *Applied Acoustics* 33.2, pp. 123–140. ISSN: 0003-682X. DOI: `10.1016/0003-682X(91)90069-Q`.

— (1993). "Binaural scale modelling for auralisation and prediction of acoustics in auditoria". In: *Applied Acoustics* 38.2, pp. 267–290. ISSN: 0003-682X. DOI: `10.1016/0003-682X(93)90056-C`.

Xiang, N., P. Goggans, T. Jasa, and P. W. Robinson (2011). "Bayesian characterization of multiple-slope sound energy decays in coupled-volume systems". In: *The Journal of the Acoustical Society of America* 129.2, pp. 741–752. DOI: `10.1121/1.3518773`.

Xiang, N. and P. M. Goggans (2001). "Evaluation of decay times in coupled spaces: Bayesian parameter estimation". In: *The Journal of the Acoustical Society of America* 110.3, pp. 1415–1424. DOI: 10.1121/1.1390334.

— (2003). "Evaluation of decay times in coupled spaces: Bayesian decay model selection". In: *The Journal of the Acoustical Society of America* 113.5, pp. 2685–2697. DOI: 10.1121/1.1562151.

Xiang, N., Y. Jing, and A. C. Bockman (2009). "Investigation of acoustically coupled enclosures using a diffusion-equation model". In: *The Journal of the Acoustical Society of America* 126.3, pp. 1187–1198. DOI: 10.1121/1.3168507.

Xiang, N., U. Trivedi, and B. Xie (2019). "Artificial enveloping reverberation for binaural auralization using reciprocal maximum-length sequences". In: *The Journal of the Acoustical Society of America* 145.4, pp. 2691–2702. DOI: 10.1121/1.5095863.

Yamashita, O., T. Tsuchiya, Y. Iwaya, M. Otani, and Y. Inoguchi (2015). "Reflective boundary condition with arbitrary boundary shape for compact-explicit finite-difference time-domain method". In: *Japanese Journal of Applied Physics* 54.7S1, 07HC02. DOI: 10.7567/jjap.54.07hc02.

Yee, K. (1966). "Numerical solution of initial boundary value problems involving Maxwell's equations in isotropic media". In: *IEEE Transactions on Antennas and Propagation* 14.3, pp. 302–307. ISSN: 1558-2221. DOI: 10.1109/TAP.1966.1138693.

Yüksel, Z. (2000). "A new approach to an ancient subject: CAHRISMA project". In: URL: http://staff.um.edu.mt/__data/assets/pdf_file/0010/79363/Cahrisma_Project.pdf.

Yüksel, Z., C. Binan, and R. Ünver (2003). "A research project in the intersection of architectural conservation and virtual reality: CAHRISMA". In: *New perspectives to save cultural heritage. Proceedings of the XIXth International Symposium CIPA 2003.* Antalya, Turkey, pp. 220–223. URL: https://www.cipaheritagedocumentation.org/wp-content/uploads/2018/11/Karabiber-Y%C3%BCksel-e.a.-A-research-project-in-the-intersection-of-architectural-conservation-and-virtual-reality_Cahrisma.pdf.

Yüksel, Z., S. Erdoğan, R. Ayangil, R. Ünver, C. Binan, and C. Can (2005). "Audio-Visual Conservation And Restitution Of The Ancient Theaters And Odea In Virtual Environment: Erato Research Project". In: *Megaron* 1.1, pp. 1–8. URL: https://megaronjournal.com/jvi.aspx?pdir=megaron&plng=eng&un=MEGARON-18291.

Zamarreño, T., S. Girón, and M. Galindo (2007). "Acoustic energy relations in Mudejar-Gothic churches". In: *The Journal of the Acoustical Society of America* 121.1, pp. 234–250. DOI: 10.1121/1.2390665.

Zhang, L. and X. Wu (2005). "On cross correlation based-discrete time delay estimation". In: *IEEE International Conference on Acoustics, Speech, and Signal Processing, 2005.* Vol. 4, iv/981–iv/984 Vol. 4. DOI: 10.1109/ICASSP.2005.1416175.

Zhong, X., W. Guo, and J. Wang (2018). "Audible Threshold of Early Reflections with Different Orientations and Delays". In: *Sound & Vibration* 52.6, pp. 18–22. ISSN: 2693-1443. DOI: 10.32604/sv.2018.03900.

Zingg, D. W. and H. Lomax (1993). "Finite-Difference Schemes on Regular Triangular Grids". In: *J. Comput. Phys.* 108.2, pp. 306–313. ISSN: 0021-9991. DOI: 10.1006/jcph.1993.1184.

Zitron, N. R. and J. Davis (1966). "A note on scattering of cylindrical waves by a circular cylinder". In: *Canadian Journal of Physics* 44.11, pp. 2941–2944. DOI: 10.1139/p66-237.

Appendix A

Measurement positions of the Sinfonia Varsovia Centrum concert hall scale model.

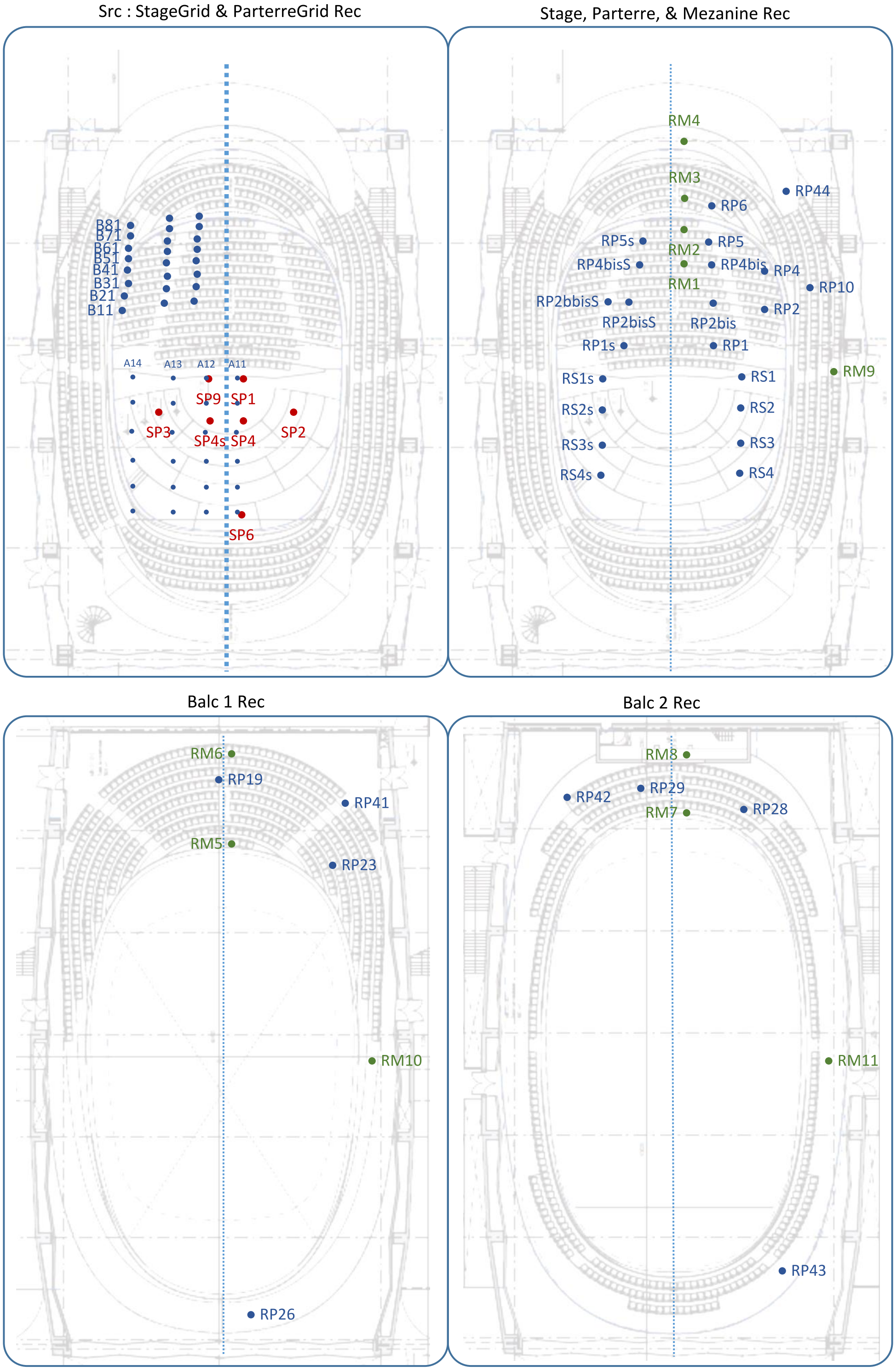

Appendix B

Invitation to participants of the coupled volume case Round Robin

Thank you for agreeing to participate in this room acoustical simulation study.

The objective of the study is to compare various contemporary (2019) implementations of numerical simulation methods (Geometrical methods, BEM, FDTD, etc.) with physical measurements in the context of room acoustics. We have chosen to use a coupled volume scale model as reference, focusing on the late reverberation modeling capabilities of complex spaces. The scale model is a very simple shoebox-type coupled volume system composed of two rooms (a main room and a single reverberation chamber) with different reverberation times linked by a single large aperture.

The measured results provided from the scale model have been corrected for scale to represent a full-scale room. Accordingly, each numerical method shall be implemented on a 3D-model representing the system resized at scale 1:1. All necessary geometrical data for model construction is provided below.

In order to avoid issues regarding different implementations of absorption or impedance conditions, we have chosen to prescribe the un-coupled reverberation time in each room so that the material properties can be calibrated as best possible for each method.

For simplicity, reverberation times shall be calibrated by adjusting material properties of walls uniformly for each room (i.e. the six walls of each room shall have the same material definitions) to match the prescribed reverberation times from the up-scaled scale model.

In addition to the vertex/plane & coordinate/connectivity data provided below, two SketchUp models are also provided which you may find useful as well as several model images.

- **FullScaleModels.skp** presents the two rooms independently, in the calibration condition. This also allows for the computation of surface areas and volumes if desired.
- **FullScaleModels_Coupled.skp** presents the rooms in the coupled test configuration. The different parts can be hidden or displayed through layers in both files.

Document Contents

GENERAL MODEL CONDITIONS

Atmospheric conditions for the full-scale conditions are 20°C and a relative humidity of 50%. All coordinated are in meters.

For comparison purposes, we have limited the study to 1 kHz octave band results. As such, the calibration procedure and subsequent simulations need only be carried out in this octave band.

The aperture's interior boundary surfaces should be attributed the same material properties as the reverberation chamber in the coupled model condition. Scattering coefficients of 20% in Room 1 and 10% in Room 2 are suggested.

Measurements have been carried out in the model for two source and two receiver positions in the reverberation chamber and two source and four receiver positions in the main room, providing a spatial sampling of the acoustic field. The corresponding positions are provided below. If for any reason you must limit yourself to a single source/receiver in each room then please use the ones indicated with an asterisk (*).

ROOM 1: MAIN/LARGE ROOM

1. VERTEX/CORNERS

ID	x	y	z
1	0.000	0.000	0.000
2	1.600	43.700	0.000
3	21.600	43.700	0.000
4	23.600	0.000	0.000
5	0.000	0.000	18.000
6	1.560	42.600	18.000
7	21.650	42.600	18.000
8	23.600	0.000	18.000

2. FACE/PLANES

ID	Corner IDs			
1	4	3	2	1
2	5	6	7	8
3	1	2	6	5
4	4	8	7	3
5	2	3	7	6
6	1	5	8	4

3. REVERBERATION TIME

	1/1 octave band 1kHz*
Rev. time T30 (s)	1.26
Standard deviation (s)	0.070

4. SOURCES

ID	x	y	z
S1*	14.8	7.00	3.60
S2	5.60	5.00	3.60

* If only one source is used

5. Receivers

ID	x	y	z
R1	8.0	18	11
R2	14	24	6.4
R3	16	29	9.4
R4	8.0	36	5.0

ROOM 2: REVERBERATION CHAMBER/SMALL ROOM

1. Vertex/Corners

ID	x	y	z
101	0.000	-0.240	0.200
102	1.003	-12.600	0.200
103	23.800	-12.600	0.200
104	23.800	-0.240	0.200
105	0.000	-0.240	18.000
106	1.100	-13.800	18.000
107	23.800	-13.800	18.000
108	23.800	-0.240	18.000

2. Face/Planes

ID	Corner IDs			
101	101	102	103	104
102	108	107	106	105
103	105	106	102	101
104	103	107	108	104
105	106	107	103	102
106	101	104	108	105

3. Reverberation Time

	1/1 octave band 1kHz*
Rev. time T30 (s)	4.52
Standard deviation (s)	0.10

4. Sources

ID	x	y	z
S3*	6.00	-8.25	3.80
S4	5.20	-4.25	3.80

* If only one source is used

5. Receivers

ID	x	y	z
R5	12	-8.25	10.2
R6	18	-6.25	8.2

ROOM 1+2 : COUPLED ROOM JOINT MODEL UNDER STUDY

1. VERTEX/CORNERS

ID	x	y	z
1	0.000	0.000	0.000
2	1.600	43.700	0.000
3	21.600	43.700	0.000
4	23.600	0.000	0.000
5	0.000	0.000	18.000
6	1.560	42.600	18.000
7	21.650	42.600	18.000
8	23.600	0.000	18.000
101	0.000	-0.240	0.200
102	1.003	-12.600	0.200
103	23.800	-12.600	0.200
104	23.800	-0.240	0.200
105	0.000	-0.240	18.000
106	1.100	-13.800	18.000
107	23.800	-13.800	18.000
108	23.800	-0.240	18.000
201	15.100	0.000	5.600
202	8.500	0.000	5.600
203	8.500	0.000	12.100
204	15.100	0.000	12.100
211	15.100	-0.240	5.600
212	8.500	-0.240	5.600
213	8.500	-0.240	12.100
214	15.100	-0.240	12.100

2. FACE/PLANES

ID	Corners				Associated room material
1	4	3	2	1	Main room
2	5	6	7	8	Main room
3	1	2	6	5	Main room
4	4	8	7	3	Main room
5	2	3	7	6	Main room
101	101	102	103	104	Rev. chamber
102	108	107	106	105	Rev. chamber
103	105	106	102	101	Rev. chamber
104	103	107	108	104	Rev. chamber
105	106	107	103	102	Rev. chamber
201	4	1	202	201	Main room
202	1	5	203	202	Main room
203	5	8	204	203	Main room
204	8	4	201	204	Main room
211	211	212	101	104	Rev. chamber
212	212	213	105	101	Rev. chamber
213	213	214	108	105	Rev. chamber
214	214	211	104	108	Rev. chamber
221	201	202	212	211	Rev. chamber
222	203	204	214	213	Rev. chamber
223	202	203	213	212	Rev. chamber
224	201	211	214	204	Rev. chamber

3. SOURCES

ID	x	y	z
S1*	14.8	7.00	3.60
S2	5.60	5.00	3.60

* If only one source is used

4. RECEIVERS

ID	x	y	z
R1	8.0	18	11
R2	14	24	6.4
R3	16	29	9.4
R4	8.0	36	5.0

DATA SUBMISSION

Please submit calculated room impulse response data of the two uncoupled/calibration rooms and for the coupled room test condition. The first allows us to confirm a common understanding of the calibration method. Please use the Room, Source, and Receiver ID numbers in the file name (rm{1,2,1+2}_s{1,2}_r{1,2,3,4}.wav). Please provide data in audio WAV format.

In addition, please provide a short description of the numerical method employed, and any pertinent parameters.

All individual entry data and curves will remain anonymous, but will would like to present a list of the methods used and possible group similar methods if there are more than one. Please let us know if this poses a problem.

It is fully our intention to submit the results of this study as a referred journal article (short format) before the end of the year.

Please send your calculated RIRs in a single ZIP file to brian.katz@sorbonne-universite.fr.

If you have any questions, please feel free to contact me at brian.katz@sorbonne-universite.fr.

Appendix C

Other piers of Notre-Dame de Paris

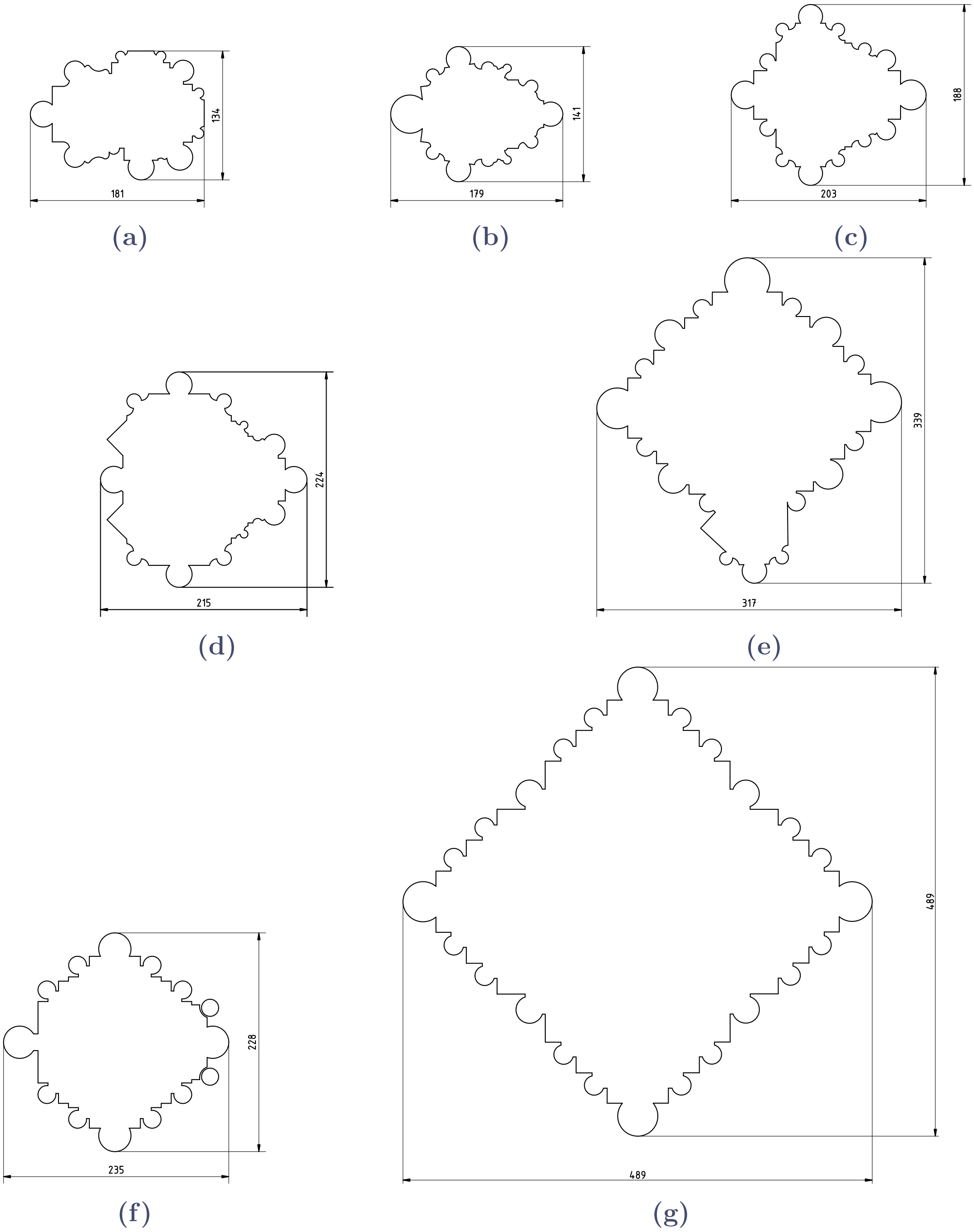

Figure C.1 (a) North choir ambulatory. (b) Radiating chapel. (c) South-east crossing. (d) North-east crossing. (e) South choir aisle entrance. Tower: (f) ambulatory and (g) nave.